Alma Mater Studiorum – Università di Bologna

Dottorato di Ricerca in Geofisica
XXIV ciclo

Integrating new and traditional approaches for the estimate of slip-rates of active faults: examples from the Mw 6.3, 2009 L'Aquila earthquake area, Central Italy

Settore Concorsuale di afferenza: 04/A4/Geo10 – GEOFISICA DELLA TERRA SOLIDA

Presentata da: Riccardo Civico

Coordinatore Dottorato **Relatore**

Prof. Michele Dragoni **Dott. Paolo Marco De Martini**

Esame finale anno 2012

To Giulia

Abstract

This thesis developed a multidisciplinary and multi-scale investigation strategy based on the integration of traditional and innovative approaches aimed at improving the normal faults seimogenic identification and characterization, focusing mainly on slip-rate estimate as a measure of the fault activity.

The L'Aquila Mw 6.3 April 6, 2009 earthquake causative fault was used as a test site for the application, testing, and refinement of traditional and/or innovative approaches, with the aim to 1) evaluate their strength or limitations 2) develop a reference approach useful for extending the investigation to other active faults in the area and 3) translate the results of the the methodological approaches as new inputs to local seismic hazard.

The April 6, 2009 L'Aquila earthquake occurred on a so far poorly known tectonic structure, considered having a limited seismic potential, the Paganica - San Demetrio fault system (PSDFS), and thus has highlighted the need for a detailed knowledge in terms of location, geometry, and characterization of the active faults that are the potential sources for future earthquakes.

To fill the gap of knowledge enhanced by the occurrence of the 2009 L'Aquila earthquake, we developed a multidisciplinary and scale-based strategy consisting of paleoseismological investigations, detailed geomorphological and geological field studies, as well as shallow geophysical imaging, and an innovative methodology that uses, as an alternative paleoseismological tool, core sampling and laboratory analyses but also *in situ* measurements of physical properties.

The integration of geomorphology, geology as well as shallow geophysics, was essential to produce a new detailed geomorphological and geological map of the PSDFS and to define its tectonic style, arrangement, kinematics, extent, geometry and internal complexities.

Our investigations highlighted that the PSDFS is a 19 km-long tectonic structure characterized by a complex structural setting at the surface and that is arranged in two main sectors: the Paganica sector to the NW and the San Demetrio sector to SE. The Paganica sector is characterized by a narrow deformation zone, with a relatively small (but deep) Quaternary basin affected by few fault splays. The San Demetrio sector is characterized by a strain distribution at the surface that is accommodated by several tectonic structures, with the system opening into a set of parallel, km-spaced fault traces that exhume and dissect the Quaternary basin.

The integration of all the fault displacement data and age constraints (radiocarbon dating, optically stimulated luminescence (OSL) and tephrochronology) resulting from paleoseismological, geomorphological, geophysical and geological investigations played a primary role in the estimate of the slip-rate of the PSDFS. Slip-rates were estimated for different time intervals in the Quaternary, from Early

Pleistocene (1.8 Ma) to Late Holocene (last 5 ka), yielding values ranging between 0.09 and 0.58 and providing an average Quaternary slip-rate representative for the PSDFS of 0.27 - 0.48 mm/yr.

We contributed also to the understanding of the PSDFS seismic behavior and of the local seismic hazard by estimating the max expected magnitude for this fault on the basis of its length (ca. 20 km) and slip per event (up to 0.8 m), and identifying the two most active fault splays at present. Our multidisciplinary results converge toward the possibility of the occurrence of past surface faulting earthquakes characterized by a moment magnitude between 6.3 and 6.8, notably larger than the 2009 event, but compatible with the M range observed in historical earthquakes in the area. The slip-rate distribution over time and space and the tectonic style of the PSDFS suggested the occurrence of strain migration through time in the southern sector from the easternmost basin-bounding fault splay toward the southwestern splays. This topic has a significant implication in terms of surface faulting hazard in the area, because it can contribute defining the fault splays that have a higher potential to slip during future earthquakes along the PSDFS.

By a methodological point of view, the multidisciplinary and multiscale-based investigation strategy emphasizes the advantages of the joint application of different approaches and methodologies for active faults identification and characterization.

Our work suggests that each approach alone may provide sufficient information but only the application of a multidisciplinary strategy is effective in providing a proper framework of active faults and robust results.

TABLE OF CONTENTS

Acknowledgements

First and foremost I offer my sincerest gratitude to my supervisor, Paolo Marco De Martini, who has supported me throughout my thesis with his patience and knowledge. Without his encouragement and effort this thesis would not have been completed or written. One simply could not wish for a better and friendlier supervisor.

I would like to express my deep and sincere gratitude to Daniela Pantosti. Her wide knowledge and her logical way of thinking have been of great value for me. Her understanding and encouraging have provided a good basis for the present thesis.

I'm also grateful to Stefano Pucci for guiding me through part of this thesis and for transferring me his experience, enthusiasm and for sharing a lot of fieldwork.

I'm much obliged to Marina Iorio, for her valuable instructions and suggestions throughout this thesis and for giving me the opportunity to collaborate with the IAMC-CNR.

Special thank goes to Steven G. Wesnousky, for the stimulating discussions and for being supportive during my time at the Center for Neotectonic Studies, University of Nevada, Reno.

During this work I have collaborated with many researchers for whom I have great regard, and I wish to extend my warmest thanks to all those who have helped me with my work at the Istituto Nazionale di Geofisica e Vulcanologia: Francesca Romana Cinti, Carlo Alberto Brunori, Antonio Patera, Alessandra Smedile, Paola Del Carlo, Andrea Cavallo, Luigi Improta, Guido Ventura, Stefania Pinzi, Luigi Cucci…..a complete list is impossible!

I'm greatly indebted to the Istituto Nazionale di Geofisica e Vulcanologia for the financial and logistical support.

I'm also grateful to other PhD students who shared study and laughter in Rome: special thanks to "i ragazzi del Pollajo".

I owe my loving thanks to Simona. Without her encouragement and understanding it would have been impossible for me to finish this work.

Finally, I am forever grateful to my mom and to my family, for supporting me through my never-ending education.

1 Introduction

Italy is one of the areas with the highest seismic hazard in the Mediterranean region. The Italian seismic history is characterized by a 2,000 yr-long history of small-to-large magnitude earthquakes occurred through the centuries that often have left a strong imprint on the country's heritage, economy, but also landscape.
One of these events was the Mw 6.3 April 6, 2009 L'Aquila earthquake, that struck a densely populated area in the central Apennines causing more than 300 casualties and leaving more than 60,000 homeless.
This earthquake was the strongest in Italy since the Mw 6.9 1980, Irpinia event and it was the first that struck so close to a densely populated Italian town (L'Aquila; ca 70,000 inhabitants) since the Mw 7.1 1908, Messina earthquake.
The L'Aquila Mw 6.3 April 6, 2009 earthquake struck a sector of the central Apennines that is characterized by the presence of several active faults accommodating prevalent NE-SW oriented extension. Some of these faults activated during historical times producing earthquakes with M up to 7; this magnitude seems to represent the Max magnitude expected for the area also on the basis of tectonic, geologic, and geomorphic observations from nearby faults.
The present knowledge on the active faults in this area derives from decades of studies in geomorphology and Quaternary geology as well as from some paleoseismological investigations. The April 6, 2009 L'Aquila earthquake is probably the best seismologically, geodetically and geologically documented earthquake so far in Italy. The large amount of experimental data acquired during the whole L'Aquila sequence concurred to image the fault that slipped during the event. This fault was reported in some of the pre-earthquake active fault compilations although, it was poorly known and because of this, considered with a limited seismic potential.
Besides underlining the fragility of our residential, historical, and monumental patrimony, the 2009 L'Aquila earthquake has highlighted the need for a detailed knowledge in terms of location, geometry, and characterization of the active faults that are the potential sources for future earthquakes. This is because, a systematically developed knowledge of the location and of the seismogenic behavior of the active faults in a region, is an innovative and relevant contribution to seismic hazard. More specifically it is a contribution to the development of earthquake recurrence and segmentation models as input for time-dependent probabilistic SHA, to the modeling of ground-motion scenarios and to the definition of fault hierarchy, evolution, migration for surface faulting hazard estimates.

To fill the gap of knowledge enhanced by the occurrence of the 2009 L'Aquila earthquake, this thesis was thought to contribute to a better knowledge of the earthquake source fault with the idea of developing a reference approach useful for extending the investigation to other active faults in the area. Actually, the focus of

this thesis was established a few months before the occurrence of this earthquake and was mostly centered on a methodological analysis and the application of different traditional and innovative approaches for the estimate of active fault slip-rates. This core of the thesis was not changed, but it was readdressed on one specific fault: the 2009 L'Aquila earthquake fault. Practically, the estimate of the slip-rate of the fault by using different approaches remains the leading subject of the thesis but, this methodological part has now an immediate practical application in the improvement of the understanding of L'Aquila 2009 earthquake fault.
Thus, the thesis has developed following a twofold path: on the one side, the application, testing, and improvement of traditional or innovative approaches for slip rate estimates, on the other side, the study of the L'Aquila earthquake fault by applying what learned methodologically to provide new inputs to local seismic hazard. Slip-rate and Max expected magnitude are the critical parameters to input in seismic hazard calculations. Slip rate is a measure of the activity of a fault as it represents the amount of strain it accommodated during a given period of time. Max magnitude is strictly related to the size of the slipping fault that is given by length and amount of coseismic slip. A further needed contribution for seismic hazard, that was strongly highlighted for the first time in Italy by the 2009 earthquake, was the definition of the surface faulting hazard (e.g. the Tempera aqueduct pipe broke because crossed by surface faulting). This awareness stimulated a substantial refinement of the fault mapping, including also the minor and blind active fault traces with the aim to define those that have a higher potential to slip during future earthquakes.

During the three years of doctorate we developed a multidisciplinary and scale-based strategy consisting of paleoseismological investigations, detailed geomorphological and geological field studies, as well as shallow geophysical imaging, and an innovative methodology that uses, as an alternative paleoseismological tool, core sampling and laboratory analyses but also *in situ* measurements of physical properties. The different approaches were integrated to provide the best slip-rate estimate for the 2009 earthquake fault, to map the fault component at the surface and to define the fault segment boundaries.
In particular we performed a three steps approach:
1) paleoseismological, including a trenching and coring campaign with the excavation of 4 trenches and the realization of 2 boreholes;
2) geomorphological and geological, integrating field survey and dating of Quaternary layers by means of Optically Stimulated Luminescence (OSL), radiocarbon dating and tephrochronology together with LiDAR-derived high resolution DEM and air-photo analysis;
3) geophysical, including high resolution petrophysical correlations, electrical resistivity tomography (ERT) and shallow seismic profiling.

The present thesis is composed of nine chapters. Apart for this introduction (namely chapter 1) a brief outline of each of the following chapters is given below.

Chapter 2 summarizes the basic concepts on faulting, and then focuses on describing some main parameters constraining the geometries of active normal faults as well as geological and geomorphological elements characterizing them. A brief description of slip-rate significance is provided too.
Chapter 3 gives a brief overview of the Mw 6.3 April, 6 2009 L'Aquila earthquake and its seismic sequence and then focuses on the coseismically induced effects on the environment, with special attention to the displacement field as imaged by DInSAR and GPS and to the surface ruptures detected during the geologic field survey performed in the epicentral area. A brief discussion on the questions raised by the occurrence of this earthquake is presented too.
Chapter 4 summarizes the main seismotectonic characteristics of the central Apennines, focusing in particular on the present-day deformation.
Chapter 5 presents the paleoseismological approach to the characterization of active faults and illustrates the main results of a paleoseismological campaign carried out across the northwestern portion of the PSDFS with the main goal to reconstruct the recent seismic history of the PSDFS and to estimate the short-term slip-rate (up to ~30 ka).
Chapter 6 introduces the basic methodologies of the geomorphological and geological investigations in active areas with particular attention to the identification, and characterization of the long-term expression of faults through the study and dating of continental deposits and landforms affected by different fault splays. The results of the detailed survey carried out in the Middle Aterno valley over an area of ~140 km^2 supported by extensive thematic mapping is presented too. The main goal of this chapter was to provide new insights on the Quaternary deformational history of the fault and to obtain a long-term slip-rate estimate (~2 Ma).
Chapter 7 illustrates the main results always in terms of offset measurement, fault location, and slip rates estimates of a multidisciplinary and multiscale-based geophysical investigation approaches; these includes an innovative methodology based on measurements of physical properties, 2D-electrical resistivity tomography (ERT), and high-resolution seismic tomography. For each of the methodology applied we have discussed both the benefits and limitations
Chapter 8 integrates and discusses the main results and implications of this thesis and presents some perspectives about its possible contribution to seismic hazard assessment.
The Conclusion chapter (namely 9), shortly summarizes the different phases of the development of this thesis, the results from each of the approaches employed and discuss their integration in the key of the seismic hazard of the area.

2 Active faults in geology

The most common class of active faults found in Central Italy are normal faults, in good agreement with the present-day regional stress conditions showing that the Apenninic belt is undergoing extension (Montone et al., 1999; Mariucci et al., 2010). Because extensional tectonics prevails in the study area, in this chapter, after a brief description of some basic concepts on faulting, we will focus on the description of geological and geomorphological evidence of active normal faults and of their evolution.

2.1 Faults: basic concepts

2.1.1 Faults and stress

Faulting occurs in response to imposed stresses and is fundamentally a brittle mechanism for achieving shear displacement along discrete fracture surfaces, under conditions of low temperatures and confining pressures.
The displacement observed along a fault can be achieved in several ways:

- by a single fault surface;
- by a "fault zone", composed of numerous sub-parallel and interconnecting closely spaced fault surfaces;
- by a shear zone, where shear displacement is achieved by a wide zone of distributed simple shear that accommodates movement of one side of the shear zone relative to the other. Shear zones are common at deep crustal level, where temperatures and confining pressures are greater.

Anderson (1905, 1951) developed the modern mechanical concepts of the origin of faults and highlighted their role in tectonics. He recognized that principal stress orientation could vary among geological provinces within the upper crust of the Earth and postulated a fundamental relationship between fault types and the orientation of the causative stress tensor relative to the Earth's surface.
Considering the boundary between the Earth surface and the atmosphere a no-shear plane and the Earth as a perfect sphere, Anderson pointed out that one principal axis of crustal stress tensors will, at any point, be close to vertical (perpendicular to the Earth's surface) and the other two axes close to horizontal (figure 2.1).
The type of faulting depends upon the principal stress directions in combination with the Coulomb criterion of failure. According to the theory of Anderson, if principal stress direction near or at the Earth's surface is vertical, and if the angle of internal friction for most rocks is about 30°, only three basic fault types should be able to form. In particular, normal, strike-slip, and thrust faults occur depending on whether $\sigma 1$, $\sigma 2$ or $\sigma 3$ respectively, is vertical.
Even if this theory is conceptually useful, it is an approximation and it does not explain the occurrence of some faults, such as low-angle normal faults (with dips of

≤30°), flat thrust faults, or faults that develop in previously fractured, anisotropic rock.

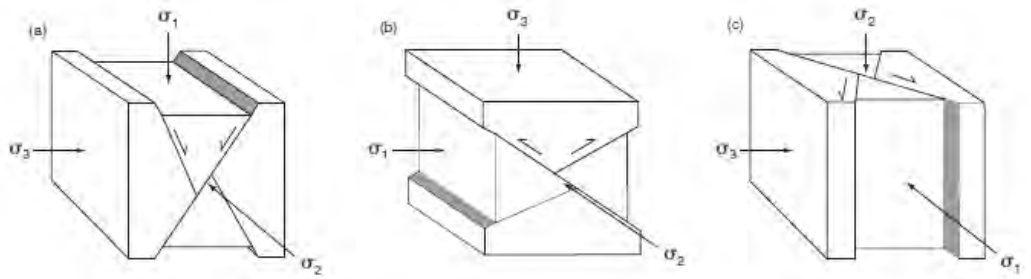

Figure 2.1 - Schematic representation of the three classes of faults determined by the orientation of the principal stresses: (a) normal fault; (b) thrust fault; (c) strike-slip fault (after Angelier, 1994). σ1, σ2 or σ3 are the three principal stress directions.

We can also identify main classes of faults with respect to the absolute direction, sense and magnitude of movement. These three components constitute the slip, which represent the actual displacement. On this basis we can recognize (figure 2.2):

- Strike-slip faults, accommodating horizontal slip between adjacent blocks;
- Dip-slip faults, characterized by translation directly up or down the dip of the fault surface. Movement on a dip-slip fault is described with respect to the relative movement of hanging wall and footwall.

Moreover, in the broad field of dip-slip faults, we can distinguish normal-slip faults, thrust-slip, reverse-slip faults (including thrust) and oblique-slip faults. A normal-slip fault, in particular, is one in which the hanging wall moves down with respect to the footwall.

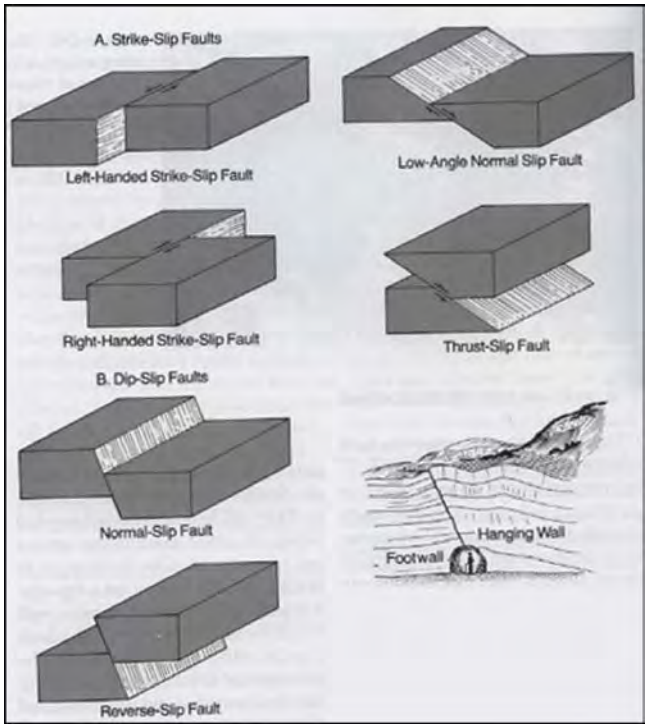

Figure 2.2 - Faulted blocks showing the characteristic displacement for the different classes of faults (modified after Davis and Reynolds, 1996).

Fault systems can range in length and displacement from small breaks with millimetric offset to regional crustal structures extending hundreds to more than 1000 km and accommodating up to hundreds of km offset.

2.1.2 Fault growing

How do faults grow from an initial rupture to a mature geological fault?
Cartwright et al. (1995) suggested two models for fault growth from an initial rupture to a mature geological fault (figure 2.3): 1) radial propagation and 2) segment linkage:

- During fault growth by radial propagation, an individual fault simply lengthens over time and accumulates displacement according to a well-defined linear relationship. Displacement increases steadily as the fault grows (figure 2.3a).
- Alternatively, small individual fault segments (t1) can gradually link up to create one large fault. In this case the total length of the fault suddenly increases, whereas the total displacement does not substantially change (t2). Over time, the composite fault may smooth out the slip deficit near the former segment boundaries (t3), re-adjusting the shape of the displacement profile following the idealized bow-shaped displacement gradient (figure 2.3b).

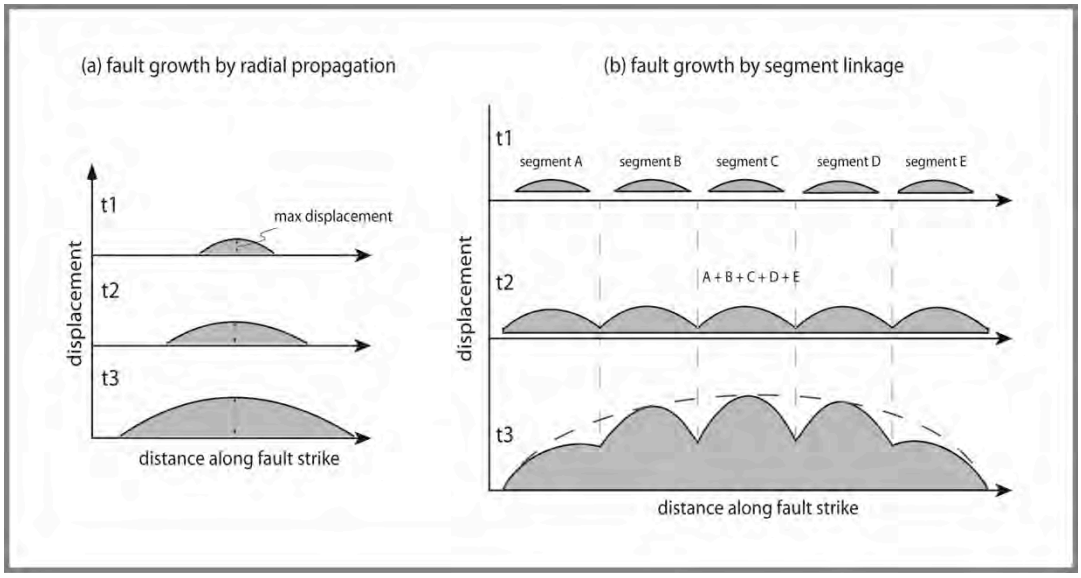

Figure 2.3 – (a) Growth of an idealized individual extensional fault (redrawn from Cartwright et al., 1995), and (b) of an idealized extensional fault array.

2.2 Active faults

2.2.1 Definition

The activity of a fault is generally defined by the way it cumulates displacement over time; we can think about an active fault as one that cumulated some displacement in the recent past and is considered likely to move again in the near future.
There is not a fixed rule about what time scale should be used to address the activity of a fault:

- According to Slemmons & De Polo (1986), to define a fault as active, we must identify two key elements: 1) the potential or probability of future displacements in the present tectonic regime; 2) the timing of the most recent displacements (historical, Holocene (11.7 ka), Quaternary (2.6 Ma) or “in the present seismotectonics regime”);
- Boschi et al. (1996) proposed a "Consensus Statement" in which "An active fault of interest for Seismic Hazard Assessment is a structure that has an established record of activity in the Late Pleistocene (i.e. in the past 125 ka) and a demonstrable or inferable capability of generating major earthquakes.";
- The State of California, in the 2007 Alquist-Priolo Earthquake Fault Zoning Act define an active fault as one which has “had surface displacement within Holocene time (11.7 ka)”;
- In the Basin and Range Province, the WSSPC - Western States Seismic Policy Council (2011) defines three classes of active faults: 1) Holocene fault – a fault whose movement in the past 11,700 calibrated years B.P.; (Cohen and Gibbard, 2010) has been large enough to break the ground surface; 2) Late

Quaternary fault – a fault whose movement in the past 130,000 years has been large enough to break the ground surface; 3) Quaternary fault – a fault whose movement in the past 2,600,000 (Cohen and Gibbard, 2010) years has been large enough to break the ground surface;

- The International Atomic Energy Agency (IAEA) guidelines (2010) make a distinction between active structures in different tectonic settings by proposing to consider an Upper Pleistocene-Holocene time frame in interplate regions and a Pliocene-Quaternary time frame in intraplate regions.

2.2.2 Faults and slip accumulation models

In order to classify fault behavior, not in function of time, Schwartz and Coppersmith (1984) proposed three models of displacement associated with individual earthquakes (figure 2.4):

Several different scenario have been proposed to accommodate a given regional strain field: in the variable slip model (a), both the amount of slip at a given point and the length of rupture may vary between successive earthquakes, producing variability in earthquake size and a uniform slip-rate along the length of the fault. In the uniform slip model (b) there is a constant displacement per event at any point, a constant slip-rate all along the fault and a constant magnitude of large earthquakes, with more frequent moderate sized events. If the fault ruptures producing earthquakes with about the same magnitude, then the fault is said to generate characteristic earthquake (c). In this latter case the displacement per event is the same at any point, while the slip-rate is variable along the length of the fault.

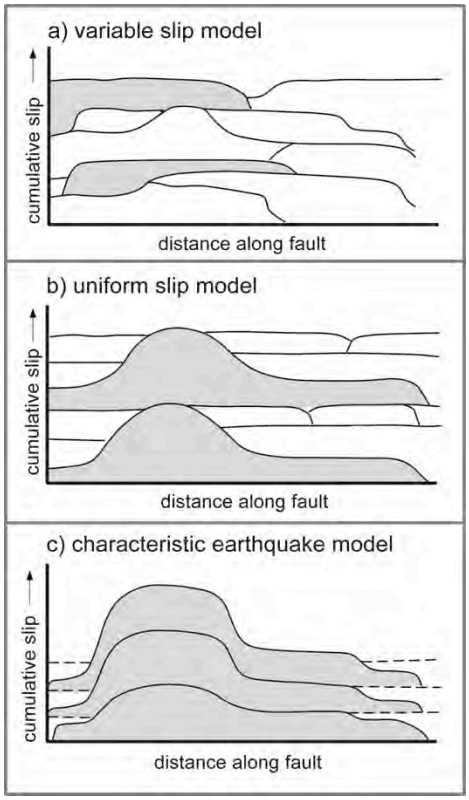

Figure 2.4 - Diagrammatic representation of three hypothetical models of slip accumulation. (redrawn from Schwartz and Coppersmith (1984).

2.2.3 Faults and strain release models

Reid (1910) proposed a theory for the earthquake cycle known as "elastic rebound theory". According to him, elastic strain accumulates for a long period on a locked fault (interseismic phase), until strain reaches a critical value (elastic limit) and the frictional resistance is overcome. An earthquake occurs when a sudden displacement of the two sides of the fault takes place to reach a position of minimum strain (coseismic phase). A third phase of the seismic cycle correspond to a period of minutes to years after an earthquake when the crust and fault both "adjust" to the modified state of crustal stress caused by the occurrence of the earthquake (postseismic phase).

Fault activity over time has been described in the literature by four main strain release models (figure 2.5).

In the "perfectly periodic" (a) model (Reid, 1910), the elastic strain energy accumulated across completely locked faults is periodically released during earthquakes of fairly uniform slip and recurrence interval. On the other and, some researchers highlighted that the time until the next earthquake and the size of earthquakes on a particular fault are not perfectly periodic and proposed two models: "time-predictable" model and the "slip-predictable" model (Shimazaki and Nakata, 1980). According to the "time-predictable" model (b), earthquakes always occur when a critical stress threshold is attained. In this model, the time of the next

earthquake can be predicted based on the slip-rate of the fault and on the size of the previous event. Alternatively, the "slip-predictable" model (c) suggests that, for any given event, all the strain energy accumulated since the last earthquake is released. This model, based on the slip-rate of the fault and on the time since the last earthquake, is able to predict the size, but not the time, of the next seismic event. All the three models assume a constant rate of far-field displacement and strain accumulation. Some faults may be characterized, at different time scales, by temporal grouping of slip events releasing the strain energy (Wallace, 1987). This latter behavior (d) is characterized by a great increase in the slip-rate for a relatively short period, separated by long quiescence intervals.

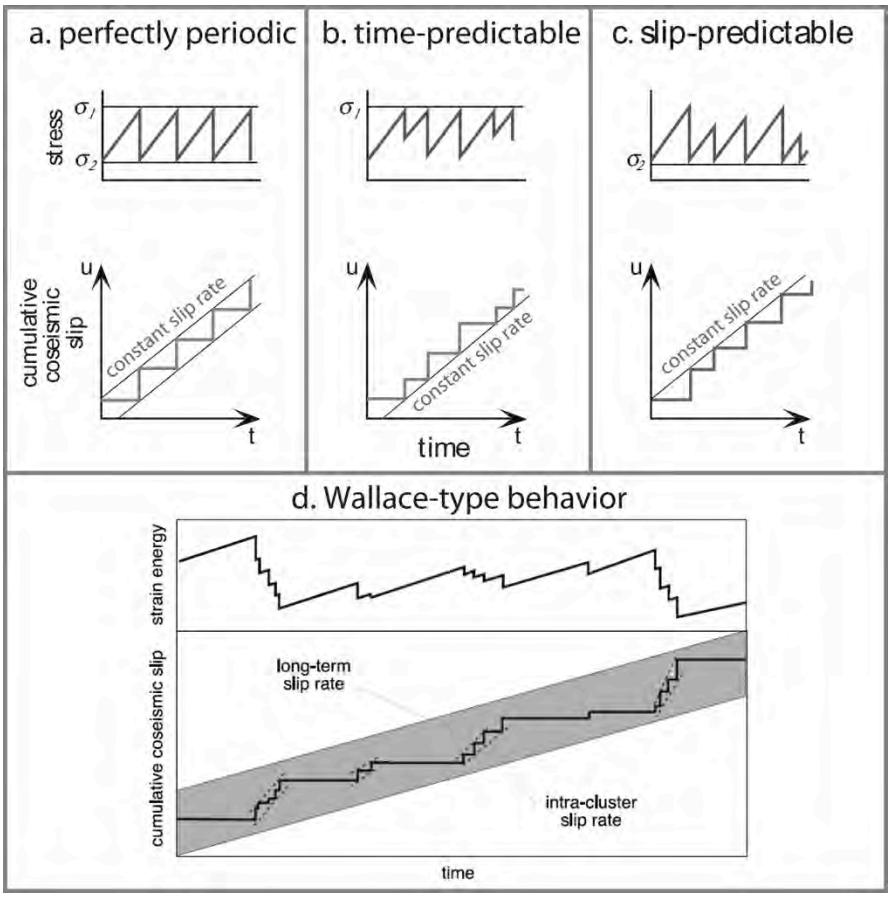

Figure 2.5 - Strain release models for earthquakes (a - c redrawn after Scholz [1990], d from Friedrich et al., 2003])

2.2.4 Faults geometry and regional stress field

We have seen in the previous section that normal faulting accommodates extension and vertical shortening, and can occur in settings where the maximum compressive stress (σ1) is vertical and there is a deviatoric tensile stress in a horizontal orientation.

Normal faults are the dominant fault class along mid-oceanic spreading centers and in rifted continental margins, as well in continental sedimentary basins and in passive margins and they represent a way in which individual rock layers, or the lithosphere itself, can lengthen and stretch in brittle or semibrittle fashion.
A great variety of normal faulting styles have been seen, or inferred, from geological outcrops or indirect geophysical surveys, including steep planar faults, strongly curved listric (concave-up) faults that become virtually flat within the upper crust, and very low-angle faults dipping at less than 20°.
For the purposes of this thesis, we will mainly focus on active normal faulting in continental regions undergoing extension today, trying to obtain different sources of information.
Regions of active continental extension experiencing present-day normal faulting include the western U.S.A., Greece, western Turkey, Italy, the Gulf of Suez, Tibet, Yunnan, Mongolia, the Lake Baykal region, parts of China and East Africa. Seismological and surface observations of seismogenic normal faults in all the above mentioned regions provide information on the three-dimensional geometry of the present-day extensional deformation.
If we look at earthquake focal depths the most important observation is that earthquakes are usually confined in the upper 10-20 km of the crust (Jackson and White, 1989).
The thickness of this seismogenic layer appears to influence the length scale of the deformation in the crust, in particular with respect to the lateral continuity of normal faults and width of the extensional basins (graben) that form in extensional provinces.
Continental normal fault systems are commonly segmented, and the maximum segment length appear to be influenced by the seismogenic thickness (T_s), being typically ~20-25 km-long with T_s ~ 15 km and increasing to ~60-100 km with the T_s ~30-35 km (Jackson and White, 1989; Wallace, 1989; Jackson and Blenkinsop, 1997;).
Control on maximum width of tilted-blocks or half-graben is supported by observations showing that maximum half-graben widths are typically ~10-25 km where T_s is 15 km but can be much wider (up to 60 km) in those parts of East Africa where T_s ~30-35 km (Jackson and Blenkinsop, 1993).
Observations coming from continental normal faulting earthquakes in a variety of location worldwide show a characteristic pattern of dips at depth that are typically confined to a range of about 30-65°, whether determined from body-wave focal mechanism, waveform modeling or centroid moment tensor (CMT) analyses (figure 2.6).

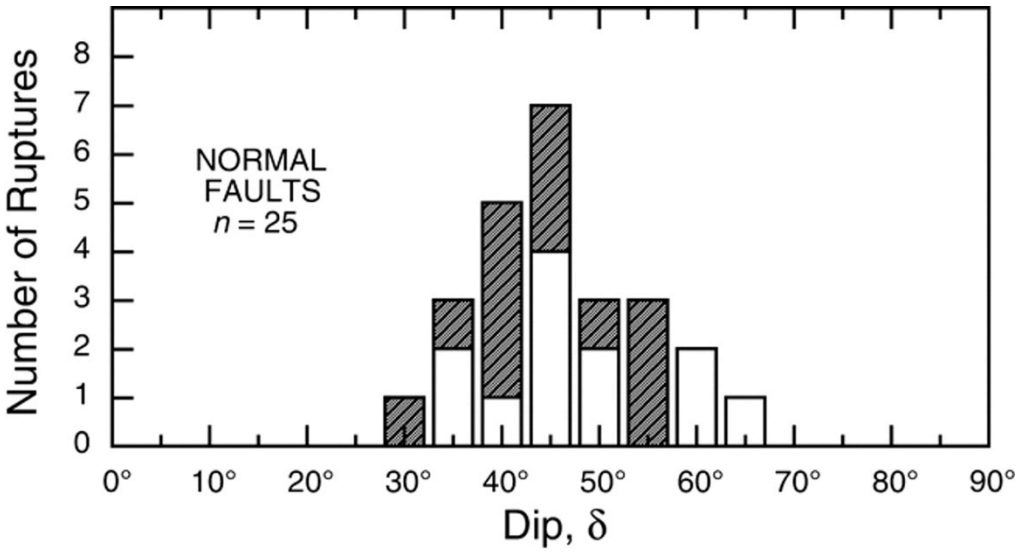

Figure 2.6 – dip distribution for continental normal faulting earthquakes with M>5.5, from compilation of Jackson and White (1989) (no pattern) and Collettini and Sibson (2001) (after Collettini and Sibson (2001)).

A schematic cross section of a region where normal faults are the dominant fault class emphasizes the presence of a set of different structures (figure 2.7).
The upper or overlying block along the master fault plane is called the hanging wall; the block below is called the footwall.
Other structures may develop mainly within the hangingwall block:

- synthetic faults (dipping in the same direction with similar sense of throw);
- antithetic faults (dipping in the opposite direction with an opposite sense of throw);
- horst, that are uplifted, unrotated blocks bounded on either sides by outward-dipping normal faults;
- graben, relatively down-dropped, unrotated block, bounded on either side by inward-dipping normal faults.

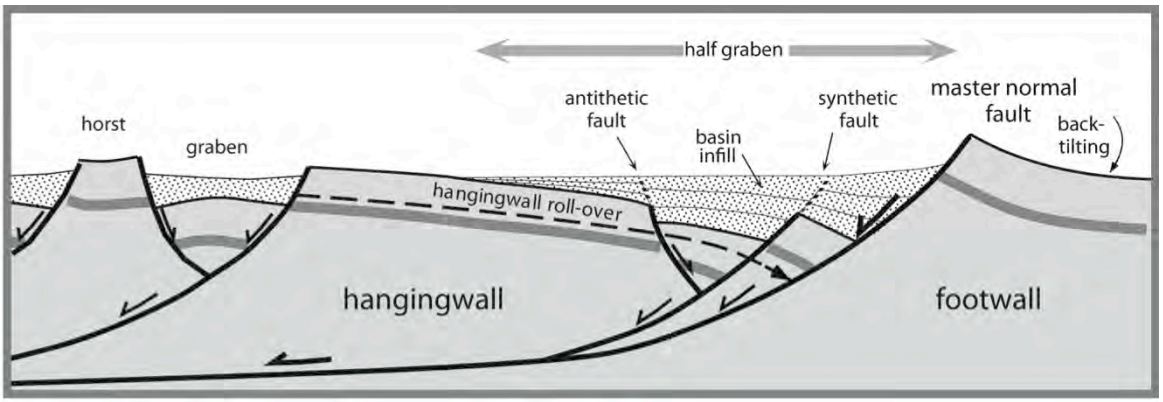

Figure 2.7 - idealized schematic cross section of a region undergoing extension (modified after Burbank and Anderson, 2001).

2.2.5 Geologic evidence of active normal faults

One of the most simple but convincing evidence of fault activity is the cross-cutting or non-cross-cutting relationship with geologic deposits of known age. The age of the offset unit and the amount of the offset can be used to calculate the fault slip-rate and thus to estimate the fault activity.

A wide variety of types of geologic deposits are commonly used in evaluating fault activity, most commonly alluvial and volcanic deposits. Chronological constraints can be obtained by means of a variety of relative and absolute dating methods; some of them will be discussed more in detail in chapter 6.

The structural aspects of geologic units adjacent to faults may also provide information about activity of a fault. Adjacent units may be brecciated and shattered, have open fissures, be tilted or warped.

2.2.6 Landforms associated with active normal faults

Some of the most remarkable topography on land and beneath the oceans is associated with crustal extension and normal faulting. Classic examples are the rift valleys, typically observable along the axes of oceanic ridges and at smaller scale on continents (i.e. the East African Rift system) and the Basin and Range Province, within the western United States.

Landscape development is the results of the interplay between tectonic processes (faulting and folding) that tend to build topography and erosional/depositional processes at the surface that act to restore the equilibrium. The basic concept is that any ongoing change in style, rate, and location of tectonic processes is able to produce, under favorable conditions, detectable changes in the landscape, creating disequilibrium in the geologic and geomorphic processes.

Earthquakes, for example, have the capability to produce instantaneous permanent deformations of the ground surface that reflect the movements occurred as a result of deep-seated processes. Landform development can thus be closely related to the active deformation taking place in the Earth's crust.

For the purposes of this thesis we will focus on those landform features produced by repeated movements along continental active normal faults as results of repeated seismic events.

Active normal faulting produces mainly vertical deformations and tends to build a typical tectonically rising and subsiding landscape characterized by key features that include the following:

- fault scarps;
- triangular facets: roughly planar surfaces with broad bases and upward-pointing apexes that occur between valley that drain the mountain ranges;
- linear and steep mountain fronts;
- fault-bounded basins.

At the time scale of a single earthquake, the most obvious manifestation of active deformation at the surface are coseismic fault scarps, tectonic landforms generally coincident with a fault plane and produced almost instantaneously when an earthquake rupture propagates up to the surface. Scarp formed by normal faulting earthquakes are generally located along preexisting faults at the contact between bedrock and colluvial or alluvial deposits or can occur as fresh, steeply inclined scarps within unconsolidated sediments (figures 2.8 – 2.9). Normal fault scarps resulting from a single increment of displacement along a fault can range in height from few centimeters to more than 10 meters.

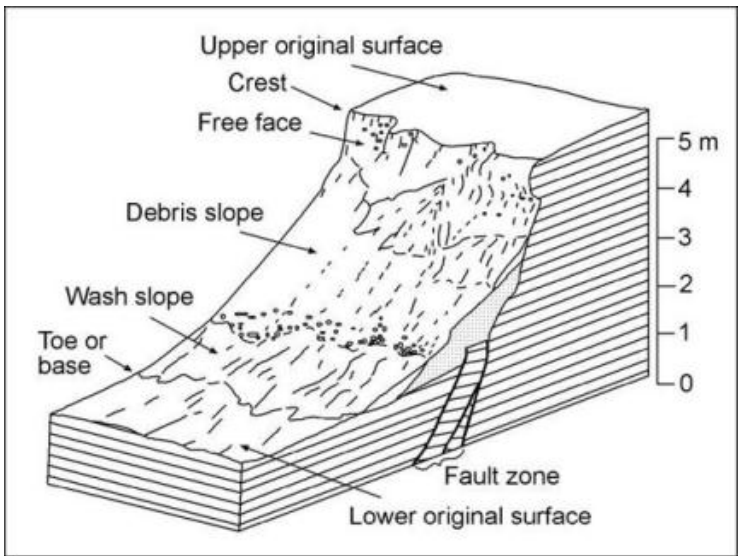

Figure 2.8 - Basic slope elements that may be present on a piedmont fault scarp (after Wallace, 1977).

Figure 2.9 - Coseismic fault scarp of the 1915 Pleasant Valley (Ms 7.7) earthquake

A more detailed description of the geomorphic characteristics of young fault scarps can be found in Wallace, 1977.

Repeated displacements along the same fault can concur to form a compound fault scarp (Slemmons, 1957), also called composite (Stewart and Hancock, 1990) or multiple-event fault scarps, as the one visible in figure 2.10.

Figure 2.10 - Compound fault scarp – Humboldt range, Nevada, USA

At a mature stage, when deformation has been cumulated for several seismic cycles, normal faulting generates a characteristic basin and range topography, common in regions of presently active extension like large parts of Nevada, Utah, Greece, western Turkey and Italy.
In these regions the most evident landforms are mountain fronts that represent zones of topographic transition between uplifted mountains and plains. A typical normal fault mountain front is characterized by an assemblage of landforms that includes the escarpment, the streams that dissect it and the adjacent piedmont landforms (figure 2.11).

Figure 2.11 - Stillwater range, Dixie Valley, Nevada

The cumulative displacements on a range-bounding normal fault create disequilibrium and a base-level fall that causes deep valleys (e.g. wine glasses valleys) to be carved in the relatively uplifted footwall block and favors the

sedimentation of alluvial-fan deposits in the subsided hangingwall (figure 2.12 - modified after Keller and Pinter, 2002).

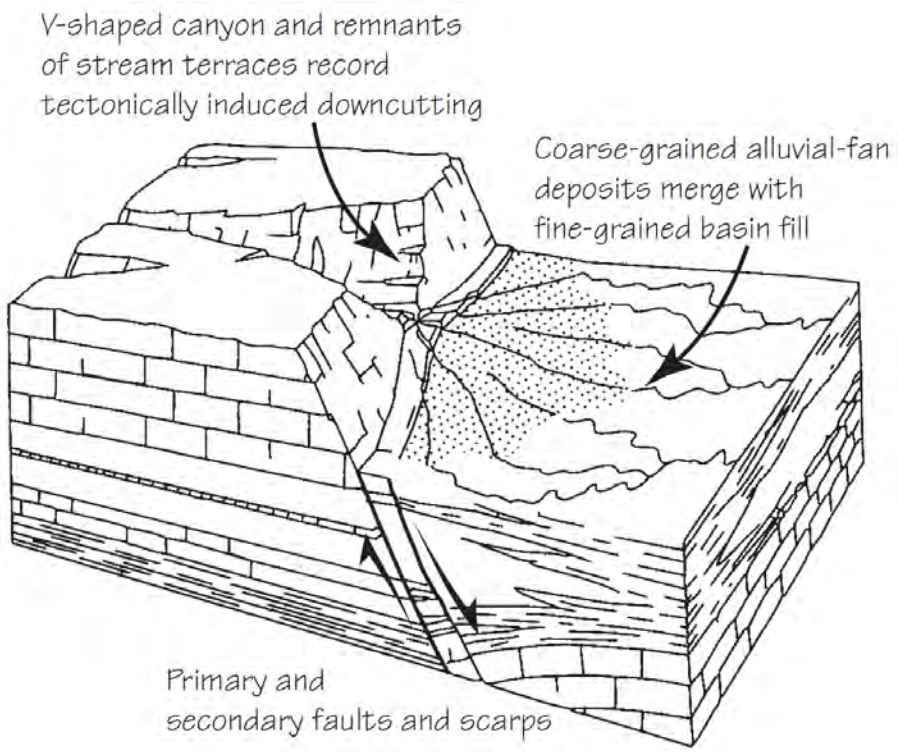

Figure 2.12 - idealized diagram showing the topographic expression of an active normal fault system (after Bull, 2007).

An ideal sequential development of a single fault-generated mountain escarpment is well depicted in figure 2.13 and may be useful to visualize some of the concepts showed before. Initial faulting creates a linear scarp (A) that later on tends to migrate away from the base of the rising range (B). At stage C, tectonically induced valleys are notched into the rising block; the occurrence of earthquakes along the same structure maintains a steep, straight mountain front (D). After cessation of uplift, or with more competitive erosional processes, the mountain front becomes sinuous and the relief starts to degrade, lowering the ridgecrests (E).

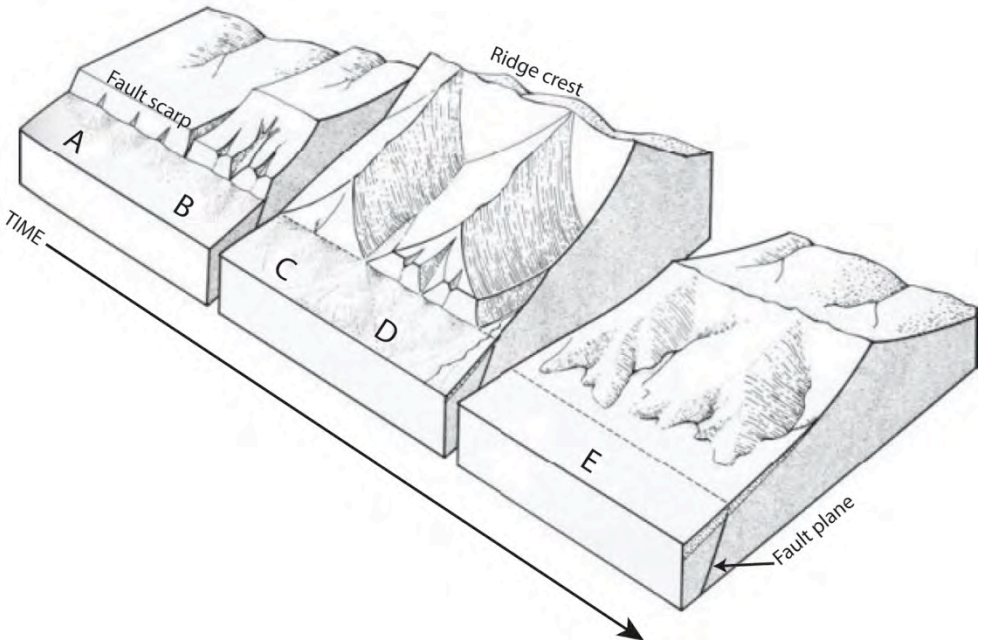

Figure 2.13 - block diagram showing the sequential development of a single fault-generated mountain escarpment (modified after Wallace, 1977)

2.3 Examples from the Basin and Range Province and from the Walker Lane, Nevada, USA

During the time I spent at the Center for Neoteconic Studies of the University of Nevada, Reno, I had the opportunity to visit some of the best morphological expressions of active normal faults in the western U.S.A., in particular the Humboldt Range and the Wassuk Range, located in the Basin and Range Province and the Walker Lane, respectively.

The Humboldt range is a uplifted block with important normal faults on both E-W sides (horst) composed primarily of Permo-Triassic metasedimentary and intrusive rocks (Silberling and Wallace, 1967; Wallace et al., 1969), with peaks rising to elevations of ~ 2900 m a.s.l. close to the adjacent basins laying at ~ 1300 m a.s.l..

Figure 2.14 is a large-scale view of the Humboldt Range, where the morphological expression of Quaternary displacement is greater along the western flank, with a set of range-front normal faults and series of echelon scarps along piedmont faults.

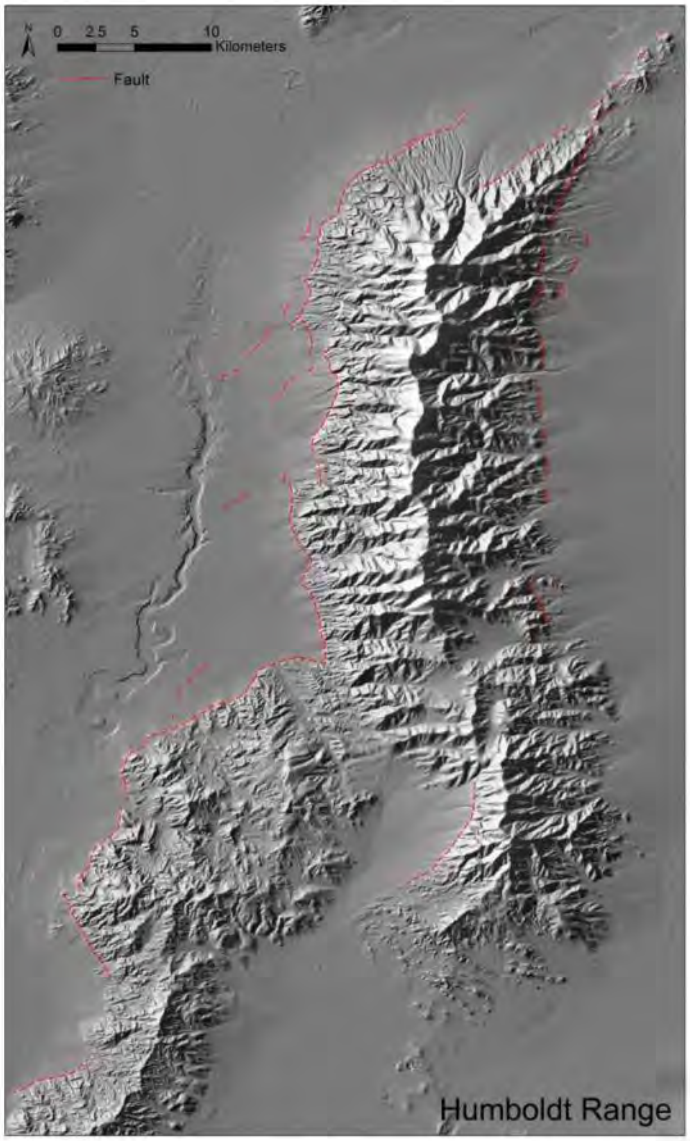

Figure 2.14 – Shaded relief of the Humboldt Range

Youthful and repeated movement along the range-bounding faults is expressed by offset of highstand shoreline features (figure 2.15) of pluvial Lake Lahontan (about 13 ka - Adams & Wesnousky, 1999) and by the truncation and progressively increasing offset of older alluvial fan surfaces (figure 2.16).

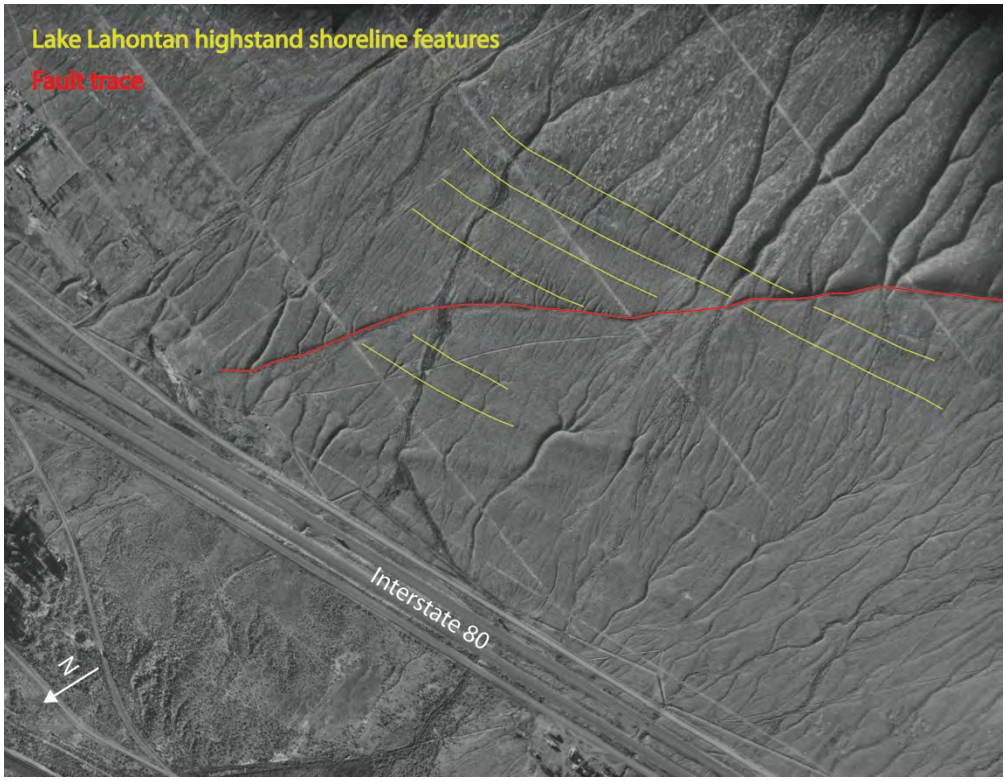

Figure 2.15 - Fault scarp truncating the highstand shoreline features of pluvial Lake Lahontan along the northern end of the fault – Humboldt Range, Nevada, USA

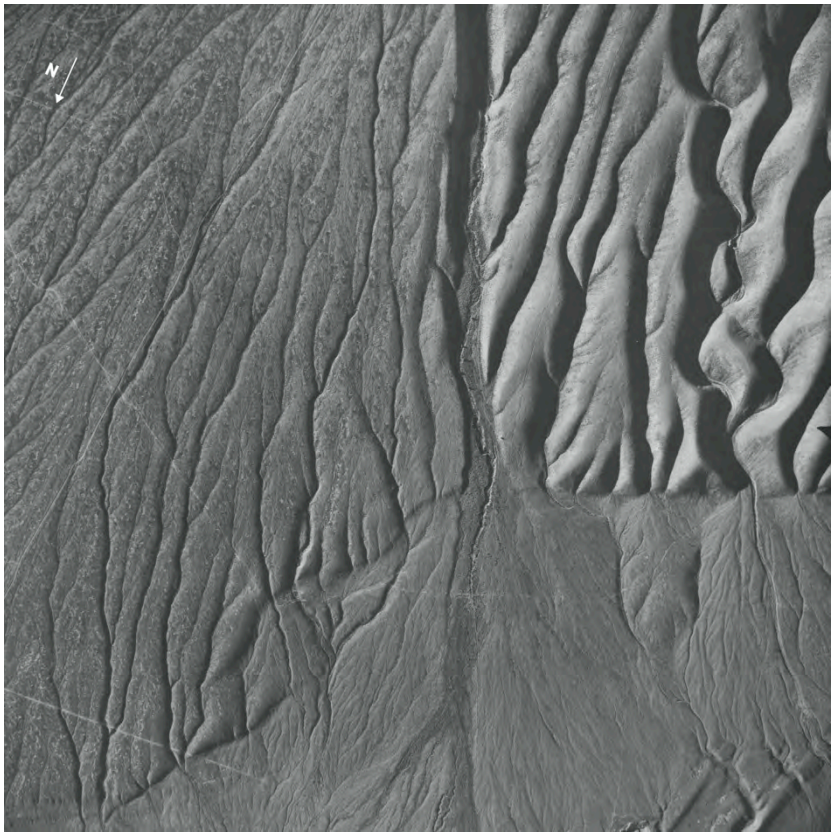

Figure 2.16 - Aerial view of alluvial fan surfaces showing progressively increasing offset; the older alluvial surface (on the right) is characterized by greater uplift and dissection – Humboldt Range, Nevada, USA

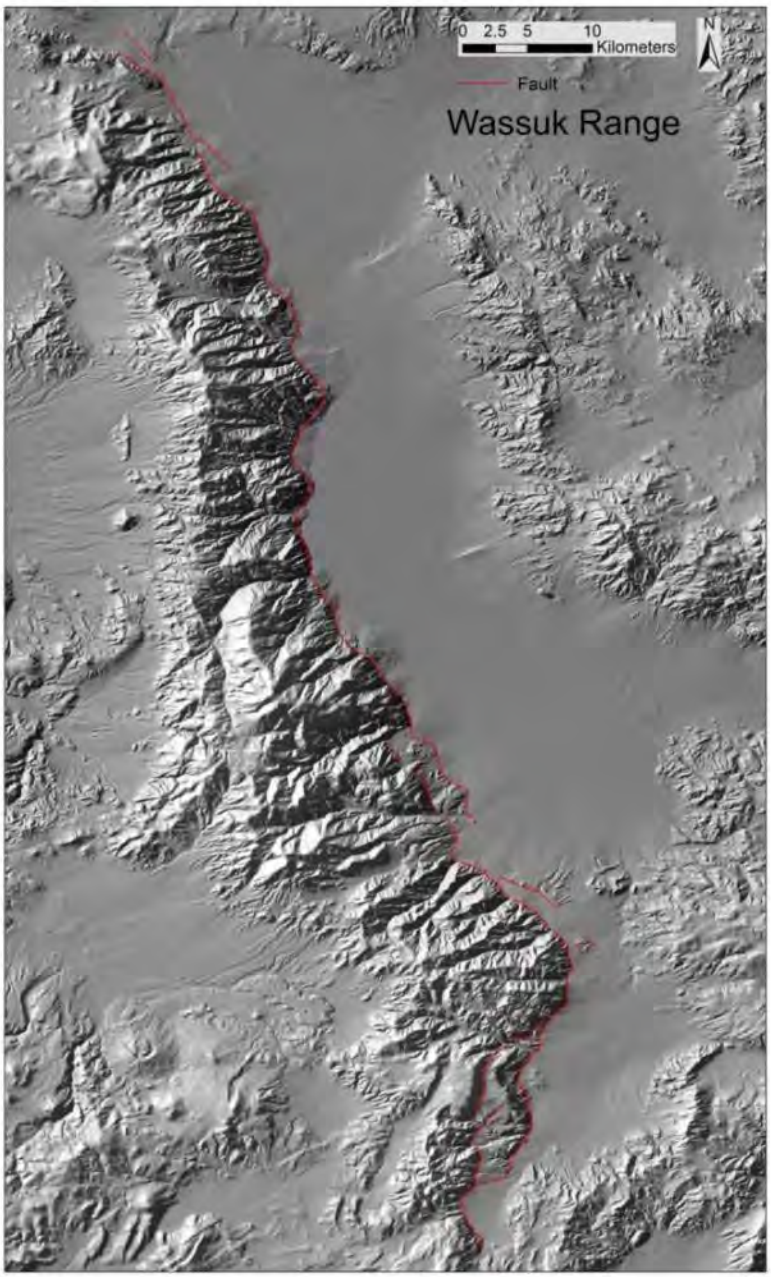

Figure 2.17 – Shaded relief view of the Wassuk Range

Moreover, the Wassuk Range is an east-tilted actively uplifting mountain block composed predominantly of granite with lesser amounts of granodiorite and metavolcanics located near the western margin of the Great Basin. The range strikes northwesterly about 90 kilometers and reaches elevations of more than 3000 m; the adjacent basin being partially filled by the Walker lake.

The overall morphology is dominated by the steep east flank, bounded by a high-angle normal fault with an abrupt sinuous trace and triangular facets, reflecting active normal faulting (figure 2.17 and 2.18).

Figure 2.18 - steep mountain front along a portion of the east flank of the Wassuk Range, Nevada, USA

Chronological constraints of the Quaternary activity of this fault come from Late Pleistocene shorelines related to the highstand of pluvial Lake Lahontan (about 13 ka - Adams & Wesnousky, 1999), preserved along the mountain front. Holocene fault scarps are present along the entire rangefront and at the mouths of active drainages commonly reach 4 to 6 m height, (figure 2.19). Longer-term Quaternary offset is visible in 20 m to 40 m high scarps truncating older alluvial fan surfaces along the northern sector of the range (Wesnousky, 2005).

Figure 2.19 - Quaternary fault scarp in alluvial fan deposits along the northern portion of the Wassuk Range, Nevada, USA

2.4 Slip-rate

The main subject of this thesis is the slip-rate and the different methodologies that can concur to estimate it.

Fault slip-rate is essentially a space/time problem, which in geology translates into a displacement/age problem.

More in detail, the slip-rate represents the amount of strain that accumulates and then is released across a fault in a given time period and is defined as the ratio of slip (displacement) to the time interval over which that slip occurred.

A key fact about slip-rate to keep in mind is that it does not represent constant motion along a fault, even though the motions of tectonic plates are constant. Instead, the slip-rate represents an average of the total slip along a fault over a certain period of time.

Slip-rate is one of the fundamental descriptors of fault activity and represents a key in understanding the relative "importance" of faults in an area, as well as tectonic activity and earthquake recurrence in a region.

As a consequence, slip-rates are critical input data for assessing the seismic hazard assessment (SHA) of active fault zones. For this reason a great amount of efforts is spent trying to estimate slip-rates and discriminate between seismically active and inactive faults.

There are several ways to estimate the slip-rate of an active fault. In any case, we need a data set containing fault displacement and precise age control on deformed deposits spanning a significant portion of a fault's life.

These data are often difficult to find, mainly because their preservation requires a delicate balance to be maintained between sedimentation, erosion, regional tectonic uplift and fault displacement through sufficiently long periods of time.

In order to obtain these data, we can use both direct and indirect approaches.

Direct approaches are those mainly related to geological disciplines, such as geology, geomorphology and tectonic, while indirect approaches are commonly related to geophysical disciplines, such as seismology, geodesy and subsurface geophysics.

Depending on the type of the available information, fault slip-rates can be estimated at different spatial and temporal scales. It is possible to estimate fault slip-rates over spans of millions of years (several seismic cycles of large-magnitude earthquakes on a fault) to hundreds of years (a single seismic cycle, or a part of a cycle).

Moreover, it is possible to estimate fault slip-rates taking into account the deformation recorded by an entire range front, or using the cumulative displacement on a surface (an alluvial fan surface, i.e.) as well as analyzing a single-event displacement.

A common and direct way to estimate the slip-rate of a fault is to find a geological or morphological feature, the age of which can be determined, that has been offset by the fault being studied. A faulted paleosurface, which may contain deposits suitable to be dated, is an excellent example. Dividing the offset showed by the two portions

of the paleosurface by the estimated time since the paleosurface was first created (before it was cut by the fault), it is possible to estimate a slip-rate for the fault.
It is important to note that geological slip-rate rate estimates are minimum estimates, because the feature used to define fault offset formed some unknown time prior to fault initiation.

3 The Mw 6.3 6 April 2009 L'Aquila earthquake

The April 6, 2009 L'Aquila earthquake, with its long aftershock sequence, probably produced the largest amount of experimental data ever recorded in Italy for a single earthquake. These include seismological, geodetic, subsurface exploration and geological data.
For the purposes of this thesis, after a brief overview of the seismic sequence and of the main event, we will focus on coseismically induced deformations on the environment, with special attention to the displacement field as imaged by DInSAR and GPS and to the surface effects and ruptures detected during the geologic field survey.

3.1 Seismic sequence and causative fault

On April 6, 2009 (01:32 UTC – 03:32 Italian time), a strong earthquake (Mw6.3) struck a densely populated area in the Apennines portion of the Abruzzi region and was felt in a wide area of central Italy (figure 3.1). More than 300 people were killed and 70000 were left homeless. Although seismic hazard maps considered this area as one with the highest earthquake probability, this disaster highlighted the fragility of our historical towns and the need for a better understanding of the Italian active faults and of their seismic potential. Data recorded by permanent and temporary stations of the National Seismic Network (RSNC) managed by the Istituto Nazionale di Geofisica e Vulcanologia (INGV), by the national and local geodetic network, remote sensing and geologic data, all allowed to define the space-time evolution of the entire seismic sequence and to obtain important information on the location and geometry of the fault system responsible for the event.

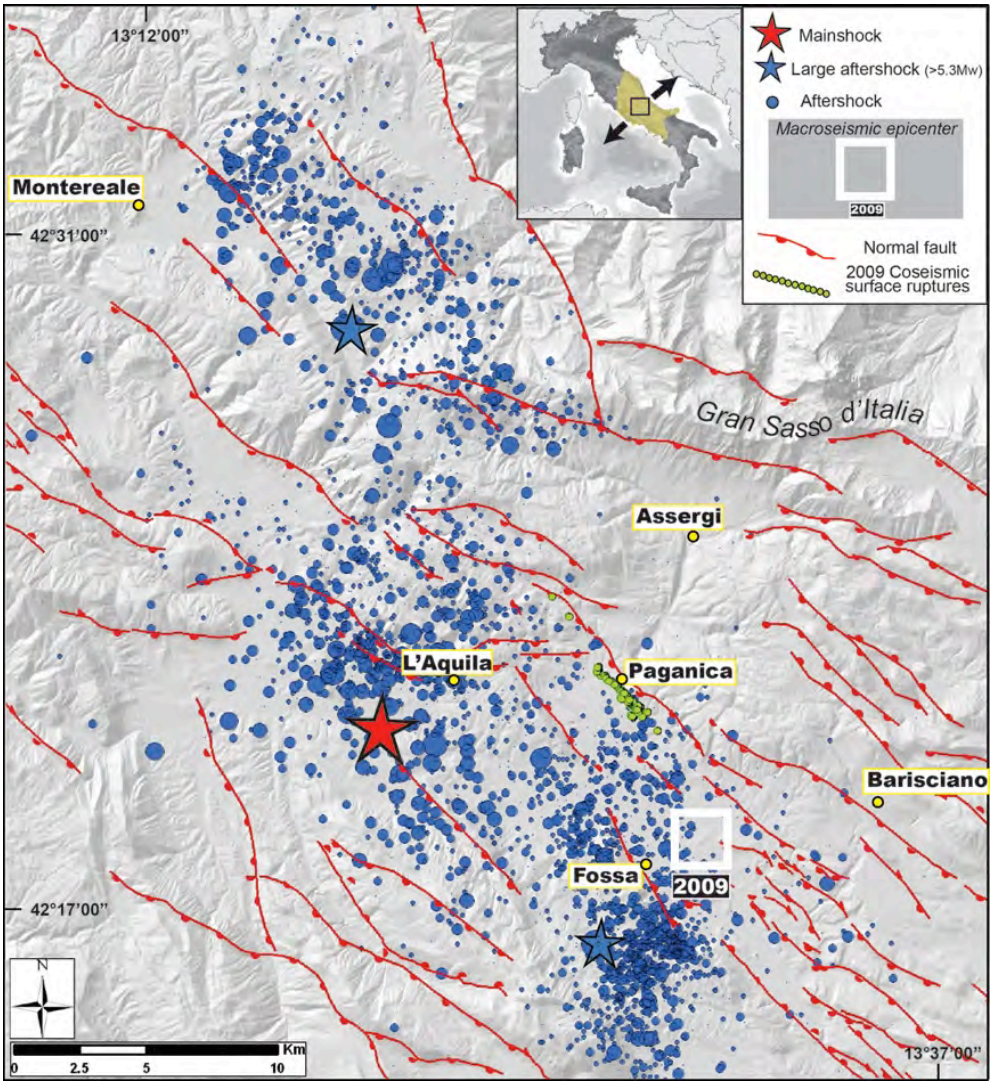

Figure 3.1 - The 2009 L'Aquila seismic sequence as recorded by the INGV Italian National Seismic Network (Chiarabba et al., 2009). Focal mechanism of the main shock and of the two largest aftershocks (Pondrelli et al., 2010) are shown (modified after Cinti et al., 2011). The macroseismic epicenter location (from damage and felt reports) of the 2009 event was computed using the Code Boxer 4.0 (Gasperini et al., 2010). The white box is the projection to the surface of the ~ 18 km-long fault modeled by Cirella et al., (2009). The white line is the expected emergence of the fault at surface. The inset in the upper right shows the direction of extension across the central Apennines (black arrows) and the regional felt area for the 6 April mainshock (colored area).

3.1.1 The Seismic sequence

The Mw 6.3 April 6, 2009 mainshock was preceded by a long seismic activity characterized by a sequence of foreshocks clustering around the main shock nucleation area. This foreshock sequence started in October 2008 and culminated with a Mw 4.4 event on march 30 2009 and a Mw 4.2 earthquake a few hours before the mainshock. The main shock is located just beneath the town of L'Aquila and nucleated in the upper crust at a depth of ~9.5 km.

Following the April 6 mainshock, a total area of more than 1000 km^2 was interested by a sequence of aftershocks, occurring both to the northeast and to the southeast

with respect to the mainshock epicenter (figure 3.1). The 2009 L'Aquila seismic sequence activated a normal fault system reaching a total length of about 50 km in the NW-trending direction. Most of the events show hypocentral depths ranging from ~15 km to ~2 km, within the typical seismogenic thickness of central Apennines. Moreover, the southern seismicity cluster was characterized by the deepest hypocentral depths, with earthquakes deeper than 20 km.

A total of seven $M_W \geq 5$ and numerous $M_W \geq 4$ aftershocks occurred during the weeks after the mainshock, with more than 30,000 seismic events recorded during the whole sequence.

The plot in figure 3.2 shows the cumulative energy released during the 2009 L'Aquila seismic sequence (from January to July 2009). It is noticeable that the relative contribution in terms of energy related to the whole foreshock sequence is comparable to the energy released by the Mw 4.4 event of March30, while is clear that most of the energy released in the whole seismic sequence is related to the Mw 6.3 April 6, 2009 mainshock. Taking into account this information, we can expect that most of the coseismic deformation at depth and at the surface is related to the April 6 mainshock.

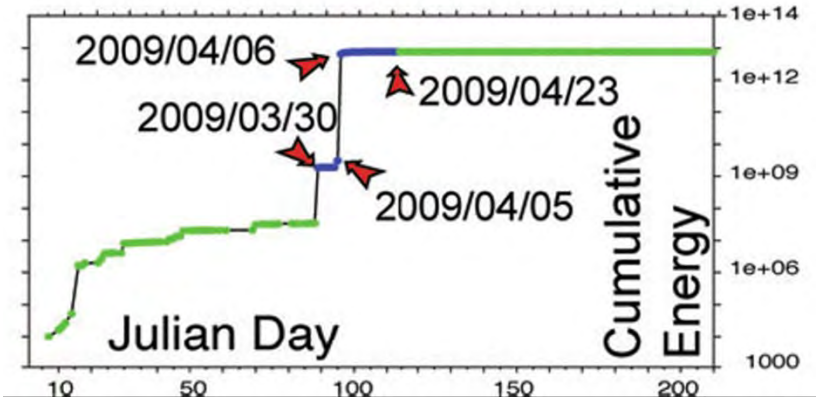

Figure 3.2 – Cumulative seismic energy release (joule) from January to July 2009 (after Pondrelli et al., 2010).

Looking at the focal mechanisms of the larger earthquakes, we can see that the entire seismic sequence is dominated by NE-SW oriented extension, in good agreement with geodesy and regional tectonics (figure 3.3), with only few events showing a strike-slip component (Pondrelli et al., 2010).

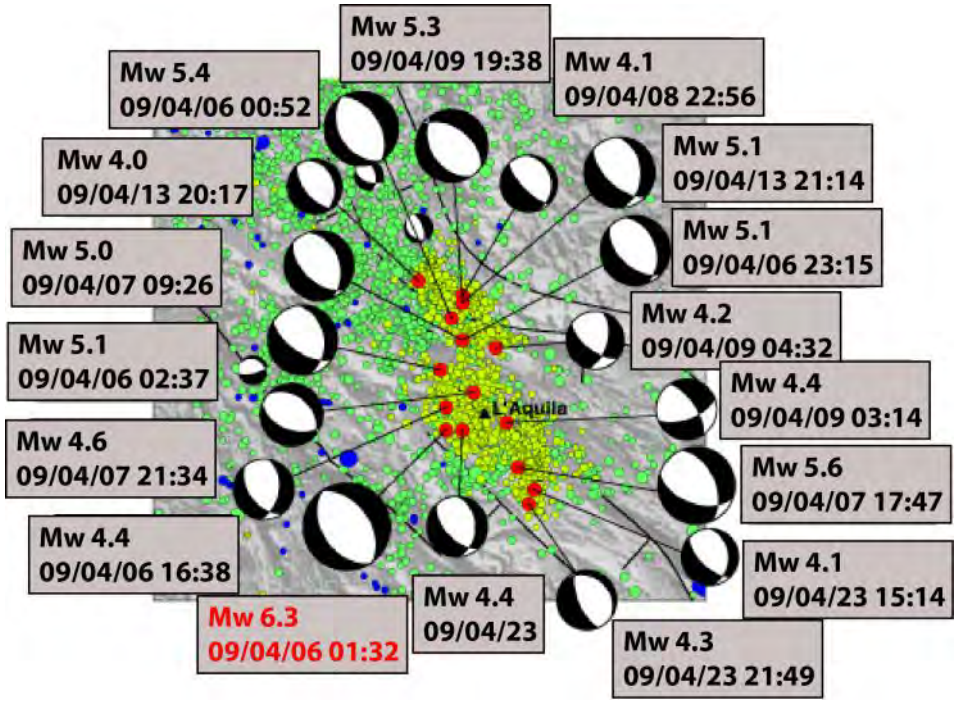

Figure 3.3 - Regional centroid moment tensors (RCMTs) with their epicenters (in red) and the smaller magnitude events of the L'Aquila 2009 seismic sequence (in yellow, Chiarabba et al. 2009). In the background (green and blue dots) previous seismicity (CSI, Castello et al. 2007) and previous available RCMTs (small focal mechanisms, Pondrelli et al. 2006; http://www.bo.ingv.it/RCMT/Italydataset.html). (Modified after http://www.bo.ingv.it/indagini-terremoto-del-06042009-in-abruzzo-laquila.html)

Although the magnitude of the mainshock is not among the largest occurred in the central Apennines in the past, the L'Aquila earthquake can be considered one of the most disastrous of the last century. The earthquake caused more than 300 deaths and left sixty thousand homeless. Severe damage was observed in the town of L'Aquila and in several villages within a radius of ~50 km. The partial or complete collapse of a significant number of old or badly maintained buildings occurred but also some reinforced concrete buildings collapsed. The very strong ground motion occurred especially close to the fault, with accelerations up to 0.63 g (Akinci et al., 2010), likely increased the damage. The effects of the shaking were recorded not only in the epicentral zone but also in distant areas like the city of Rome (~90 km from the epicenter).

The macroseismic survey performed after the main shock (Galli and Camassi 2009) shows that the largest damage is distributed in a NW-SE oriented direction, with a maximum assessed intensity of 9–10 MCS (Mercalli – Cancani - Sieberg scale) and a total of 16 localities suffering intensity larger than 8 MCS (figure 3.4).

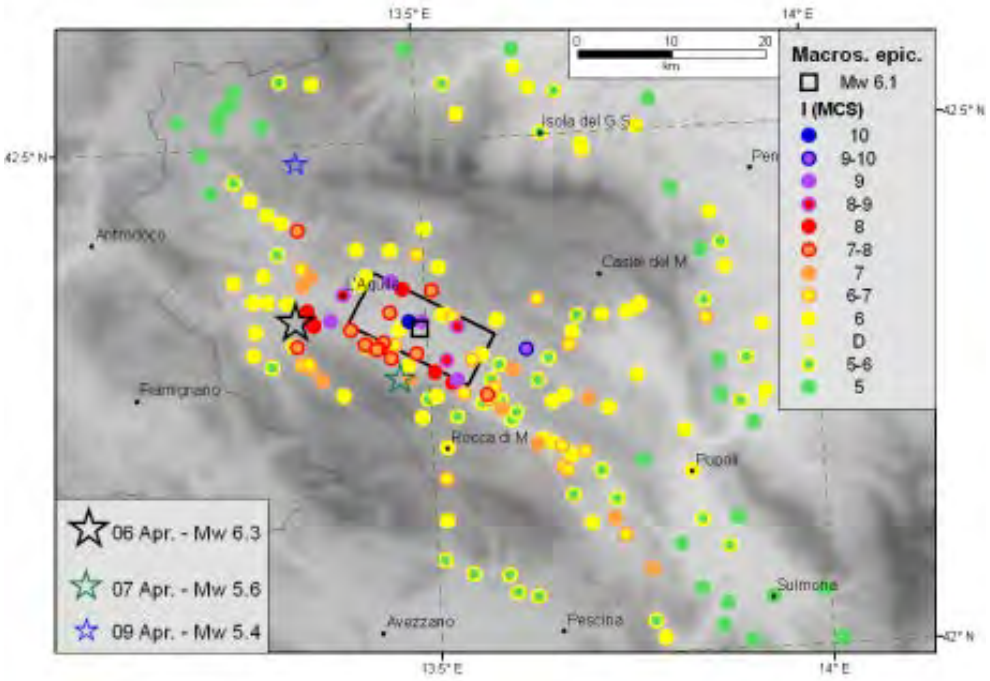

Figure 3.4 – Map showing the results of the macroseismic survey. The black rectangle indicates the macroseismic box based on the distribution of macroseismic intensities. (after Galli and Camassi, 2009).

3.1.2 The earthquake causative fault: the Paganica fault

The large amount of data acquired during the sequence was used to constrain the location and the geometry of the fault system responsible for the 2009 L'Aquila mainshock. In particular the aftershocks distribution (figure 3.5), together with DInSAR analysis, body waves seismology, strong motion records and GPS observations and surface faulting all concurred to image the geometry of the fault responsible for the 6 April main shock.

Source modeling resulting from the inversion of geodetic and seismological data revealed a heterogeneous slip distribution on the fault plane (Anzidei et al., 2009; Atzori et al., 2009; Cheloni et al., 2010; Cirella et al., 2009; Pino & Di Luccio, 2009; Trasatti et al., 2011). The rupture pattern was characterized by two main slip patches: the largest slip concentration at depth was located southeastward from the hypocenter and showed a maximum slip of ~1.1 m; a second smaller patch was observed above the hypocenter and was characterized by a maximum slip of ~0.7 m. The rupture history is characterized by directivity effects, with an up-dip initial rupture propagation followed by a second rupture propagating along fault strike to the south-east (Cirella et al., 2009; Pino & Di Luccio, 2009). Slip on the fault plane is predominantly normal dip-slip (Chiarabba et al., 2009; Pondrelli et al., 2010), with a minor right-lateral component (Cirella et al., 2009; Walters et al., 2009).

All the modeling efforts (Anzidei et al., 2009; Atzori et al., 2009; Cheloni et al., 2010; Chiarabba et al., 2009; Cirella et al., 2009; Pino & Di Luccio, 2009; Trasatti et al., 2011; Walters et al., 2009) converge toward a causative fault characterized by:

- a NW-SE orientation;
- 15-18 km of length;
- 42°- 55° dip to the SW.

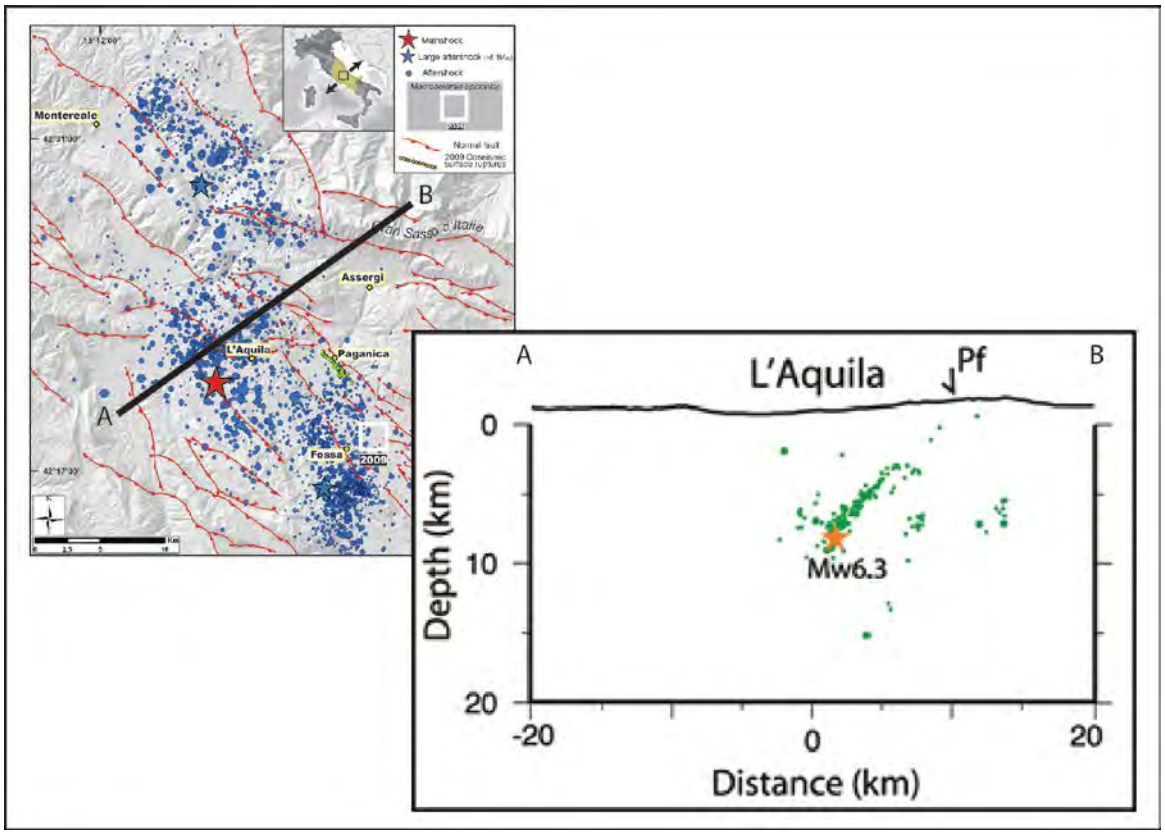

Figure 3.5 – Vertical section across the Paganica Fault with aftershocks showing fault geometry.

3.2 Earthquake effects on the environment

The 2009 Mw 6.3 L'Aquila earthquake was associated with an extensive and complex set of surface coseismic deformations, involving an area of hundreds of km^2.

In the following section the whole coseismic deformation pattern will be illustrated, starting from the "big picture" revealed by DInSAR and GPS analysis and then describing the most relevant surface ruptures recognized during the field survey.

3.2.1 Coseismic deformation

An important amount of information on the coseismic deformation related to the 2009 Mw 6.3 earthquake came from satellite data (DinSAR and GPS, mainly).

Differential SAR Interferometry (DInSAR) is a microwave remote sensing technique that uses the phase difference (interferogram) between two temporally separated Synthetic Aperture Radar (SAR) images of an investigated area to detect elevation

changes in the radar line of sight (LOS) over large areas. DInSAR is an effective technique in measuring ground deformations and provides spatially dense deformation fields with great accuracy (1 cm or less) (Gabriel et al., 1989).
After the 2009 L'Aquila earthquake several authors applied this technique to the L'Aquila area, with the aim to image the coseismic ground deformation at a large scale.
The deformation induced by the earthquake as seen by DInSAR is almost vertical and is detectable over an area of about 500 km^2 extending SE from the mainshock epicenter. The concentric color fringe pattern visible in the three interferograms, (figure 3.6) define the displacement field which is evident as subsiding areas (~65%) in the hangingwall of the Paganica fault and as uplifted areas (~35%) in the footwall block.
The maximum displacement (lowering) occurred between L'Aquila town and Fossa village, with values ranging from 16 to 28 cm for COSMO ascending and ENVISAT ascending and descending, respectively while the maximum footwall uplift not exceeded 10 cm (Atzori et al., 2009; Walkers et al., 2009; Papanikolaou et al., 2010; Trasatti et al., 2011).

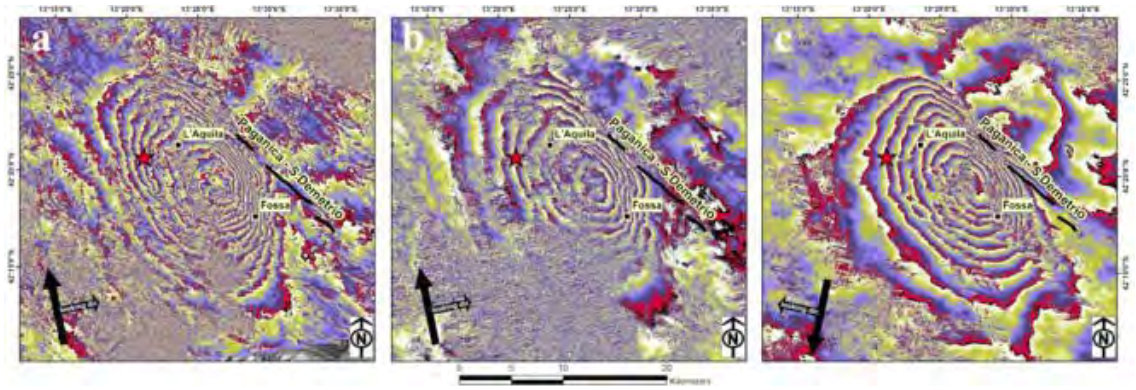

Figure 3.6 - Differential interferograms from: (a) COSMO-SkyMed ascending, (b) Envisat ascending, (c) Envisat descending (with looking directions). The main event of the 6 April 2009 and the Paganica fault are also shown (after Atzori et al., 2009).

The spatial variability of ground deformation is highlighted by a set of cross sections drown both perpendicular and parallel to the activated fault plane (figure 3.7 - Papanikolaou et al., 2010). The abovementioned profiles revealed an asymmetric deformation pattern, with the maximum subsidence recorded near the hangingwall center (Profiles A03 and B03 in figures 3.8 and 3.9).

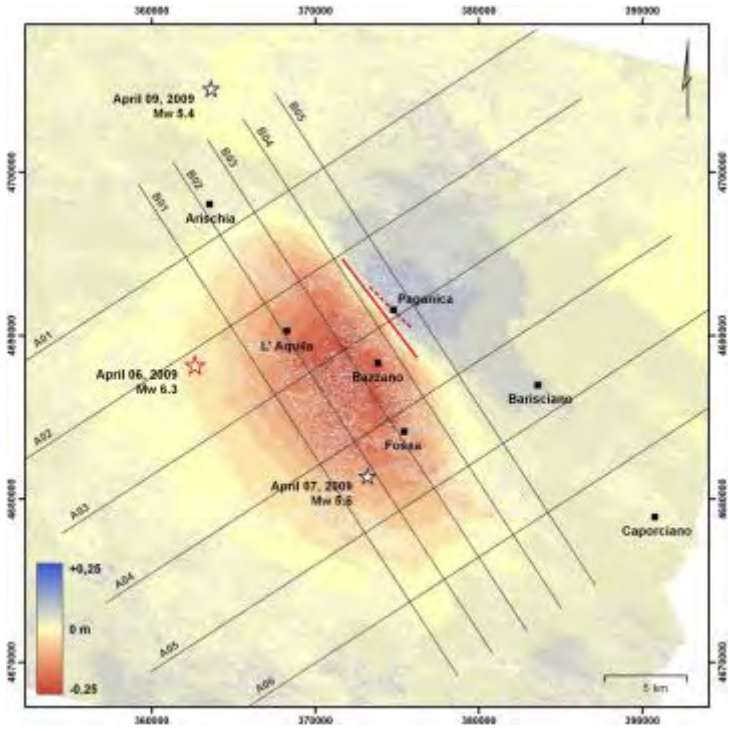

Figure 3.7 – Displacement field of the 6 and 7 April 2009 earthquakes and location of the cross-sections showing differences in the deformation field (after Papanikolaou et al., 2010).

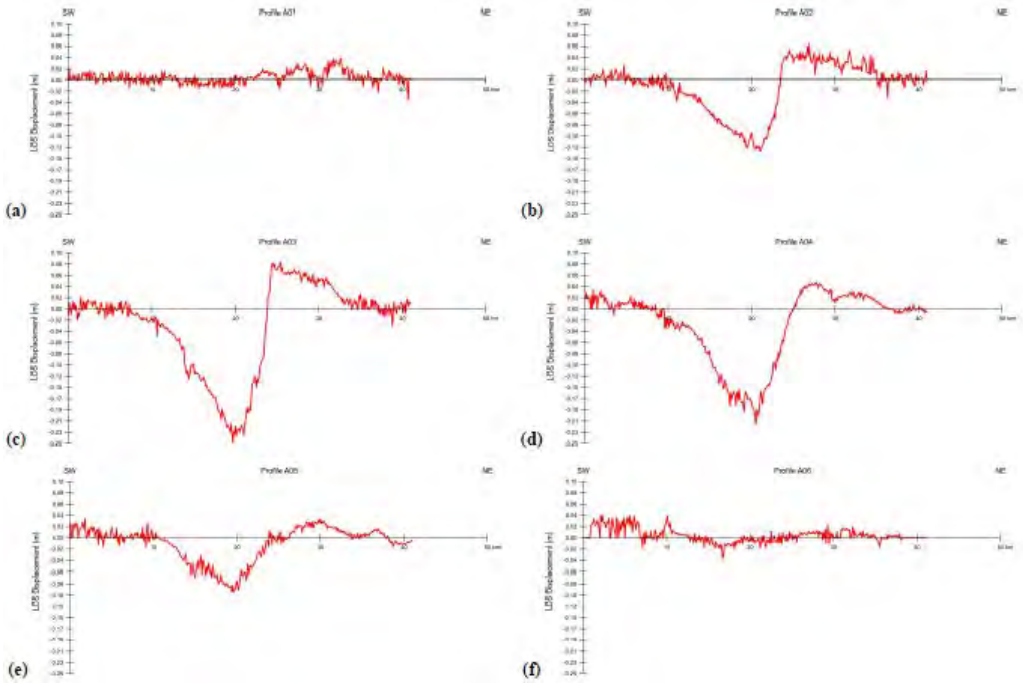

Figure 3.8 - Profiles perpendicular to the activated fault plane (after Papanikolaou et al., 2010).

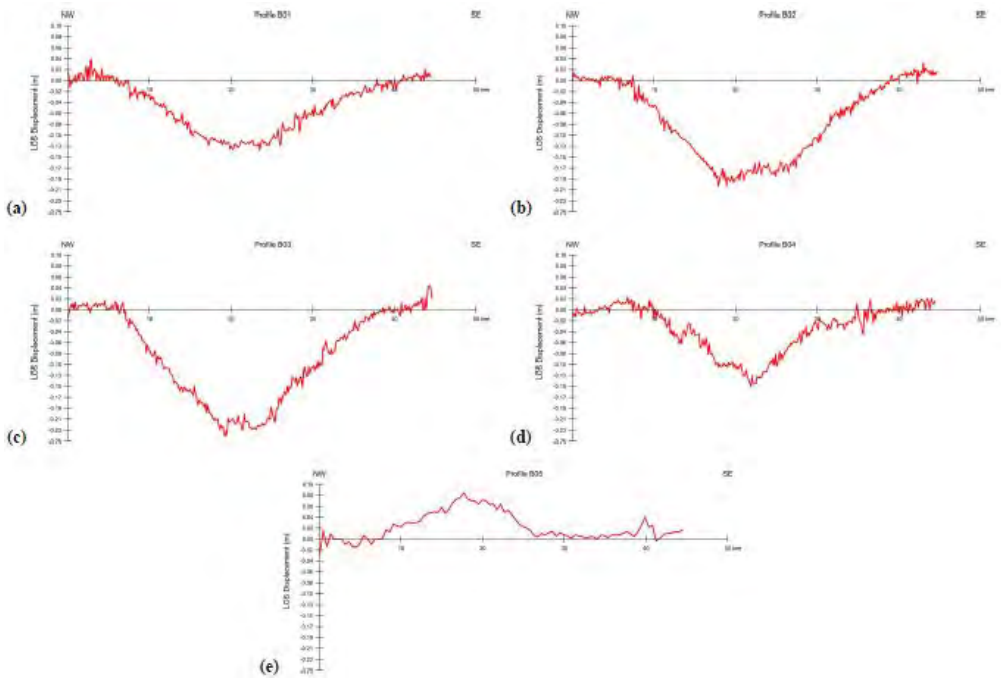

Figure 3.9 – Profiles parallel to the activated fault plane (after Papanikolaou et al., 2010).

Furthermore, interesting information was derived from continuous and survey-style GPS stations located in the epicentral area of the mainshock.

The Global Positioning System (GPS) is a geodetic space technique effective in defining the relative positions of observation sites located on the Earth's surface with centimetric precision and without the limitation of the terrestrial techniques, such as the mutual visibility between the observation sites. This technique allows to study tectonic processes both on regional and local scale and to estimate the ongoing crustal deformation within a region.

Analysis based on continuous and survey-style GPS stations that measured directly the coseismic displacement, allowed researchers estimating the deformation due to the L'Aquila earthquake (Anzidei et al., 2009; Cheloni et al., 2010) and highlighted significant horizontal and vertical permanent deformations in the epicentral area, within a radius of ~ 60 km from the mainshock (figure 3.10).

GPS sites showed clear evidence for coseismic offset, with maximum horizontal and vertical coseismic displacements of ~10 and ~ –15 cm, respectively, observed in the hangingwall of the Paganica fault, while the displacement related to the footwall motion was ~ 7 cm.

Due to the daily sampling of the GPS time-series, Cheloni et al., 2010 provided also an estimate of the afterslip occurred during the first day, that reach values between 1.0 and ~5 cm (figure 3.11).

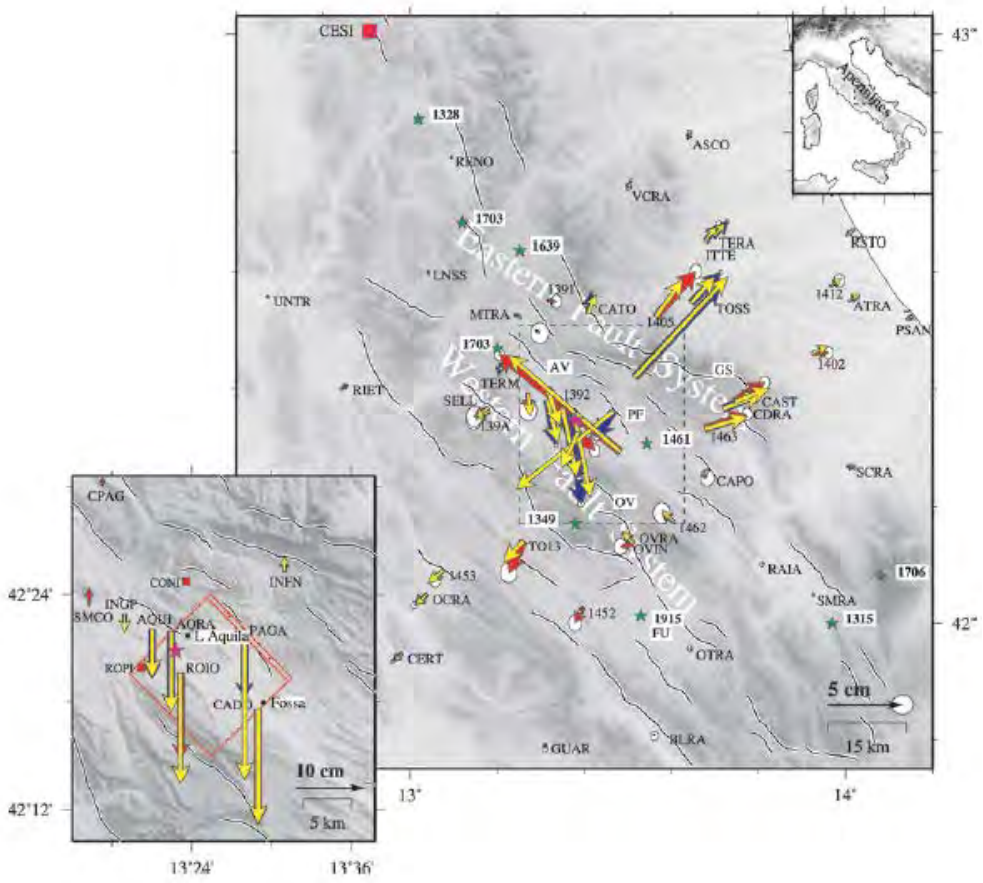

Figure 3.10 - GPS coseismic displacements of the 2009 April 6th Mw 6.3 L'Aquila earthquake (pink star, epicentre; blue vectors, continuous GPS; red, survey-style GPS; yellow, uniform slip dislocation model; error ellipses at 95 per cent C.I.; green stars, Imax > X historic earthquakes labelled with A.D. epoch). Black lines are active faults from Galli et al. (2008), Boncio et al. (2004) and Roberts & Michetti (2004). The red square indicates the position of the station CESI. The inset shows observed (blue) and calculated (yellow) vertical displacements. (after Cheloni et al., 2010)

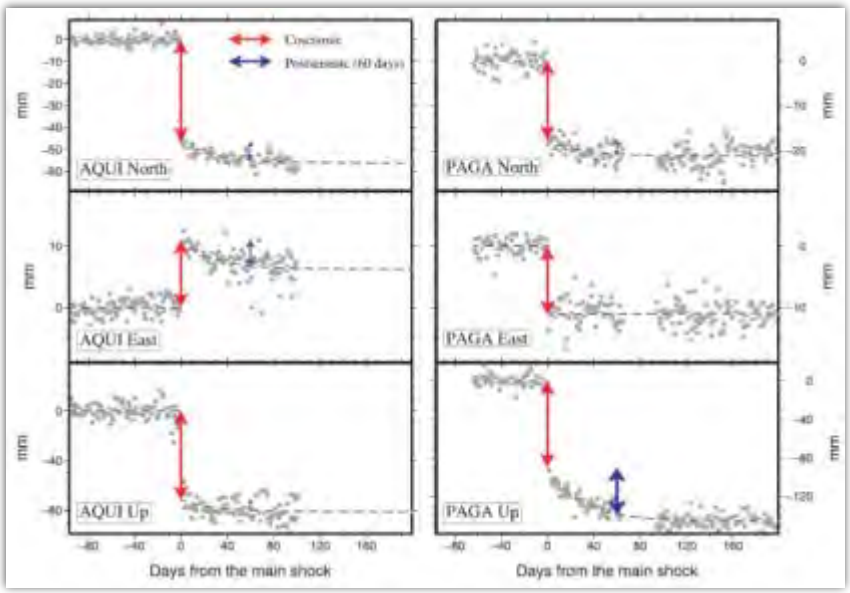

Figure 3.11 - Time-series of PAGA and AQUI sites. The dashed line is the best-fitting exponential function. Arrows correspond to estimated coseismic offsets (red) and post-seismic cumulated displacements (blue). (after Cheloni et al., 2010)

3.2.2 Coseismic surface effects and ground ruptures

Immediately after the April 6 2009 mainshock and in the following weeks, a field geological survey was performed in the epicentral area by several geologists, among them the EMERGEO Working Group (INGV prompt geological survey team), in order to identify and to characterize the coseismic surface effects. During my work at the INGV, I had the opportunity to join the geological survey team and to gather observations and data regarding type, style and magnitude of the coseismic surface deformations. The data collected (about 400 sites) during the post-earthquake field campaigns evidenced a widespread and diversified set of geological surface effects (figure 3.12).

Most of the deformation at the surface was expressed as tectonic ruptures with or without throw, showing similar, if not identical strikes. These coseismic features were mostly observed on Quaternary deposits along pre-existing scarps, paralleling the Paganica fault. Other discontinuous, short, open cracks occurred along both pre-existing fault traces or on the plain and these effects may be interpreted as related mainly to triggered slip or seismic shaking. Rock falls, landslides, liquefactions, soil compactions and mobilization of loose deposits were among the other secondary surface effects observed in the epicentral area and likely related to seismic shaking and/or gravitational phenomena.

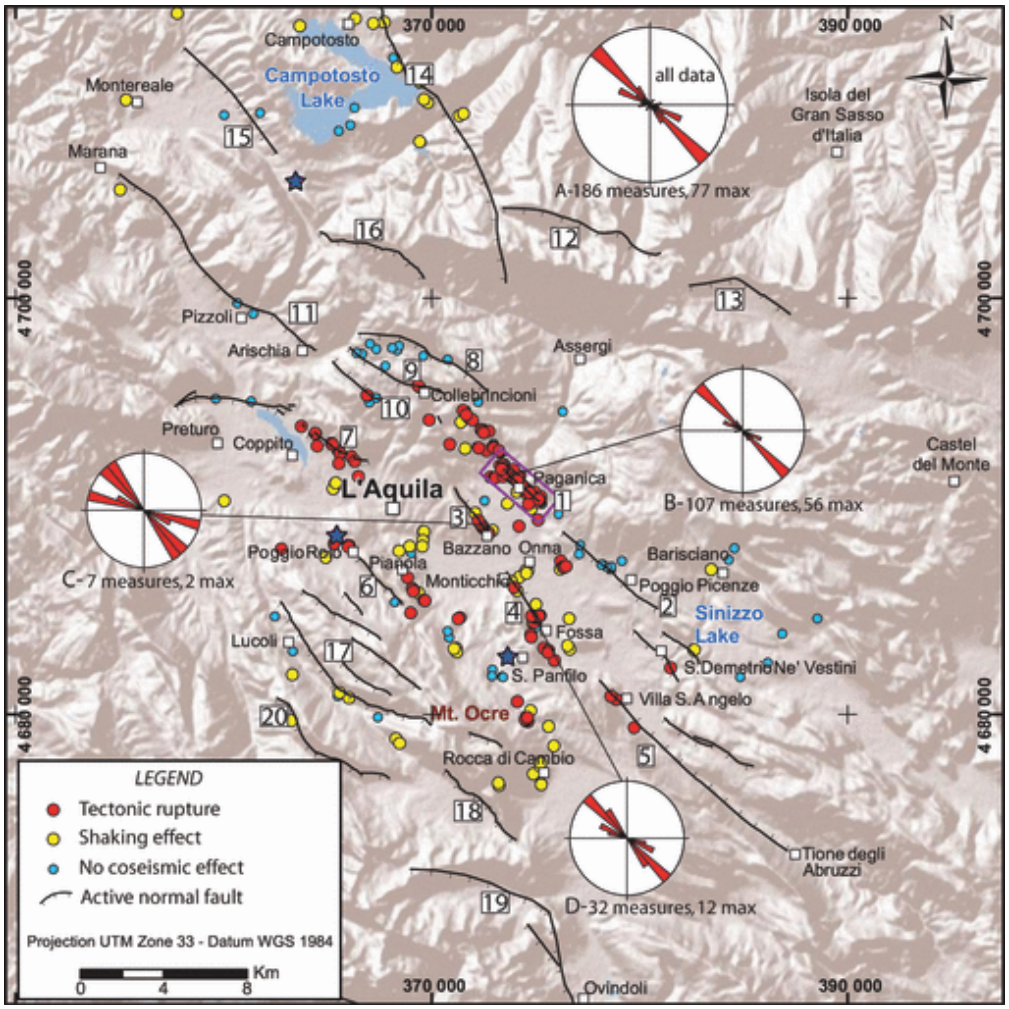

Figure 3.12- Map of the investigated sites for the survey of coseismic geological effects. Colors indicate sites with different types of observations: tectonic ruptures and shaking effects. The purple box includes the Paganica ruptures, which are interpreted to be primary surface faulting. We also show the sites along faults where no ruptures or other effects were observed. Stars indicate the three main events. Rose diagrams of the tectonic surface ruptures: (A) total data; (B) Paganica fault; (C) Mt. Bazzano fault and (D) Monticchio-Fossa fault. We do not report rose diagrams when the data are less than five measurements.

The observed coseismic ground effects in the epicentral area were arranged in a typical pattern for a M~6 earthquake, as described by the idealized schematic block-diagram of figure 3.13 (Dramis & Blumetti, 2005).

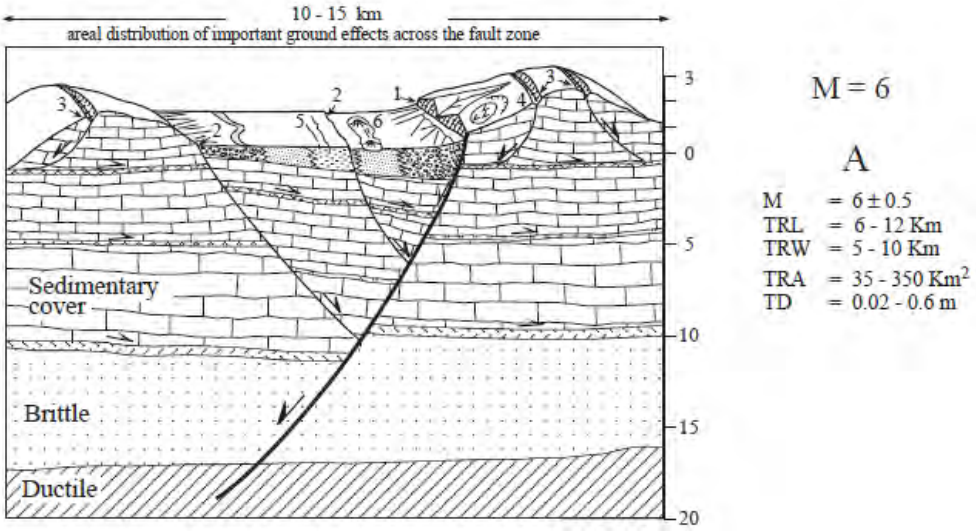

Figure 3.13 – Schematic block-diagram of a Quaternary intramontane basin associated with a ≅M 6 earthquake. Typical seismo-tectonic and seismo-gravitational landforms related to the repetition of coseismic effects along the same seismogenic structure. 1) primary surface ruptures; 2) secondary and sympathetic surface ruptures; 3) deep-seated gravitational deformation; 4) landslide; 5) ground failure; 6) liquefaction. (after Dramis and Blumetti, 2005).

Among all the surveyed coseismic effects, the most prominent tectonic ruptures were observed in the east side of the Middle Aterno Valley, along a portion of the NW-trending, SW-dipping Paganica normal fault system. Here the surface ruptures can be observed with a clear expression for a continuous extent of ~3 km in coincidence with the long-term morphological expression of the fault and are usually confined within ~30 m from the fault scarp (figure 3.14).

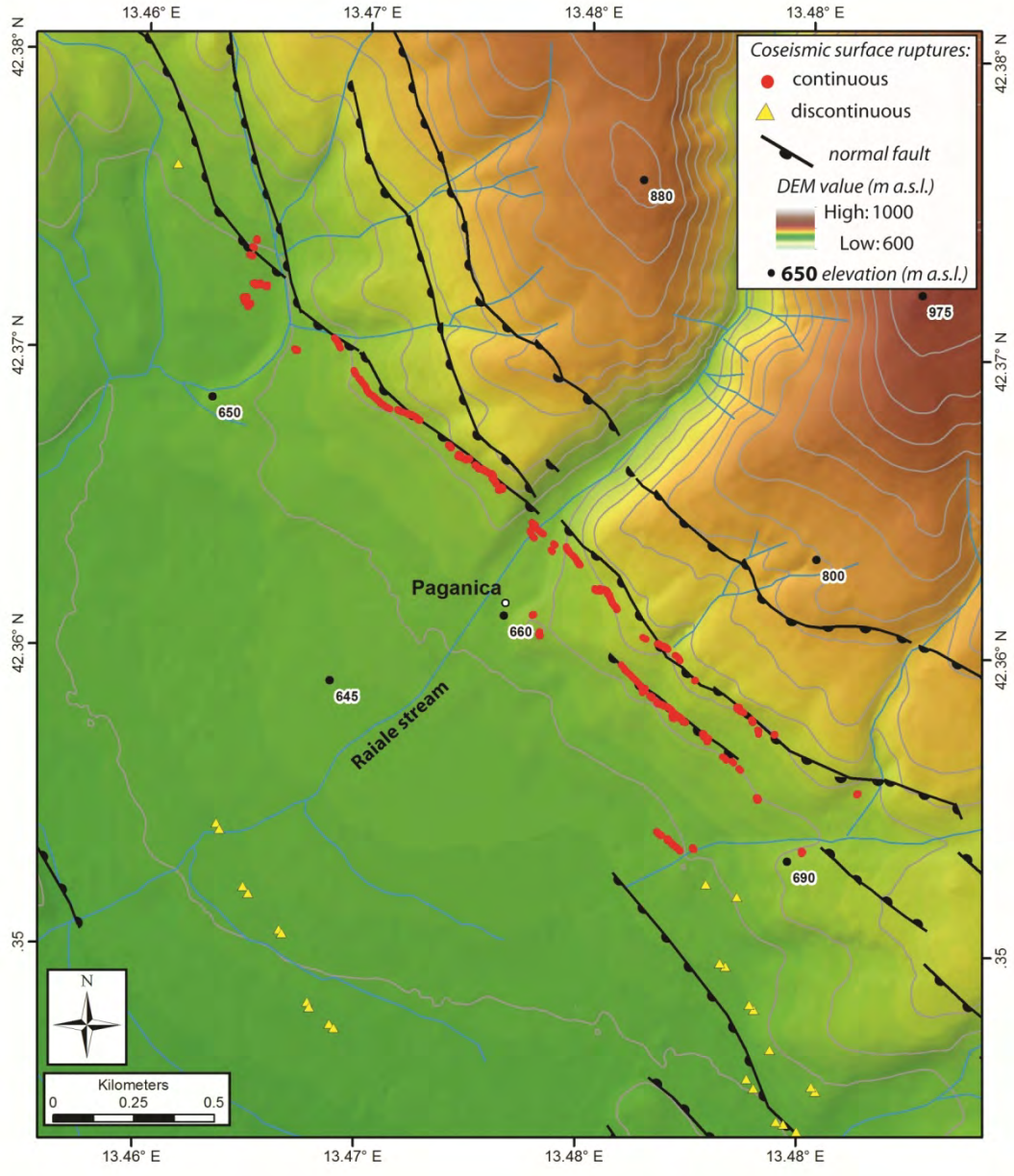

Figure 3.14 - Detail of the area of the 3 km long continuous surface ruptures along the escarpment bounding the Paganica village. Topographic color ramp derived from a 5 m resolution DEM. Contour lines interval is 25 m. (modified after Cinti et al., 2011)

The main characteristics of the surface ruptures along the Paganica fault are:

- mostly open cracks (maximum opening ~10 cm) – figure 3.16;
- vertical dislocations or flexural scarps with a maximum vertical throw of 15 cm (southwest-side down) – figure 3.15;
- the alignment of the ruptures shows a clear spatial continuity and persistent orientation of N130° - N140°;
- commonly organized in en-echelon arrangement;
- occur regardless of slope angle, the type of deposits crossed or the type of manmade feature, and thus independently from gravitational effects.

Figure 3.15 - Surface rupture along the Paganica fault with a maximum throw of 15 cm.

Figure 3.16 - Surface rupture along the Paganica fault with a maximum opening of 10 cm and a negligible throw.

Despite maximum vertical throws not exceeding 15 cm, the location, continuity and the consistency of the surface ruptures along the Paganica fault where not observed along any other structure within the epicentral area.

Both to the north and to the south of this ~ 3 km continuous section, the surface ruptures fade out and discontinuous open fissures occurred along similar trends.
Depending on whether or not these discontinuous fissures are interpreted as evidence of coseismic slip on the Paganica Fault at depth, different interpretation report the length of the 6 April 2009 primary surface faulting between 3 and 19 km (Falcucci et al., 2009; Boncio et al., 2010; Emergeo Working Group, 2010; Galli et al., 2010, Vittori et al., 2011).

3.3 Summary

Summarizing, both DInSAR and GPS dataset analysis revealed the amount and spatial extent of the coseismic deformation field and allowed to model the source parameters and the slip distribution on the fault plane (Atzori et al., 2009; Cirella et al., 2009; Cheloni et al., 2010; Walters et al., 2009, Papanikoalou, 2010).
The location of the 3 km-long surface faulting zone observed during the field campaign coincides with the zone of maximum coseismic slip at depth imaged through the joint inversion of GPS and strong motion data (Cirella et al., 2009).
Moreover, the aftershocks distribution, the focal plane solutions, the geometry and kinematics of the 2009 surface ruptures along the Paganica fault and the whole coseismic displacement field are all consistent with the long-term trace of the PF. In fact, the coseismically uplifted areas coincide with the footwall block of the PF while the subsiding areas with the basin in the active hangingwall (figure 3.17).

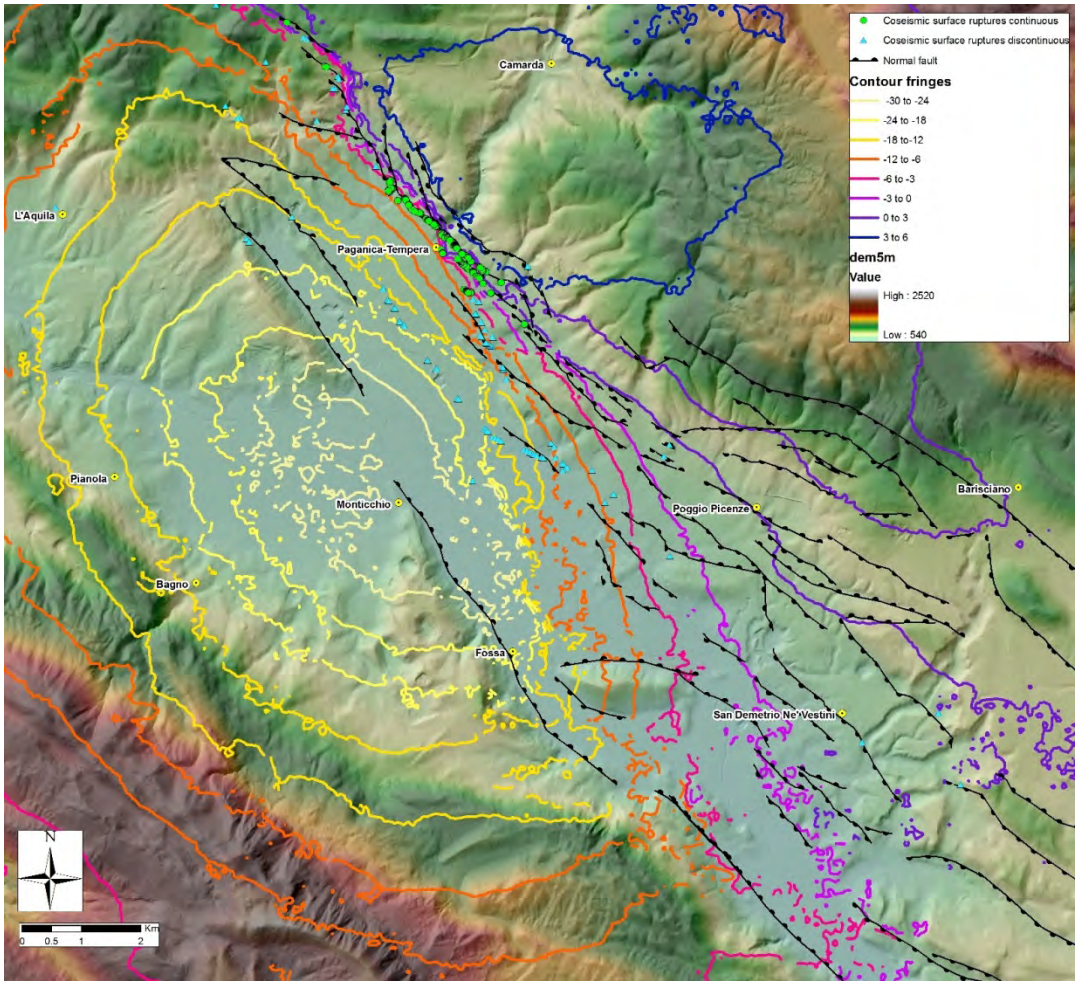

Figure 3.17 - The coloured contour fringes define the displacement field from the ENVISAT differential Interferogram. The maximum lowering is ca. 0.28 m N of Monticchio. Green dots represent continuous coseismic surface ruptures, light blue triangles are discontinuous open fissures.

Taking into account all these observations, there is evidence that the Mw 6.3 April 6, 2009 earthquake occurred on the previously mapped NW-SE, SW-dipping Paganica fault (Bagnaia et al., 1992; Vezzani and Ghisetti, 1998; Boncio et al., 2004; Geological Map of Italy, scale 1:50.000, sheet 359, L'Aquila, APAT, 2006).

A detailed description of the field geological survey and of the observations of the surface geological effects in the epicentral area is available in the attached Terra Nova article *"Evidence for surface rupture associated with the Mw 6.3 L'Aquila earthquake sequence of April 2009 (Central Italy)"* which I co-authored.

From now on, we will refer to the 2009 earthquake causative fault as the Paganica – San Demetrio fault system (PSDFS herein) after, also according to the work of Bagnaia et al., 1992.

3.4 Open questions raised by the 2009 earthquake

The occurrence of the 2009 L'Aquila earthquake has highlighted the need for a detailed knowledge in terms of location, geometry, and characterization of the active faults that are the potential sources for future earthquakes.

The comparison between the length of the coseismic surface ruptures with observed throws (3km) and the length of the long-term expression of the PSDFS as defined by geology and geomorphology by previous works (9 to 15 km) highlighted that the 2009 L'Aquila earthquake coseismic surface ruptures clearly reactivated only a 3 km-long portion of the whole PSDFS.

A second point was that the centimetric coseismic throw (max 0.15 m near Paganica) that occurred in 2009, can hardly contribute to the growth of the fault escarpment, which is in places up to tens of meters high. In fact, in order to compete with erosional and depositional processes, coseismic surface displacements substantially larger than those observed in 2009 are needed.

The limited consistency between the observed coseismic ruptures and the long-term morphologic expression of the PSDFS, both in terms of location and size, raised some questions about the maximum expected magnitude on the fault

Given the abovementioned open questions, a better understanding of the seismic potential of the PSDFS was needed in order to provide new insights on its Quaternary deformational history and thus to contribute to seismic hazard assessment for the area struck by the 2009 L'Aquila.

3.5 Other examples of surface faulting earthquakes and coseismic deformation

During my work at the INGV, I had the opportunity to survey other surface faulting earthquakes, with different magnitude and prevalent extensional kinematic (normal dip-slip and mixed strike-slip and normal dip-slip). In this section I will present a summary on the surface deformations related to the 2010 Mw 7.2 El Mayor-Cucapah (Mexico) and to the 1915 Pleasant Valley (Ms 7.7), 1954 Fairview Peak (Ms 7.2) and Dixie Valley (Ms 6.8) earthquakes.

3.5.1 The 2010 (Mw 7.2) El Mayor-Cucapah earthquake

The 2010 Mw 7.2 El Mayor-Cucapah earthquake occurred within the Mexican Pacific margin in northern Baja California (BC), a region of high seismicity straddling the complex Pacific–North America plate boundary (figure 3.18). The principal plate boundary in northern Baja California consists of a series of northwest-trending strike-slip (transform) faults that are separated by pull-apart basins accommodating NW-SE oriented extension. At the latitude of the 4 April 2010 earthquake, the Pacific plate moves northwestward with respect to the North America plate at about 45 mm per year.

This earthquake produced a ~120 km-long discontinuous surface rupture extending from the northern tip of the Gulf of California northwestward to nearly the Mexico-USA border. The surface rupture pattern was complex, with breaks along multiple fault strands (figure 3.19, 3.20, 3.21), including minor re-activation of the fault scarps associated with the 1892 Laguna Salada earthquake and several other older seismic events.

Few months after the earthquake, I surveyed the northern half of the rupture that extends ~20 km along the Laguna Salada and Pescadores faults and then it jumps in a left step-over to the Borrego fault.

The southern part of the rupture consists of a zone of distributed fracturing and liquefaction that cuts across the Colorado River delta.

Displacements due to the earthquake involved both normal and strike-slip motion, with horizontal displacements generally larger. The maximum measured displacement occurred along the Borrego fault in Borrego Valley and was about 3.1 m of strike slip and another 2 m of east-down dip slip on a nearly vertical fault, yielding an oblique slip of nearly 4 m.

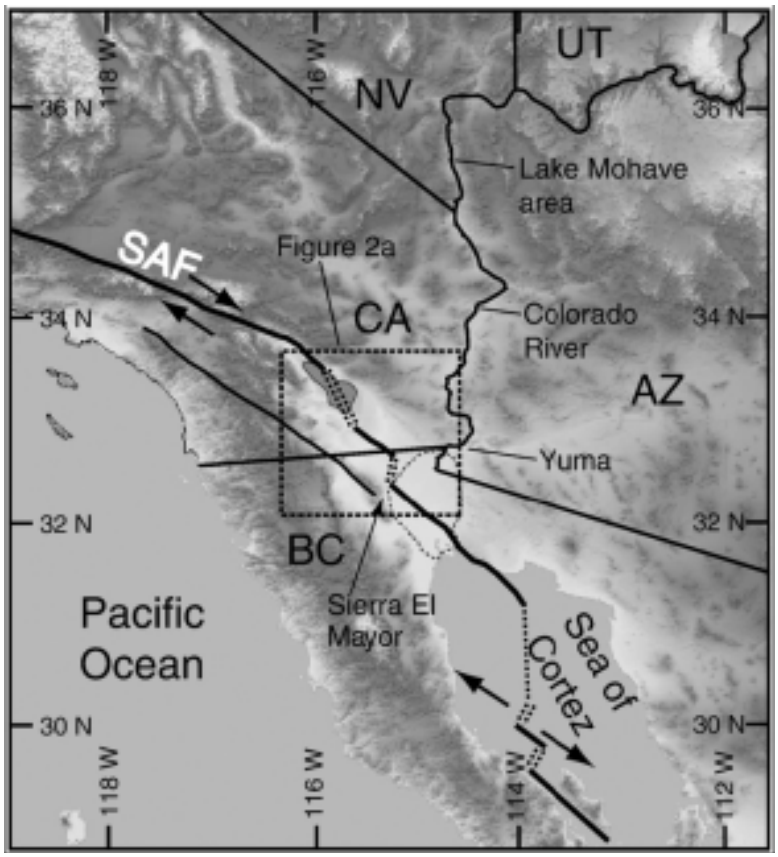

Figure 3.18 - Regional map of topography and main faults of the San Andreas fault system in the southwestern United States and northwestern Mexico. ABF—Agua Blanca fault; CDD—Canada David detachment; CPF—Cerro Prieto fault; E—Ensenada; ECSZ—eastern California shear zone; EF—Elsinore fault; IF—Imperial fault; LA—Los Angeles; LSF—Laguna Salada fault; SAF—San Andreas fault; SD—San Diego; SJFZ—San Jacinto fault zone; SSPMF—Sierra San Pedro Martir fault; T—Tijuana; WSDF—West Salton detachment fault; Y—Yuma. (after Dorsey et al., 2011).

Figure 3.19 - Borrego fault, ground ruptures with mainly dip-slip displacement confined in a narrow zone at the base of the long-term mountain front - Sierra Cucapah, Baja California, México.

Figure 3.20 – Coseismic fault scarps at the base of the range forming a zone of distributed deformation

Figure 3.21 - Coseismic fault scarps emerging on the slope in a zone of distributed deformation

Figure 3.22 – Cosesimic fault scarp crossing the alluvial plain

3.5.2 The 1915 Pleasant Valley (Ms 7.7), 1954 Fairview Peak (Ms 7.2) and Dixie Valley (Ms 6.8) earthquakes and their surface ruptures

During the months I spent at the Center for Neoteconic Studies of the University of Nevada, Reno, I had the opportunity to survey the surface ruptures related to the 1915 Pleasant Valley (Ms 7.7), 1954 Fairview Peak (Ms 7.2) and Dixie Valley (Ms 6.8) earthquakes.

Those events occurred in the Central Nevada Seismic Belt (CNSB), a ~300 km-long NE-SW oriented zone of strike-slip, oblique-slip and dip-slip historical surface faulting earthquakes that extend northward through eastern California and central Nevada (figure 3.23).

In particular, the 1915 Pleasant Valley earthquake (Ms 7.7) was the largest event of the historical sequence, and it produced predominantly normal faulting with vertical displacements up to 4 m while only in few locations it was observed some dextral offset.

The Ms 7.2 Fairview Peak earthquake occurred on 16 December 1954 in central Nevada and was followed ~ 4 minutes later by the nearby Ms 6.8 Dixie Valley earthquake. The focal mechanism of the Fairview Peak event shows right-oblique motion on an east-dipping fault, while a best fit for the Dixie Valley event shows a pure dip-slip motion on an eastward-dipping plane (Doser, 1986). Normal-right-oblique surface ruptures related to the 1954 Fairview Peak and Dixie Valley earthquakes were distributed among six different faults that together define a complex zone extending northward for about 100 km and over 15 km wide.

More in detail, the Fairview event produced a 32 km-long surface rupture with right-oblique slip and a maximum of 3.8 m of vertical separation and 2.9 m of lateral offset.

The 1954 Dixie Valley created ~ 50 km of fault scarps which dipped 50° to 70° to the east. The sense of slip was normal, with a maximum vertical offset observed of 2.8 m (Caskey et al., 1996).

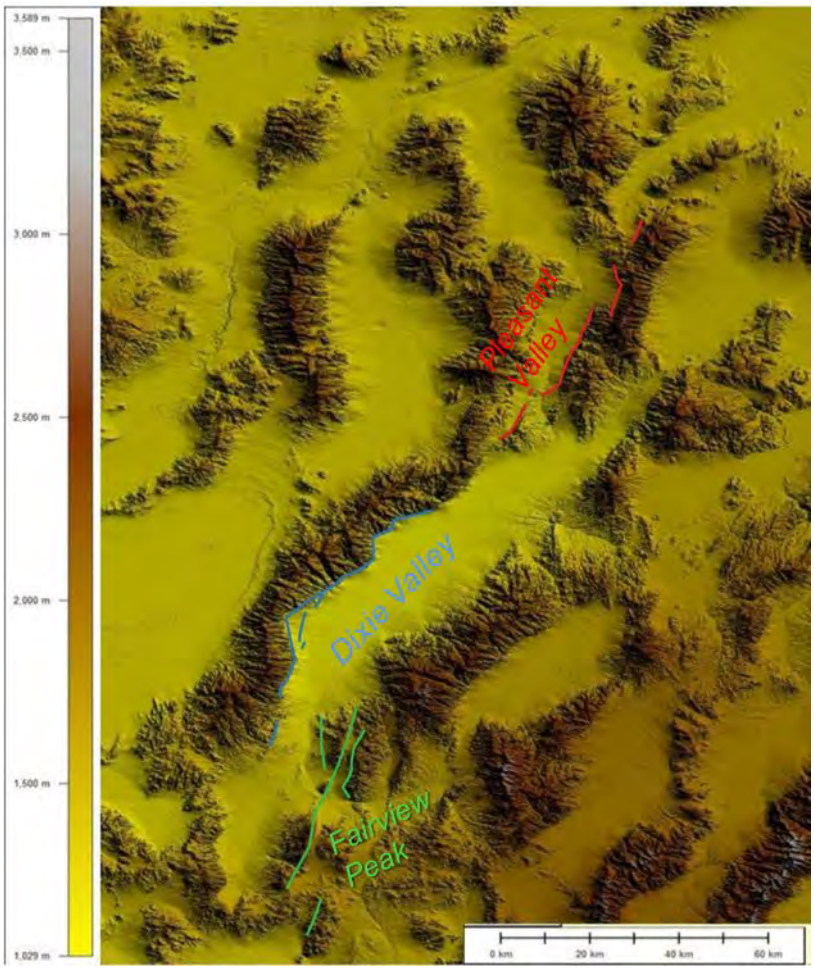

Figure 3.23 - Location of some of the historic earthquakes occurred in the Central Nevada Seismic Belt (CNSB).

Figure 3.24 – Coseismic fault scarp (white strip) at the base of the range – Pleasant Valley, Nevada (1915 Ms 7.7Pleasant Valley earthquake).

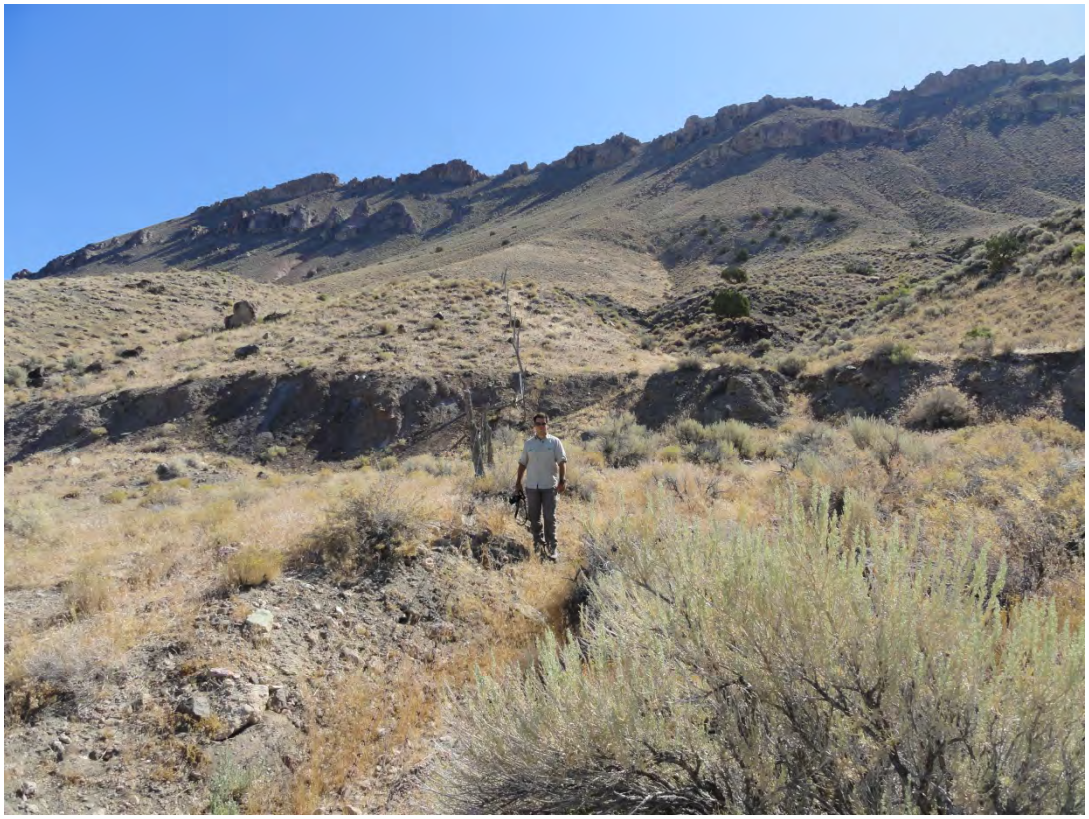

Figure 3.25 - Coseismic fault scarp at the base of the range (1915 Ms 7.7Pleasant Valley earthquake).

Figure 3.26 - Willow canyon – coseismic graben with almost null vertical separation (1954 Ms 6.8 Dixie Valley earthquake)

Summarizing, the observations of the surface ruptures associated with the abovementioned earthquakes allowed to make some general considerations highlight some differences and to make some comparison with respect to what we saw in the L'Aquila 2009 earthquake.

Despite the differences in the energy released and in the prevalent kinematics, the 2009 L'Aquila, 2010 Baja California and some of the historical CNSB earthquakes are characterized by a similar style of deformation, with different scale structures arranged in well-defined and recurrent geometries.

A lesson learned is that coseismic deformations in earthquakes with a pure or large normal dip-slip sense of motion generally occur in a relatively narrow zone at the base of the morphological range (figures 3.19 3.20 3.24 3.25), even if sometimes is possible to follow the ground breakages up in the slopes or within the valley floor (figures 3.21, and 3.22).

In some other cases the ground ruptures branch out in multiple overlapping strands that tend to distribute the coseismic displacement in a wider zone of deformation.

It has been observed that the deformation due to several seismic cycles, as a general rule, tends to occur along the same fault zone for a significant period of time.

Consequently, this behavior results in the creation of typical assemblages of landforms for active normal faults, characterized by cumulative fault scarps and mountain fronts that record progressively longer period of time and progressively larger displacements.

Accordingly to this concept, coseismic ground ruptures (their location, continuity and consistency) may guide our investigation for short and long-term slip-rate estimates.

4 Brief seismotectonic overview of the Central Apennines

The central Apennines are part of a northeast-verging imbricate fold-and-thrust mountain belt formed during Neogene-Quaternary times as a result of the subduction of Tethyan ocean crust and the collision between African continental fragments and the Eurasian plate (Boccaletti et al., 1971; Doglioni et al., 1996).
The Central Apennines are bordered to the east by a foredeep, filled up by Pliocene-Pleistocene deposits (Casnedi et al., 1981; Consiglio Nazionale delle Ricerche, 1992) and to the west by the Tyrrhenian back arc basin (Kastens et al., 1988) developed at least since middle Miocene. The orogenesis affected Triassic to Miocene sedimentary sequences belonging to different basin and platform paleogeographic domains of the Adria Mesozoic paleomargin (e.g., Ben Avraham et al., 1990; Ciarapica and Passeri, 2002; Lentini et al., 2002; Patacca and Scandone, 2007).
During the formation of the belt the external compressional front progressively migrated toward east and north-east as a consequence of the geodynamic and kinematic processes that were the objects of different interpretations in the literature (e.g. Lavecchia, 1988; Patacca et al., 1990).
The progressive migration of the compressional deformation toward the Adriatic foreland is clearly documented by the development and evolution of a series of eastward progressively younger foredeep basins and by the occurrence of several piggyback basins, which developed on top of the advancing allochthonous units (Patacca and Scandone, 2001). During the Quaternary, the flexural subsidence, the compressional deformation and the eastward retreat of the subduction hinge all decreased dramatically (Patacca et al., 1992; Cinque et al., 1993) and the Apennines became dominated by crustal extension and by significant regional uplift. This new stress regime led to a crustal thinning that favored the arising of magmas during the Pleistocene and the formation of volcanic districts along the Tyrrhenian margin of the chain (Cosentino and Parotto, 1986; Cavinato et al., 1994).
The extensional regime is contemporary to the chain regional uplift (D'Agostino et al., 2001; Salustri Galli et al., 2002; Centamore and Nisio, 2003; Galadini et al., 2003a; Pizzi, 2003) and is responsible for the activity of the normal and normal-oblique faulting during most of the Quaternary.
The Apennines extensional belt consists of active and seismogenetic, mainly NW-SE and NNW-SSE striking normal and normal-oblique faults, paralleling the physiographic and structural axis of the chain and offsetting the fold-and-thrust belt inherited by the compressive deformation.
The important vertical displacements related to the activity of these faults have controlled the development of several intermontane tectonic depressions, such as L'Aquila, Sulmona and Fucino basins, partially filled with sequences of continental deposits of Plio-Quaternary age up to hundreds of metres-thick (Cavinato & De Celles, 1999).

The onset of the continental deposition occurred during Pliocene, thus indicating the emersion of the Central Apennine belt since this period (e.g. Bosi et al., 2003, Galadini et al., 2003a).
The Quaternary normal faults activity was not stationary; in fact stratigraphic data suggest an estward migration (Galadini and Messina, 2004;). As a result of this migration, some of the normal faults located in the western part of the Apennines are not active nowadays (on the basis of lack of recent dislocation at the surface and of the scarce seismicity, both historical and instrumental). Conversely, persistent activity at least since the Lower Pleistocene is shown by several faults located in the eastern sectors.
At present the Central Apennines are characterized by active extension.

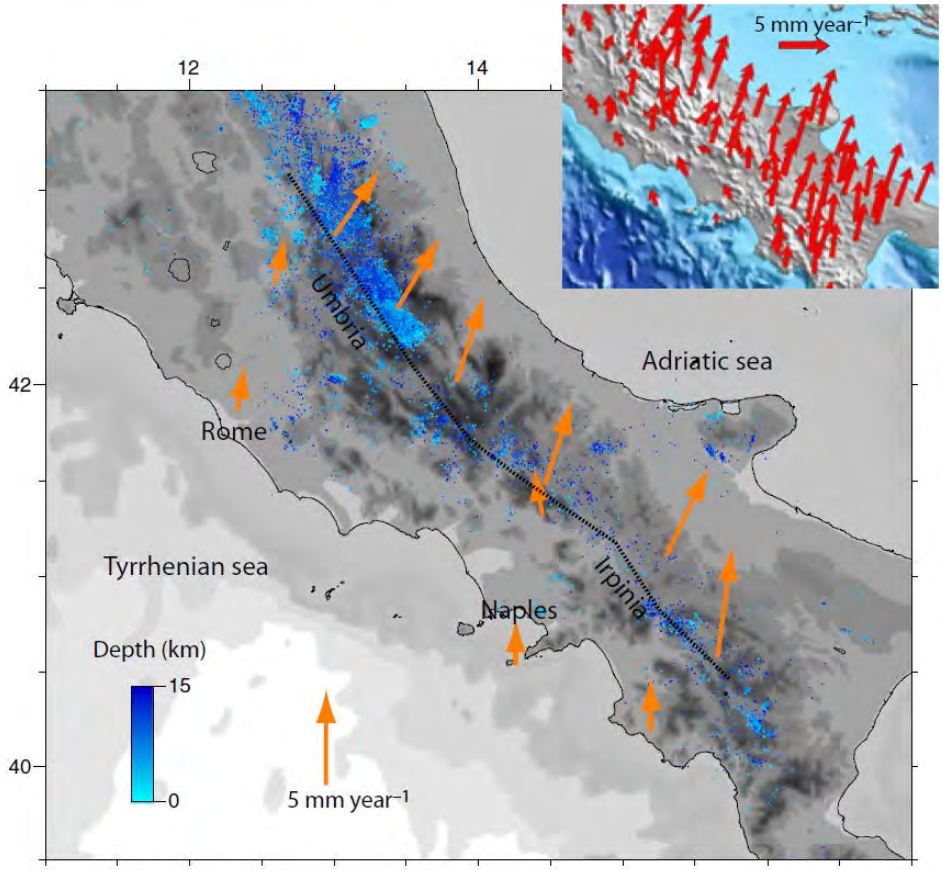

*Figure 4.1 - Seismicity map of the central–southern Apennines for 2003–2009. Hypocenters are from relocation using the criteria of the CSI 1.1 catalogue (http://csi.rm.ingv.it/) with data from Centro Nazionale Terremoti of INGV. Arrows are a selection of GPS site velocities with respect to a fixed Eurasia (Avallone et al., 2010). The dashed line is the narrow zone where the extension is concentrated. The inset in the upper part of the figure shows the GPS velocity field relative to Eurasia (http://www.gm.ingv.it/images/stories/LabGIS/Mappe_G8/GPSitaly2_1500*2143.jpg).*

Active extension follows the main topographic ridge and is concentrated in 40-60 km wide belt where, in general, historical and instrumental seismicity, as well as active faults, are located (figure 4.1, 4.2 and 4.3).

The current rate of extension, estimated in 2–3 mm/year (Hunstad et al., 2003, D'Agostino et al., 2011), together with stress indicators (fault slip data, borehole breakout measurements and focal mechanisms of earthquakes) point out a well-defined nearly NE-oriented active extension (e.g. Calamita & Pizzi 1994; Lavecchia et al. 1994; Montone et al. 1999; Montone et al. 2004; Pondrelli et al. 2010).
Looking more closely at our study area, the Abruzzi region of the Central Apennines is characterized by the presence of several active faults accommodating the prevalent NE-SW oriented extension. The present knowledge on the active faults in this area derives from decades of studies in geomorphology and Quaternary geology as well as from some paleoseismological investigations. The active tectonic structures are made of segments, usually dipping towards W and SW, with length ranging between 5 and 20 km. Shorter segments are organized in fault systems made by 3-to-5 minor faults. The length of the fault systems rarely exceeds 33 km (i.e. the cases of the Fucino fault and the Assergi - Campo Imperatore fault system).
Some of these faults during historical times were responsible for earthquakes with M up to 7; notably this magnitude seems to represent the Max magnitude expected for the area also on the basis of tectonic, geologic, and geomorphic observations from nearby faults.
The slip-rates estimated in this area on nearby faults (figure 4.2) range from 0.4 to 1.2 mm/yr, with intermediate values preferred, i.e. 0.6-0.8 mm/yr (Galadini and Galli, 2000; Galli et al., 2008 and references therein).

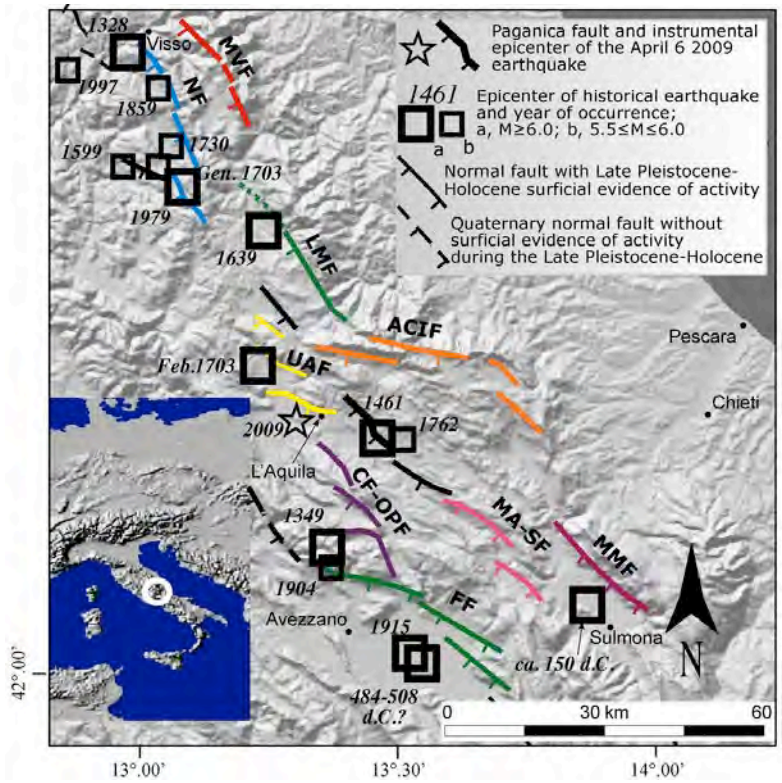

Figure 4.2 - Seismotectonic framework of the central Apennines (after Galadini et al., 2009). MVF - Mt. Vettore fault; NF – Norcia fault system; LMF - Laga Mts. fault; UAF - Upper Aterno fault system; ACIF – Assergi-Campo Imperatore fault system; CF-OPF - Campo Felice-Ovindoli-Pezza fault system; MA-SF - Middle Aterno-Subequana valley fault system; MMF - Mt. Morrone fault; FF - Fucino fault.

The Italian historical records report that the Abruzzi region has been repeatedly hit by large magnitude, destructive earthquakes (figure 4.2). The available catalogs report the 1349, 1703, and 1915 events (all having M≥6.5 and I>10 MCS) as the strongest earthquakes in this area (*CPTI Working Group*, 2004) and occurring within 35 km from the 2009 epicenter.
The historical earthquakes closest to the L'Aquila area (figure 4.3) have M<6.5 and are the 1791 Maw 5.4, 1762 Maw 5.9 and the 1461 Maw 6.4 events (Maw=average weighted Magnitude derived from macroseismic intensities (*CPTI Working group*, 2004).

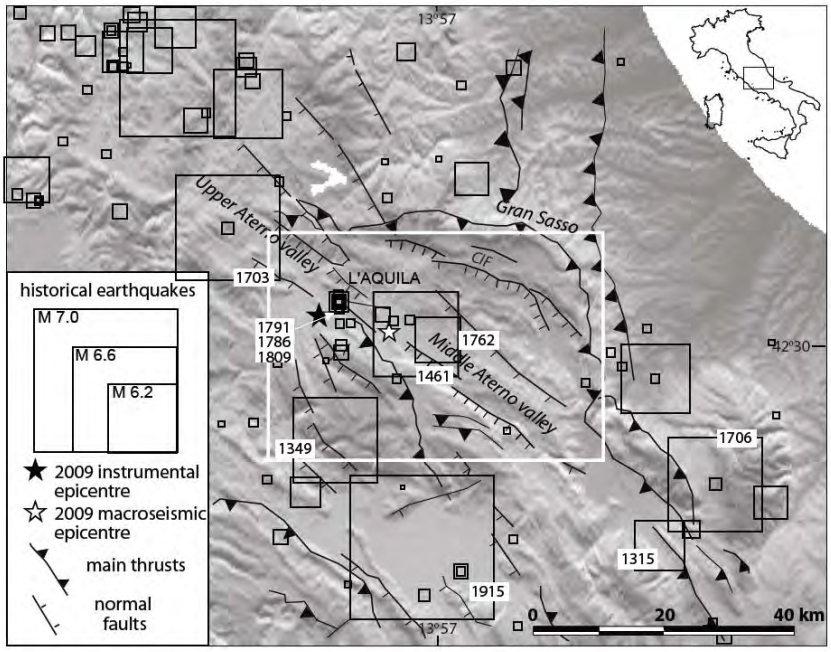

Figure 4.3 - Historical seismicity (squares) from the Catalogo Parametrico dei Terremoti Italiani (CPTI Working Group 2004). A simplified tectonic framework of the Central Apennines is also shown. (after Tertulliani et al., 2009).

The analysis of the instrumental seismicity in the area show low levels of seismicity during the past 20 years (Chiarabba et al., 2005). In fact, during the latter period the area has only been affected by minor seismic episodes (in 1992, 1994 and 1996), while the background seismicity is sparsely distributed (Bagh et al., 2007 and Chiaraluce et al., 2009). Minor sequences are located close to the L'Aquila area, with a maximum magnitude M_L=4.0 (De Luca et al., 2000; Pace et al., 2002; Boncio et al., 2004; and Ciaccio et al., 2009).
The historical record and the instrumental seismicity in the 2009 epicentral area seems to describe only moderate-size seismicity, with earthquakes less energetic than in the surrounding region. However, this difference may be only apparent, since from paleoseismological studies we learn that the average recurrence time for M>6.5 earthquakes in the region is on the order of one or more millennia (Michetti et al., 1996; Pantosti et al., 1996; Galadini & Galli 1999; D'Addezio et al., 2001; Galli et al., 2002; Moro et al., 2002; Galadini et al., 2003; Salvi et al., 2003).

5 Paleoseismological approach

5.1 Introduction

Immediately after the field geological survey to collect the evidence of the 2009 L'Aquila earthquake geological coseismic effects, we organized a paleoseismological campaign to be carried out across the northwestern portion of the Paganica - San Demetrio fault system (PSDFS hereinafter). The main goal of this campaign was to reconstruct the recent paleoseismological history of the PSDFS and to estimate the short-term (~30 ka) slip-rate.

As already discussed in Chapter 4, the long-term morphological expression of a fault is the result of repeated displacements along the same tectonic structure.

Active normal faulting produces mainly vertical deformations that, when cumulated for several seismic cycles along the same fault, can concur to form compound fault scarps (Slemmons, 1957), also called composite (Stewart and Hancock, 1990) or multiple-event fault scarps.

Taking into account this concept, and considering all the logistic limitations due to the density of buildings and activities in the area, we selected the best trench sites along the fault system section that consistently ruptured the surface in 2009 where we could expect the preservation of the evidence of repeated surface faulting events.

We studied in detail four paleoseismological trenches/cuts by analyzing stratigraphy and structures and developing a reference chronological framework based on radiocarbon dating and archeological evaluation of pottery fragments found within the deposits involved in the deformation.

All the studied trenches were located at the base of the main fault escarpment bounding the Paganica village (figure 5.1), along the portion of the SW-dipping PSDFS where the most significant 3 km-long continuous surface ruptures occurred and that were considered to be direct evidence for fault displacement at depth (Falcucci et al., 2009; Boncio et al., 2010; Emergeo Working Group, 2010).

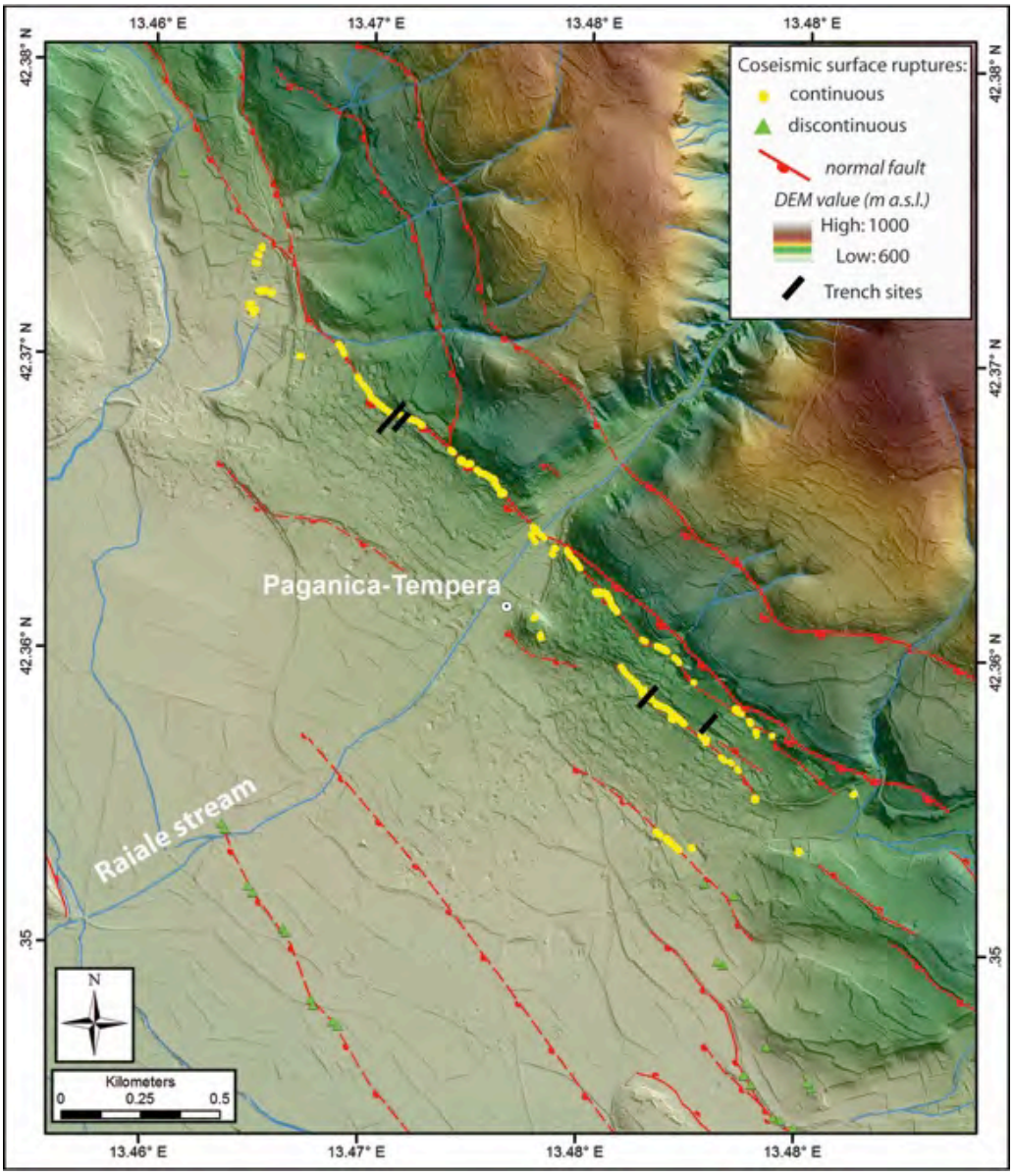

Figure 5.1 - Detail of the area of the 3 km long continuous surface ruptures along the escarpment bounding the Paganica village and location of trench sites. Topographic color ramp is derived from a 1 m resolution LiDAR-derived DEM.

The excavations were realized in a densely populated area that made difficult the selection of the trench sites. Two trenches were newly excavated (Zaccagnini and Mo'Tretteca sites), whereas other two sites took advantage of artificial cuts (250K and Aqueduct site).

We also drilled two cores at Aqueduct and Mo'Tretteca sites in order to check the stratigraphy and to measure the vertical offset of correlative deposits deeper than the trench walls exposure.

5.2 Paleoseismology - method

Paleoseismology is the study of the earthquakes of the past through the recognition of their geological and geomorphic signatures. Paleoseismology allow the definition

of the location (link of the earthquake with its causative fault) timing and size of earthquakes of the past both historical and pre-historical.
Paleoseismological investigations permit to study the distribution of individual paleoearthquakes in space and over time. The main goal is to extend the instrumental and historical seismicity record over periods of thousands or tens of thousands of years. This allows a better understanding of fault seismic behavior and thus contribute to the upgrade of the related seismic hazard.
The main assumption at the base of the paleoseismological approach is that moderate (moment magnitude, M_w >5.5) or greater earthquakes are able to produce detectable permanent deformations of the ground surface that may be directly related to the fault movement at depth.
These deformations may appear clearly on the Earth surface at the intersection of the fault plane with the ground surface where fault scarps occur (see Chapter 2), but also within an area of tens to hundreds km^2 around the seismogenic structure where both horizontal and vertical deformations take place.
Paleoseismological investigations are also based on the fact that the permanent coseismic deformations of the ground surface are able to produce a disequilibrium, both at local and regional scale in the erosional and depositional processes that were acting at the surface at the time the earthquake. This disequilibrium is mainly due to the coseismic formation of relatively uplifted and subsided areas, of dammed or offset drainages etc. This results in the generation of new erosional features and related depositional processes that take place in the attempt to restore the pre-earthquake equilibrium. These earthquake triggered features represent the geological records of the occurrence of past earthquakes.
The possibility that these records can survive through time is strictly dependent on the geomorphic and geologic setting of the area where the earthquake occurred (topography and lithology) as well as on the climatic conditions.
Under favorable conditions, the geological records of earthquakes of the past can be preserved by burial by younger deposits, allowing the paleoseismologist to recognize the cumulative deformation due to repeated earthquakes along a fault and/or the evidence for the occurrence of individual paleoearthquakes.
Paleoseismological studies take advantage of different investigations methods and techniques, performed both at regional and local scale:

- interpretation of aerial and satellite imagery and digital elevation models (DEMs) in order to detect indicators of paleoseismic events (e.g. uplifted marine shorelines, linear range fronts, offset drainages, etc.);
- study of near-fault geomorphology (fault-scarps, streams, fans, alluvial terraces, etc.);
- realization of exploratory trenches across and\or parallel to the investigated faults;
- analysis of the landscape features and deposits associated with ground shaking (liquefactions, turbidites, landslides, etc.);
- study of tsunami-related deposits.

The results of those types of investigations can furnish useful information to estimate some of the principal parameters describing a seismogenic fault:

- fault geometry, length and prevalent kinematics;
- fault displacement and its variability along strike;
- time elapsed since the last event;
- average recurrence time and related variations;
- slip-rates.

5.2.1 Trenches

Even if there are no standard techniques to perform paleoseismological investigations because they depends a lot on the type of structure, problematic and environment, trenching of a fault scarp is probably the most common and effective method for investigating an active fault with surface deformation.

This methodology consists in the preparation of an artificial exposure (trench wall) crossing the investigated fault to recognize the evidence of repeated fault displacements as recorded in the trenched stratigraphic sequence. As already mentioned above, the geological records do not have the same likelihood to be preserved through time at every site along a fault. A careful trench site selection, thus, represent a crucial step in paleoseismology.

The trench site should be selected taking into account two main factors:

- the location of the fault should be known with a certainty of a few meters;
- the geomorphological setting of the site should favor the preservation of the geological records of paleoearthquakes (little or null erosion and moderate deposition);
- presence of soft and recent datable sediments across the fault.

A paleoseismological trench is usually dug in the ground using a backhoe (figure 5.2) or, less commonly, by hand excavation. Trenches are excavated depending on the type of fault to be studied. Dip-slip faults trenches are generally opened perpendicularly with respect to the fault because deformation can be seen in a 2D across-fault view. Conversely, strike-slip faults require a double set of trenches (parallel and perpendicular to the fault) because deformation is best seen in 3D.

The dimensions of a trench are dependent on the width of the fault zone to be investigated. In general, a trench is 20 to 40-m long, 3 to 4-m deep and 1 to 4-m wide. Size depends strongly on the safety of the workers involved, so it can be increased if shoring and other tools increasing wall stability are adopted.

In any case the trench should be extended enough in order to include all the possible deformation zones.

Figure 5.2 - Example of a paleoseismological trench dug with a backhoe.

After a preparatory phase (cleaning and gridding), a log of the trench wall is realized by hand-drawing and/or photomosaicking the stratigraphy and its relationships with the tectonic structures, highlighting the possible geological records of individual surface-deforming earthquakes of the past. In unlucky cases it is possible to recognize only the evidence of cumulated deformation due to repeated paleoearthquakes.

The stratigraphic level that was the ground surface at the time the earthquake occurred is generally known as the event horizon.

Some features that are widely accepted as evidence for paleoearthquakes include:

- colluvial wedges, wedge shaped deposits that accumulate at the base of a scarp following the sudden and sharp elevation change of the ground surface caused by dip-slip earthquakes, or because of lateral juxtaposition of topography. A Colluvial wedge represents a post-earthquake deposit and the event horizon will be located at its base (figure 5.3a);
- upward fault terminations, an abrupt upward termination of faults against an unconformity (the event horizon) at several locations in the trench (figure 5.3b);
- tilted or folded strata overlaid by less deformed strata, forming an angular unconformity that represents an event horizon;
- increasing amount of deformation with increasing age of sediments (figure 5.3c). When a stratigraphic unit shows a greater amount of displacement with respect to the overlaying sequence, the boundary between the sequences can be interpreted as an event horizon. This can be particularly clear when there is a vertical component of slip;
- identification of fissure infills (figure 5.3d);
- identification of liquefaction features within the stratigraphy.

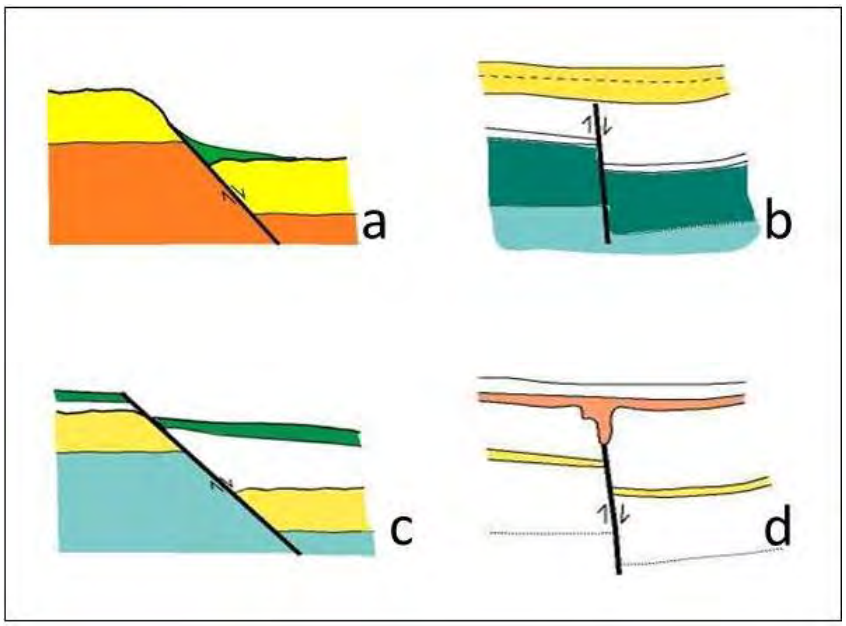

Figure 5.3 - Some features widely accepted as evidence for paleoearthquakes. a) colluvial wedge (green wedge-shaped deposit); b) upward fault termination; c) increasing amount of deformation with increasing age of sediments; d) fissure infill. Figure courtesy of D.Pantosti.

5.2.2 Coring

Shallow cores (1 to 10 m in depth) represent another useful tool to investigate and characterize fault zones.

Drilling cores can be considered as a preliminary method to investigate recent faulting in unconsolidated continental deposits and to extend the paleoseismic record beyond the limits of trenching (Mattson et al., 2003) or can provide a viable alternative when trenching is impractical (Improta et al., 2010).

In order to extend the depth of investigation and reach older sediments involved in the deformation, during the paleoseismological campaign in L'Aquila, two cores were extracted from boreholes drilled by a vibracoring system (gasoline-powered percussion hammer) at Aqueduct and Mo'Tretteca sites.

The equipment used in this work is a percussion drilling set for heterogeneous soils with gasoline-powered percussion hammer (Atlas COPCO COBRA TT1).

The drilling set contains, among other accessories, the following main equipments:

- gasoline-driven percussion hammer (figure 5.4);
- percussion gouges (figure 5.4) in various diameters (from 40 to 100 mm) and lengths (50, 100 and 200 mm);
- core sampler equipped with a PVC sampling tube;
- mechanical extraction system.

Figure 5.4 – gasoline-powered percussion hammer (to the left) and percussion gouges with extensions rods (to the right).

This drilling set can be used to take reasonably undisturbed samples from depth to about 10 meters, without the use of drilling liquid. The design of the percussion gouges allows easy emptying and cleaning operations. Moreover, the PVC sampling tube with the undisturbed sample can be sealed for transport and further analyses in a laboratory.

The characteristics of the abovementioned drilling tool enable an easy transportation of the entire set to the desired investigation area, even in unfavorable logistic conditions. The main limitations are generally related to the type of materials to be drilled: gouges will not penetrate soft rock, large stones or sound concrete.

5.2.3 Chronological constraints

A critical step of the paleoseismological investigations is to obtain temporal constraints for the coseismic displacement of the past. Dating of the identified paleoearthquakes is crucial to estimate the average slip-rate of the fault and to evaluate the average recurrence time between earthquakes on the same fault segment.

Once the layer that represents the event horizon (the ground surface at the time of the paleoearthquake) is set in the stratigraphy, it is possible date the paleoearthquake by using the maximum and minimum ages from sediments deposited shortly before the earthquake and shortly after the event, respectively.

During our paleoseismological investigations, we developed a chronological framework based on 27 samples collected for radiocarbon dating as well as on archeological evaluation of pottery shards found within late Holocene deposits.

5.2.3.1 Radiocarbon dating

Radiocarbon dating is probably the most common method for dating in paleoseismology. Quaternary continental deposits may contain charcoal fragments, shells, bones, organic layers and soils that may be suitable for ^{14}C dating.

Radiocarbon dating has been one of the first radiometric techniques to be developed (the first radiocarbon measurements were published in 1949) and perhaps the most widely used. This is an isotopic method based on the radioactive decay of the naturally occurring ^{14}C isotope of carbon. The other two isotopes, ^{12}C and ^{13}C are both stable, while ^{14}C is unstable and undergoes β-decay to a stable form of ^{14}N. Atoms of ^{14}C are constantly produced by the interaction of cosmic rays and nitrogen. The atoms produced in this process are then combined with oxygen to form a particular form of $^{14}CO_2$. This is the way the ^{14}C becomes part of the earth's global carbon cycle and is assimilated by plants through the photosynthesis and by animals through the ingestion of plant tissues. When plants and animals die, they stop exchanging carbon with the biosphere and their ^{14}C content then starts to decrease at a rate determined by the law of radioactive decay.

Radiocarbon dating is essentially a method designed to measure residual radioactivity. By knowing how much ^{14}C is left in a sample, the age of the death of the organism can be known. The half-life of a ^{14}C atom is $5{,}730 \pm 40$ years, and under normal circumstances, the limit of measurement of ^{14}C activity is eight half-lives. This translates into an upper age limit of around 45,000 years.

This method can be applied to a wide range of materials that contain carbon originally fixed from atmospheric CO_2, including wood, macrofossils, shells, bones, charcoals, soils and paleosols, peat and pedogenic carbonate.

Physical and chemical pretreatments are done on these materials to remove possible contaminants before they are analyzed for their radiocarbon content.

Two approaches are generally in use for measuring the residual ^{14}C activity in samples relative to modern standards. 1) Beta counting, measures the ^{14}C activity of the sample by decay counting the beta particles emitted by a given sample. Beta particles are products of radiocarbon decay; 2) accelerator mass spectrometry (AMS), which employs a particle accelerator to count the relative number of ^{14}C atoms in a sample, as opposed to the decay products.

The calculation of radiocarbon ages of samples assumes that the specific activity of the ^{14}C in the atmospheric CO_2 has been constant through time. However, early in the history of radiocarbon dating it was recognized that atmospheric ^{14}C was not constant. After measurements are done, it is thus important to calibrate ^{14}C-dating results in order to convert raw radiocarbon ages (usually reported in years Before Present –BP, where "present" means 1950 by convention) to calendar years. This can be done using a calibration dataset constructed by measuring the radiocarbon age of tree rings of known age or other independently dated samples. The radiocarbon ages used in this work were corrected according to Calib Rev 6.0 (Stuiver, Reimer and Reimer, 2005; Reimer et al., 2004) and reported as AD/BC for Holocene ages and as BP for Pleistocene ages (table 5.1).

In order to compare the results and assure reliable ages, our radiocarbon samples (both charcoals and bulk) were sent to two different specialized laboratories (Beta Analytics. Inc – Florida, USA and Poznan Radiocarbon Laboratory – Poland).

Site	Unit	Sample, Lab Code[a]	Type	Conventional Age BP[b]	Calibrated Age[c]	Probability Distribution
ACQ	90	ACQ-B3, Beta-273363	bulk	31370 ± 260	36490–35150 BP	1.000
ACQ	93	ACQ-B4, Beta-273364	bulk	24600 ± 150	30050–28920 BP	1.000
ACQ	82	ACQ-B5, Beta-273365	bulk	7500 ± 50	6440–6250 BC	1.000
ACQ	93	ACQ-B7, Beta-273366	bulk	25560 ± 160	30850–30170 BP	0.934
					30010–29730 BP	0.066
ZAC	80	ZAC-B2, Poz-33712	bulk	14810 ± 90	18510–18230 BP	0.365
					18150–17680 BP	0.635
ZAC	50	ZAC-B4, Poz-33711	bulk	4440 ± 40	3330–3210 BC	0.341
					3190–3160 BC	0.069
					3130–2930 BC	0.589
ZAC	38	ZAC-B5, Poz-33710	bulk	1410 ± 35	580–670 AD	1.000
ZAC	35	ZAC-C1, Beta-273371	charcoal	1400 ± 40	570–680 AD	1.000
TRET	60	TRET-B50, Poz-33714	bulk	1330 ± 30	650–720 AD	0.814
					740–770 AD	0.186
TRET	80	TRET-C805, Poz-33716	charcoal	755 ± 35	1220–1290 AD	1.000
TRET	81	TRET-C300, Poz-33720	charcoal	1205 ± 30	690–700 AD	0.005
					710–750 AD	0.091
					770–890 AD	0.904
TRET	81	TRET-C1, Beta-266355	bulk	1330 ± 40	650–770 AD	1.000
TRET	80	TRET-C31, Poz-33719	charcoal	1025 ± 30	900–920 AD	0.029
					970–1040 AD	0.945
					1100–1120 AD	0.023
					1140–1150 AD	0.004
TRET	80	TRET-C4, Poz-33718	charcoal	1035 ± 30	900–920 AD	0.056
					950–960 AD	0.009
					960–1040 AD	0.935
TRET	90	TRET-C2, Poz-33721	charcoal	2020 ± 35	150–140 BC 110	0.020
					BC–60 AD	0.980
TRET	90	TRET-C11, Poz-33722	charcoal	1130 ± 30	780–790 AD	0.008
					810–840 AD	0.054
					860–990 AD	0.939
TRET	210	TRET-B10, Poz-33715	bulk	2460 ± 35	760–680 BC	0.265
					670–410 BC	0.735
TRET	200	TRET-C30, Beta-266356	charcoal	2510 ± 40	790–510 BC	0.987
					440–420 BC	0.013
TRET	90	TRET-B20, Beta-273368	bulk	1070 ± 40	890–1020 AD	1.000
TRET	302	TRET-S1a, Beta-273370	bulk	22210 ± 130	27570–27210 BP	0.104
					27110–26170 BP	0.896
250K	62	250K-B1, Poz-32265	bulk	2605 ± 30	820–760 BC	0.985
					680–670 BC	0.015
250K	70	250K-B2, Poz-32266	bulk	6010 ± 40	5000–4800 BC	1.000
250K	60	250K-B3, Poz-32267	bulk	2535 ± 35	800–720 BC	0.360
					690–540 BC	0.640
250K	90	250K-B30, Beta-273359	bulk	23500 ± 140	28610–27920 BP	1.000
250K	80	250K-B50, Beta-273360	bulk	15520 ± 70	18870–18580 BP	1.000
250K	65	250K-B70, Beta-273361	bulk	4200 ± 40	2900–2830 BC	0.286
					2820–2660 BC	0.702
					2650–2640 BC	0.012
250K	50	250K-C101, Beta-273362	charcoal	20 ± 40	1690–1730 AD	0.216
					1810–1920 AD	0.717
					1950–1955[d] AD	0.067

Table 5.1 – Measured and calibrated ages of the ^{14}C samples collected (from Cinti et al., 2011)

[a]Lab. code: Beta, Beta Analytics Inc. (Florida); Poz, Poznan Radiocarbon Laboratory, Poland. [b]Measured radiocarbon age corrected for isotopic fractionation, calculated using the delta 13C. It is not calendar calibrated. [c]Age dendrochronologically corrected for the C12/C14 changes in the atmosphere according to Calib Rev 6.0.0 and rounded to the nearest decade. Holocene ages are given as AD/BC, and Pleistocene ages as BP. 2σ range. [d]Denotes influence of nuclear testing C14.

5.2.3.2 Archeological evaluation of pottery shards

Human settlements and economic ascent in the area since ~ 1000 AD (the town of L'Aquila was founded in 1229 AD) facilitated the presence of archeological remains within the very recent deposits of this portion of the Middle Aterno basin.

The reference chronological framework obtained by means of radiocarbon dating was thus also integrated with age estimates from archeological evaluation of pottery shards (figure 5.5) found within the stratigraphy of the trenches. A summary of the evaluation of pottery fragments is provided in Table 5.2.

Sample	Unit	Age Interval[a]
250K-P4	61	XI–XIII century
TRET-PY	50	XIV–XV century
TRET-P3	50	XIII–XIV century
TRET-P2	90	XI–XIII century
TRET-P10	90	XI–XIII century
TRET-P200	90	XI–XIII century
ACQ-P2	10	XII–XIII century
ACQ-P1	81	<XII–XIII century

Table 5.2 - Evaluation of Pottery Fragments. [a]Expert evaluation of archeologists: Enrico Cirelli and Hermann Borghesi.

Figure 5.5 – pottery fragments found within the stratigraphy of Mo'Tretteca trench.

5.3 Paleoseismological trenching along the PSDFS

As already mentioned above, we studied in detail four paleoseismological trenches along the northwestern portion of the PSDFS. The trench sites selection was guided primarily by the field observations of the 2009 coseismic ruptures and by the geomorphological long-term expression of the PSDFS, and represented the best compromise between specific geologic targets and logistic/environmental difficulties.

All the investigated sites (Aqueduct, Zaccagnini, Mo'Tretteca and 250K) are located at the base of the main escarpment bounding the Paganica village and share a similar stratigraphic setting.

In particular, the lowermost deposits common to all trench walls are represented by middle Pleistocene alluvial fan and alluvial deposits, made of calcium carbonate

gravels generally clast-supported in a fine-grained sandy matrix (numbered as unit 100 at all sites).
The top of this deposit is abruptly truncated by an erosional surface on which developed brown to dark brown paleosols that predate the Last Glacial Maximum (LGM, ~22-19 ka - Yokoyama et al., 2000). Slope deposits overlie the paleosols and are truncated by a second erosional surface associated with the LGM. This surface is overlain by a series of Holocene fine to coarse-grained alluvial and slope-derived deposits.
For the purposes of this thesis we will describe the results of our paleoseismological investigations focusing on those data that allowed us to estimate a slip-rate for the Late Pleistocene and Late Holocene.

5.3.1 Aqueduct site

This excavation is the result of the rupture of the Gran Sasso water pipeline due to the 2009 coseismic surface faulting along the PSDFS. The ejected over-pressurized water (25 atm, Cinti et al, 2011) deeply scoured the ground and opened an 80 m-long and up to 4 m-deep trench. We then deepened (1 to 2 m) and rectified the NW wall in order to better analyze the stratigraphic sequence.
This excavation provided an exceptional exposure of sediments and fault structures across the ~ 20 m-high compound scarp of the PSDFS, and allowed us to characterize the main fault zones and to estimate the short-term (~30 ka) slip-rate by correlating units across the fault zones.
More in detail, the northeastern (upper) portion of the excavation (from meters 36 to 78.5, figure 5.6) exposed a sequence of calcareous conglomerates with whitish, fine-grained silty/sandy matrix and interbedded layers of brown clayey silt. These deposits are affected by several high-angle (50°-70°), mostly SW-dipping normal faults. At m 35-36 a fault (F in Figure 4b) marks the separation between the upper portion of the excavation and younger sequence of alluvial, colluvial and slope wash deposits (meters 0 to 36).

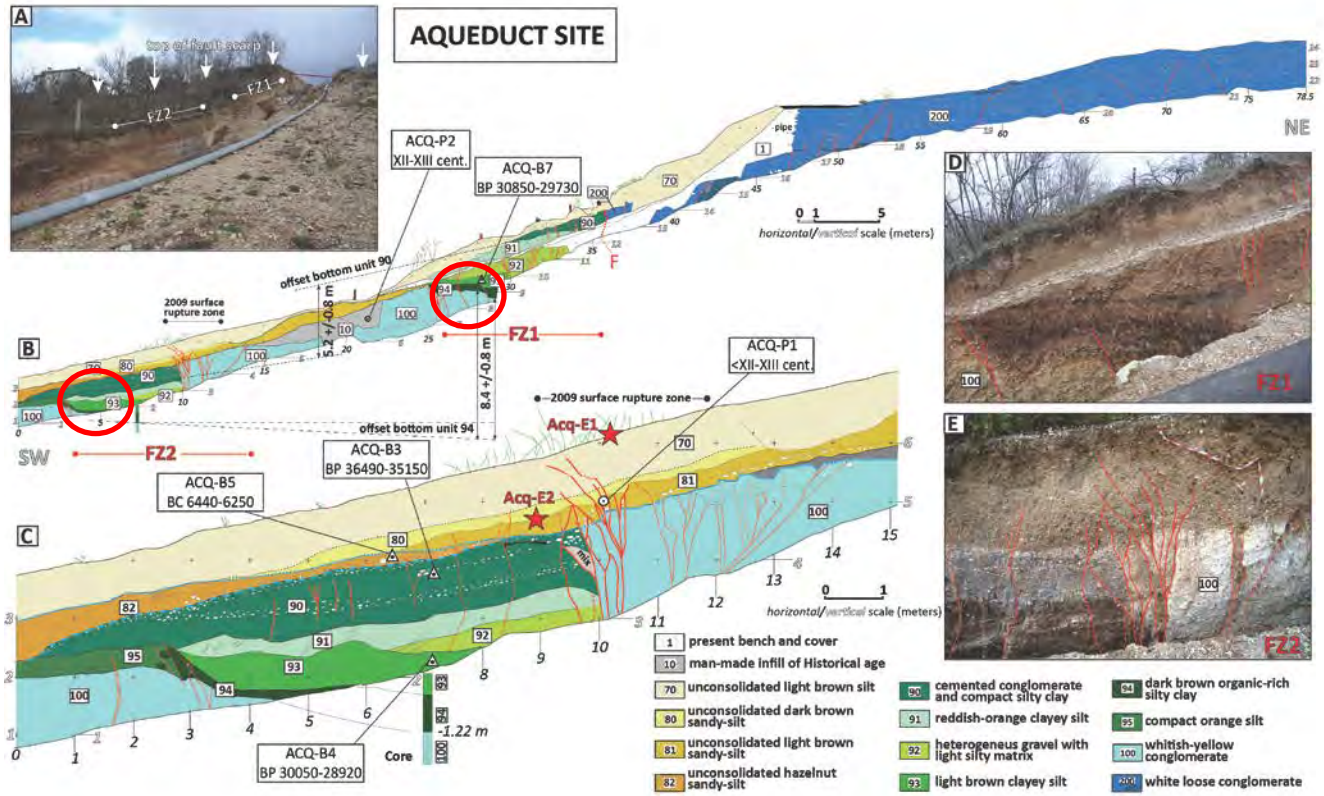

Figure 5.6 - Acq site. (a) View of the excavation along the water pipeline where it crosses the ~20 m high cumulative scarp. (b) Simplified log of the NW wall from a 1:20 scale survey. Triangles indicate dated radiocarbon samples (Table 1); circles indicate evaluated pottery shards (Table 2). Dashed gray lines show correlations of units for long-term vertical slip rate evaluation. Dashed and dotted blue thick lines mark erosional contacts associated with the LGM and with probable medieval quarrying, respectively. (c) Enlargement of fault zone FZ2. Symbols are the same as in Figure 4b; red stars indicate location of event horizons (ground surfaces at the time of surface faulting earthquakes). (d) View of the graben associated with fault zone FZ1 approximately between m 25 and 33. (e) View of the active fault traces of fault zone FZ2 approximately between m 8 and 12. In this zone the 2009 ruptures produced diffuse deformation accompanied both by cracking and warping. After Cinti et al., 2011.

Two main fault zones characterize this portion of the exposure: fault zone 1 (FZ1) at m 25-36 and fault zone 2 (FZ2) at m 3-13 (figure 5.6). The two fault zones share a similar graben-like structure formed by closely spaced, high- angle, SW and NE dipping normal faults and show clear evidence of repeated paleoearthquakes. Both fault zones involve also the same depositional sequence. In order to completely expose this sequence within the graben of FZ2, we drilled a borehole at meter 7 which confirmed that unit 100 is capped by the same units (93-94) that fills the base of the FZ1 graben.
This correlation is also supported by radiocarbon ages of ~30 ± 1 ka from unit 93 in both fault zones (ACQ-B4 and ACQ-B7 in table 1).
The evidence for similar deposits with the same age (red solid circles in figure 5.6) allowed us to measure the vertical separation between the same units and to estimate a vertical slip-rate.
We can use the apparent offset at the base of unit 94 (which is the oldest unit preserved into the graben structures) across FZ2, between borehole at meter 7 and the FZ1 graben, to roughly estimate a total throw of 8.4 ± 0.8 m. Dividing the measured total throw by the ages of unit 93 (calibrated age of 30850-28920 BP, ACQ-B4, ACQ-B7, table 5.1), we obtain a vertical slip-rate of 0.25-0.32 mm/yr since 30 ka (Late Pleistocene).
Moreover, using the age and throw of the penultimate event at Aqueduct site, we can estimate a slip-rate for a younger time interval at this site. In fact, dividing the measured cumulated offset of unit 81 (0.35 – 0.4 m) by the age constraints derived from a pottery found within the same unit (ACQ-P1, XII–XIII century, table 5.2), we can estimate a Late Holocene slip-rate of 0.41-0.53 mm/yr.
At this site we found evidences for 1 paleoearthquake, that is event Acq-E2, showing a throw of 0.35-0.4 m.

5.3.2 Zaccagnini site

The Zaccagnini trench is located ~30 m SE of the Aqueduct site (figure 5.1); at this location the 2009 coseismic surface ruptures consist of a SW facing free face with a throw of about 0.10 ± 0.05 m, locally accompanied by ground warping. The overall geomorphic situation is the same as at the Aqueduct site, with the 2009 ruptures running along the base of the main scarp. The trench was NE-SW oriented and about 12 m-long.

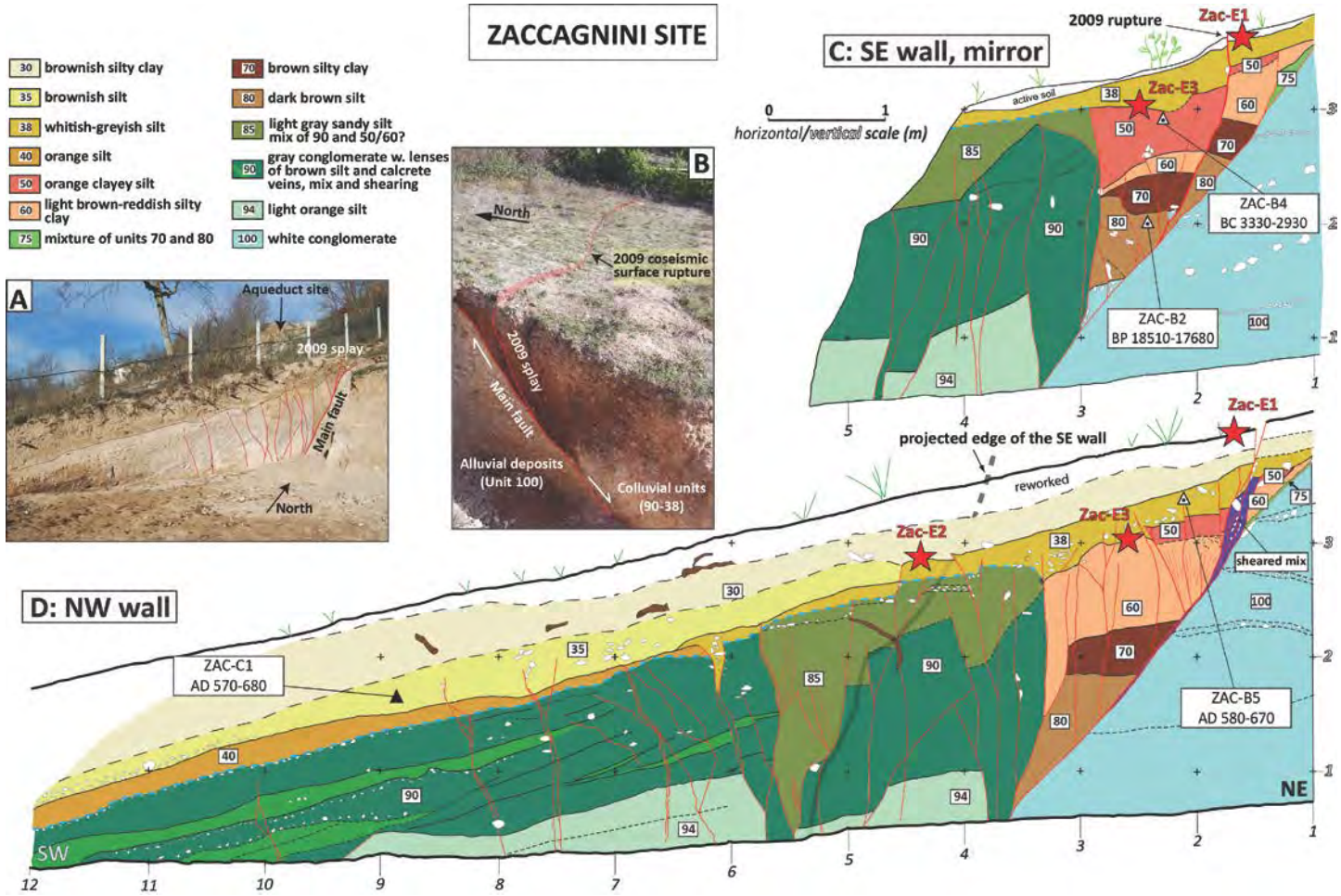

Figure 5.7 - Zaccagnini site. (a) View of the NW trench wall. (b) View of the shorter SE trench wall. (c) Simplified log of the SE wall from a 1:20 scale survey. Triangles indicate dated radiocarbon samples (Table 1), red stars indicate location of event horizons, dashed thick blue line marks the erosional contact associated with the LGM. (d) Simplified log of the NW wall, symbols are the same as in figure 5.6c. After Cinti et al., 2011.

This excavation exposed a prominent N130° striking and 50°– 55° SW dipping main normal fault and a 4 m wide zone of subvertical hanging wall faults, which includes the 2009 ruptures, with a very similar geometry with respect to that of FZ2 at the Aqueduct site.
Based on their sedimentological and stratigraphical characteristics, some of the deposits exposed at Zaccagnini site can be correlated with those exposed at the nearby Aqueduct site.
The Zaccagnini site provided evidence for at least two paleoearthquakes: event Zac-E2 with a throw of 0.10-0.15 m and event Zac-E3 with a throw of 0.25-0.30 m.
Using the age (BC 3330 670 AD, with the younger part of the interval preferred) and the cumulated throw of these events (0.45-0.55 m), we can estimate a Late Holocene slip-rate at this site of 0.09 – 0.43 mm/yr, with the higher slip-rate value preferred.

5.3.3 Mo'Tretteca site

The Mo'Tretteca trench was dug across a secondary splay of the 2009 coseismic ruptures occurred along a ~ 5 m-high, southwest facing minor scarp of the PSDFS. Here the 2009 coseismic rupture displayed up to 0.1 m of vertical displacement, a few cm of warping and up to 0.05 m of opening. The trench was NE-SW oriented, about 20 m-long and up to 3 m-deep, and was cut across an abandoned alluvial fan surface.
In coincidence of the 2009 surface rupture, the trench wall exposed a single, 2 m wide, V-shaped fault zone composed of a main fault plane and several synthetic splays (figure 5.8).

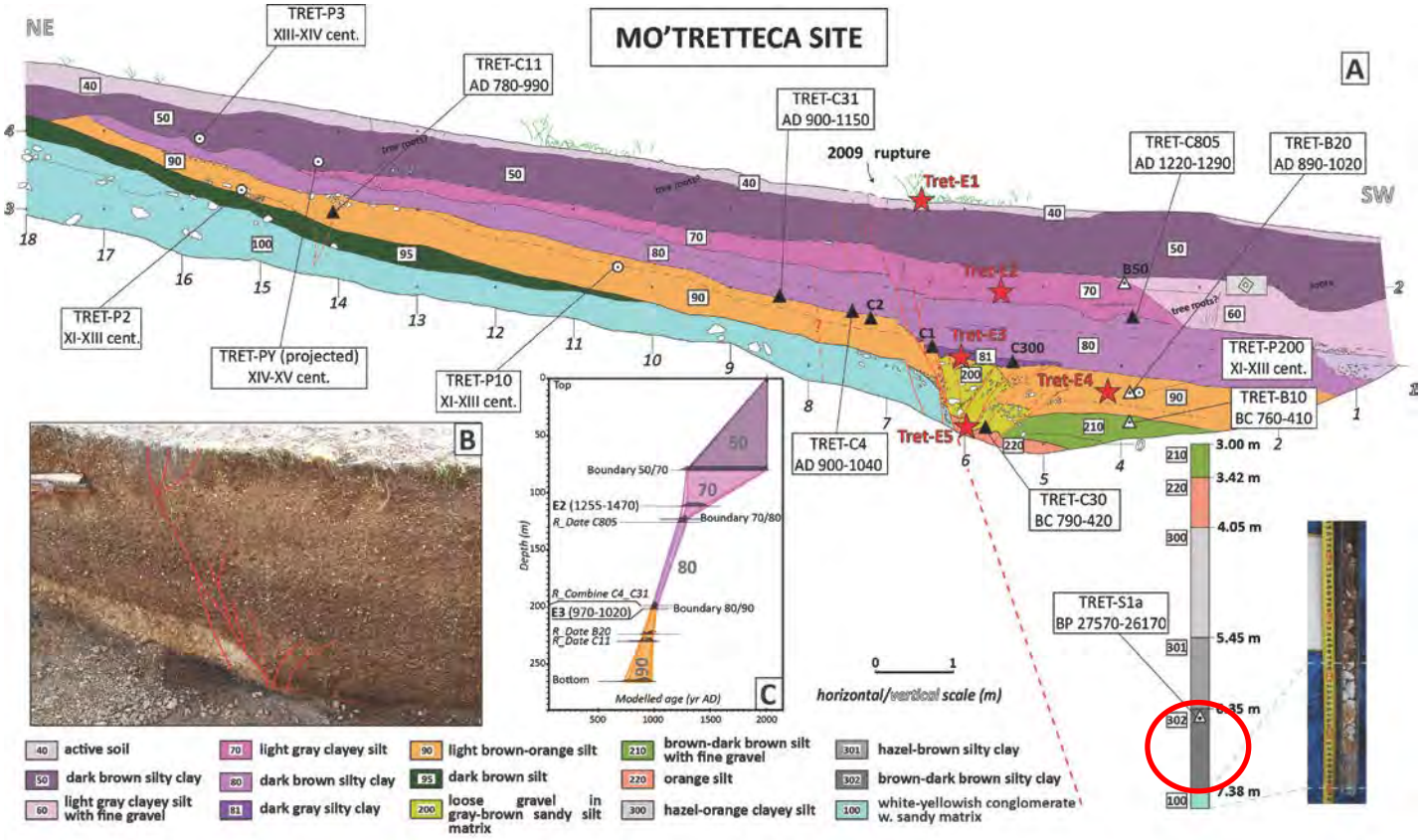

Figure 5.8 – Tret site. (a) Simplified log of the SE wall from a 1:20 scale survey. Triangles indicate dated radiocarbon samples (Table 5.1), circles indicate evaluated pottery shards location (Table 2), red stars indicate location of event horizons. (b) Photo of the fault zone approximately between m 4 and 8. (c) Age-depth model obtained for units 90 to 50 using a P sequence from OxCal v4.1.5 [Bronk Ramsey, 2008, 2009]. The best estimate of the age ranges of events Tret-E2 and Tret-E3 are derived from this model. After Cinti et al., 2011.

The sedimentary sequence exposed in this trench is composed of partially cemented whitish alluvial gravel within a yellow sandy matrix (unit 100) buried under a silty to silty clay colluvial sequence deposited during the past 3 millennia (see details in Cinti et al., 2011).
With the aim of finding deposits correlative with the oldest ones exposed on the footwall (units 95 and 100), we cored the hanging wall to a depth of 7.6 m. The core intercepted the gravel of unit 100 between m -7.38 and -7.60 (although we cannot preclude that this material may be reworked and that the in situ unit 100 is a little deeper).
Taking into account the dip of unit 100 from the trench wall and assuming limited erosion of the footwall, we can estimate a minimum throw of about 4.7 $\pm$ 0.1 m.
A late Pleistocene vertical slip-rate of 0.16-0.18 mm/yr can be estimate for this splay of the PSDFS dividing the measured throw by the age constraints derived from a bulk sample collected in the core one meter above unit 100 (red solid circle in figure 5.8, calibrated age of 27570-26180 BP, TRET-S1a, Table 5.1).
We can also use the age and throw of the recognized individual events to estimate the following Late Holocene slip-rates at this site. If we consider the cumulated throw of individual events at this site (1.15 – 1.4 m) and divide it by the age of the deposits (calibrated age of BC790 – 410, TRET-C30 and TRET-B10, table 5.1), we obtain a Late Holocene slip-rate of 0.42-0.6 mm/yr.
At Mo'Tretteca site we found evidences for 4 paleoearthquakes, characterized by different throw per event: event Tret-E2, with a throw of 0.15-0.20 m; event Tret-E3, with a throw of 0.10-0.20 m; event Tret-E4, with a throw of 0.30-0.45 m and event Tret-E5, with a throw of 0.35 m.

5.3.4 250K site

At this site we took advantage of a NE-SW cut in a building yard located in between the two 2009 coseismic rupture splays (figure 5.1). This artificial excavation was logged in detail because it contained faulted late Pleistocene and Holocene deposits. The stratigraphic sequence is composed by a set of colluvial deposits overlying the white middle Pleistocene alluvial gravel found also at the other sites (unit 100). Two main normal fault zones displace the entire sequence (figure 5.9).

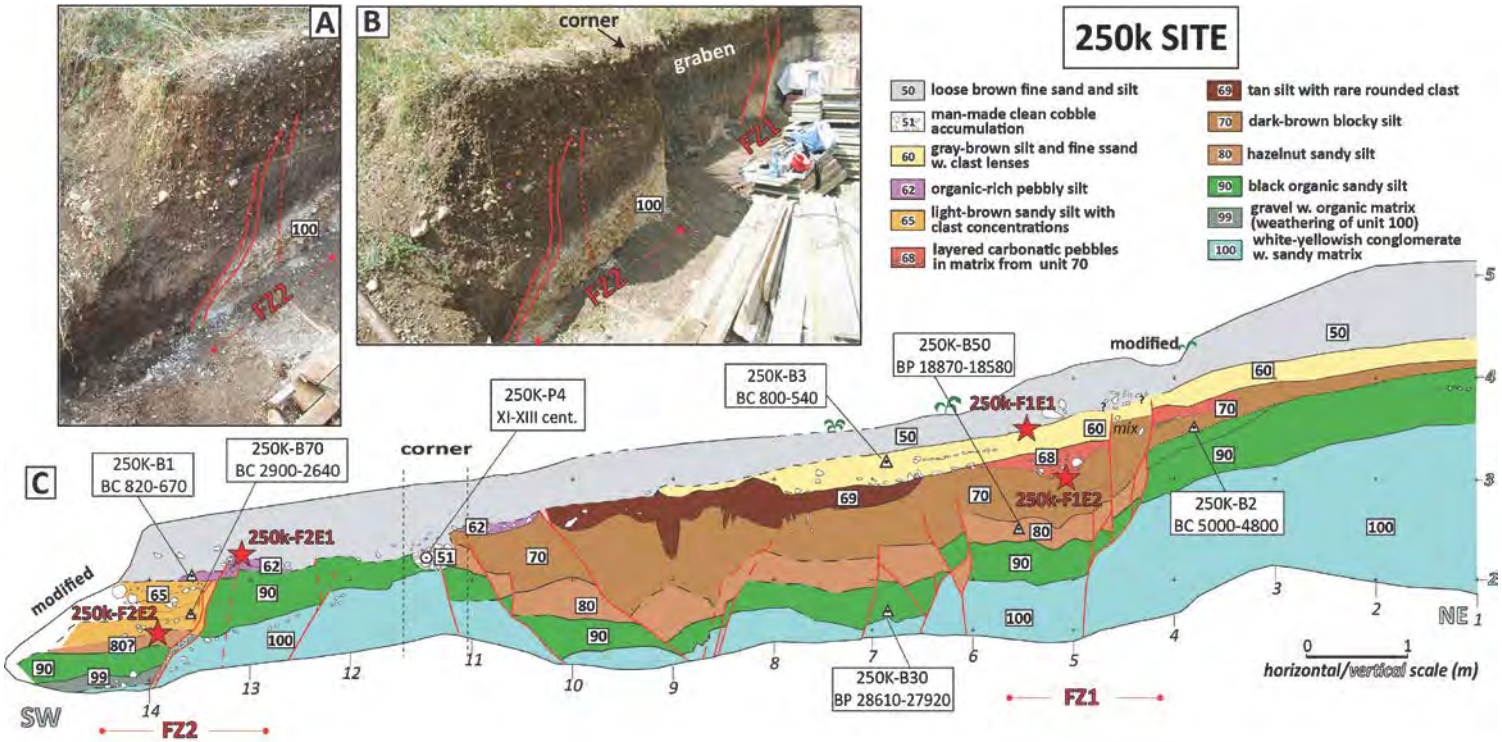

Figure 5.9 – The 250k site. (a) View of fault zone FZ2 on the NW wall of the excavation juxtaposing the colluvial wedge unit 65 (on the right) with unit 90. (b) View of the NW wall of the excavation. The two fault zones FZ1 and FZ2 and part of the FZ1 graben are visible; the wall is not rectilinear but forms a corner between m 12 and 11. (c) Simplified log of the NW wall from a 1:20 scale survey. Triangles indicate dated radiocarbon samples (Table 1), circles indicate evaluated pottery shards location (Table 2), red stars indicate location of event horizons. Notice that because of the corner in the wall between m 11 and 12, the distance between these two reference lines exceeds 1 m. After Cinti et al., 2011.

Fault zone 1 (FZ1) is composed of a set of subvertical fault splays that merge in a single plane within unit 100. This fault zone is faced by a ~ 6 m wide graben structure formed by a set of synthetic and antithetic fault splays, showing a similar deformational style compared to the Aqueduct site. Fault zone 2 (FZ2,) is exposed at the SW edge of the wall and appears composed by a set of subvertical, normal, down to the SW, fault splays. Unfortunately, the record on the hanging wall side of this fault zone has been partially removed and thus it was not possible to clearly observe the relationship between this tectonic structure and the 2009 coseismic rupture mapped ~15 m southwest.

Projecting the top of unit 100 across FZ1 and FZ2, and assuming minor/null erosion in the footwall, the net vertical offset is up to 2 m. Using the measured throw and dividing it by the age of the overlaying unit (calibrated age of 28610 - 27920 BP, 250K-B30, table 5.1), we can estimate a Late Pleistocene slip-rate of 0.07 mm/yr. However, because this site does not cross the entire zone of deformation, this value should be considered as a minimum.

Moreover, we are also able to estimate a Late Holocene slip-rate at this site. Given the cumulated deformation (1.2 -1.3 m) due to the occurrence of the recognized paleoearthquakes at this exposure and the available age constraints (between calibrated ages of 5000 BC, 250K-B2, and 540 BC, 250K-B3, table 5.1), we may estimate a Late Holocene slip-rate of 0.17 – 0.52 mm/yr for this site.

At this site we found evidences for 2 paleoearthquakes, characterized by different throw per event: event 250K--F1/F2 E1, with a throw of 0.40-0.50 m and event 250K--F1/F2 E2, with a throw of 0.80 m.

5.4 Main results

On the basis of the paleoseismological investigations, including trench analysis and coring, we reconstructed the recent paleoseismological history of the northwestern portion of the PSDFS and obtained Late Holocene and Late Pleistocene vertical slip-rates. The main results of this study in term of slip-rate evaluation are summarized in table 5.3.

Site	Time interval	Vertical slip-rate
Aqueduct	Late Holocene (last 5 ka)	0.41 - 0.53 mm/yr
Zaccagnini	Late Holocene (last 5 ka)	0.09 - 0.43 mm/yr
Mo'Tretteca	Late Holocene (last 5 ka)	0.42 - 0.60 mm/yr
250 K	Late Holocene (last 5 ka)	0.17 - 0.52 mm/yr
Aqueduct	Late Pleistocene (30 ka)	0.25 - 0.32 mm/yr
Mo'Tretteca	Late Pleistocene (30 ka)	0.16 - 0.18 mm/yr

Table 5.3 - Late Holocene and Late Pleistocene vertical slip-rates estimated by means of paleoseismological investigations.

Moreover, we derived average vertical slip-rate values from the two time intervals by averaging the minimum and maximum values from table 5.3.
The results are listed as follows:

- the average Late Holocene vertical slip-rate is of 0.27 - 0.52 mm/yr.
- the average Late Pleistocene vertical slip-rate is of 0.21 - 0.25 mm/yr.

The other paleoseismological results, including the description of the evidences for the occurrence of distinct paleoearthquakes, the timing and correlation of the events, along with the implications for fault segmentation, recurrence and seismic hazard, are described in detail in the attached article "Evidence for surface faulting events along the Paganica fault prior to the 6 April 2009 L'Aquila earthquake (central Italy)", published on Journal of Geophysical Research in 2011, which I co-authored.

6 Tectonic geomorphological and geological approach

6.1 Introduction

In this chapter we present the extensive 1:10.000 scale geomorphological and geological investigations, supported by field survey and by aerial photo and digital topography analyses, carried out in the Middle Aterno valley over an area of ~140 km^2. We focused on the identification, and characterization of the long-term expression of Paganica-San Demetrio Fault System (hereinafter PSDFS), through the study of continental deposits and landforms affected by cumulative offset. The main goal is to provide new insights on the Quaternary deformational history of the PSDFS and to obtain long-term (up to ~2 Ma) slip-rate estimates.

Through the field survey, a total number of ca. 500 observations points of data collection were georeferenced (figure 1) using a hand-held Global Positioning System (GPS) device. Most of the collected observations points are located along the eastern flank of the Middle Aterno valley, where most of the deformation is concentrated.

All the collected field survey data were organized in a Geographical Information System (GIS) environment to analyze spatial relationships as well as to model spatial processes.

The software used is ArcGIS® Desktop, an integrated suite of software and data used to view and manage information in three dimensions with specialized tools as 3D Analyst and Spatial Analyst.

The GIS environment was particularly useful in analyzing all the data and in managing the high-resolution topographic dataset, as well as in integrating the topographic data and raster imagery with geomorphologic and geologic mapping.

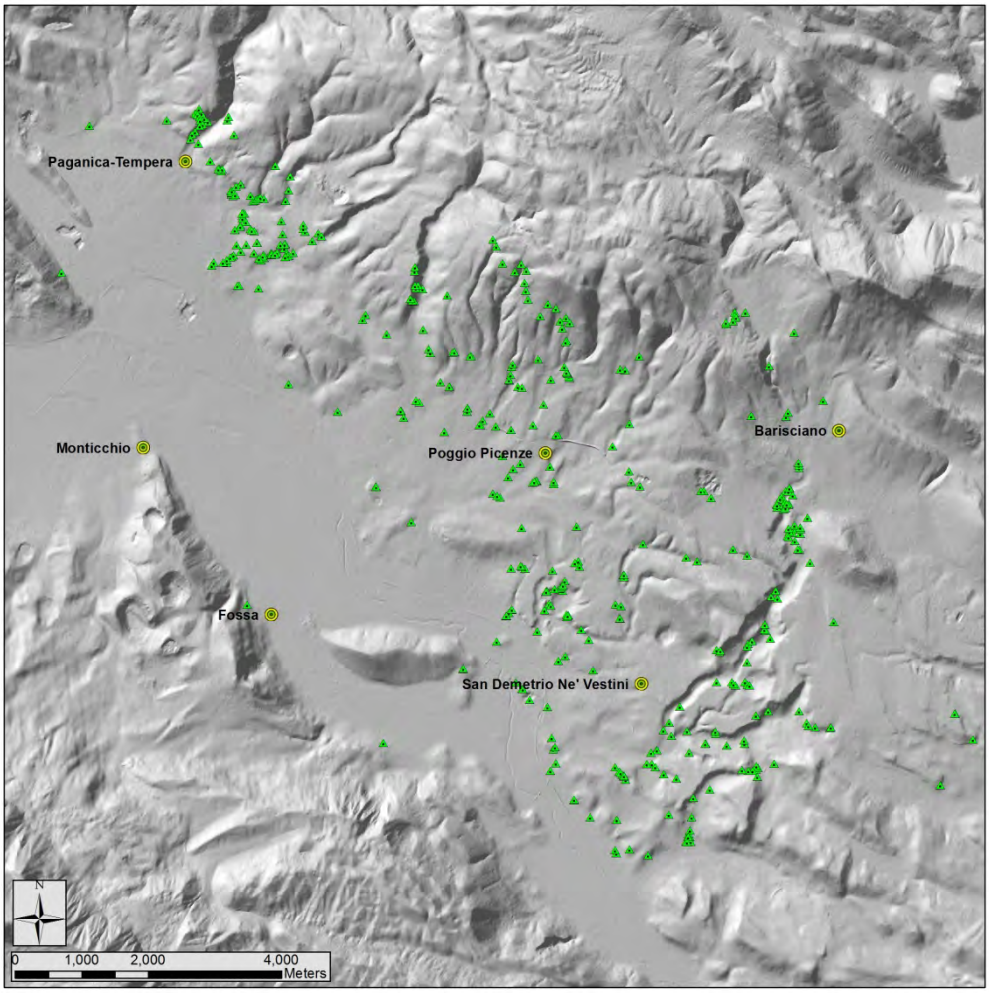

Figure 6.1 - Observation points collected along the Paganica-San Demetrio fault system

6.2 Tectonic geomorphology approach

Tectonic geomorphology is based on the study of landforms and landscapes developed in subaerial conditions that are deformed by tectonics and record a measurable tectonic signal (i.e. geomorphic markers; Burbank and Anderson, 2001). This allows to recognize and understand deformational processes over a wide and relatively recent range of spatial and temporal scales, according to the morphogenic epoch duration (i.e. from Plio-Pleistocene to Holocene in the study area). In particular, tectonic geomorphology analysis is a useful tool to estimate geometrical and behavioral parameters of active faults, such as their crucial rate of slip and its distribution along the fault strike.

In order to estimate the amount of deformation related to tectonic processes, it is typically necessary to have an identifiable and measurable feature of the landscape that has been tectonically displaced. The best geomorphic markers are usually readily recognizable landforms, surfaces or linear trends characterized by: 1) an hypothetical undeformed geometry; 2) a determinable age; 3) a high preservation potential with respect to the time scale of the process being investigated.

Therefore active tectonic studies must begin with a detailed analysis of the recent landscape. In fact, the first step in this study was to undertake a detailed geomorphological analysis aimed at identifying, among other features and other tectonic-related landforms, individual fault scarps that cross displaced geomorphic markers that can be used as piercing points for the measure of the offset amount . The main assumption to use measured displacements in the estimate of slip-rates is that slip occurs repeatedly on a fault, cumulates through time and produce scarps or displacements in the landscape which are thus representative of the amount of deformation occurred since their formation. In the case of normal faulting, for example, fault scarp may reach heights of hundreds of meters.
In this work, landscape analysis and mapping were performed at a 1:10.000 scale using LiDAR-derived Digital Elevation Model (DEM) and its standard derivatives (hillshade, slope, aspect, etc.), by observations and interpretation made on 1:33,000 scale aerial photographs (Gruppo Aereo Italiano – GAI, 1954/1955) and other raster imagery, as well as by fieldwork.
Among all the landforms identified and reported on the map, particular attention was devoted to those morphological features that contribute to the identification of tectonic lineaments, such as scarps, base of scarps, slope changes, paleosurfaces, saddles and ridges, as well as to the morphological features related to the drainage system (terrace risers, piracies, wind gaps, paleovalleys, strong incisions, drainage diversions, etc.).

6.2.1 LiDAR

An airborne LiDAR (Light Detection And Ranging, also known as Airborne Laser Swath Mapping or ALSM) survey was performed few days after the 6 April 2009 L'Aquila mainshock by the Civil Protection of Friuli Venezia Giulia (Italy). We took advantage of the availability of this high-resolution topographic data for the area highly hit by the 2009 April earthquake to generate a high-resolution digital elevation model.
Airborne LiDAR is a recent technology that allows rapid and low-cost measurement of topography over large areas using an active sensory system (laser light) to determine distances. When mounted on a moving platform like an aircraft, this device can rapidly measure distances between the sensor on the airborne and points on the ground surface, collecting densely spaced and highly accurate elevation data. The LiDAR measures and collects multiple returns of a laser beam aimed at the ground and is able to discriminate between the first return, usually from the top of the forest canopy, and the last return, from the bare earth surface. Moreover, by isolating the last returns, LiDAR is capable of revealing the ground surface even in highly vegetated areas.
High-resolution digital topographic data products such as LiDAR-derived digital elevation models (DEMs), allows studying, both qualitatively and quantitatively,

some of the processes responsible for landscape development, including tectonic, fluvial, hillslope, biological and anthropogenic.
Earth-science applications of LiDAR survey include coastal change studies (Sallenger et al., 1999), landslide analysis (Dietrich et al., 2001; Glenn et al., 2006;), volcanic deformation monitoring (Hasegawa et al., 2007), identification and mapping of fault traces and recently active breaks (Haugerud et al., 2003; Sherrod et al., 2004; Cunningham et al., 2006; Kondo et al., 2008; Arrowsmith & Zielke, 2009), slip-rate estimate from offset geomorphic features (Frankel et al., 2007; Amos et al., 2011), definition of fault geometry and kinematics (Begg & Mouslopoulou, 2010). Only a limited number of works took advantage of high-resolution LiDAR-derived topography data focusing on detailed fault scarp morphologic analyses (De Long et al., 2010; Hilley et al., 2010) and on the investigation of the spatial distribution of slope and aspect on active fault scarps (Brunori et al., 2011 submitted).
The LiDAR survey in the area struck by the 2009 L'Aquila earthquake was performed using the Optech ALTM 3100 EA Airborne Laser Terrain Mapper System. The main technical parameters related to the LiDAR acquisition are listed in table 6.1.

System	Optech ALTM 3100 EA
Operating altitude	80 – 3500 m
Vertical accuracy	10 cm < 1000 m (1 sigma) 15 cm < 2000 m (1 sigma) 20 cm <3000 m (1 sigma)
Horizontal accuracy	1/5500 x flying altitude (1 sigma)
Range resolution	1 cm
Scan angle	Variable from 0 to ± 25°
Swath width	Variable from 0 m to 0.93 x altitude
Angular resolution	0.01°
Scan frequency	Variable, maximum 70 Hz
Laser wavelength	1064 nm
Laser repetition rate	Variable from 33 to 100 kHz
Beam divergence	Variable: 0.2 mrad (1/e) or 0.8 mrad (1/e)
"Eye safe" altitude limit	80 m @ 0.8 mrad 400 m @ 0.2 mrad
Intensity	Measurement of intensity of each pulse received
Collected data	Simultaneous measurement in range of first and last pulse for each pulse emitted
Laser classification	Class IV laser products (FDA CFR 21)
GPS receiver	Internal Novatel Millenium DL
Power requirements	28 VDC @35 A peak
Operating temperature	15-35 °C
Humidity	0-95 % non-condensing

Table 6.1 - summary of the LiDAR acquisition parameters

The entire mass of points produced by LiDAR was acquired as a point cloud (x_i, y_i, z_i, where x and y are the horizonal coordinate axes, z is the vertical, and $_i$ is the index of

the point). Vertical and horizontal errors associated with the LiDAR acquisition are less than 0.2 and 0.5 meters, respectively.
Subsequently, the original LiDAR point cloud was processed in order to obtain a regular 1 by 1 m DEM and several derivative digital maps (hillshade, slope, aspect, etc.), suitable for geomorphologic and geologic analyses. Among these maps, hillshade is a hypotetical shaded relief with customizable illumination source angle and shadows derived from a surface raster (i.e., LiDAR DEM).
Moreover, the high-resolution topographic data stored in the LiDAR-derived DEM may be digitally manipulated to enhance and reveal subtle topographic features, something not possible with most aerial photographs, satellite imagery, or lower-resolution digital elevation data.
Figure 6.2 compares the resolution of traditional photogrammetry-generated (5 m resolution - figure 6.2a) and LiDAR-generated hill-shades (figure 6.2b) of the San Demetrio nè Vestini region (SE of the study area). Both the figures highlight how the very high-resolution (1m) LiDAR-derived representation of the ground surface can be a very effective tool in visualizing the landscape with unprecedented detail.

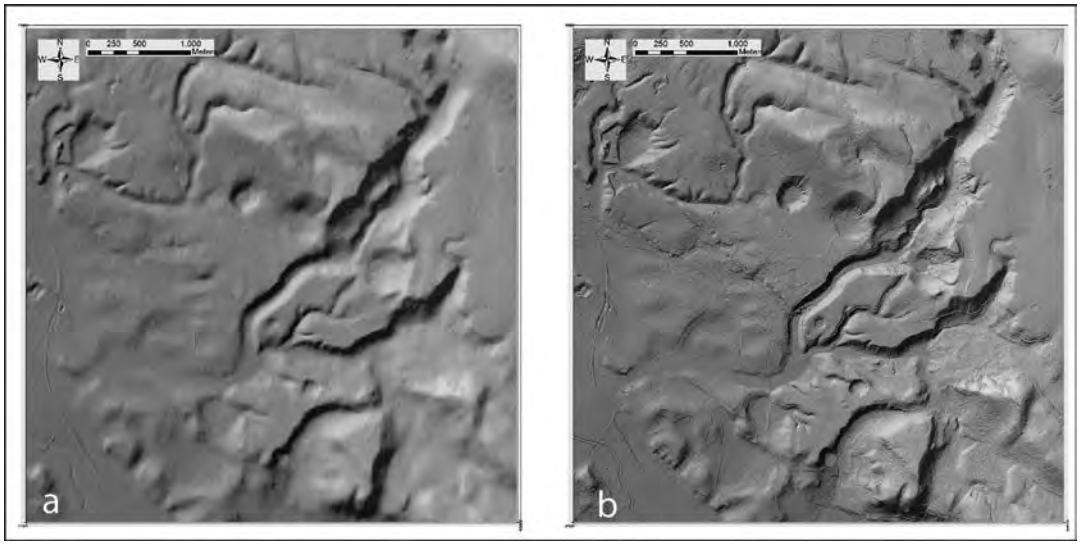

Figure 6.2 - Comparison between 5m resolution (a) and 1-m resolution (b) hillshades

More in detail, in figure 6.2 we note how the LiDAR-derived hillshade has the potential to sustantially increase the confidence to locate and trace the faults through an enanched visualization and consequent mapping of the morphological features that may be related to faulting activity. In figure 6.3 the LiDAR-derived hillshade of the area close to the San Gregorio village (south of the Paganica village) allows to display, among other, some subtle landforms like small fault-related scarps and enhanced drainage incisions (entrenchment that testifies the uplifted fault hangingwall).

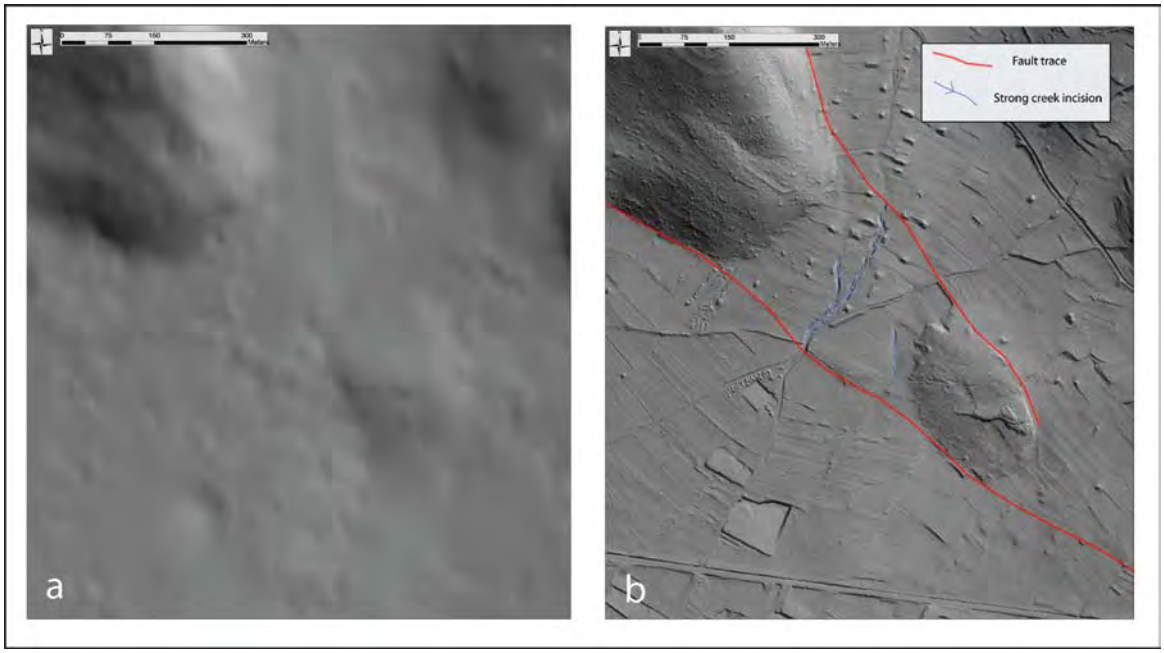

Figure 6.3 - Comparison between 5m resolution (a) and 1-m resolution (b) hillshades

6.2.2 Large-scale view of the Middle Aterno basin

The Middle Aterno basin is a 17 x 5 km intermountain depression located in the axial zone of central Apennines. The basin floor lies at about 600 - 550 m a.s.l., whereas the eastern and western ranges reaches elevations of 1400 m and 1200m, respectively.

The eastern flank of the basin appears strongly controlled by the activity of the PSDFS that produce a staircase-like landscape, with paleosurfaces separated by scarps (mostly in the southern portion).

The western flank of the Middle Aterno basin shows a completely different morphologic expression with respect to the eastern one, with steep slopes controlled by the activity of the antithetic Monticchio – Fossa fault system.

6.2.3 Landforms

All the morphological elements identified and mapped by means of geomorphologic analysis can be grouped into three main categories: 1) planar, 2) linear and 3) punctual landforms.

1) The recognized planar landforms are predominantly represented by paleosurfaces. We should mention that erosional and/or depositional processes act continuously to modify geomorphic markers like paleosurfaces, so what we observe in the present-day landscape are only fragments of a formerly continuous landscape. Several patches of remnant land surfaces were identified and mapped within the eastern flank of the Middle Aterno valley from LiDAR topography and aerial optical images interpretation. Most of the paleosurfaces are located in the southeastern

portion of the basin (figure 6.4), lying at different elevations with respect to the basin floor and ranging in size from ~0,002 to ~0,62 km^2. These include both erosional surfaces carved on the local bedrock and alluvial depositional surfaces, displaying different architecture and amount of preservation depending on their age and elevation. These landscape features are particularly important because they provide useful piercing points to measure tectonic displacement, provided a good knowledge of their original shape.

Figure 6.4 - Paleosurfaces in the southeastern sector of the Middle Aterno river valley

2) The intersection of the fault planes with the surface presents a morphologic expression, called "tectonic lineament", characterized by the alignment of linear features of the landforms. Most of these linear features of the landforms are scarps. As already mentioned in Chapter 3, normal faulting produces mainly vertical deformations. Repeated movements cumulated for several seismic cycles along active normal faults can concur to form compound or multiple-event scarps that separate an uplifting footwall block from a subsiding hangingwall block, building a typical tectonically rising landscape bounded by basin-like areas.
Among all the linear features identified and reported on the map, particular attention was devoted to landforms such abrupt change in the slope dip angle, inner and outer edge of paleosurfaces, hinge line of saddles and ridges. We took in consideration the fact that these morphological features can be produced by both tectonic and erosive/depositional processes, so the tectonic origin of the identified lineaments was inferred using at least one of the following criteria: a) the linear feature is independent and far from the influence of the of the erosive/depositional

players (e.g. fluvial or lacustrine dynamics); b) the linear feature is not of anthropic genesis; c) the lineament is represented by a scarp that trends parallel or sub-parallel to other known faults; d) the lineament is a lateral continuation of a clearly identifiable fault-trace.

Different fault scarp sets are mapped with different strokes on the basis of their morphological expression, taking into account in particular the continuity of the trace, the preservation of the fault scarp and its height. Active normal faults characterized by large escarpments are reported on the map with a red bold continuous line, other active normal faults are mapped with a solid red line while both inferred and buried normal fault traces are mapped using a red dashed line.

Together with tectonic scarps, most of the linear features recognizable in the landscape are related to fluvial processes. The drainage system is very sensitive to any little change on its longitudinal profile induced by both local or regional scale tectonics (i.e. fault-related dislocations and regional uplift/subsidence, respectively). On this light, it is possible to recognize linear landforms as the response to such perturbations in fluvial system and to assess recent near-fault activity. With this aim, near-fault river valleys characterized by a V-shaped cross-section and strong incisions are mapped since they are witnesses of footwall uplift. Other linear features include fluvial terrace risers that bound fluvial terraces. Terrace risers are typically due to the downcutting of the channel on alluvial and fluvial deposits as well as in bedrock, in response to base level lowering (mainly due to either changes in climate and/or to local or regional tectonic uplift). Following this idea, we also highlighted other landscape features like average drainage directions.

3) In this area we also identified some punctual geomorphic features, such as peaks and sinkholes. Peaks highlighted the presence of double crests along the slope, morphological features commonly associated with normal faulting. Sinkholes are also present in our study area, and are interestingly aligned along main escarpments. Being usually related to significant fluid circulation, an alignment of several sinkholes may suggest a tectonic origin for the escarpment (fault).

The main results of landform analysis and mapping are illustrated in the geomorphological map of figure 6.5.

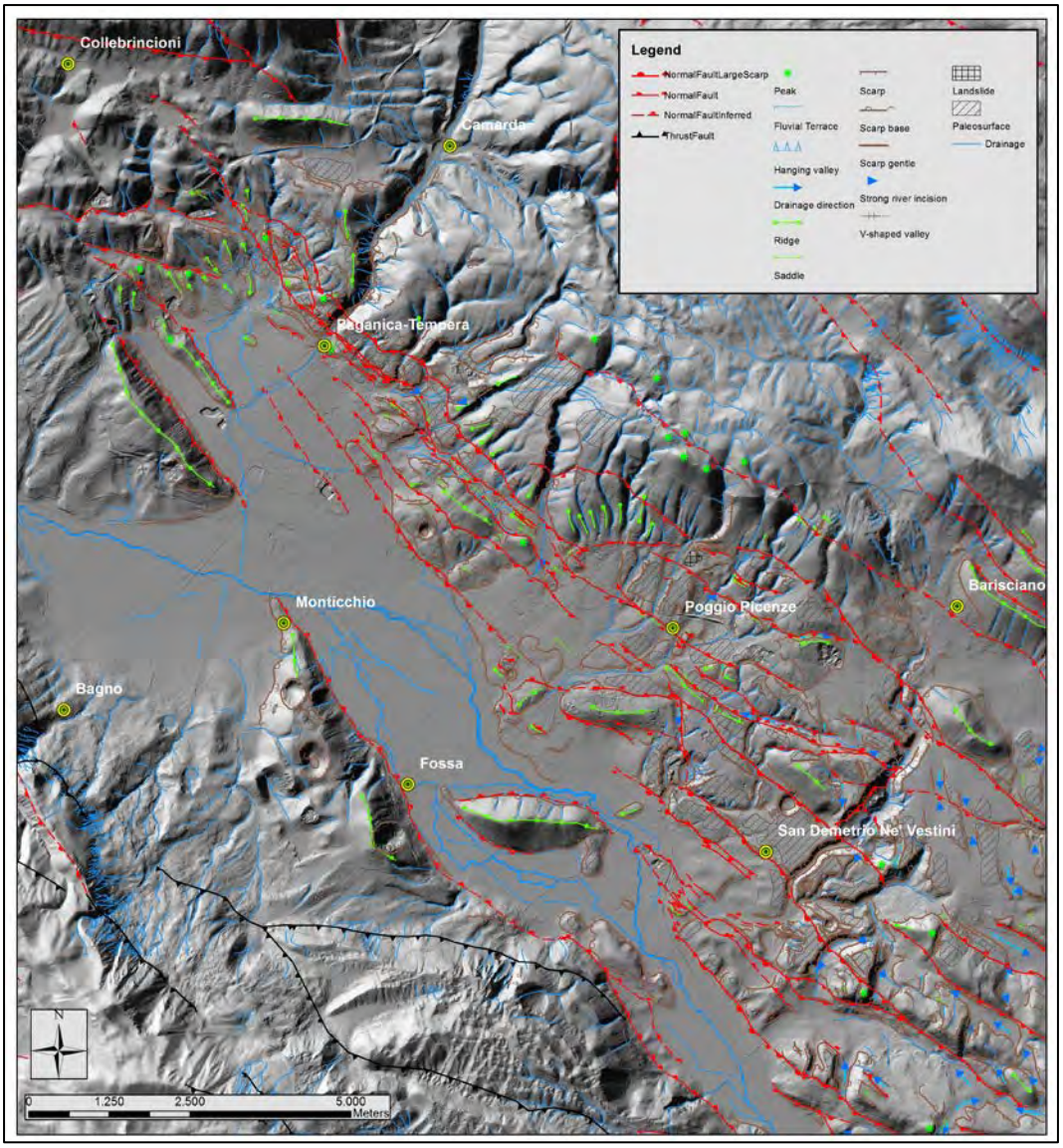

Figure 6.5 - Geomorphological map of the PSDFS

Geomorphological analysis was crucial to identify and map several tectonic structures in the study area, as well as to characterize their predominant dip-slip (or better normal-slip) behavior.
At the surface, the structural setting of the PSDFS is quite complex being characterized by the presence of several normal parallel fault splays (i.e. overlapping strands with similar trends) frequently arranged in a quasi-fractal sequence of horsts and grabens of variable size.
Looking at the surface pattern of faulting of the PSDFS, we can distinguish two main different structural arrangements: along the northern portion of the PSDFS, between Collebrincioni and Paganica villages, the deformation is localized on few closely spaced splays, in a ~ 1 km-wide band.
In the southeastern sector, the structural arrangement become more complex, the deformation appears to be accommodated by several tectonic structures with the PSDFS opening into a set of parallel, km-spaced fault traces.
In order to reduce the complexity of the PSDFDS at the surface and to identify the main tectonic elements, we combined all the individual fault traces into splay taking into account, among other criteria, the relative location (in map view) of fault traces with respect to neighboring faults. Fault traces (both synthetic and antithetic) that are aligned or approximately aligned to a main fault trace were, for example, assumed to be part of the same fault splay and consequently named.
As a rule, we decided to name all the fault splays using different prefixes to differentiate between the two sectors (e.g. P1 stands for splay number 1 in the Paganica sector, S6 for splay number 6 in the San Demetrio sector).

6.2.4 Across-strike topographic profiles

In order to calculate morphological throws associated with previously recognized fault splays and to define a first-order hierarchy among the numerous fault splays affecting the eastern flank of the Middle Aterno valley, once a reference frame for the surface patter of faulting was created, a series of 29 topographic profiles across the PSDFS were extracted from the high-resolution (1m) LiDAR-derived DEM.
The 29 topographic profiles were referenced to a baseline (red bold solid line in figure 6.6) that averages the strike of the fault splays identified along the PSDFS and is located on the fault system footwall. The average spacing between each profile is ~650 m, with minimum and maximum profile lengths of 5200 m and 9500 m, respectively.

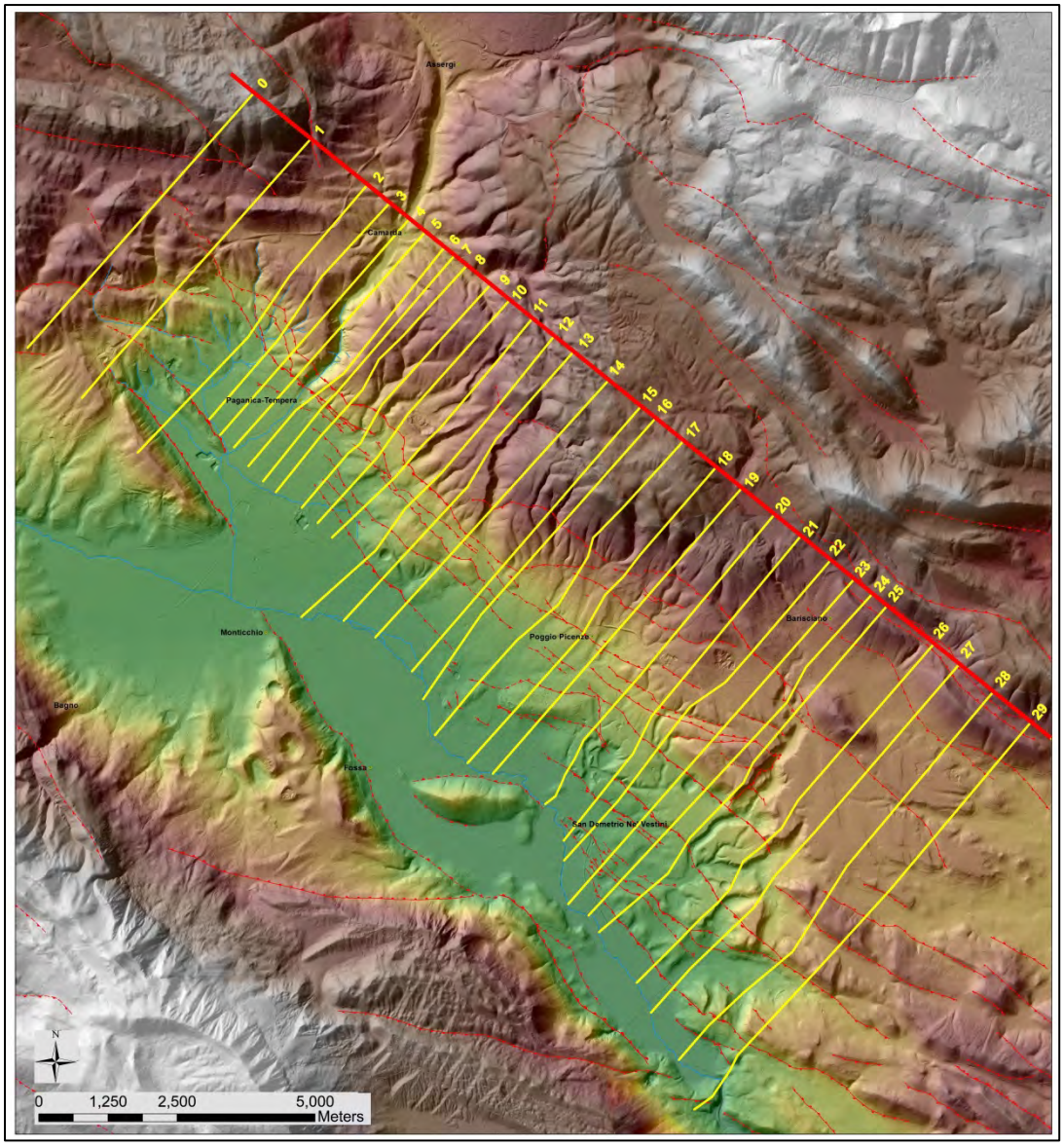

Figure 6.6 - Traces of the 29 topographic profiles across the PSDFS

The trace of each topographic profile was drawn in order to describe and to measure those displaced geomorphic markers previously identified by geomorphological mapping.

Each topographic cross section shows the position of the fault splays and the morphological throws associated with their cumulated activity through time. Particular attention was devoted to the analysis of paleosurfaces, both erosional and depositional, used as piercing points to measure fault throws. Moreover, when two different inclinations of the original surfaces can be reasonably assumed, we measured both morphological throw values, using in our calculations a single average value with its uncertainty.

Total morphological throw values for each profile were also measured considering the difference between the maximum elevation at the footwall of the PSDFS (in

correspondence of the starting line of each profile) and the elevation of the Middle Aterno basin floor at the hangingwall.

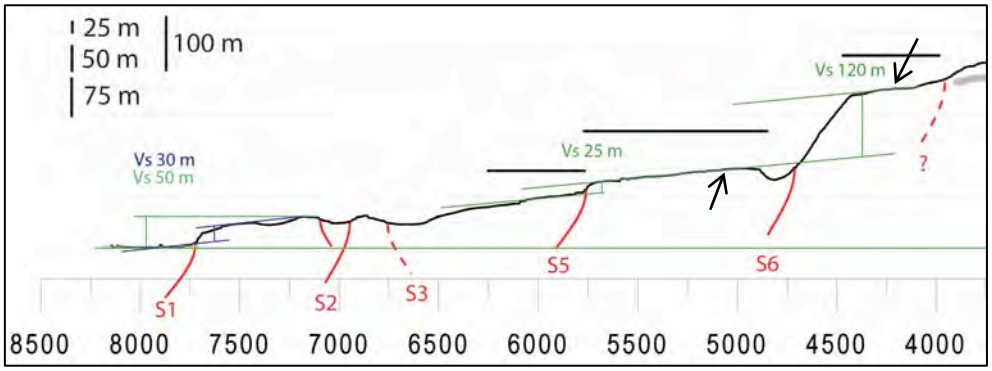

Figure 6.7 - Examples of measurements made on topographic profiles. Vertical exaggeration associated to the topographic profiles is 3x. The measured morphological throws are represented by the vertical component of the separation between an upper and a lower original reference surface (black arrows in figure 6.7). The methodological uncertainty associated to each offset measurement is about 10 meters.

We should always be aware of the fact that a fault scarp (but also lake shorelines and terrace risers), once is formed, immediately begins to degrade, changing its morphology through time. Erosional processes tend to dismantle the footwall, while in the hangingwall depositional processes are dominant.

These topographic profiles are also useful in describing the morphology of the slopes bounding the eastern flank of the Middle Aterno valley. In fact, this flank of the basin appears to be strongly controlled by the activity of the PSDFS. To analyze more in detail its overall morphology 3 topographic profiles are selected among the 29, from the northwestern, central and southeastern sector of the fault, respectively (figures 6.8, 6.9 and 6.10).

Looking at the shape of the selected topographic cross sections, we can appreciate how the northwestern sector (figure 6.8 and profiles 3-14 in Appendix D1-D2) is characterized by steep slopes and by the presence of few fault splays (<7) accommodating the long-term deformation located mainly at the base of the range front. In the central section (figure 6.9 and profile 15-21 in Appendix D2-D3) the range bounding the eastern flank of the Middle Aterno valley reach its maximum elevation. This sector of the PSDFS is characterized by the presence of relatively few fault splays (< 7).

The southeastern sector of the Middle Aterno valley (figure 6.10 and profile 22-29 in Appendix D3-D4) shows a completely different morphology. The long-term expression of the slopes appears strongly controlled by the activity of numerous fault splays (> 7) that tend to dissect the original surfaces producing a staircase topographic profile, characterized by the presence of erosional and depositional paleosurfaces separated by fault scarps.

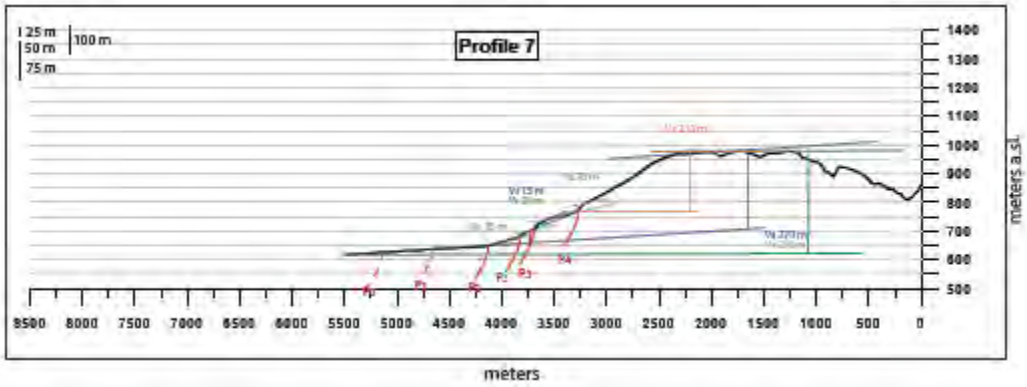

Figure 6.8 – Topographic profile across the northwestern sector of the PSDFS

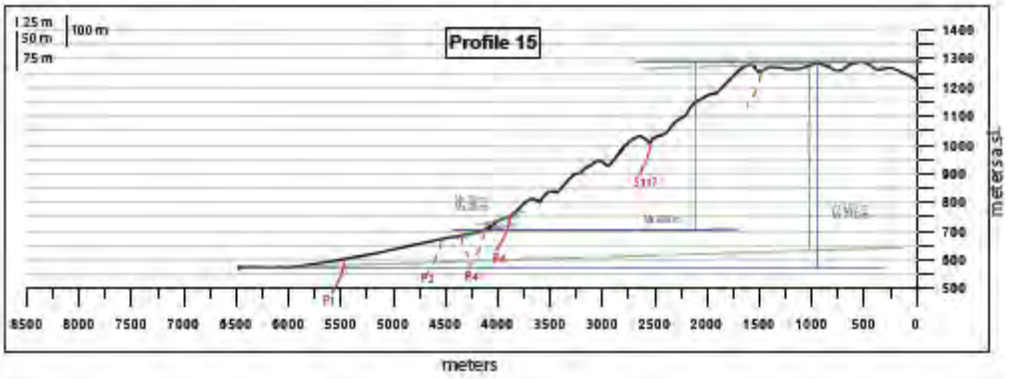

Figure 6.9 – Topographic profile across the central sector of the PSDFS

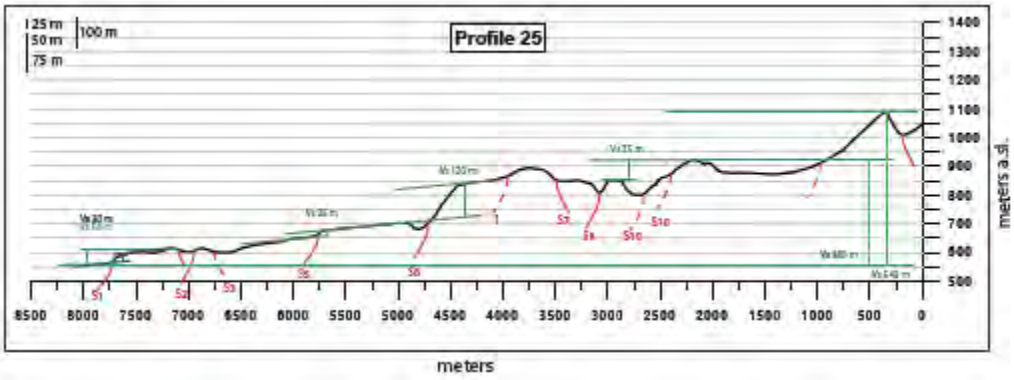

Figure 6.10 - Topographic profile across the southeastern sector of the PSDFS

6.2.5 Main results of the tectonic geomorphology approach

We analyzed the cumulated displacement distribution by plotting on the baseline the morphological throw values measured from the 29 topographic profiles (with the exception of those small fault splays showing a null or non-measurable offset). The resulting figure 6.11 shows the total morphological throws reported with a black solid line. Differently, morphological throws for each fault splay are presented in different colors and with different symbols to distinguish between throw values calculated from offset reference surfaces (i.e. piercing points) carved in bedrock or in unconsolidated deposits or a combination of the abovementioned.

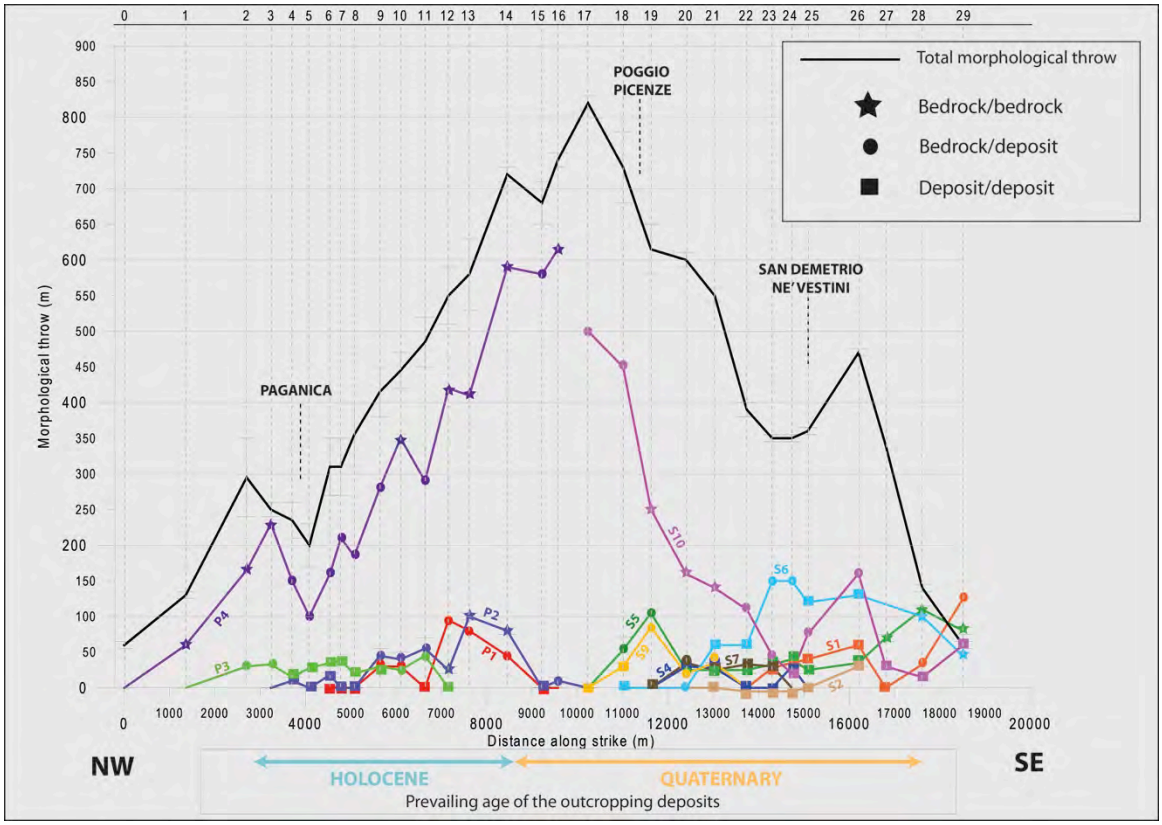

Figure 6.11 – Along-strike plot of the morphological throws measured from the topographic profiles across the PSDFS. Morphological throws for each fault splay are presented in different colors and with different symbols to distinguish between throw values calculated from offset reference surfaces (i.e. piercing points) carved in bedrock (star) or in unconsolidated deposits (square) or a combination of the abovementioned (point).

The preservation, continuity and height of the tectonic escarpments, as well as the morphological throws, concurred to define a first-order hierarchy among all the tectonic structures recognized in the area.

A summary of some statistical properties associated with the PSDFS is displayed in figure 6.12. Individual fault splays display an average strike of 140° and an average length of 4500 m. Measurable average vertical offsets range from 5 m to 280 m, while maximum vertical displacements range from 30 m to 615 m.

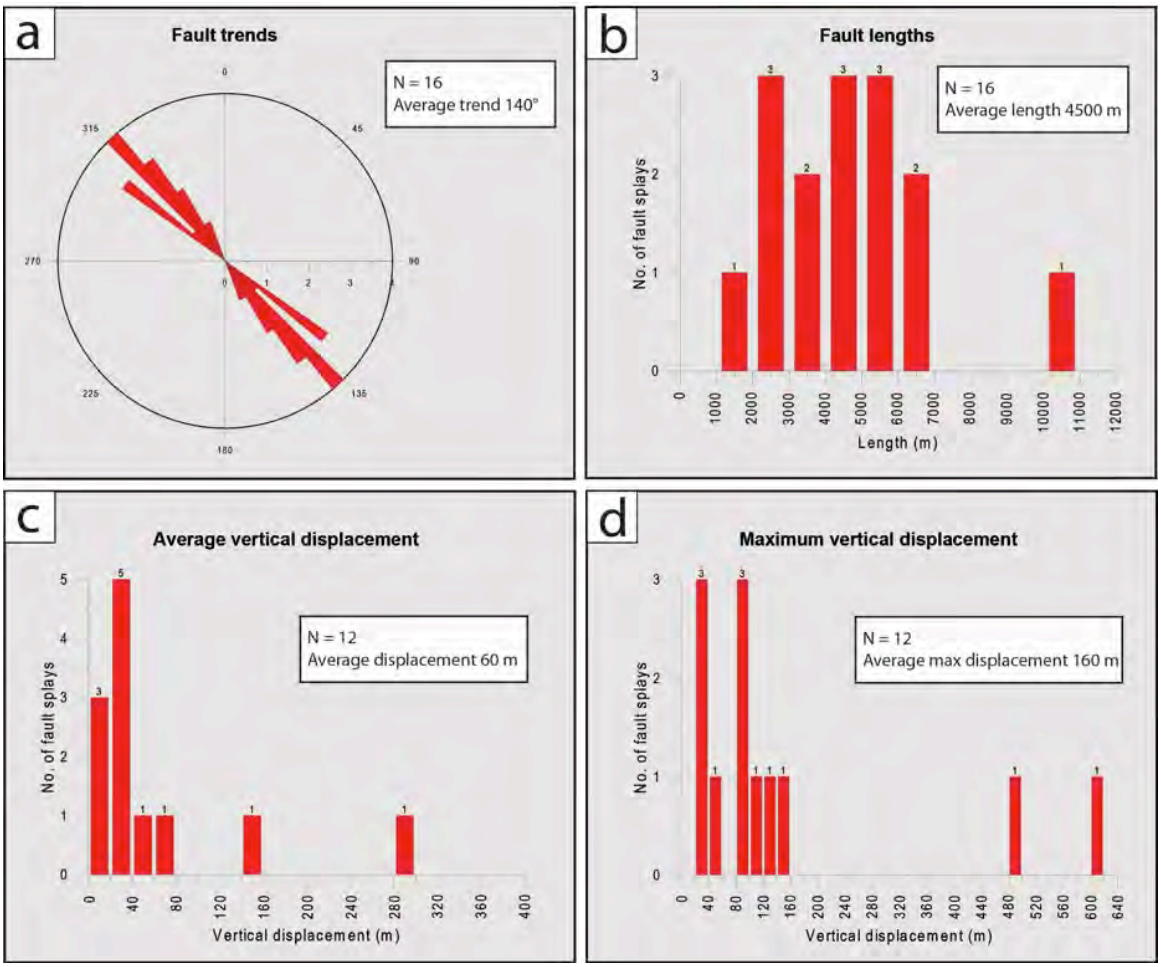

Figure 6.12 - Some statistical properties associated with the major fault splays of the PSDFS. a) Rose diagram illustrating the distribution of trends of the faults within the PSDFS; b) Histogram showing the lengths of fault splays; c) Histogram of the average vertical displacements; d) Histogram of the maximum fault displacements.

Looking at figure 6.13, we note that the total morphological throw graph (black solid line) approximates a symmetric bell-shaped curve, reproducing a throw profile comparable to that of an isolated individual extensional fault (see Chapter 2).
The maximum value of morphological throw reaches as much as 820 meters, and the overall length for long-term expression of the PSDFS as shown from the topographic profiles analysis approximates 19 km, thus in good agreement with the length of the seismogenic fault that ruptured during the April 6 earthquake, as defined by coseismic seismologic and geodetic observations (from 15 to 18 km - see Chapter 3).
Figure 6.14 is another plot of all the morphological throw values measured from the abovementioned 29 topographic profiles: the orange dotted curve represents the aggregation of individual fault splays, built summing up the relative contribution of each fault, while the green and the blue solid lines represent the sum of all the other fault splays with exception of P4 and S10, respectively. In order to highlight the relative contribution of the splays displacing Quaternary sediments (without considering throw values measured from the bedrock) we also reported two

different colored areas for the Paganica sector (in green) and the San Demetrio sector (in blue).

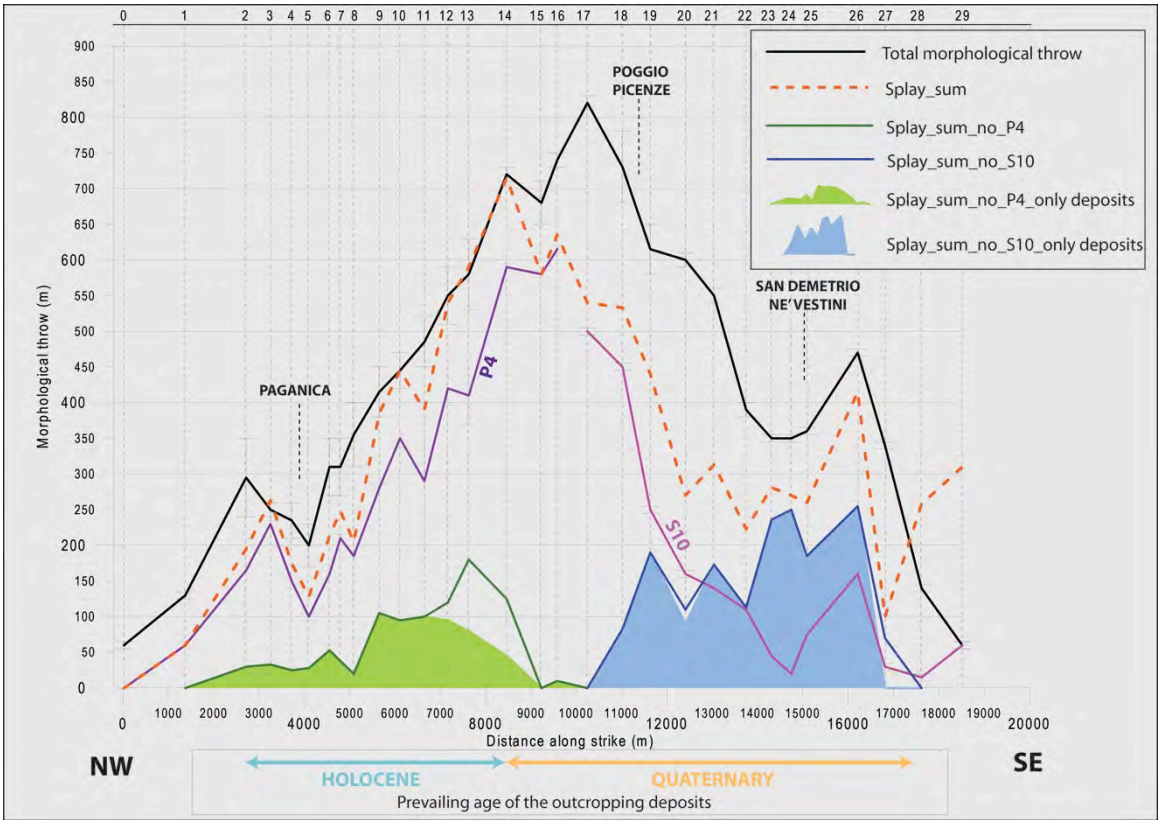

Figure 6.13 - Along-strike plot of all the morphological throw values measured from the topographic profiles. The orange dotted curve represents the sum of the relative contribution of each fault, while the green and the blue solid lines represent the sum of all the fault splays with exception of P4 and S10, respectively. Green and blue areas show the relative contribution of the splays displacing Quaternary sediments in the Paganica and San Demetrio sector, respectively.

A first-order consideration is that two different behaviors are visible from the morphological throw plot of figure 6.14: from profile 0 to profile 14 the orange curve mimics both shape and magnitude (81%) of the long-term deformation measured as total morphological throw. Differently, moving from profile 15 to the end of the PSDFS, the sum of the contributions of all individual fault strands take account of only 68% of the total morphological throw.
The mismatch between total morphological throw (black solid line) and the sum of all tectonic contributions (orange dotted curve) could be tentatively explained by:

- a systematic bias introduced by the morphological throw measurements, affecting mainly the San Demetrio sector where the deformation appears to be accommodated by several tectonic structures;
- the evidence of syntectonic deposition of some of the Quaternary sediments, that could result in a possible underestimation of the morphological throw values;
- the presence of an inherited paleotopography.

More in detail, we can note that most of the deformation in the area appears to be accommodated by the two most external fault splays (P4 and S10 – figure 6.13 and 6.14) affecting mainly the bedrock. These tectonic structures bound the Middle Aterno basin and contribute for 68% (P4 - northwestern sector) and 34% (S10 - southeastern sector), respectively, to the total morphological throw.

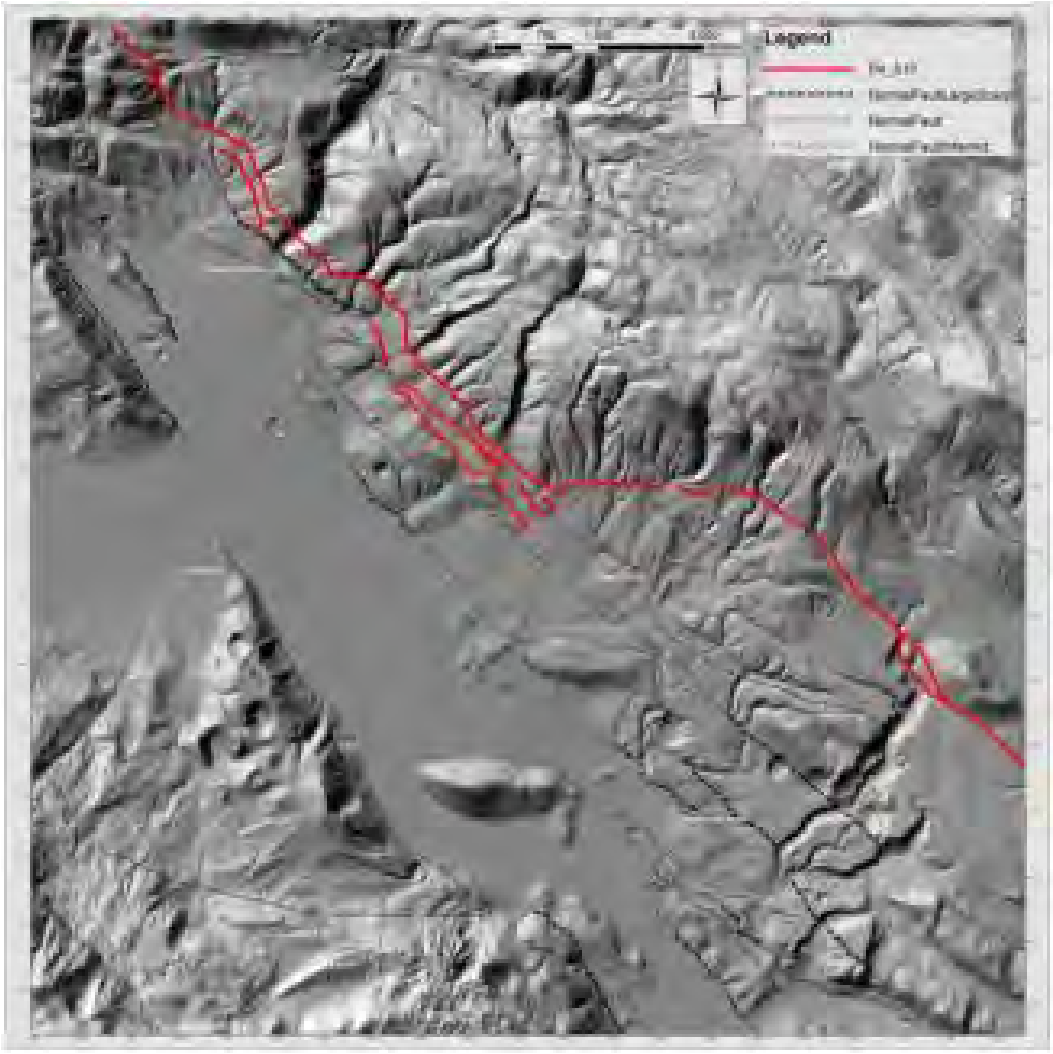

Figure 6.14 – Fault splays P4 and S10

Moreover, the amount of deformation related to the other tectonic structures affecting the Quaternary deposits (green and blue areas in figure 6.13) appears to be variable between the two sectors.
The Quaternary fault splays in the Paganica area account for an average ~ 15% of the total deformation, with a maximum value of ~ 25%, while in the San Demetrio sector the amount of deformation reaches values of ~ 40% (average) and ~ 70% (maximum). It is interesting to note that the relative contribution of the Quaternary tectonic structures tends to become predominant in the San Demetrio sector (in particular starting from profile 23), in correspondence of the decrease in throw values measured for splay S10 (figure 6.13).

In summary the morphological approach was useful to define the fault system structure, extent, geometry and boundaries. The most important limitation using this approach is that the morphological-derived throws do not allow age estimations and thus, we are missing information to calculate slip-rates.

6.3 Geological approach

As already highlighted chronological constraints are needed to translate displacement measurements into slip–rates. The following paragraph presents the geological investigations carried out in the area of the Middle Aterno valley with the aim of integrating the morphologic analysis with geological information and chronological constraints on displaced features and deposits.
The geological approach consisted in mapping and dating the deposits outcropping in the Middle Aterno valley.

6.3.1 Geological mapping

Geological mapping was carried out at a 1:10.000 scale and comprised several fieldwork campaigns performed during the whole 3 years-long PhD period. The survey started from the verification of previously published maps (Geological Map of Italy, scale 1:50.000, sheet 359, L'Aquila, APAT, 2006; Bertini and Bosi, 1993;) and benefited also of new public data collected for seismic microzonation after the 2009 L'Aquila earthquake (Italian Civil Protection Department), and was therefore integrated with new, essential field survey data.
Particular attention was devoted to the detailed differentiation of the continental deposits outcropping in the area, with the aim of obtaining chronological constraints useful for the long-term (~ 2 Ma) slip-rate estimate of the PSDFS.
In most of the cases, the Plio-Quaternary deposits subdivision and the relative ages already proposed by Bertini and Bosi (1993) were adopted also in our mapping. Accordingly to this subdivision, our ages refer to the pre-2009 global chronostratigraphical scale, with the base of the Pleistocene epoch set at ~1.8 Ma BP.
The stratigraphic sequence of the pre-Plio-Quaternary bedrock in the study area was mapped following the subdivision already proposed by the Geological Map of Italy, scale 1:50.000, sheet 359, L'Aquila (APAT, 2006).
The Middle Aterno valley is characterized by the presence of an extensive cover of lacustrine and alluvial Quaternary deposits accumulated upon a mainly Meso-Cenozoic bedrock.
The substratum is characterized by three different stratigraphic sequences of marine origin characterized by the presence of several units belonging to the

transitional domain between the Lazio-Abruzzi carbonate shelf platform and the Umbria-Marche pelagic basin, as well as by sin-orogenic turbidite deposits pertaining to the Miocene foredeep:

A. Monte Ocre - Valle Aterno - Monte Camarda: Lazio-Abruzzi carbonate platform and edge sequences; flysch sequences of the Lazio-Abruzzi domain;
B. Monte Cappellone – Paganica: basin and slope sequences of the Gran Sasso and Conca Subequana;
C. Monte Pettino: basin and slope sequence.

6.3.2 Quaternary deposits

The Pliocene? – Quaternary Middle Aterno Basin infill is prevalently composed by terrigenous sediments. These deposits overlying the bedrock sequence were investigated in the past by several authors (Bosi and Bertini, 1970; Bertini and Bosi, 1993; D'Agostino et al., 1997).

It is worth noting that the continental sedimentary units found in the Middle Aterno basin can be correlated to other continental deposits found in other of the intermountain basins of central Apennines. A stratigraphic framework of the Plio-Quaternary continental deposits in the Latium-Abruzzi Apennines is available in Bosi et al., 2003.

Detailed geological field surveys allowed us to recognize, in several outcrops, 16 main Plio-Pleistocene to Holocene continental sedimentary units outcropping in the Middle Aterno basin; these are generally separated by unconformities and/or juxtaposed by the several fault splays detectable in the area.

The main sedimentary units are listed below:

- "Valle Valiano" - Pliocene? - Early Pleistocene: this unit comprises the oldest deposits detectable in the area. It consists of slope-derived breccias with etheropic alluvial fan deposits, made of angular to rounded carbonate pebbles and cobbles. The basal portion of the unit comprises boulders up to some m^3 within a whitish silty-sandy matrix. This unit can be mainly found at the north-eastern flank of the continental basin.

- "Fonte Vedice" unit - Early Pleistocene: slope-derived cemented limestone breccias with a typical orange-pink matrix. D'Agostino et al., 1997 defined a reverse magnetic polarity for this unit, which suggests an age older than ~781 ka. This unit unconformably covers the top of the Valle Valiano unit.

- "Valverde" unit - Early Pleistocene: is composed of few tens of meters of well layered limestone rounded gravels, occasionally well cemented; in the upper part the calcium carbonate gravels are interfingered with sand and sandy-silt layers. This unit represents an alluvial fan body entrenched in the Valle

Valiano unit and could be partially interfingered with the San Nicandro unit deposited at the edge of the lacustrine basin.

Figure 6.15 - Valverde Unit

- "San Nicandro"- Early Pleistocene: The unit is predominantly made of whitish, well layered carbonate silts occasionally containing rounded gravel layers. These deposits are related to a lacustrine environment with few gravelly channels and landslides, located in particular close to the basin edge. This formation predominantly crops out in the southeastern portion of the investigated area and reaches a maximum thickness of more than 100 meters. Paleomagnetic analyses revealed a reverse magnetic polarity (Speranza, personal communication, 2011), thus suggesting for this unit an age older than the Bruhnes-Matuyama limit (~781 ka). This unit generally appears to overlap the "Valle Valiano" unit.

Figure 6.16 – San Nicandro Unit

- “Vall’Orsa” unit - Early Pleistocene: this unit is made of gravels and conglomerates, locally within a whitish silty lacustrine matrix and locally is characterized by a typical foreset-bedding attitude of the strata, possibly related to a deltaic complex progradating into the lacustrine basin. Generally covers but occasionally interfingers the “San Nicandro” lacustrine silts.

Figure 6.17 - Vall'Orsa unit

- “Valle dell’Inferno” unit - Middle Pleistocene: it is usually a well-layered calcium carbonate conglomerate and gravel with subordinated silty-sandy lenses. The total thickness of the unit is variable from a few meters in the southeastern sector to tens of meters in the western sector. The top depositional surface related to this unit is preserved at several locations.
  This unit unconformably lays on the Vall’Orsa unit.

Figure 6.18 - Valle dell'Inferno unit

- “San Mauro” unit – Middle Pleistocene: this unit can be subdivided into two main sub-units composed by alluvial fan and fluvial related deposits, respectively. Silts rich in volcanic minerals or component, sands and

rounded calcium carbonate gravels are common. Age constraints were derived from the abundance of tephra layers, which are completely missing in the underling deposits, and from one optically stimulated luminescence (OSL) sample. The resulting ages define a time interval for the deposition of the alluvial fan and fluvial deposits of 561±2 ka - 172±12 ka (see OSL sample SEF 2 – and Table 6.1 in this chapter).

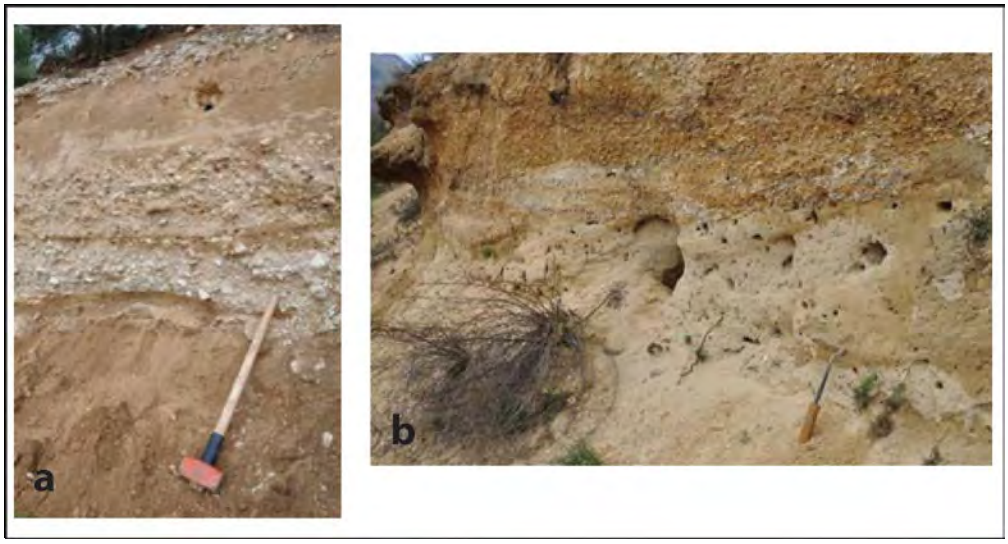

Figure 6.19 – San Mauro unit (a – alluvial fan related deposits; b – fluvial related deposits)

- Late Pleistocene - Holocene alluvial fan unit: fan-shaped heterometric deposits composed by unconsolidated or poorly cemented well-stratified limestone gravels and sands. These deposits appear to be deeply entrenched in the older basin infill deposits and produced a set of telescopic alluvial fans, particularly clear in the SE part of the basin. Age constraints for this unit are derived from one Optically Stimulated Luminescence sample, that gave an age of ~27 ka and from 14C dating, resulting in ages of ~30 ka (see OSL sample GREG FAN in the table 6.3 and sample ACQ-B4, ACQ-B7 in Chapter 5 - table 5.1).

Figure 6.20 - Late Pleistocene- Holocene alluvial fan unit

All these units are unconformably covered by slope debris and fluvial, alluvial, eluvial, colluvial and alluvial fan deposits.

The geological mapping is synthesized in the geological map of figure 6.21.

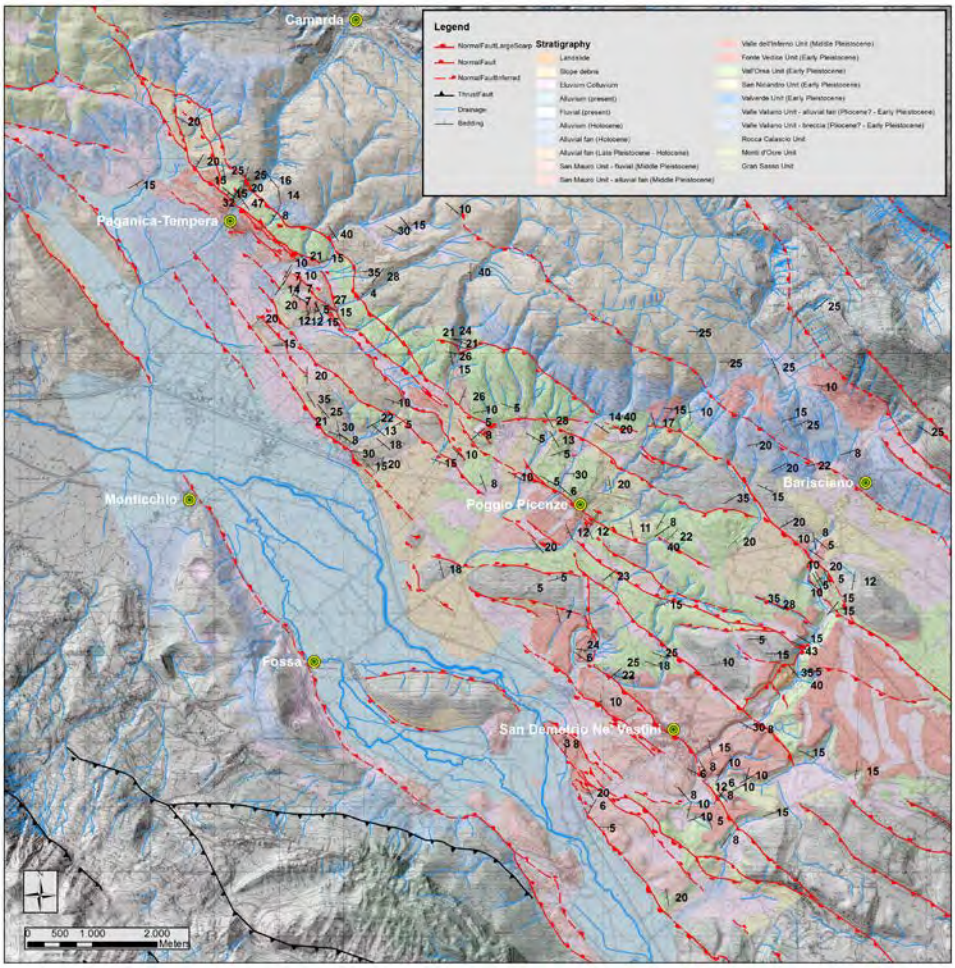

Figure 6.21 - Geological map of the PSDFS

The detailed geological investigations undertaken in the area of the Middle Aterno valley and in particular along the PSDFS allowed us to highlight the presence of several continental deposits characterized by different facies suggesting a complex history in the development of the Middle Aterno basin.
This depositional evolution from the clastic deposits at the edge of a fault-controlled basin to a low-energy deposition at the depocenter, followed by a clastic phase characterized by a sequence of entrenched alluvial bodies, suggests a progressive closure of the basin, possibly related to an exhumation of the Quaternary deposits that could testify a local tectonic uplift.

6.3.3 Chronological constraints

In order to determine the rate at which a fault slips or a surface is deforming, a critical issue is to provide a chronological constrain for the observed displacements/offsets. To acquire such information, we needed to date the displaced geomorphic markers wherever recognized.

A great variety of Quaternary dating methods are available. A useful classification is based on the type of age provided: numerical-age, calibrated-ages, relative-ages and correlated-ages methods. Numerical-age dating methods are those able to provide an absolute numerical age (in years), producing quantitative estimates of ages and uncertainty on an absolute time scale. Common examples are represented by radiogenic methods like luminescence dating or by isotopic methods like radiocarbon dating. Correlated-age dating methods are those that are not related to time-dependent processes. To obtain an age estimate, a geologic unit is supposed to be coeval to another geologic unit, which has been independently dated by means of a variety of properties. A common example is represented by tephrochronology.

It is often difficult to obtain chronological constraints on continental deposits mainly due to the scarcity of guide fossil remains with respect to the marine environment and to the limited applicability of direct dating methods providing numerical ages. This is because not all the deposits are suitable for dating due to the lack in their composition of the necessary minerals or organic matter (e.g. Quartz for OSL and charcoal for C14) and due to limitation in the time range of applicability of the dating method itself. Most of the chronological constraints in literature were based on stratigraphic and paleontological correlations. Very limited direct dating existed. To overcome this paucity, we focused on the refinement of previously published chronological data through the collection and analysis of new samples within the continental deposits in the area of the Middle Aterno valley.

In this work we dated displaced Quaternary landforms and deposits using predominantly numerical-age and correlated-age dating methods, in particular radiocarbon dating, optically stimulated luminescence (OSL) and tephrochronology.

We developed a chronological framework based on 27 samples collected for radiocarbon dating (already presented in Chapter 5 - Paleoseismological investigations), 4 samples for OSL dating and 27 samples for tephrochronology (figure 6.21), as well as on archeological evaluation of pottery shards found within late Holocene deposits (already presented in Chapter 5 - Paleoseismological investigations). In the following the background of OSL dating and tephrocronology is presented.

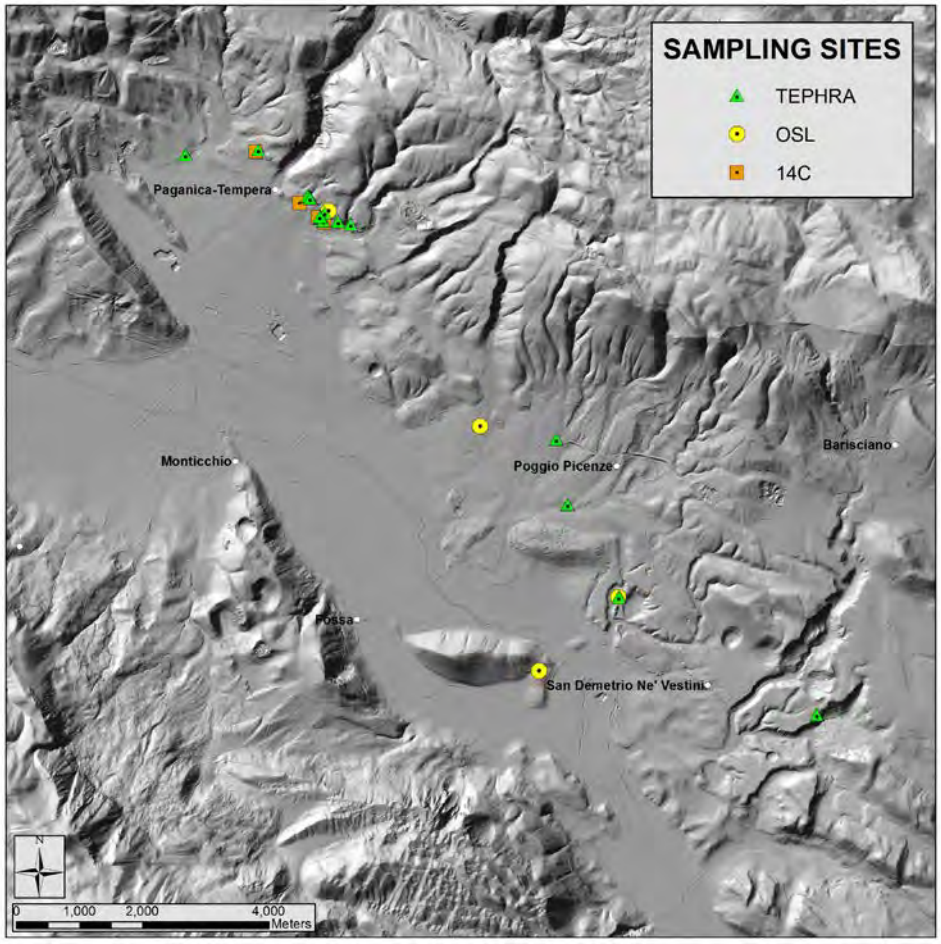

Figure 6.22 - location of the 14C, OLS and tephra samples collected along the PSDFS

6.3.3.1 Optically stimulated luminescence (OSL)

In this work we took advantages from optically stimulated luminescence (OSL), a valuable Quaternary dating method that can be applied in a variety of continental stratigraphic settings (eolian, fluvial, alluvial and colluvial, among others). This method is able to provide ages for the deposition of sediments using the most common minerals on the Earth face, quartz and feldspar, covering a time range spanning from a few years up to ~300 – 500 ka (Murray and Olley, 2002; Duller, 2004; Wintle, 2008). The advantage of luminescence dating over other dating methods is its ability to give a constraint for the time a sediment was buried by other deposits, measuring the time elapsed since the last exposure to light or heat of its quartz and feldspar mineral grains.

OSL dating method is based on the fact that sediments are exposed to ionizing radiation emitted by materials containing naturally occurring radioactive isotopes, such as ^{238}U, ^{232}Th or ^{40}K, as well as, in the near surface, by cosmic rays. This radiation emits α, β and γ particles at a rate dependent on the amount of radioactive elements in the sediments. The emitted particles remain trapped in mineral lattice defects and chemical impurities until electronic traps are saturated, becoming subsequently a source for luminescence signals. This signal generally increases with

time, reflecting a longer exposure time to environmental radiation. If irradiation continues, then electron traps will fill until a further dose of radiation will not result in more luminescence being measured; this condition is referred to as ‘‘saturation’’.
When exposed to sunlight, the electrons are released and the inherited luminescence signal is reduced (bleached) to a low definable level. This level, called the residual level, is the point from which, after burial, the luminescence signal starts again to accumulate.
An important assumption in using OSL is that daylight exposure was sufficient to completely remove any pre-existing luminescence signal. OSL dating takes advantages from the fact that the inherited time-dependent luminescence signal can be released in the laboratory in response to some external stimulus, such as by visible light exposure. OSL measures the release of electrons from the light-sensitive mineral traps, the radiation level necessary to reproduce the stimulated signal (equivalent dose) and the environmental radioactivity of the sediment (dose rate). By dividing the equivalent dose by the dose rate it is possible to define an age for the time the sediment was buried by other deposits.
The selection and sampling of sediments represent a crucial step in OSL dating. By a practical point of view, in order to insure samples integrity, sediments were collected in the field at about 1 m below the surface, in order to insure samples integrity, by hammering into the suitable deposits an aluminum pipe (5 cm in diameter and 25 cm long), keeping the sample in the dark using end caps (figure 6.23). In order to allow dose rate and mineralogic and granulometric analyses, additional ca. 100 g of the same material were collected.

Figure 6.23 - example of sampled sediments for OSL dating and sampling technique

The 4 samples collected in the area were then sent to the Luminescence Dating Research Laboratory of the Department of Earth and Environmental Sciences, University of Illinois at Chicago (USA) and to the University of Catania (Italy).
The main results of OSL dating are shown in table 6.2.

Site	Sample	Optical age
San Gregorio fan	GREG FAN 2	27030 ± 1845
Fossa Prinesca	SEF 2	171610 ± 12170
Sant'Eusanio Forconese	CAT 1	Still under analysis
Paganica	PAG 2	>28340 (saturated)

Table 6.2 – Main results from OSL dating

6.3.3.2 Tephrochronology

Tephrochronology is a correlated-age dating method that uses distinct physical or chemical characteristic of the sampled material to allow the identification of volcanic products belonging to a well-defined eruption.

Tephra is the term used to describe all pyroclastic materials erupted from a volcanic vent and transported at least in part through the air or by volcanic gases (Thorarinsson, in Westgate and Gold, 1974). Volcanic eruptions are usually relatively short-lived events, and products like tephra have the possibility to be injected into the atmosphere and be transported for large distances.

Tephra layers offer precise correlation and dating of various geological archives in both terrestrial and marine environments since they represent virtually instantaneous events, isochrones, are rapidly deposited and often have a widespread distribution. Moreover, one of the key factors in using tephra as a stratigraphic age marker and correlation tool is distinguishing between primary tephra and reworked tephra.

Tephra layers possess essential physical and chemical characteristics by which they can be distinguished one from another regardless of the location at which they are found. Three main components can be found in a tephra which are useful for a proper identification: lithic fragments, volcanic glass and mineral crystals. Tephra layers may be in some cases dated directly using primary minerals (such as zircon, K-feldspar, biotite, quartz) or glass from within the tephra layer, or indirectly on enclosing or encapsulated material: in this case the resulting chronological constraints will be greatly improved.

Field work allowed us to find a variety of tephra layers in the area of the Middle Aterno valley, and after appropriate field examinations, we collected 27 tephra samples, mainly from depositional and erosional paleosurfaces (figure 6. 24).

Figure 6.24 - examples of tephra layers found in the study area (red arrows).

To assure a proper identification of the collected tephra layers we performed petrographic examinations and electron probe microanalysis (EPMA) at the INGV laboratories (thanks to Dr. Paola Del Carlo and Dr. Andrea Cavallo) (figure 6.25). Geochemistry was used to confirm correlation of the tephra layers to a source volcano and/or eruption event, while morphology and geochemistry were used to discriminate between primary or reworked tephra.

Figure 6.25 - Electron micoprobe image of one of the tephra samples analyzed at the INGV laboratory.

Some of the analyzed samples were very weathered such that the tephra component were unrecognizable. The preserved samples showed physical and chemical characteristics that fit with those related to the main activity of some peri-Tyrrhenian volcanoes of the Roman Comagmatic Province (Colli Albani, Sabatini, Cimini, Vulsini and Vico). More in detail, we found evidences for the presence of discrete tephra layers and cryptotephra belonging to the activity of two of the nearest eruptive centers, the Colli Albani and Sabatini volcanic complexes. The reported activity for these volcanoes covers a time span ranging from 561±2 ka to 365±4 ka (Kerner et al., 2001; Marra et al., 2009), thus suggesting a Middle Pleistocene age for the related deposits (table 6.3).

Site	Sample	Primary/Reworked/ Cryptotephra	Volcanic source	Age
Acquedotto	FED-P3	Reworked	Colli Albani - Carapelle tephra	561 ± 2 ka [a]
Gallinaro	GAL-P1	Primary	Colli Albani - Pozzolane Rosse	456 ± 3 ka [a]
Gallinaro	GAL-P2	Primary	Colli Albani - Pozzolane Rosse	456 ± 3 ka [a]
Gallinaro	GAL-P3	Primary	Sabatini - Tufo Rosso a Scorie Nere	449 ± 1 ka [b]
Case alte	CAL-P1	Primary	Sabatini - Tufo Rosso a Scorie Nere	449 ± 1 ka [b]
Case alte	CAL-P2	Primary	Sabatini - Tufo Rosso a Scorie Nere	449 ± 1 ka [b]
Case alte	CAL-P3	Primary	Colli Albani - Pozzolane Rosse	456 ± 3 ka [a]
Antithetic trench	MTA-P1	Reworked	Colli Albani - Carapelle tephra	561 ± 2 ka [a]
250 k	250K-P1	Primary	Sabatini - Tufo di Villa Senni	365 ± 4 ka [a]
Tornante	TFS-P1	Primary	Colli Albani - Pozzolane Rosse	456 ± 3 ka [a]
Parete plastica verde	PPV-P1	Primary	Colli Albani - Carapelle tephra	561 ± 2 ka [a]
Tempera	TEMP-1	Cryptotephra	Colli Albani - Carapelle tephra	561 ± 2 ka [a]
Accircia	ACC	Cryptotephra	Colli Albani - Carapelle tephra	561 ± 2 ka [a]
Fossa Prinesca	SEF-P2	Reworked	Colli Albani - Carapelle tephra	561 ± 2 ka [a]
Fossa Prinesca	SEF-P3	Reworked	Colli Albani - Carapelle tephra	561 ± 2 ka [a]
Poggio Picenze	PPT1	Cryptotephra	Colli Albani - Carapelle tephra	561 ± 2 ka [a]
Poggio Picenze	PPT2	Cryptotephra	Colli Albani - Carapelle tephra	561 ± 2 ka [a]

Table 6.3 – Main results from tephrocronological analyses ***[a] : Marra et al., 2009; [b] : Karner et al., 2001.***

6.3.4 Geological cross sections

In order to obtain a long-term (~ 2 Ma) slip-rate estimate of the PSDFS, a set of 4 geological cross-sections (Appendix C) was drawn across the PSDFS, on the basis of the 1:10.000 scale geological map. The cross-sections aimed at reconstructing the subsurface structure of the PSDFS, focusing on the geometry of the faults and on the stratigraphy of the Quaternary deposits, and allowed us to obtain throw values for the numerous fault splays of the PSDFS by measuring the offset of geological features.

As a first order consideration, we can note that moving southward along the PSDFS (from cross-section 1 to cross-section 4, Appendix C), the number of Quaternary tectonic structures accommodating the net offset increases, in agreement with the results obtained by means of geomorphological mapping.

By a practical point of view, we measured from each geological cross-section the throw associated with the faults dissecting the Quaternary sedimentary units previously identified by means of geologic mapping.

Figure 6.26 shows an example of an offset geologic feature: we can note that the base of the oldest Quaternary deposit outcropping in the area, the "San Nicandro" unit (yellow unit in figure 6.26), appears in this geological cross-section to be downthrown of ~420 meters to the SW, due to the activity of the numerous fault splays recognized in this sector of the PSDFS.

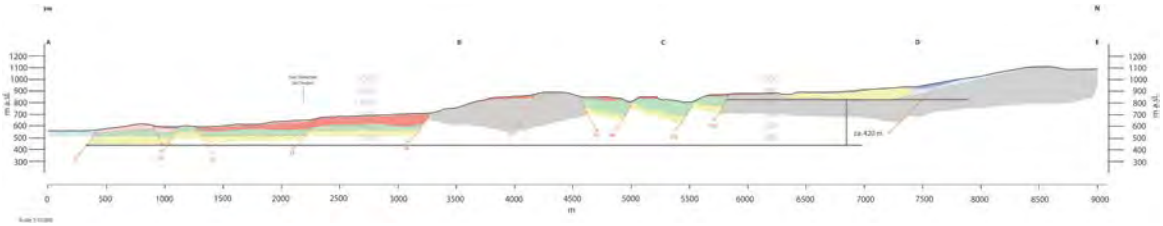

Figure 6.26 - example of the throw measurements on an offset geologic feature. In yellow the "San Nicandro" unit.

By repeating this type of measurements for the other Quaternary units, we were able to define the throw values for the Quaternary deposits deformed by normal faulting along the PSDFS.

Taking into account the age of the deposits involved in the deformation, it was then possible to estimate a vertical slip-rate for the PSDFS covering different time intervals, starting from the Early Pleistocene to the late Middle Pleistocene (table 6.4).

In the example shown in figure 6.26, the Early Pleistocene (1.8 Ma – 781 ka) throw of lacustrine deposits of ~420 m results in a minimum vertical slip-rate of 0.23 – 0.54 mm/yr, depending on the considered time interval.

Code	Cross section	Fault	Time interval	Throw (m)	Age max (years)	Age min (years)	Vertical slip-rate min	Vertical slip-rate max
B1	1 - Paganica	P3	Vall'Orsa unit - Early Pleistocene (1.8 Ma - 781 ka)	60	1800000	781000	0,03	0,08
A1	**2 - Pescomaggiore**	**P3 P2 P1 P0**	**San Nicandro unit - Early Pleistocene (1.8 Ma - 781 ka)**	**290**	**1800000**	**781000**	**0,16**	**0,37**
B2	**2 – Pescomaggiore**	**P4 P3 P2 P1 P0**	**Vall'Orsa unit - Early Pleistocene (1.8 Ma - 781 ka)**	**300**	**1800000**	**781000**	**0,17**	**0,38**
C1	**2 – Pescomaggiore**	**P3 P2**	**Valle Inferno unit - Middle Pleistocene (781 - 561 ka)**	**120**	**781000**	**559000**	**0,15**	**0,21**
A2	**3 – San Valentino**	**P1**	**San Nicandro unit - Early Pleistocene (1.8 Ma - 781 ka)**	**180**	**1800000**	**781000**	**0,10**	**0,23**
B3	**3 – San Valentino**	**P4 P2 P1**	**Vall'Orsa unit - Early Pleistocene (1.8 Ma - 781 ka)**	**450**	**1800000**	**781000**	**0,25**	**0,58**
B3a	3 – San Valentino	P1	Vall'Orsa unit - Early Pleistocene (1.8 Ma - 781 ka)	200	1800000	781000	0,11	0,26
B3b	3 – San Valentino	P4 P2	Vall'Orsa unit - Early Pleistocene (1.8 Ma - 781 ka)	250	1800000	781000	0,14	0,32
C2	**3 – San Valentino**	**P4 P2 P1**	**Valle Inferno unit - Middle Pleistocene (781 - 561 ka)**	**210**	**781000**	**559000**	**0,27**	**0,38**
C2a	3 – San Valentino	P1	Valle Inferno unit - Middle Pleistocene (781 - 561 ka)	80	781000	559000	0,10	0,14
D1	**3 – San Valentino**	**P1**	**San Mauro unit – Middle Pleistocene (561 - 172±12 ka)**	**50**	**563000**	**159600**	**0,09**	**0,31**
A3	**4 – Valle dell'Inferno**	**S10 - S2**	**San Nicandro unit - Early Pleistocene (1.8 Ma - 781 ka)**	**420**	**1800000**	**781000**	**0,23**	**0,54**
A3a	4 – Valle dell'Inferno	S6	San Nicandro unit - Early Pleistocene (1.8 Ma - 781 ka)	230	1800000	781000	0,13	0,29
A3b	4 – Valle dell'Inferno	S10	San Nicandro unit - Early Pleistocene (1.8 Ma - 781 ka)	140	1800000	781000	0,08	0,18
B4	**4 – Valle dell'Inferno**	**S10 - S2**	**Vall'Orsa unit - Early Pleistocene (1.8 Ma - 781 ka)**	**260**	**1800000**	**781000**	**0,14**	**0,33**
B4a	4 – Valle dell'Inferno	S6	Vall'Orsa unit - Early Pleistocene (1.8 Ma - 781 ka)	210	1800000	781000	0,12	0,27
C3	**4 – Valle dell'Inferno**	**S10 - S5**	**Valle Inferno unit - Middle Pleistocene (781 - 561 ka)**	**300**	**781000**	**559000**	**0,38**	**0,54**
C3a	4 – Valle dell'Inferno	S6	Valle Inferno unit - Middle Pleistocene (781 - 561 ka)	230	781000	559000	0,29	0,41

C3b	4 – Valle dell'Inferno	S10	Valle Inferno unit - Middle Pleistocene (781 - 561 ka)	40	781000	559000	0,05	0,07
D2	**4 – Valle dell'Inferno**	**S5 - S1**	**San Mauro unit – Middle Pleistocene (561 - 172±12 ka)**	**65±10**	**563000**	**159600**	**0,34**	**0,47**
D2a	4 – Valle dell'Inferno	S1	San Mauro unit (FLUVIAL) – Middle Pleistocene (561 - 172±12 ka)	40±10	563000	159600	0,19	0,31
D2b	4 – Valle dell'Inferno	S5	San Mauro unit (ALL. FAN)– Middle Pleistocene (561 - 172±12 ka)	25	563000	159600	0,13	0,19

Table 6.4 - vertical slip-rate estimates for the PSDFS covering different time intervals, starting from the Early Pleistocene to the late Middle Pleistocene.

7 Geophysical approach

7.1 Introduction

A multidisciplinary and scale-based geophysical investigation approach was carried out at different sites in the Middle Aterno basin across the Paganica – San Demetrio fault system (PSDFS).

To obtain high-resolution stratigraphic correlations able to highlight possible tectonic offsets, we experimentally applied an innovative methodology that employs core sampling and laboratory and *in situ* measurements of physical properties We also performed 2D electrical resistivity tomography (ERT) and contributed to a high-resolution seismic tomography campaign.

The main objectives of this approach are: 1) confirm and/or obtain detailed information from sites previously investigated by paleoseismological trenches; 2) include subsurface data in the estimation of cumulative throws; 3) define the precise positions and geometry of blind faults 4) obtain complementary images of the basin with respect to the information gathered by means of geomorphological and geological investigations.

7.2 High-resolution petrophysical correlations

7.2.1 Introduction

During the whole PhD period, we tested an innovative methodology that uses physical properties measurements of continental deposits as an alternative paleoseismological tool. In order to relate measured physical properties to sediment characteristics and to investigate deformation in recent unconsolidated continental deposits, we experimentally used an automated, non-destructive, high-resolution, multi-sensor tool commonly applied to marine and lacustrine sediments,

Determining physical properties of rocks and deposits plays a significant role in a wide range of geological and environmental studies as well as in the oil and gas exploration and mining industries. Physical properties data are generally considered as good indicators of sediment's composition, depositional and environmental conditions, furnishing proxies for sediment mineralogy as well as for depositional and erosional processes, oceanographic and climatic changes and post-depositional processes such as consolidation and early diagenesis (among many others, Kim et al, 2001; Casas et al., 2006).

A previous work performed in Southern Italy (Improta et al., 2010) highlighted that laboratory physical logging of cored sediments can also be an effective tool in obtaining high-resolution stratigraphic correlations among continental cores. This method is able to provide a viable alternative to detect possible tectonic offsets across faults when sediment characteristics prevent conventional stratigraphic correlations and/or trenching is impractical.
Taking into account what we learned in that pioneering experiment, we decided to continue testing this methodology and performed physical properties measurements both at a previously investigated trench site (Mo'Tretteca site, see Chapter 5) and directly on an artificial wall close to Fossa village where a secondary fault splay crops out.

7.2.2 MoTretteca site

The main goal at Mo'Tretteca site was to experimentally use the physical properties of continental sediments in order to obtain complementary information from the previously investigated paleoseismological trench. More precisely, the test was focused on the development of an alternative tool able to reproduce the stratigraphy and the deformation of correlative deposits obtained by means of trench logging. Finally, the results of this test are used to estimate the slip-rates associated with that specific fault splay. As already discussed in Chapter 5, the Mo'Tretteca trench was located in the Paganica village at the base of the main fault escarpment and crossed a secondary splay of the 2009 coseismic surface rupture. The SE wall of the trench was studied by means of trench-wall stratigraphic logging, providing a measured total vertical offset of ~0.65 m for the exposed colluvial sequence deposited during the past 3 millennia.
After Mo'Tretteca site trench was interpreted from a paleoseismological point of view (see Chapter 5), four cores were drilled from the top surface, close to the SE wall of the trench down to maximum depth of ~3.2 m. Figure 5.1 shows the location of the cores: two were extracted from the fault footwall (TR-S9 and TR-S8) and the other two from the fault hangingwall (TR-S5 and TR-S4).
We used a vibracoring (gasoline power percussion hammer – see Chapter 5) and sampled the cores with PVC tubes in order to have almost undisturbed sediments to be measured in the laboratory.

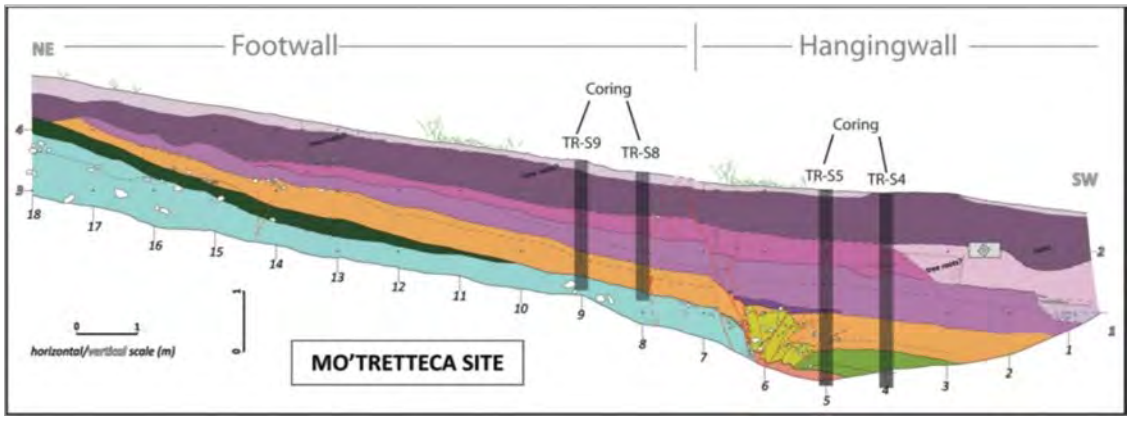

Figure 7.1 – Simplified log of the SE wall of Mo'Tretteca site showing the location of the drilled cores (modified after Cinti et al., 2011).

The sampled cores were then accurately sealed to prevent moisture loss and taken in the laboratory to perform a conventional stratigraphic description and to measure their physical properties using a non-pervasive logging system.

We used a fully automated GEOTEK Multi Sensor Core Logger standard (MSCL-S) available at the IAMC-CNR Petrophysical Laboratory (Naples, Italy). The MSCL-S is a very versatile system that can be easily moved and used in laboratories ashore or at sea (on board drilling ships during Integrated Ocean Drilling Program – IODP expeditions, for example) and is able to perform non-destructive, high-resolution (centimetric scale) and multi-sensor physical properties measurements both on whole and split cores.

The MSCL-S configuration used in this work is floor mounted on legs and includes a Bartington MS2E Point sensor and a Bartington MS2C loop sensor for measuring the low-field magnetic susceptibility, a Gamma Ray Attenuation Porosity Evaluator (GRAPE) sensor to determine the bulk density (GRP), a Minolta Spectrophotometer CM 2002 to measure the reflectance parameter L% (the percentage of reflected energy in 10 nm wavelength steps), and two Acoustic Rolling Contact (ARC) transducers, for evaluating the P-wave velocity (figure 5.2).

Generally, individual core sections between 50 and 150 mm in diameter and up to 1.55 m long can be logged by this system at spatial intervals as small as a few millimeters.

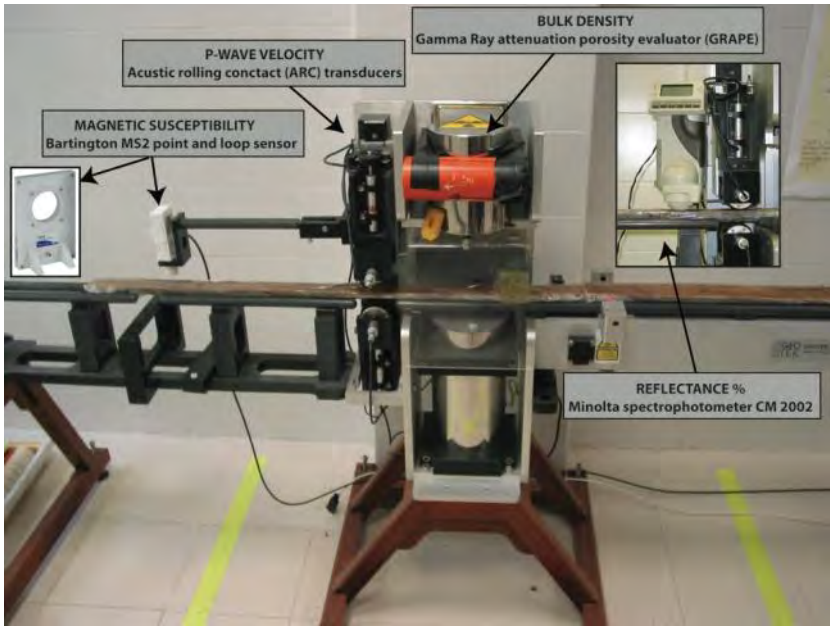

Figure 7.2 – Geotek Multi Sensor Core Logger standard (MSCL-S) available at the IAMC-CNR Petrophysical Laboratory (Naples, Italy).

In our experiment sequential core sections were loaded onto the rails while a pusher system automatically measured the length of each core section and pushed it through the stationary sensor array. In this way a complete core was logged in a continuous process while both the raw and processed data were graphically displayed in real time on a PC screen.

Our laboratory measurements of cored sediments started collecting magnetic susceptibility data for TR-S9, TR-S8, TR-S5 and TR-S4 cores using the Bartington loop sensor (MS2C) on whole cores. Logging was done at a centimetric scale (2 cm interval between each measurement) on all four cores.

At first, we checked the magnetic susceptibility signals measured from the cores in order to detect possible technical problems.

The data were of good quality and thus suitable for the correlation procedure. In figure 7.3 the magnetic susceptibility logs of boreholes TR-S9, TR-S8, TR-S5 and TR-S4 are shown.

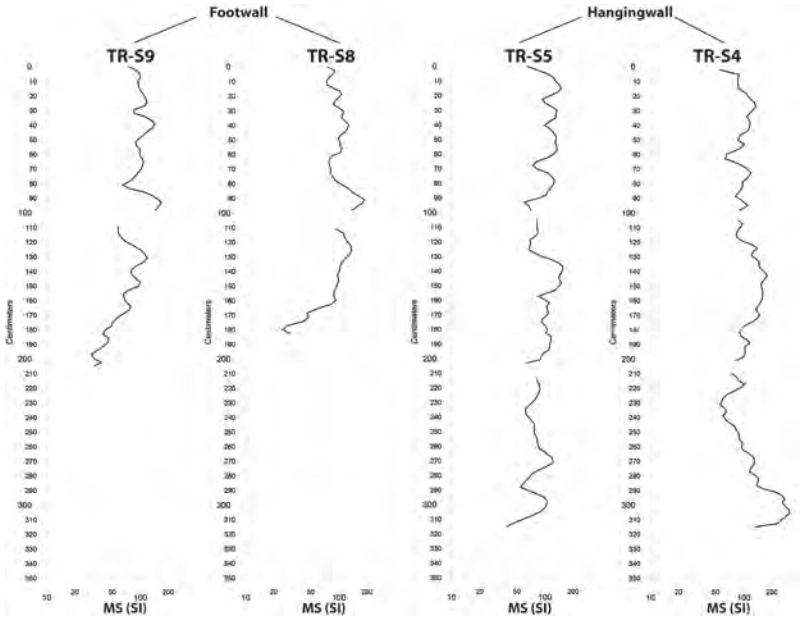

Figure 7.3 - Magnetic susceptibility logs for cores TR-S9 - TR-S8 (footwall sector) and TR-S5 - TR-S4 (hangingwall sector).

We then opened the four cores in order to perform a conventional stratigraphic description and to analyze the cored deposits with the other sensors mounted on the MSCL-S. Unfortunately, the sediments characteristics (the lack of a sufficient amount of matrix and the presence of pebbles up to cm 5 in diameter and coarse deposits, see figure 7.4 prevented to perform a conventional stratigraphic correlation to be done and the other petrophysical properties to be acquired along the entire length of the cores.

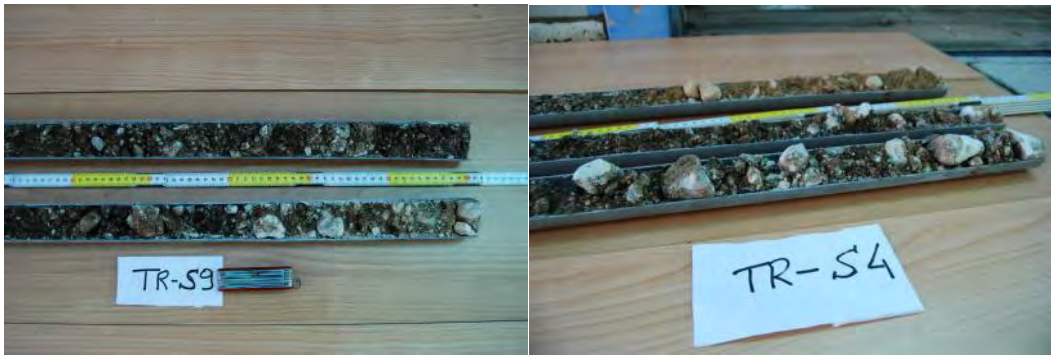

Figure 7.4 – Splitted sections of cores TR-S9 and TR-S4 showing the presence of coarse sediments and pebbles.

In the previous experiment performed in Southern Italy (Improta et al., 2010) we learned that in continental environments the magnetic susceptibility measurements can be highly informative when a significant amount of volcanic material is included in the deposits. Thus, taking into account the abundance of tephra layers embedded in some of the Quaternary deposits found in our study area, we used the magnetic

susceptibility signals with the aim to reproduce the stratigraphy of the trench and the deformation observed at Mo'Tretteca site by means of paleoseismological investigations.

We thus carefully inspected the four magnetic susceptibility logs obtained with the loop sensor in order to identify characteristic patterns of the signal, as well as single prominent peaks and troughs that could be correlated between cores.

Overall, we can note that the logs present comparable trends among each pair of "twin" cores drilled in the footwall (TR-S9 and TR-S8) and in the hangingwall (TR-S5 and TR-S4), respectively.

As a first step we identified the main trends that dominate the magnetic susceptibility signals, (red bold lines in figure 7.5) and then, refining our observations, we identified 13 homologous points between cores TR-S9 and TR-S8 and 15 homologous points between cores TR-S5 and TR-S4.

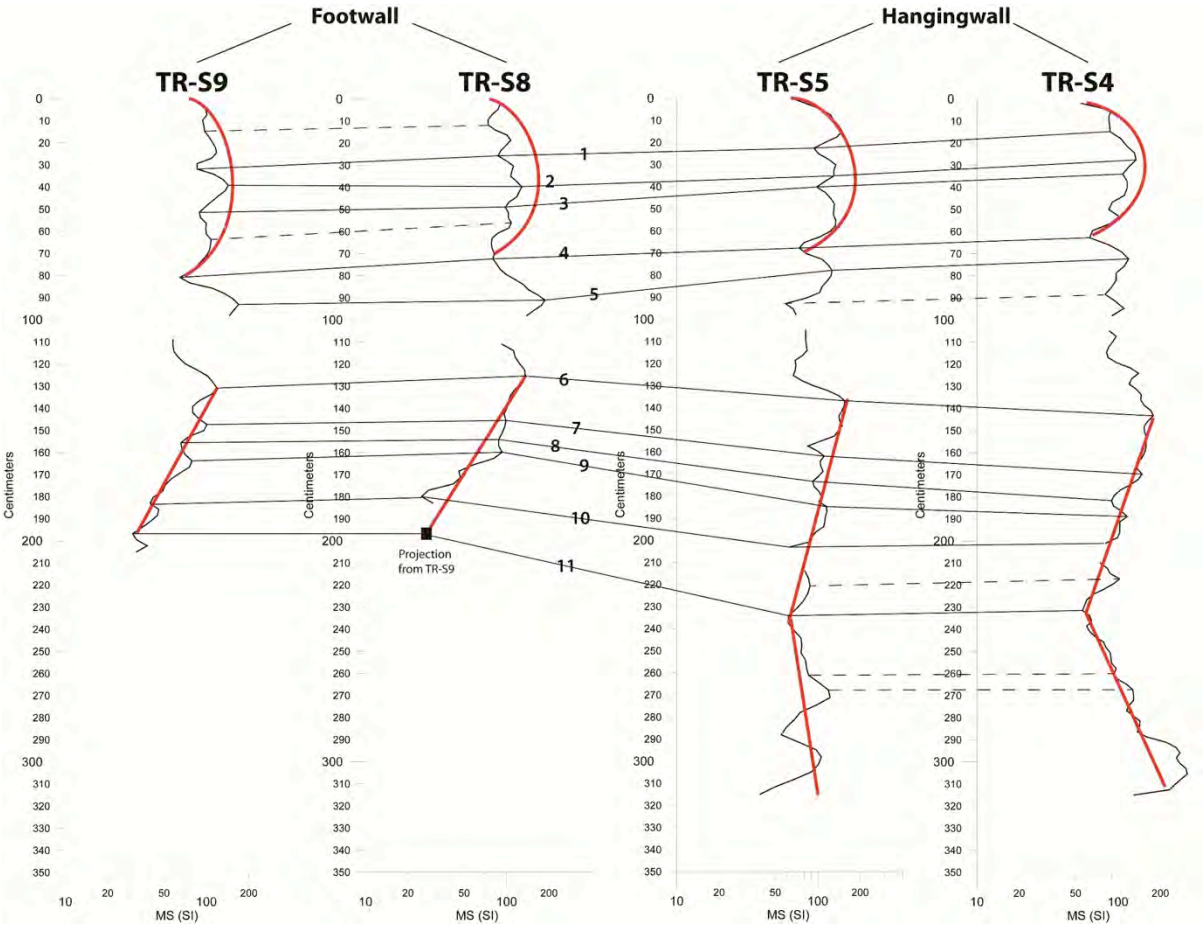

Figure 7.5 – Magnetic susceptibility logs for cores TR-S9, TR-S8, TR-S5 and TR-S4 with main trends of the signals (red solid lines). Correlated piercing points are represented by black solid lines (correlations recognizable between each pair of "twin" cores and between the footwall and hangingwall sector) and by black dotted lines (correlations recognizable only between each pair of "twin" cores).

The overall similarity between cores TR-S9 – TR-S8 and TR-S5 – TR-S4, respectively, is evident from the generally horizontal correlation lines between each pair of piercing points of the two "twin" cores (figure 7.5).
We then measured the vertical offset between each pair of piercing points of the two "twin" cores and plotted these values versus depth (figure 7.6). As we can expect, the vertical offset values are quite aligned along a straight line, suggesting no internal deformation in the footwall and hangingwall areas.

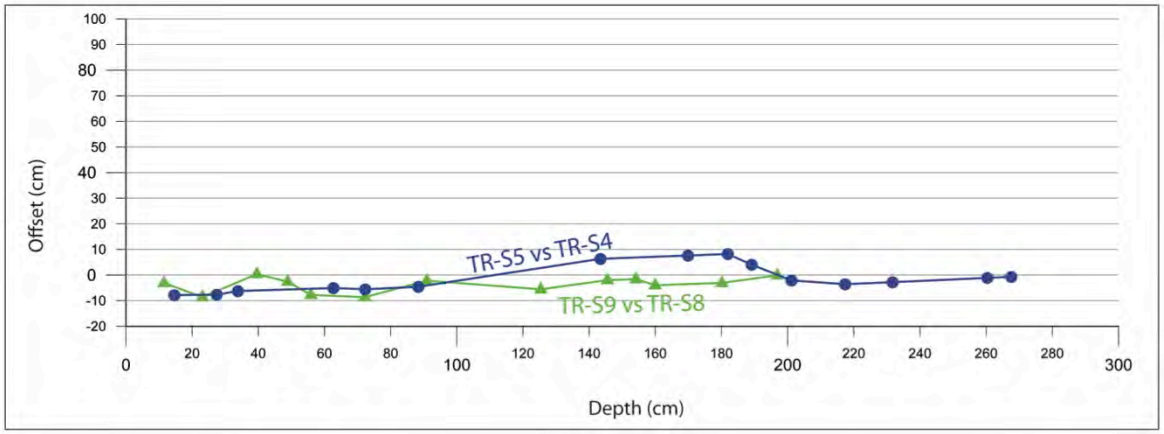

Figure 7.6 – Vertical offset versus depth plot for footwall (TR-S9 and TR-S8) and hangingwall cores (TR-S5 and TR-S4).

After that, we started a careful inspection and comparison of the cores across the fault zone, trying to identify as many as possible homologous points to better constrain the correlation across the fault zone. As a result, we recognized 11 possible homologous points between TR-S9 and TR-S8 cores in the footwall and TR-S5 and TR-S4 cores in the hangingwall, respectively (figure 7.5).
Due to technical problems during drilling, the signal of core TR-S8 does not reach the same depth of the "twin" TR-S9 core, and it was thus not possible to precisely identify the last homologous point between cores TR-S9 and TR-S8. Taking into account the general similarity between the two signals, we extrapolated the position of the last piercing point in core TR-S8, projecting it from core TR-S9.
Remarkably, if we look at the pattern of the resulting high-resolution correlations between the footwall and hangingwall sector, we note a clear change in the angle of the correlation lines.
This pattern reflects a downward increment of the difference in depth of the homologous points between core TR-S5 with respect to core TR-S8 across the fault. This implies an increment of the deformation with depth(figure 7.5).
In order to better define the trend of the deformation at depth, we measured the vertical offset shown by all the pairs of homologous points and plotted the resulting values versus TR-S5depth (figure 7.7).

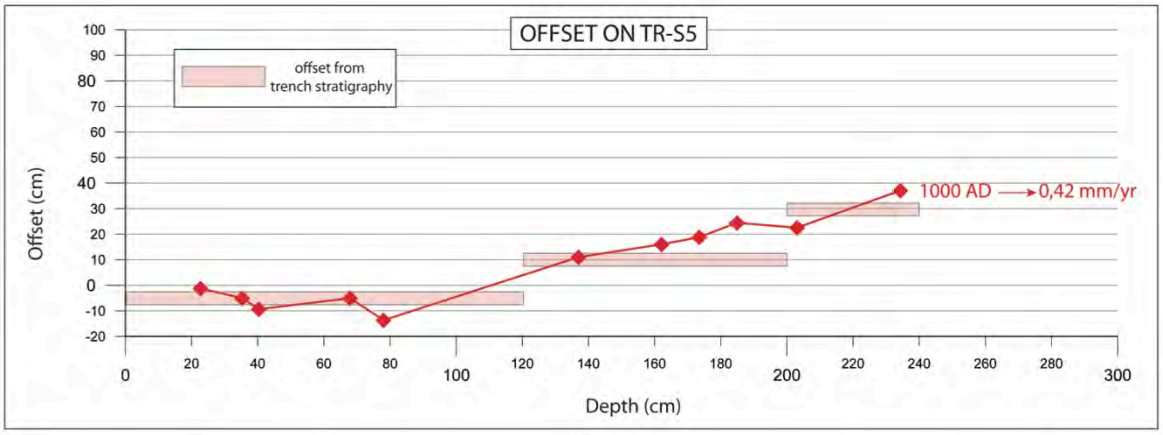

Figure 7.7 - Vertical offset versus depth for TR-S5 core

Figure 7.7 shows the distribution of the vertical offset for TR-S5 core measured by petrophysical logging (red solid line) compared with conventional trench stratigraphic analysis at the same investigation depth (pink boxes).

As a first order consideration, we confirm an increasing vertical offset with depth for both the trench stratigraphy and the petrophysical correlations plots. We can interpret this vertical offset distribution as due to the accumulation of the deformation through time along the fault splay. From figure 7.7 the sediments of the hangingwall at a depth of 2.4 m show a cumulative displacement of 0.42 m that is in good agreement with the trench observations.

In particular, the offset versus depth pattern derived from trench analysis shows a staircase pattern, outlining three different groups of deposits characterized by a well-defined offset (pink boxes in figure 7.7). This vertical offset distribution is due to individual events of displacements able to produce repeated vertical separations at the surface of ~0.15-0.2 m.

Looking at the vertical offset distribution resulting from petrophysical correlations (red solid line in figure 7.7)the increasing offset with depth is clear, however, in this case, is not possible to recognize individual events of deformation. This limitation is likely due to the limited resolution of the petrophysical correlations with such small displacement increments.

Taking into account the total amount of vertical offset measured (0.42 m) by means of high-resolution petrophysical correlations and divide it by the average age of the deposits obtained by means of ^{14}C dating (~1000 years – see Chapter 6 – Mo'Tretteca site), we can estimate a vertical slip-rate of 0.42 mm/yr.

7.2.3 Fossa site

We performed another test of the high-resolution petrophysical correlation method at the Fossa site, located on the western side of the Middle Aterno basin, along the north-east dipping Monticchio-Fossa fault (figure 7.8).

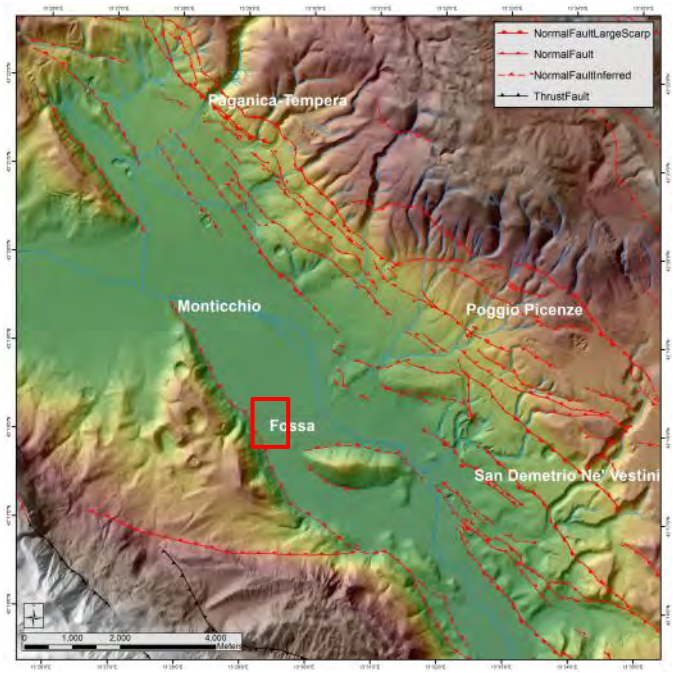

Figure 7.8 – Large-scale view of the Middle Aterno basin showing the location of the Fossa site (red box).

At this site an artificial excavation across the scarp exposed part of the fault zone in unconsolidated colluvial and slope wash deposits. Here, just after the 2009 L'Aquila mainshock, newly formed open cracks without appreciable vertical displacement where observed along pre-existing fault planes. Conventional stratigraphic logging revealed evidence of a constant stratigraphic dip-slip paleo-offset of ~0.22 m , with NE-side down and along the main fault plane (figure 7.9). To obtain a reference age for the offset sediments, we dated two samples at this site by means of ^{14}C: Sample 4A yielded an age of 30490-30070BP whereas Sample 9A 5660-5520BC.

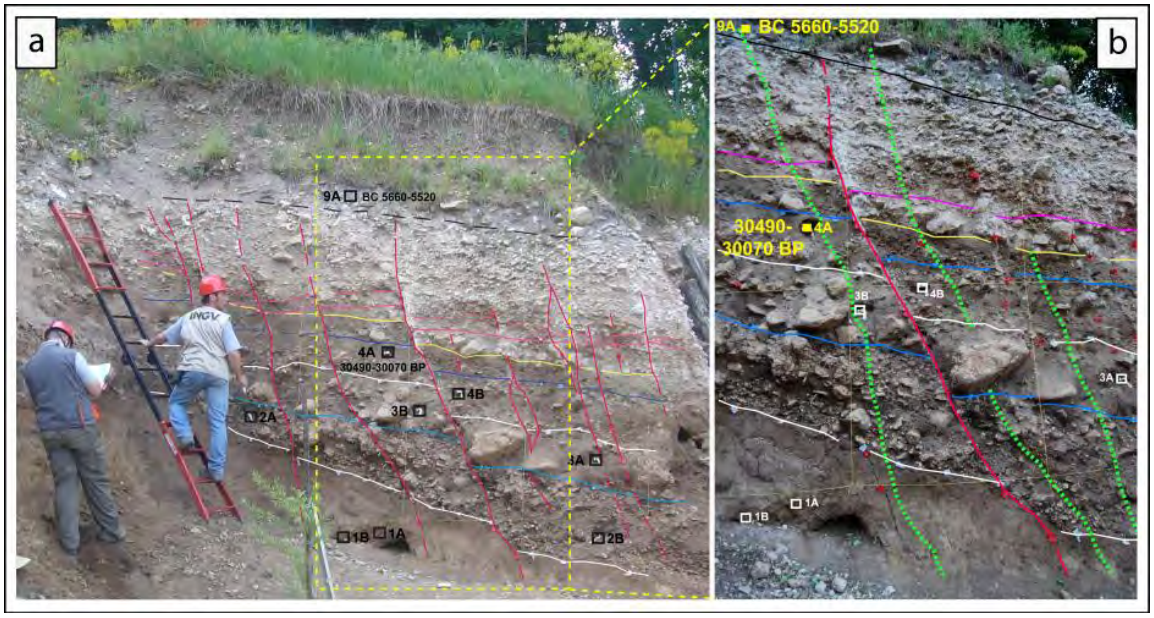

Figure 7.9 – Stratigraphic log of the Fossa site wall (a) and (b) traces of the magnetic susceptibility measurements performed directly on wall (green dotted lines).

As coring was impractical at this site due to the characteristics of the deposits (presence of cobbles and boulders within coarse to fine matrix), we decided to test the high-resolution petrophysical correlation approach by performing the magnetic susceptibility measurements directly on wall, using a hand-held Bartington MS2E point sensor.

Magnetic susceptibility measurements on the wall were collected on both sides of the main fault at a centimetric scale (2 cm interval between each measurement) positioning the sensor directly on the silty-sandy matrix (figure 7.10). We carefully choose our measurements paths on the footwall and hangingwall sector (green dotted line in figure 7.9) in order to avoid the coarser deposits to be measured. We performed two overlapping measurements on the hangingwall , due to the presence of a boulder impeding the sensor to work properly.

Figure 7.10 - Bartington MS2E point sensor performing magnetic susceptibility measurements directly on wall.

The resulting measurements are reported in the magnetic susceptibility logs of figure 7.11 (we merged the hangingwall sector signals obtaining a synthetic log). We used the same procedure of Mo'Tretteca site and recognized 20 piercing points between the footwall and the hangingwall signal.
The pattern of the obtained high-resolution correlations between the footwall and hangingwall sector does not shows a significant variation in the angle of the correlation lines. This behavior suggests the presence of a constant offset produced by a single deformational event affecting the whole exposed stratigraphy.

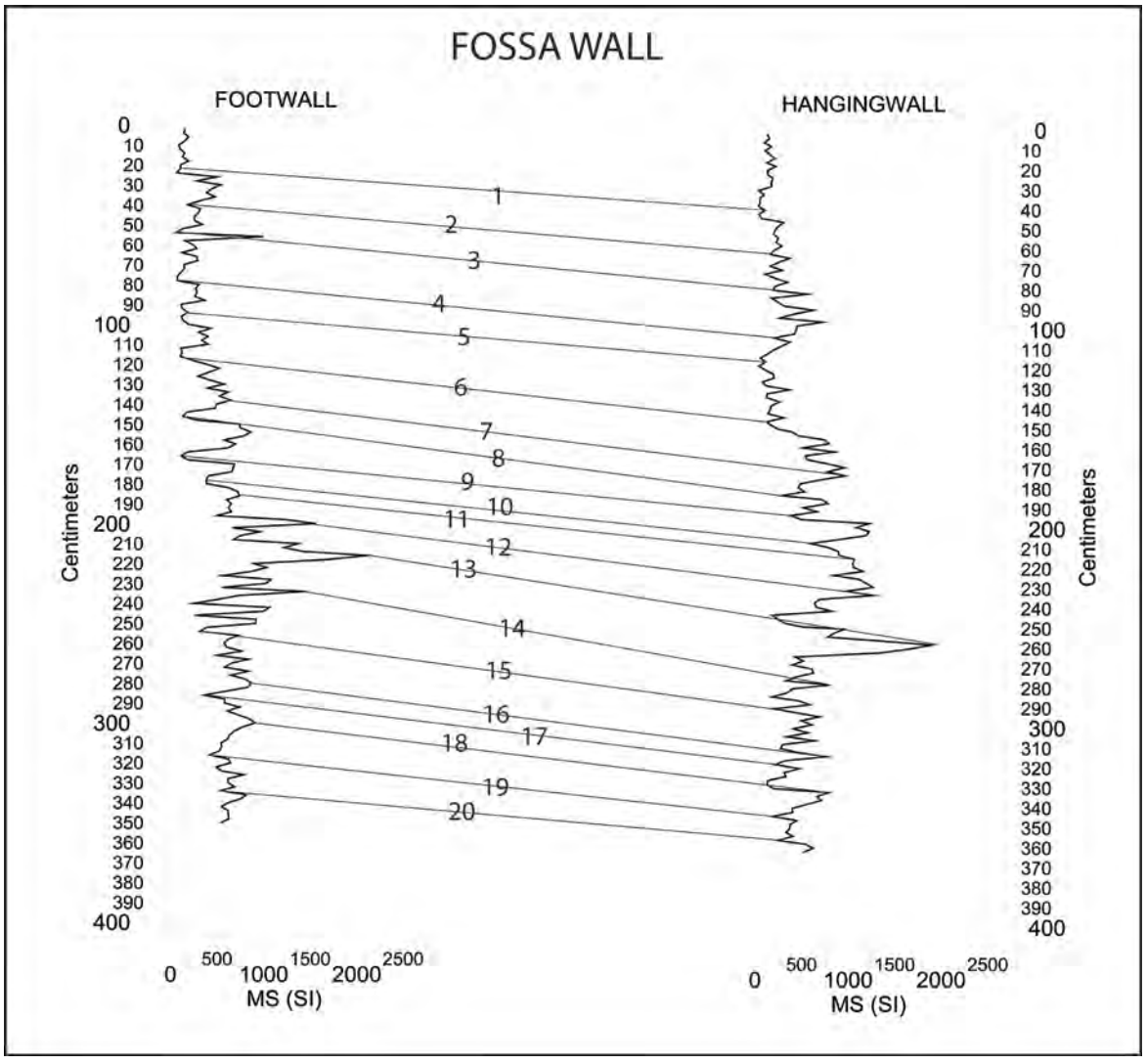

Figure 7.11 - Magnetic susceptibility logs for the footwall and hangingwall sectors at Fossa site. Correlated piercing points are represented by black solid lines.

We then measured the vertical offset of all the pairs of homologous points and corrected these values taking into account the dip of the strata, which showed a different inclination between the top and the bottom section of the exposed wall.
The plot of the vertical offset values obtained by high-resolution petrophysical correlations versus depth is shown in figure 7.12 (red solid line).

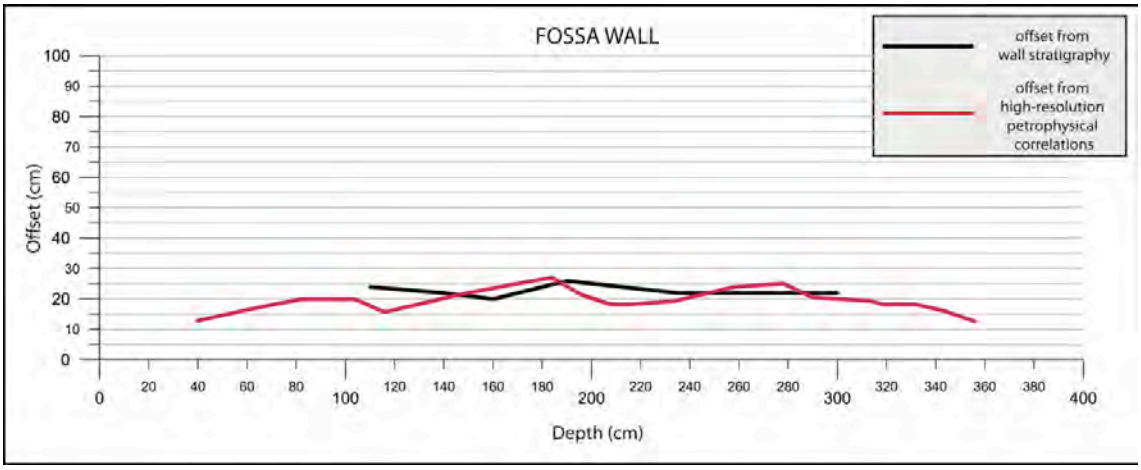

Figure 7.12 – Comparison of the vertical offset versus depth plots obtained by means of stratigraphic analysis (black line) and high-resolution petrophysical correlations (red line).

Figure 7.12 also reports the plot of the offset values obtained by means of conventional stratigraphic logging on the wall (black solid line). A comparison between the two lines highlights that the high-resolution measured offset (average 20 cm) is consistent with the stratigraphic offset (average 22 cm). The magnetic susceptibility measurements were thus effective in reproducing the stratigraphy exposed at this site, with a minimum variability (±5cm from ~110 cm to ~300 cm depth) with respect to the offsets measured with a conventional stratigraphic approach.

7.3 Electrical resistivity tomography

During our field investigations, we also selected six sites suitable for a high-resolution electrical resistivity tomography (ERT) campaign. The ERT surveys were performed along the PSDFS in order to complement the information acquired by means of geomorphological and geological investigations, focusing our efforts on confirming the tectonic nature of previously recognized morphological scarps, calculating the associated fault throws by including also subsurface data, and select new sites for paleoseismological trenching/coring.

7.3.1 Method

ERT is a relatively low cost, noninvasive and widely applied geophysical technique for obtaining 2D high-resolution images of the resistivity subsurface distribution from electrical measurements made on the ground surface.

This near surface imaging technique is effective in detecting active faults and estimating the vertical displacement in Quaternary deposits (e.g. Storz et al., 2000; Suzuki et al., 2000; Demanet et al., 2001; Caputo et al., 2003; Nguyen et al., 2003; Wise et al., 2003; Nguyen et al., 2005).

It consists in transmitting an alternating electrical current into the subsurface via two potential electrodes and in measuring the resulting potential difference ΔV between two other electrodes. The fundamental physical law used in resistivity surveys is Ohm's Law that governs the flow of current in the ground. The equation for Ohm's Law in vector form for current flow in a continuous medium is given by:

$$J = \sigma E$$

where σ is the conductivity of the medium, J is the current density and E is the electric field intensity.

The apparent resistivity is given by the following relationship:

$$\rho = K\frac{\Delta V}{I}$$

with K being a geometrical factor which only depends on electrode position. The apparent resistivity ρ is the ratio of potential obtained in situ with a specific array and a specific injected current by the potential which will be obtained with the same array and current for a homogeneous and isotropic medium of 1 Ωm resistivity.

The apparent resistivity measurements give information about resistivity for a medium whose volumes is proportional to the electrode spacing. It follows that the larger the electrode spacing is, the higher the investigated volume. Several parameters influence electrical resistivity: water content, temperature, particle size, ionic content, and porosity, among many others.

From a technical point of view, we carried out ERT investigations using a Syscal R2 resistivity meter (Iris instruments), coupled with a multielectrode acquisition system (64 electrodes). We performed eight ERT profiles at six sites, setting different array configurations (Wenner and Dipole-Dipole) and electrode spacing, depending on the desired maximum depth of investigation and considering the sensitivity of the array to the vertical and horizontal changes in the subsurface resistivity, the horizontal data coverage and the noise level (figure 7.13 and table 7.1).

In general, the Wenner array configuration is sensitive in resolving vertical changes in the subsurface resistivity but relatively poor in detecting horizontal changes.

Conversely, the dipole-dipole array is most sensitive to horizontal changes in resistivity, but relatively insensitive to vertical changes in the resistivity.

Moreover, when compared to the Wenner array, the dipole-dipole configuration has a shallower depth of investigation.

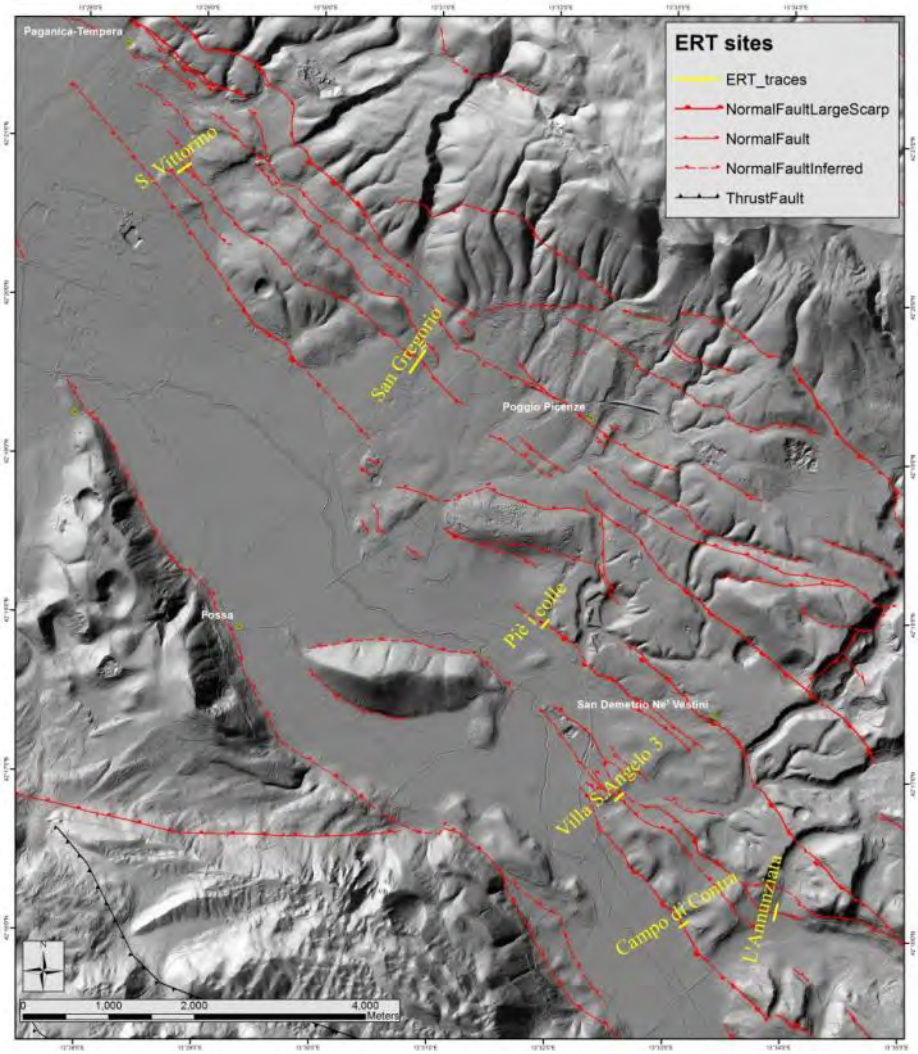

Figure 7.13 – Location of the Electrical Resistivity Tomography (ERT) surveys performed along the PSDFS.

Site	Array configuration	Electrode spacing (m)	Length (m)
San Gregorio	Wenner	5	320
L'Annunziata	Wenner	3	192
	Dipole-dipole	2	128
San Vittorino	Wenner	3	192
	Dipole-dipole	2	128
Pie' i colle	Wenner	2	128
Villa Sant'Angelo	Wenner	2	128
Campo di Contra	Dipole-dipole	2	128

Table 7.1 – Electrical Resistivity Tomography (ERT) configurations.

The system automatically performed the pre-defined sets of measurements and provided direct reading of injected current, potential difference and electrode location. In order to obtain a resistivity image from apparent resistivity data it was

necessary to carry out an inversion that produced a model (a spatially varying distribution of resistivity) that gave an "acceptable" fit to the data and satisfied any other prescribed constraints. The Wenner and Dipole-Dipole ERT data were inverted using the RES2DINV software, a completely automatic program that uses the smoothness-constrained least-squares inversion technique (Loke et al. 2003) to produce a 2D model of the subsurface from the apparent resistivity data.

7.3.2 Results

In the following section each ERT profile will be briefly described, highlighting its relative contribution to the interpretation of the nature of the geomorphological features observed at the surface and/or to the estimation of fault throw. Even if we were aware of the fact that resistivity values can be extremely variable, it was possible to tentatively associate resistivity values with main lithostratigraphic units thanks to the data gathered through field geological investigations and exploratory boreholes. High resistivity values were in general associated with the presence of limestone bedrock or calcium-carbonate conglomerates and gravels, while low-resistivity values should correspond to fine-grained, silty-sandy eluvial, colluvial and alluvial deposits.

7.3.3 San Vittorino site

Geomorphological analysis at San Vittorino revealed the presence of a subtle NW-SE trending, SW facing morphological scarp (figure 7.14) within a graben-like structure. Moreover, the small morphological scarp, being in line with a clearly identifiable fault-trace to the SE, displays a high potential for a tectonic origin.
In order to verify the nature of the morphological scarp (fault scarp vs. erosional scarp) and to derive a possible throw associated with the activity of the tectonic lineament, we performed two ERT surveys with different configurations.

Figure 7.14 - overview of the San Vittorino site with the subtle morphological scarp (at the transition between the green and brown fields. View is toward the WSW.

As a first step, we performed an ERT profile with a Wenner-type array configuration, targeting a maximum investigation depth of ~30 m and crossing the abovementioned morphological scarp approximately between 60 and 90 m distance (figure 7.15 a).

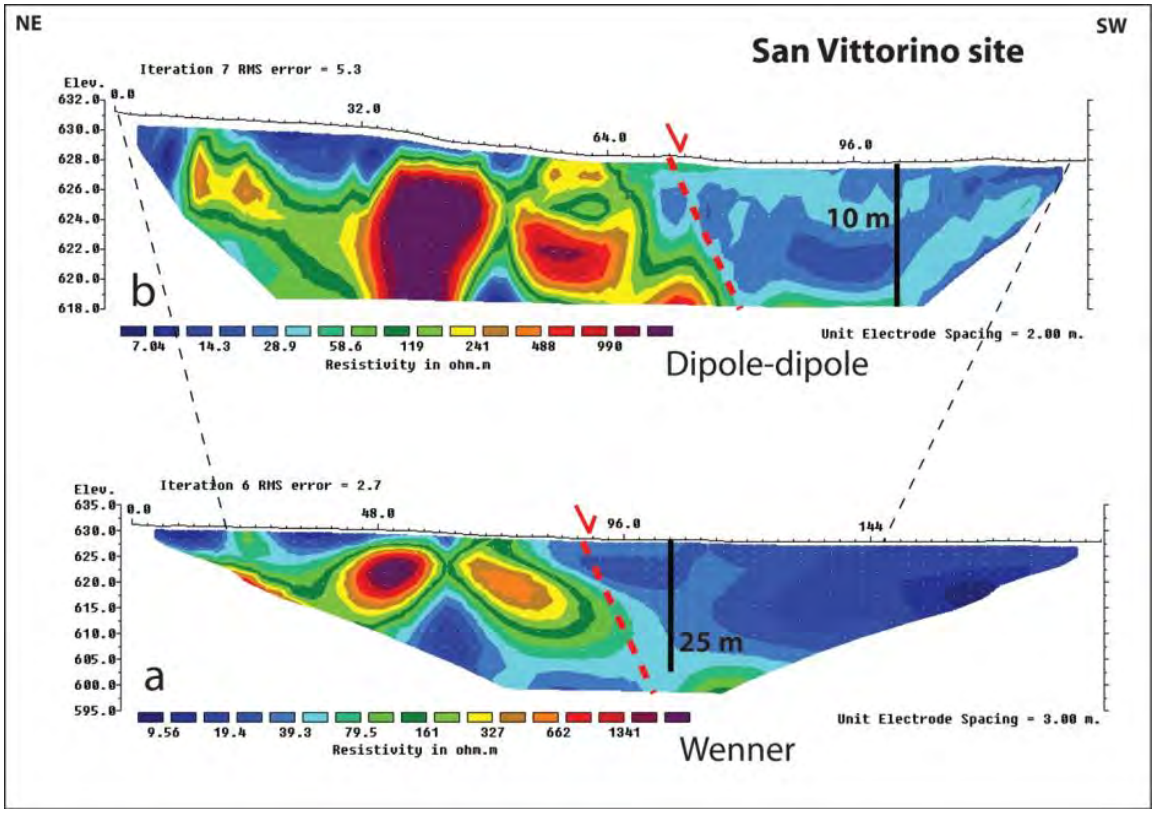

Figure 7.15 – ERT profiles performed at San Vittorino site.

This wenner survey was effective in highlighting a resistivity pattern characterized by a lateral resistivity contrast (red dotted line in figure 7.15a) and in locating a high-resolution ERT performed using a dipole-dipole array aimed at investigating the same feature with a smaller investigation depth (~10 m) but an improved spatial resolution.

The major feature displayed by the high-resolution D-D ERT (figure 7.15b) is a sharp lateral variation of the resistivity, with higher values found in the presumed fault footwall and a decrement in the resistivity values observed in the presumed fault hangingwall.

Taking into account the results of the ERTs at this site, we can confirm the presence of a tectonic lineament (red dotted line in figure 7.15a-b) juxtaposing a high-resistivity body (gravels and conglomerates) in the footwall with low-resistivity deposits in the hangingwall (eluvial-colluvial deposits). Moreover, the ERT profiles gathered information about the displacement associated with this fault. Because the high-resistivity values found in the footwall are not visible at the deeper part of the hangingwall, and considering the normal faulting style of the structure, the correlative high-resistivity deposits are expected to be at a greater depth. Therefore,

a minimum throw value for this fault splay of ~25 m can be estimated (black bar in figure 7.15a-b).

7.3.4 Villa S. Angelo site

We performed an ERT survey at Villa Sant'Angelo site in order to confirm the tectonic nature of a NE-facing scarp (antithetic to the main faults) identified by means of geomorphological investigations.

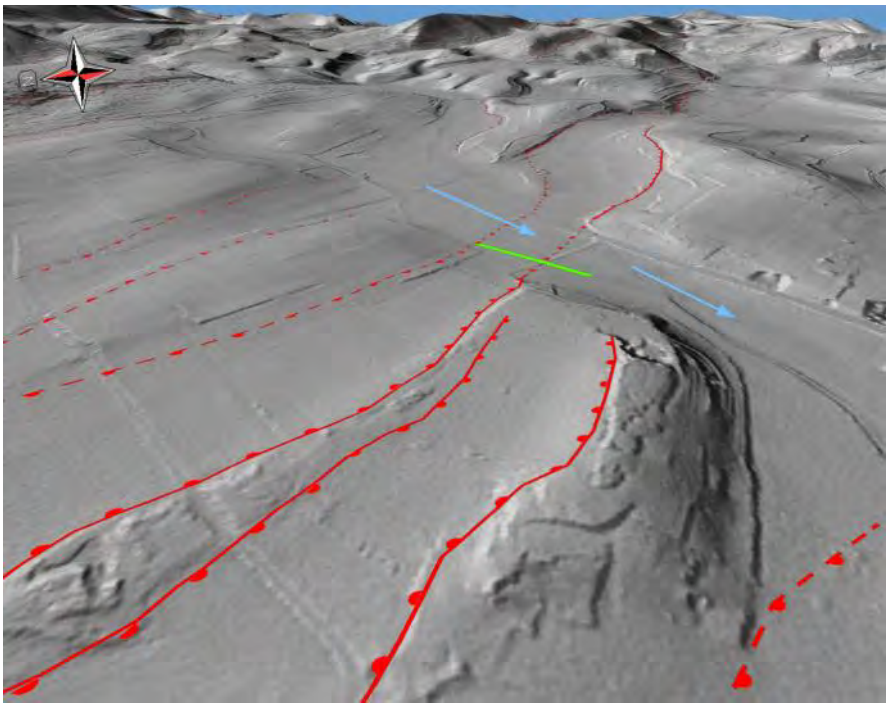

Figure 7.16 – overview of the Villa Sant' Angelo site. The green bar represents the ERT profile (128 m-long); sky-blue arrows indicate main drainage direction.

This morphological scarp could represent the surficial expression of an antithetic splay of the PSDFS, possibly acting like a damming structure for sediments coming from upslope (figure 7.16).

From figure 7.17 we can note that the ERT Wenner profile performed at this site was effective in detecting a fault splay and in highlighting the presence of a thin layer of low-resistivity deposits at the top of the fault hangingwall, likely associated with the presence of alluvial and colluvial fine deposits.

Moreover, the ERT profile of figure 7.17 provides information about the displacement associated with this fault: the high-resistivity values found in the footwall can be correlated with those in the hangingwall whose top is at ~5 m depth. Therefore a ~5 m throw value for this fault splay (black bar in figure 7.17) can be estimated thus representing a minimum because some footwall erosion may have occurred.

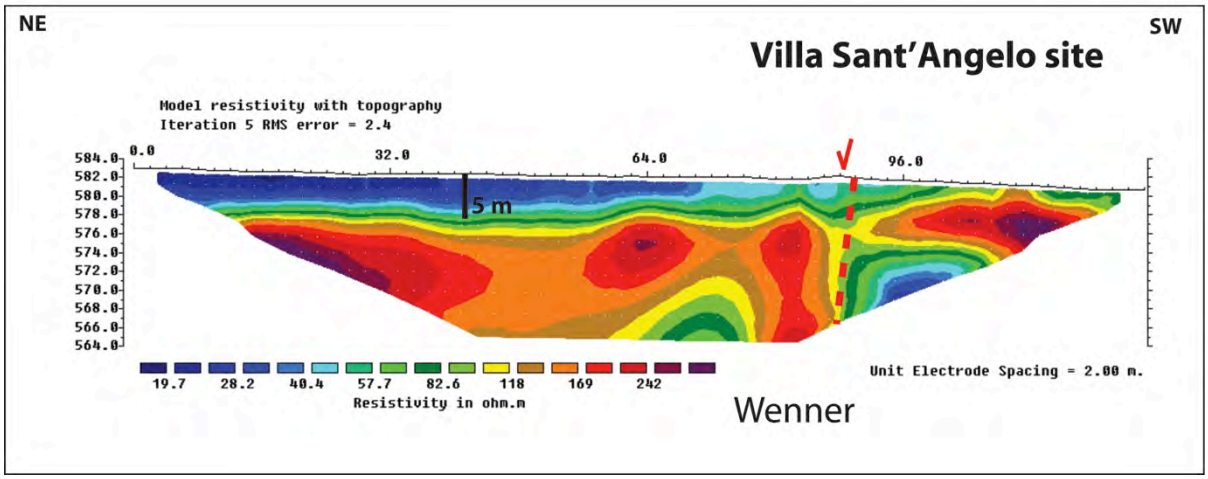

Figure 7.17 – ERT profile performed at Villa Sant'Angelo site.

7.3.5 L'Annunziata site

At this site the main morphological features suggesting the occurrence of a fault splay are represented by the presence of a clear, partially anthropogenically modified scarp on fine alluvial and colluvial deposits, separating two well-defined morphological surfaces (figure 7.18). Interestingly, at this site a strong linear incision only localized at the footwall of the presumed fault also hints at the presence of a tectonic lineament.

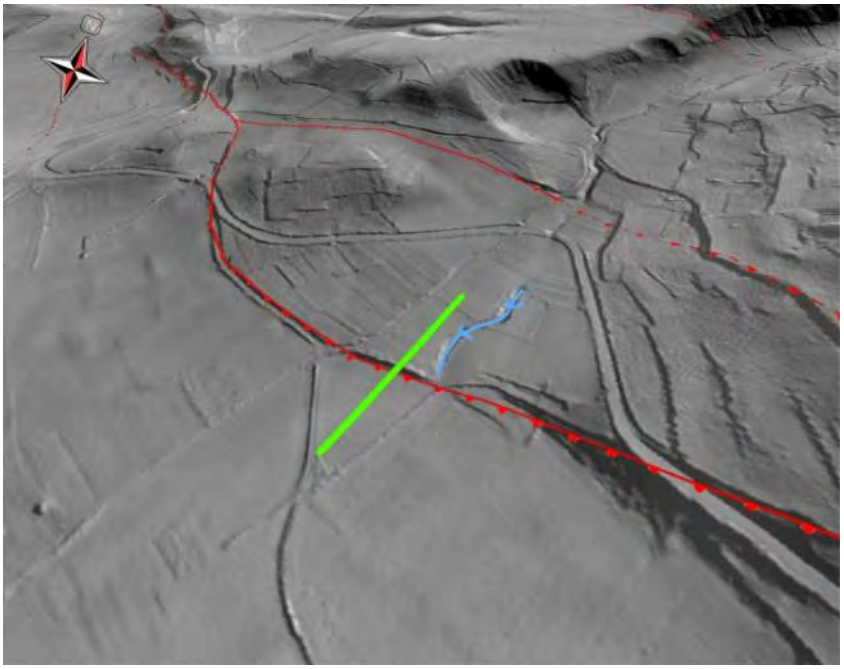

Figure 7.18 – overview of the L'Annunziata site. The green bar represents the ERT profile trace (192 m-long); sky-blue line highlights the strong drainage incision.

We performed two ERT profiles with different resolutions and investigation depth, obtaining the images showed in figure 7.19. The Dipole-Dipole ERT profile (figure 7.19b) we can note that the morphological scarp lies in correspondence of the

variation of resistivity values at depth, confirming the presence of a tectonic lineament affecting the investigated deposits. From the Dipole-Dipole ERT profile of figure 7.19b we could not gather information about the displacement associated with this fault, mainly due to low horizontal resistivity contrast of the deposits.

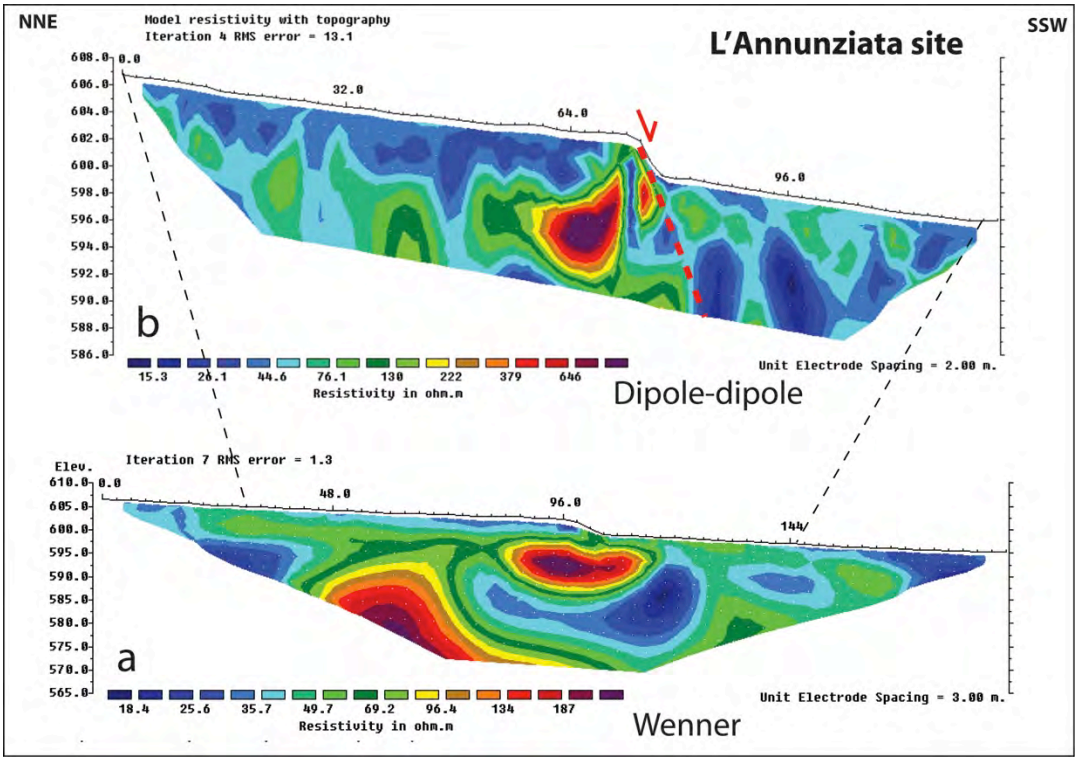

Figure 7.19 - ERT profiles performed at L'Annunziata site.

7.3.6 San Gregorio site

The overall geomorphology of this site is characterized by the presence of a NW-SE oriented limestone ridge bounded by normal faults and defining a horst-like structure. Evidence for surficial faulting at this site is mainly related to the presence of a small SW-facing scarp affecting the alluvial fan deposits dissecting the ridge and to the presence of a strong drainage incision confined between the fault traces (figure 7.20).

The ERT profile done at this site aimed principally at defining the vertical component associated with the activity of the SW-facing fault splay. We realized a more than 300m-long ERT Wenner profile, targeting a maximum depth of ~50 m. The profile started on top of the small bedrock ridge, and then run on alluvial fan deposits.

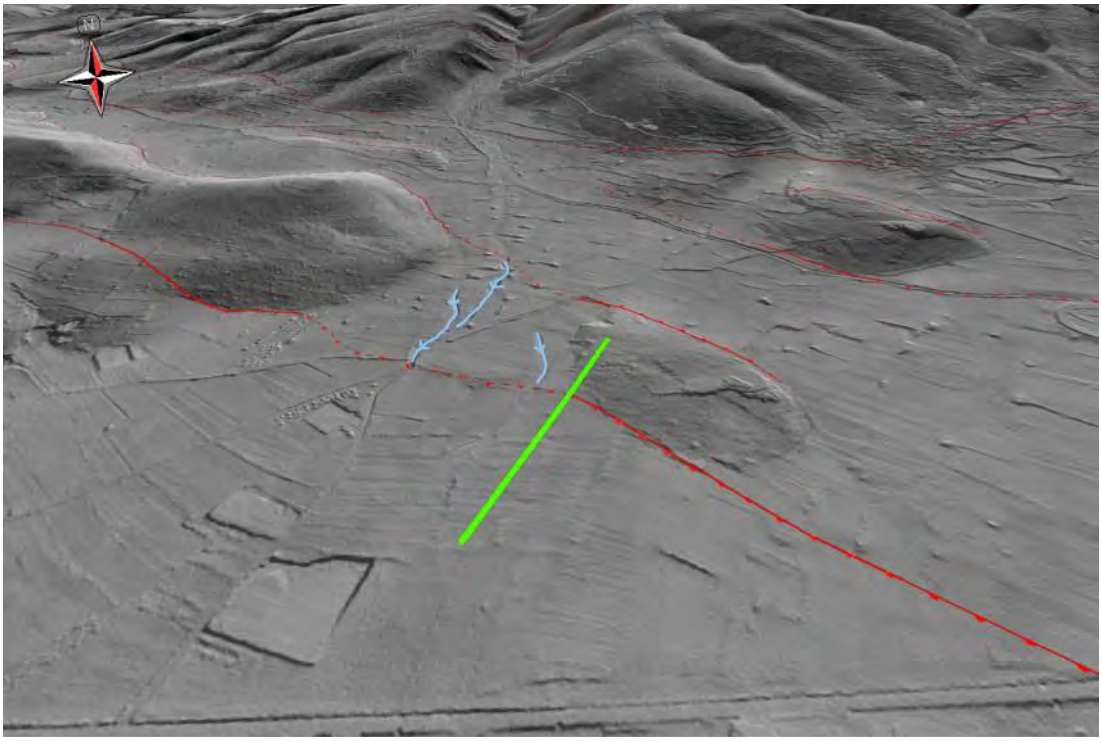

Figure 7.20 - overview of the San Gregorio site. The green bar represents the ERT profile trace (320 m-long); sky-blue line highlights the strong drainage incisions.

The main results of this investigation are presented in figure 7.21 and allowed us to confirm the tectonic nature of the surficial scarp (red dotted line). The high-resistivity body, characterized by values of more than 3500 Ωm, corresponds to the same limestone bedrock exposed at surface, while the low resistivity values are likely associated with the alluvial fan deposits.
Moreover, ERT allowed us to calculate a minimum vertical offset at this site of ~50 m, due to the lack of the high-resistivity body at the fault hangingwall. Taking into account a minimum throw value of ~10 m resulting from topographic profile number 16 (Chapter 6 and appendix D), we obtain a total minimum throw of the bedrock at this point of ~60 m.

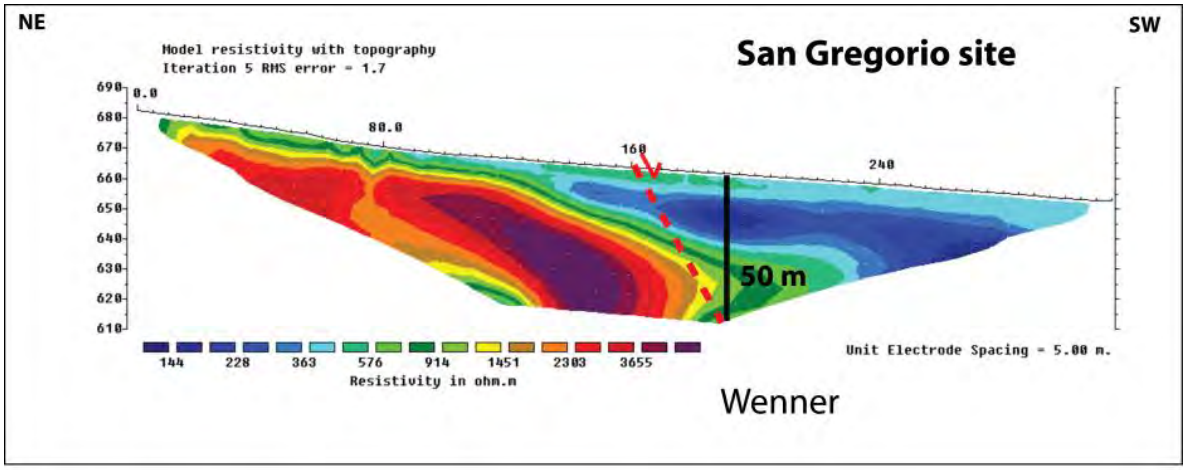

Figure 7.21 - ERT profile performed at San Gregorio site.

7.3.7 Pie' i colle site

From geomorphological and geological investigations the Pie' i colle site is characterized by the presence of a small morphological scarp (figure 7.22) lying along the lateral continuation of a well expressed fault scarp (~30 m height) affecting Middle Pleistocene alluvial deposits.

Figure 8.7.22 - overview of the Pie' i colle site. The red dotted line lies at the base of the small morphological scarp possibly related to a tectonic lineament. The yellow line is the ERT profile trace (128 m-long). View is toward the NE.

We performed a Wenner ERT profile aimed at verifying a possible continuation of the tectonic lineament and at calculating relative fault throw.

The results of Pie' i colle ERT are shown in figure 23, here a high-resistivity body at the very bottom of the NE portion of the profile is overlaid by a ~15 m thick sequence of low-resistivity deposits .

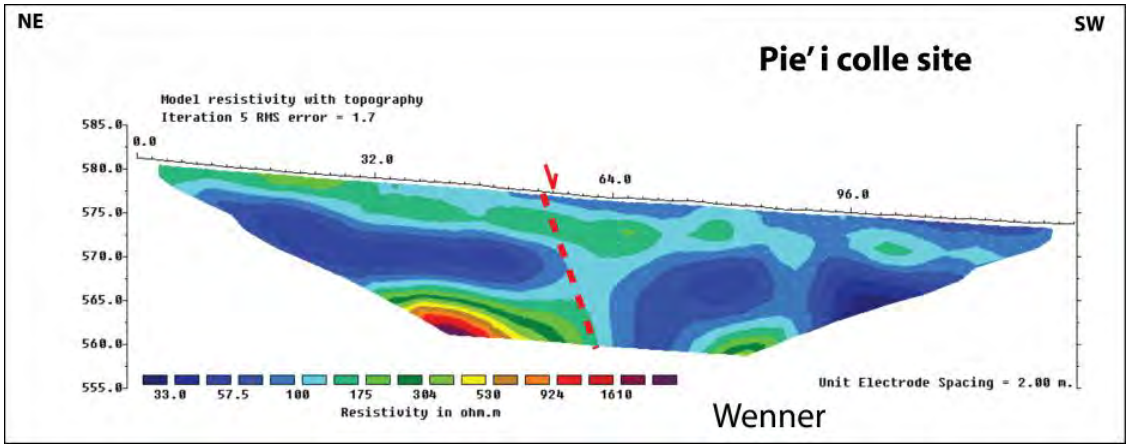

Figure 7.23 - ERT profile performed at Pie' i colle site.

The ERT survey performed at this site did not provided a clear evidence for a very shallow fault splay. We can speculate about the presence of a fault splay at larger depth if we interpret the morphological scarp observable at this site as related to the mimicking at the surface of a deeper fault with respect to the depth investigated. Due to low horizontal resistivity contrast of the deposits overlaying the high-resistivity body it is however difficult to discriminate the deformation produced by the tectonic lineament.

Another possibility is that the footwall has been eroded away by a strongly incising river, but this interpretation may be difficult to sustain due to the lack of an important drainage at this site.

7.3.8 Campo di Contra site

At Campo di Contra site we were mainly interested at verifying the presence at depth of a tectonic structure, suggested by a small morphological scarp lying at the base of the main fault escarpment at the surface.

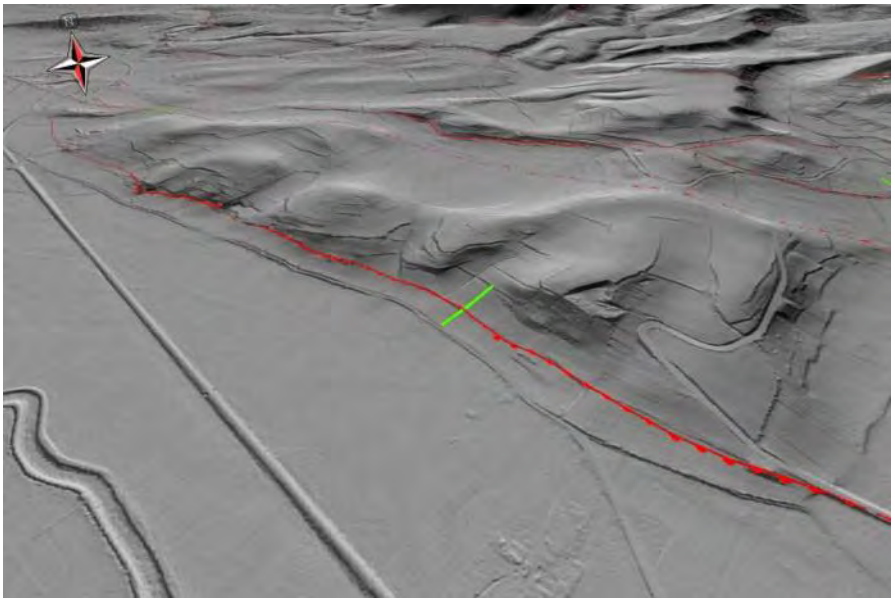

Figure 7.24 - overview of the San Gregorio site. The green bar represents the ERT profile trace (128 m-long);

We performed here an ERT profile using a Dipole-Dipole array configuration, with a target investigation depth of ~ 10 m. The ERT investigations revealed the presence of sedimentary bodies characterized by relatively small resistivity contrast and affected by three faults.

Figure 7.25 shows that the main resistivity contrasts are visible in the NE portion of the ERT profile, outlining a fault zone characterized by a graben-like structure at the base of the main fault escarpment. The resistivity pattern also suggests the presence of a synthetic fault splay in correspondence of the small morphological scarp visible at the surface.

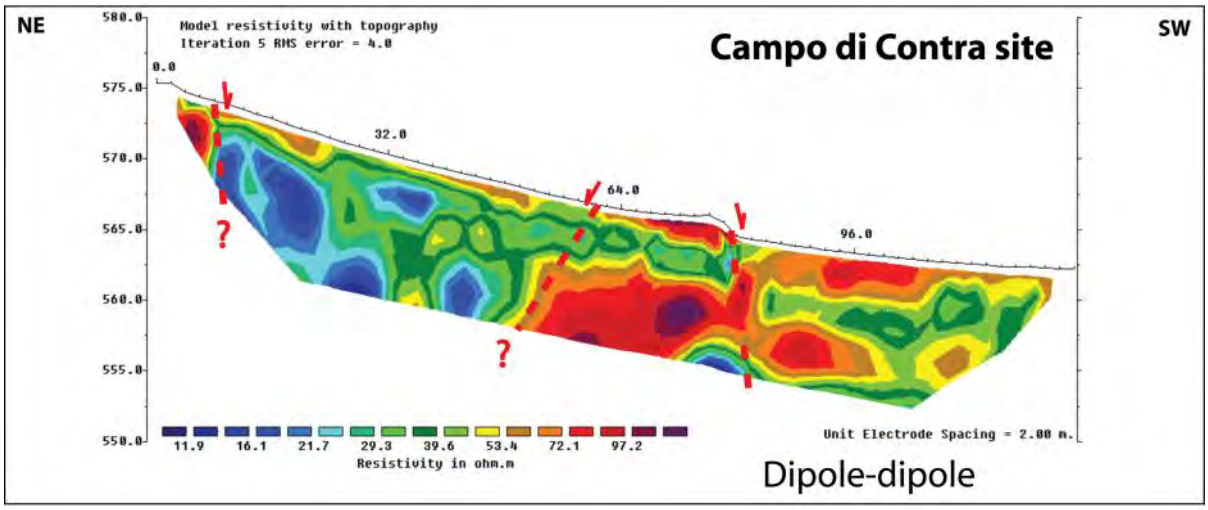

Figure 7.25 - ERT profile performed at Campo di Contra site.

This ERT profile was thus effective in providing new subsurface data about the structure of the fault zone along this fault splay. Due to low horizontal resistivity contrast of the deposits overlaying the high-resistivity body it is however difficult to define the amount of the deformation produced by the tectonic lineament at this site.

7.4 High-resolution seismic tomography

During my PhD program I had the opportunity to join a team of researchers of the Istituto Nazionale di Geofisica e Vulcanologia (INGV, Italy) during a ten-day-long experiment aimed at acquiring high-resolution shallow seismic profiles across the Middle Aterno Valley.

7.4.1 Method

High-resolution shallow seismic profiling is an effective tool in imaging near-surface fault systems and providing valuable information about shallow basin geometry (Morey and Schuster, 1999; Improta et al, 2003; Improta et al., 2010).
No commercial seismic exploration data were acquired in the epicentral area, so no reliable subsurface constraints about the basin structure were available. The seismic survey was carried out in order to image both the subsurface geometry and internal architecture of the Middle Aterno basin, as well as to estimate possible fault throws across the PSDFS.
The seismic experiment was realized through the acquisition of 5 NE-SW profiles for a total length of ~ 7 km, targeting the northwestern portion of the Middle Aterno basin in the Paganica – Bazzano sector (figure 7.26).

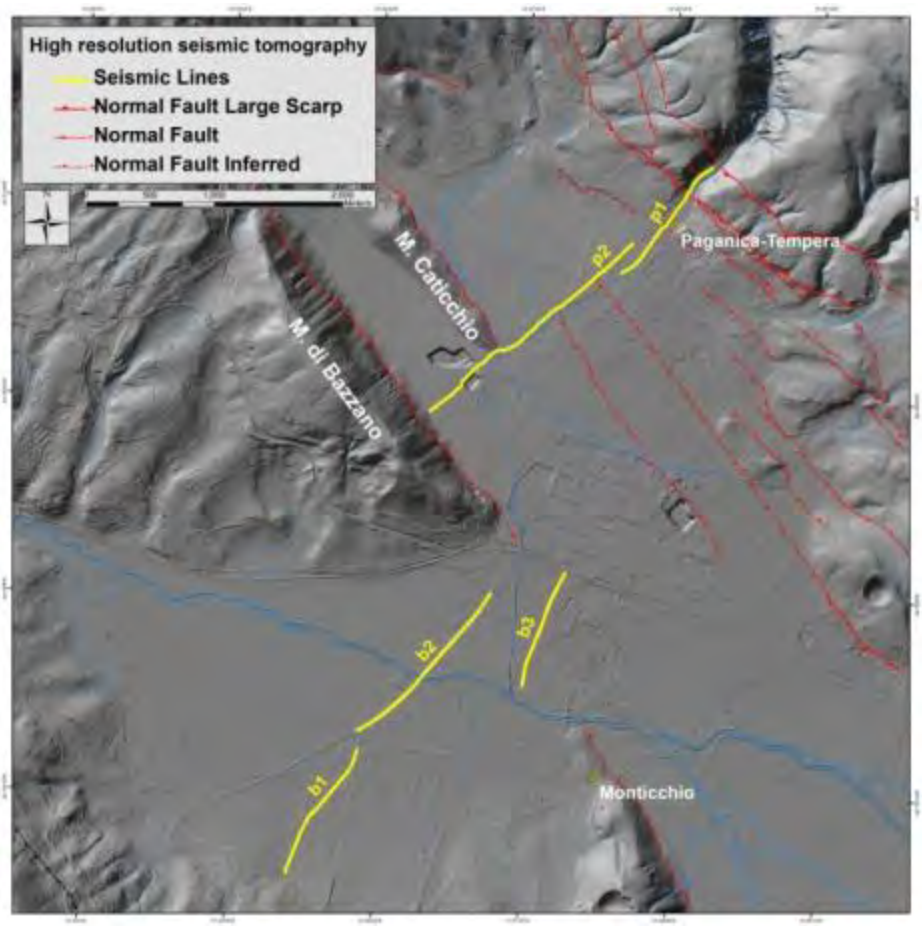

Figure 7.26 - Shaded relief topography of the Middle Aterno basin with location of the five seismic lines and main fault splays.

The survey geometry was designed based on preliminary analysis of aerial photos and geological investigations and represented the best compromise between specific geologic targets and logistic/environmental difficulties.
Specific target sites of the investigations were:

- the sector of the basin where the clearest coseismic surface ruptures were observed (profile p1);
- the hanging-wall of the PSDFS and NE-dipping antithetic splays (profile p2);
- the extensional faults bounding the Bazzano-Monticchio ridge (profile b3);
- the sector of the basin that experienced the maximum coseismic subsidence (profiles b1 and b2) (see Chapter 3).

Seismic data were collected according to the innovative dense wide aperture acquisition geometry (Operto et al., 2004), combining both seismic reflection imaging and seismic tomography techniques.

7.4.2 Results

Being a very complex work involving several researchers, picking and interpretation of the data is still ongoing, however some preliminary results are available. Figure 7.27 shows the long-wavelength Vp model for the profile Paganica 2, representative

of the large-scale basin structure in the western portion of the hangingwall of the PSDFS. This profile runs for a length of ~2080 meters and ends to the SW against the eastern slope of the Bazzano ridge.

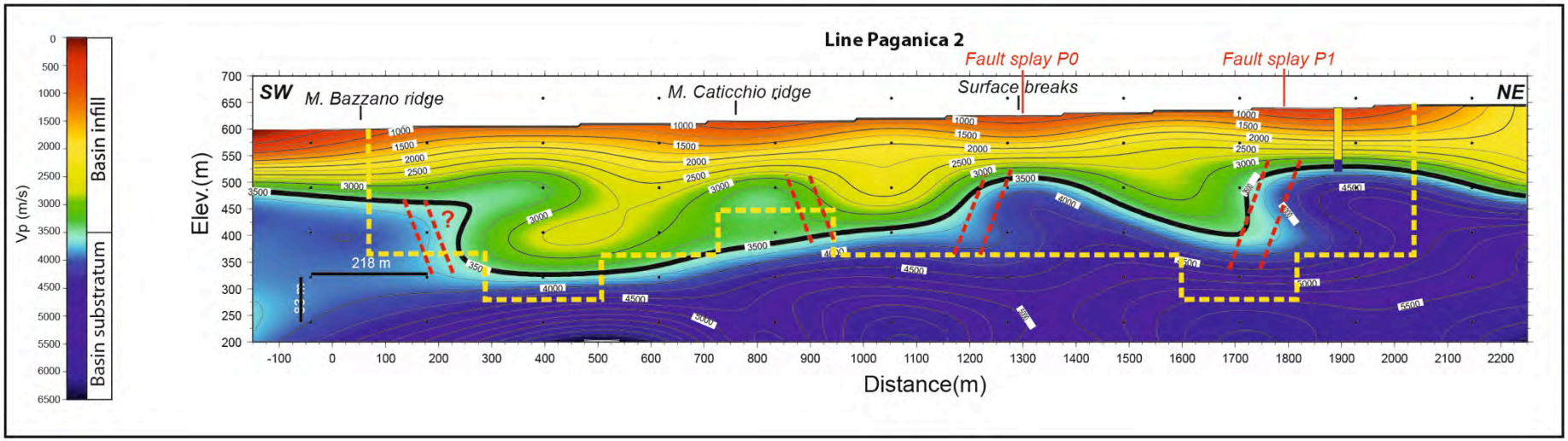

Figure 7.27 – Long wavelength Vp model of line p2. The figure also shows the location of the borehole reaching the bedrock at -78 m depth and the location of some of the discontinuous surface breaks reported in Chapter 3.

At a basin-wide scale, we note that the tomographic image (figure 7.27) shows a velocity field characterized by strong lateral Vp variations, with high-velocity (Vp > 3250 m/s) bumps located at ~800, ~1300 and ~1900 m distance along the line.
On the basis of the analysis of ray paths of critical refractions and of the projection of the bedrock drilled at 78 m depth (id 156626 - http://sgi1.isprambiente.it/GeoMapViewer/index.html), the ~3500 m/s contour line (black bold line in figure 7.27) may tentatively be considered as the top of the Meso-Cenozoic basin substratum, suggesting that the basin reaches ~ 250 m depth in the PSDFS hangingwall.
The bodies characterized by Vp<3500 m/s are interpreted as the Quaternary continental deposits forming the basin infill.
Moreover, the top of the basin substratum seems to be characterized by an articulated geometry: the rise of the ~3500 m/s contour line approximating the top of the bedrock at the SW end of the line is in agreement with the presence of the Bazzano limestone ridge at the surface, bounded by an antithetic fault. To the NW, strong lateral heterogeneities and steps (high Vp bumps located at ~1100-1300 m and ~1700-1900 m distance) may be evidence of buried SW-dipping fault splays (red dotted line in figure 7.27) of the PSDFS that juxtapose bedrock limestone against basin infill deposits. Seismic tomography provides also hints for estimating displacements along these fault splays, with throw values of ~100 m and ~150 m, respectively.
Interestingly, the surface projection of the step at ~1100-1300 m distance coincides with the occurrence of some aligned discontinuous surface ruptures (figure 7.28 – see also Chapter 3).
The subsurface geometry in this sector of the PSDFS hangingwall appears therefore to be more complicated than suspected from surface geomorphological and geological investigations likely because high sedimentation rates compared to tectonic rates. However, this complexity appears still coherent with the overall PSDFS structural setting.
Profile p1 is currently under elaboration and will not be presented in this chapter. The other profiles of the high-resolution seismic tomography investigations as well as the technical details of seismic experiment are presented in the attached article which I co-authored: “High-resolution controlled-source seismic tomography across the Middle Aterno basin in the epicentral area of the 2009, Mw 6.3, L’Aquila earthquake (central Apennines, Italy), in press on the Italian Journal of Geoscience.

8 Discussion

The multidisciplinary approach proposed in this thesis was designed to better define the tectonic style, geometry, kinematics and texture of the whole Paganica – San Demetrio fault system (PSDFS hereinafter), as well as to define its behavior over time and space. These results are translated into seismic fault behavior parameters and discussed in the light of the seismic hazard of this area.

8.1 Tectonic style

The detailed geomorphological and geological analysis of the PSDFS, also integrated with subsurface geophysical investigations, was used to define the fault system tectonic style, arrangement, kinematics, extent, geometry and boundaries.

At a basin-wide scale, the multidisciplinary investigations highlighted the existence of a complex structural setting of the PSDFS at the surface. This is characterized by the presence of several normal parallel fault splays (i.e. overlapping strands with similar trends) frequently arranged in a quasi-fractal sequence of horsts and grabens of variable size.

Looking at the surface pattern, we can distinguish two main sectors of the PSDFS characterized by different structural arrangements (figure 8.1 and Chapter 6) and by diverse extent and age of outcropping deposits.

In the Paganica sector (northern portion of the PSDFS), the deformation is accommodated by a narrow fault zone, forming a less than 1 km-wide deformational band and controlling the basin evolution with a persistent depocenter location since Early Quaternary (~2 Ma).

In the San Demetrio sector (southern portion of the PSDFS), the structural arrangement of the fault system becomes more complex and the deformation appears to be accommodated by several tectonic structures, affecting a wider fault system with respect to the northern area. In fact, here the PSDFS opens into a set of parallel, km-spaced fault traces that exhume and dissect the Quaternary basin and produce a staircase landform with deposits progressively younger and less elevated toward the present Aterno River bed. This setting is suggestive of a progressive migration in time of the basin depocenter toward the present-day valley bottom.

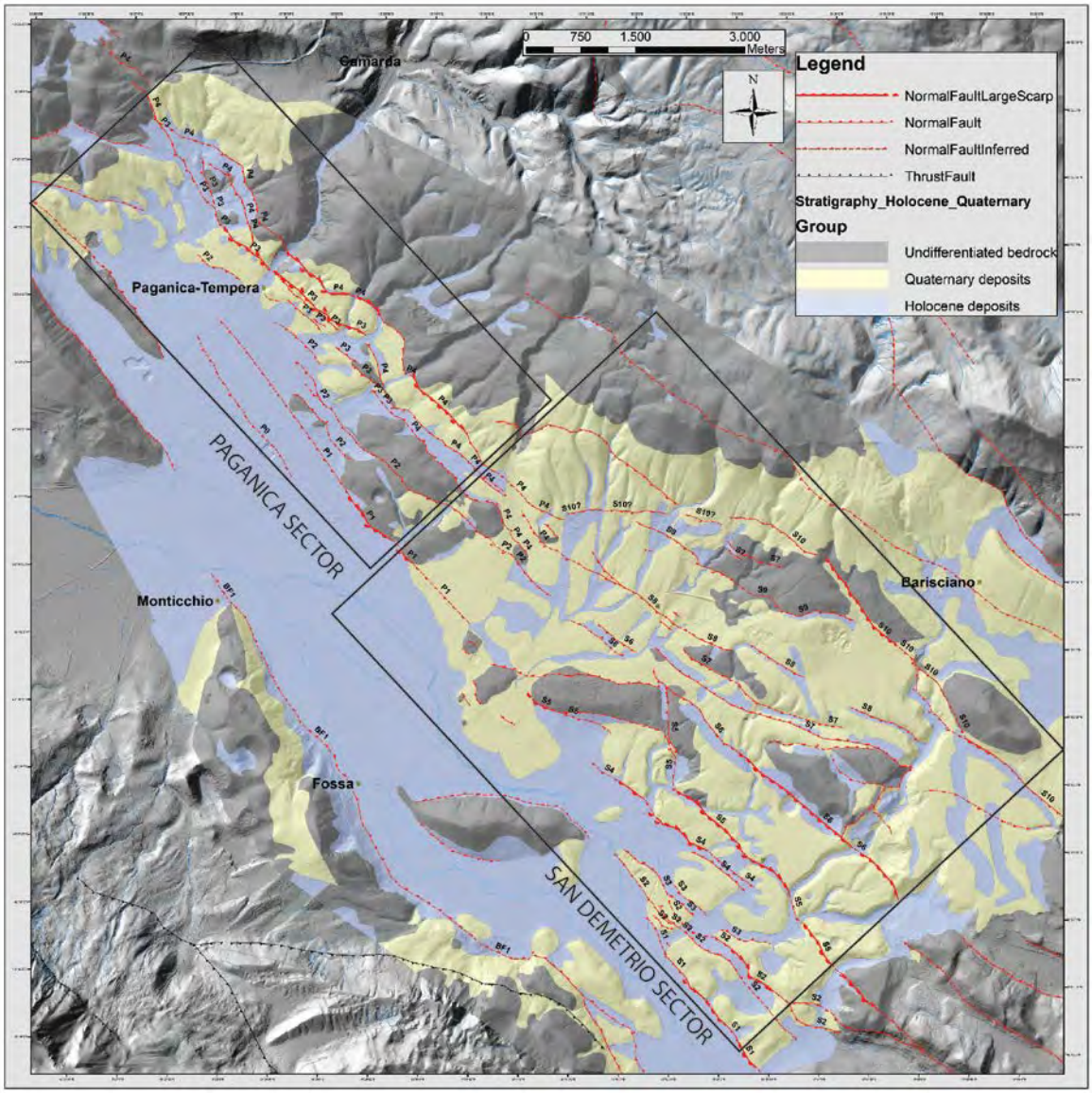

Figure 8.1 - Map of the PSDFS showing the structural arrangement of the fault system and the extent and age of outcropping Quaternary and Holocene deposits. Boxes enclose the Paganica and San Demetrio sectors.

8.2 PSDFS length

Tectonic geomorphological analysis allowed also us to define the extent of the fault system at the surface as well as a first-order hierarchy, in terms of relative contribution to the net deformation, among the numerous fault splays that characterize the morphological expression of the PSDFS.

The complexity of the fault system setting makes it difficult to define its actual extent and boundaries on the basis of classical geomorphological and structural approaches (e.g. Schwartz and Coppersmith, 1984; Burbank and Anderson, 2001). To overcome this difficulty we built up an along-strike plot of all the morphological throw values measured across the PSDFS (Chapter 6). This was done following the concept that, in individual normal faults, the deformation tends to distribute along strike following a typical symmetric bow-shaped curve (see Chapter 2). By summing

up the along-strike contribution of all the single fault splays of the PSDFS, we obtained the morphological throw graph of figure 8.2 (yellow solid line) that actually approximates a symmetric bell-shaped curve. On this basis the tips of the curve represent the fault boundaries that can be considered stationary at least for the last morphogenic phase of landform shaping (possibly up to ~2 Ma). The northern boundary is placed near the village of Collebrincioni, where a series of WNW trending, right, en echelon splays occur and may act as a structural boundary. The southern boundary is set about 3 km south of the latitude of San Demetrio nè Vestini village, and coincides with the southern edge of the Quaternary basin and with a subtle deviation of the trend of the tectonic structures with respect to the average PSDFS strike, as shown by fault splays to the south of the Ripa valley.

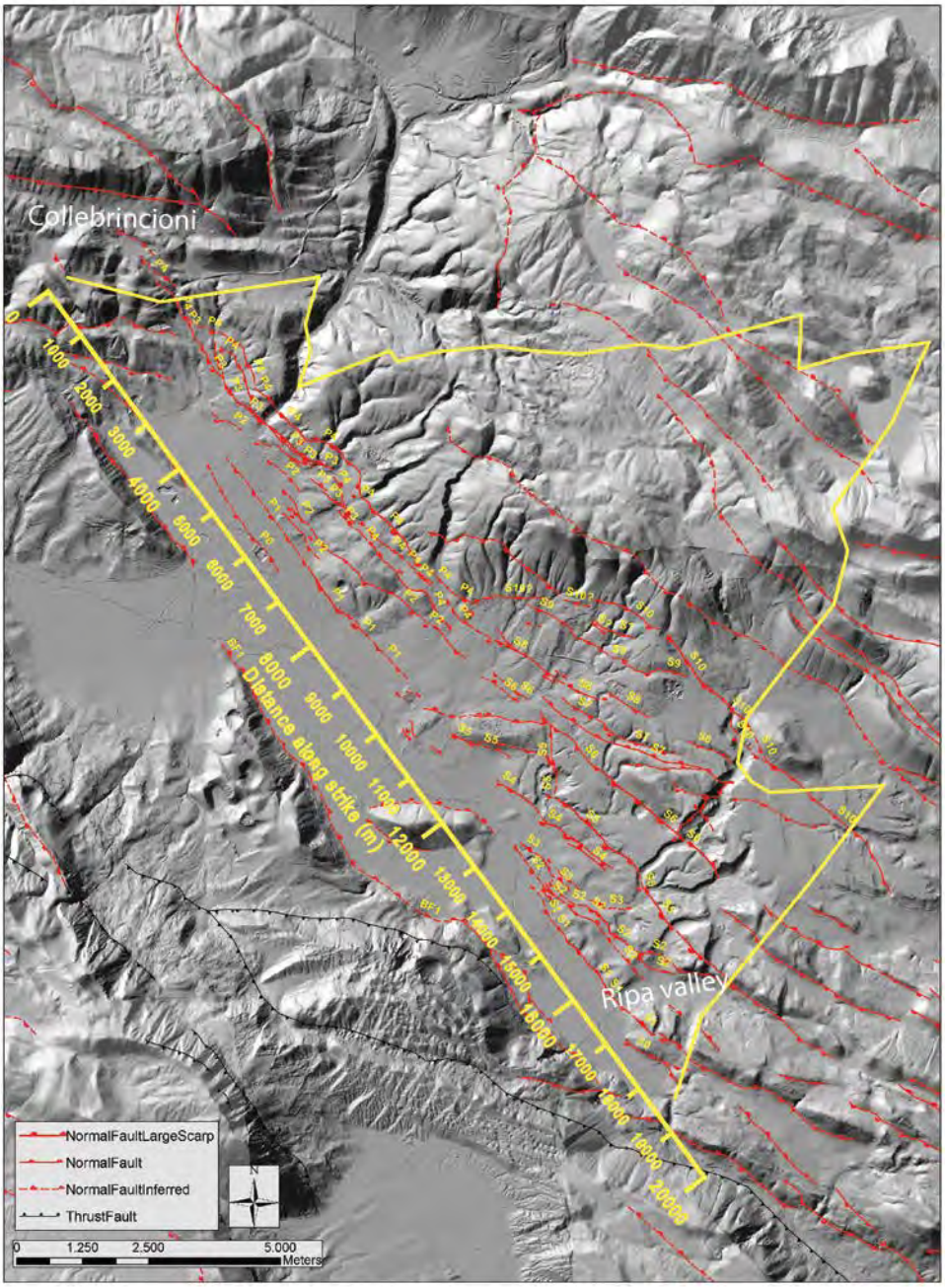

Figure 8.2 – overall length of the PSDFS as defined by the plot of the morphological throws.

Under this interpretation, the resulting overall length of the PSDFS approximates 19 km. This is in good agreement with the length of the seismogenic fault that ruptured at depth during the April 6 earthquake, as defined by coseismic seismologic and geodetic observations (from 15 to 18 km, see Chapter 3).

Primary coseismic surface ruptures observed in 2009 occurred only along a 3 km-long part of the Paganica sector and in few sparse locations along the central and northern part of the fault system. Therefore, the 19 km-long geomorphic expression of the fault cannot have been built up by repeated 2009-type earthquakes, but in the past, the system should have ruptured the surface for all its length.

Thus, larger magnitude earthquakes or earthquakes with a different and more superficial slip distribution with respect to the 2009 event, are expected on the PSDFS.

8.3 Partitioning of deformation along the PSDFS

The overall symmetric bell-shaped curve of figure 8.3 suggests a persistence of the deformation through time and for the whole length of the fault system, although partitioned across a narrow zone (Paganica sector) and a wider zone (San Demetrio sector).

The plot of figure 8.3 shows the different contribution of individual fault splays to the overall deformation across the PSDFS.

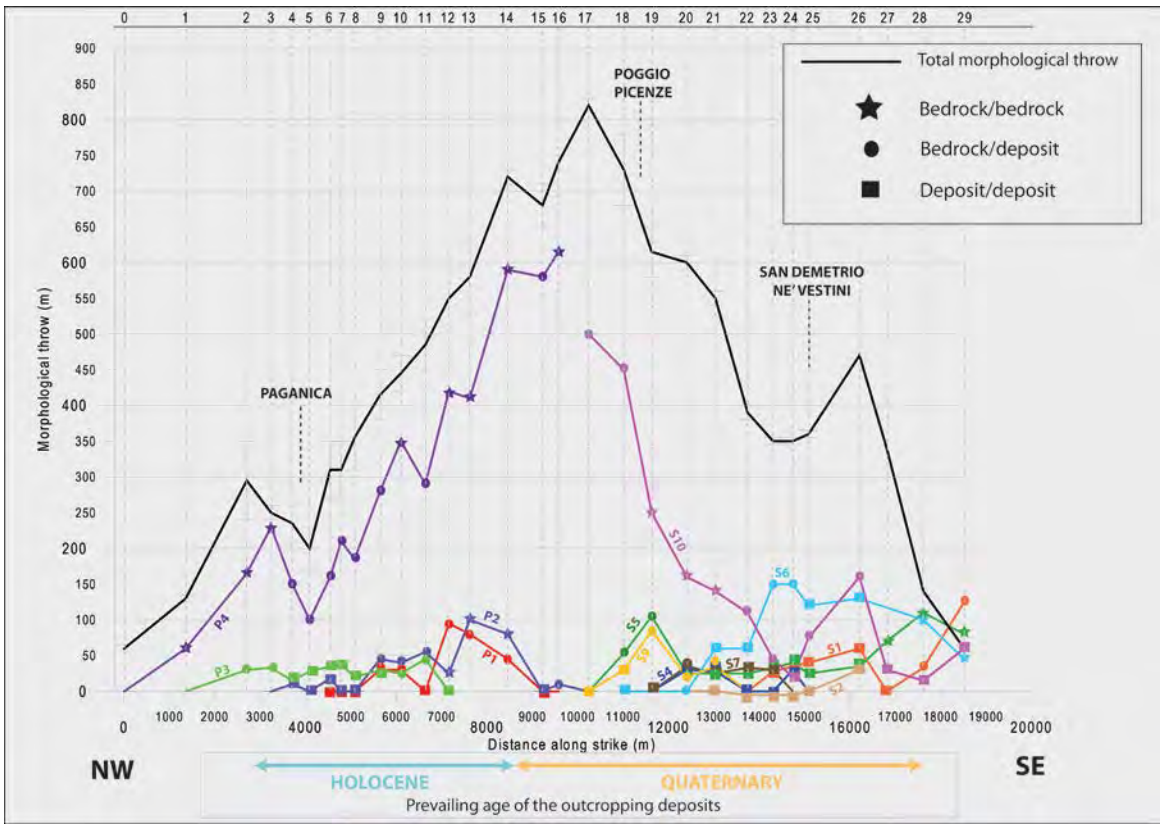

Figure 8.3 - Along-strike plot of the morphological throws measured from the topographic profiles across the PSDFS (see also Chapter 6).

Most of the deformation in the area is accommodated by the two easternmost basin-bounding fault splays (P4 and S10) that, because affect mainly the geomorphic markers carved in bedrock, cannot be dated and confidently used to define the present fault system behavior. Conversely, among the fault splays affecting mainly the Quaternary deposits (last ~2Ma), an important contribution to the overall deformation is accommodated by fault splays P3 and S6.

Interestingly, these two fault splays are quite aligned in map view and share a similar prominent geomorphic expression. The lack of clear surface evidence of fault-related deformation between the two splays in the central portion of the PSDFS can be justified by the intersection with an alluvial fan that had a Late Pleistocene (ca. 27 ka – Chapter 7) strong activity that buried/eroded the missing fault scarp (see also Chapter 7 – ERT profiling at San Gregorio site).

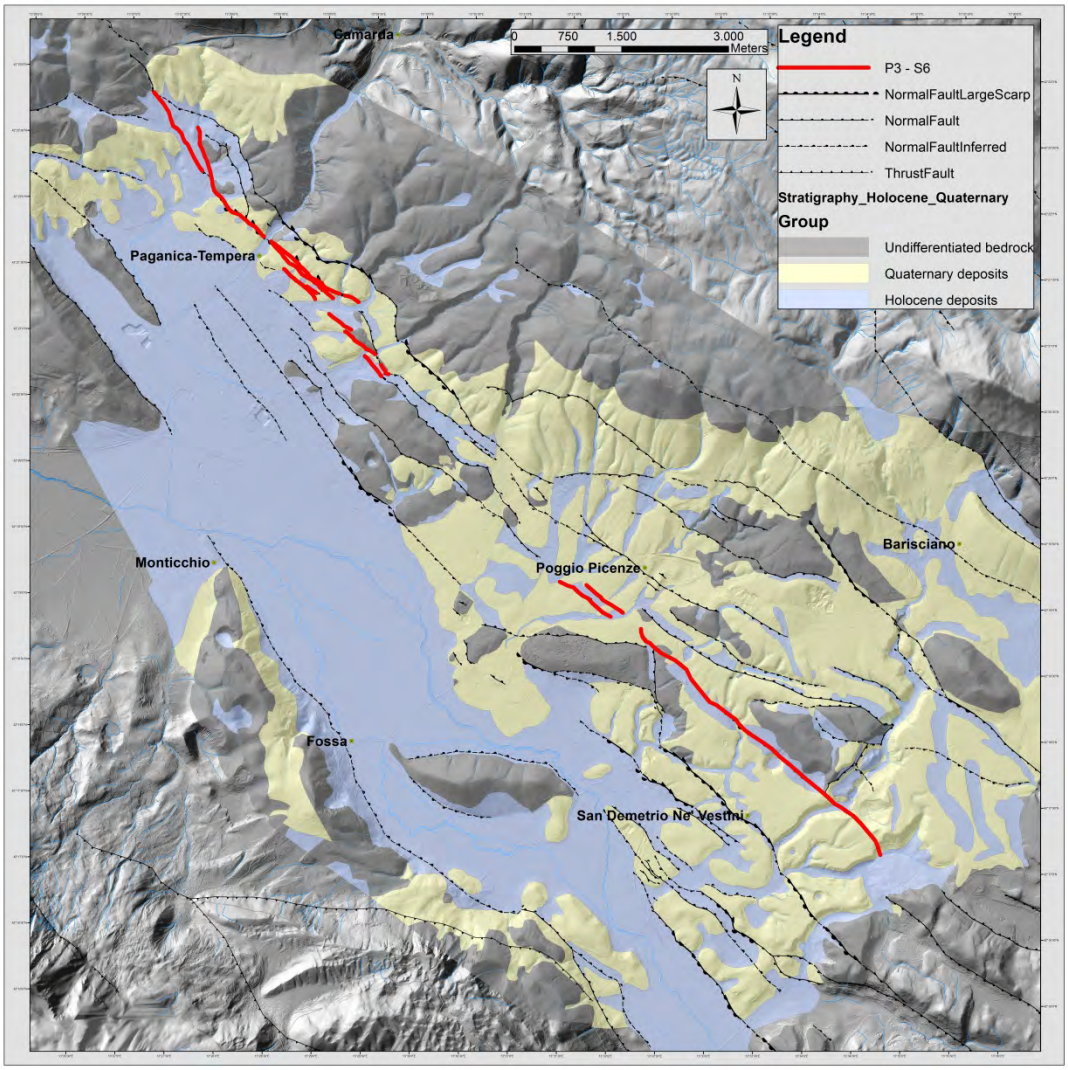

Figure 8.4 - - Map of the PSDFS showing the possible linkage of fault splays P3 (to the northwest) and S6 (to the southeast).

The linkage of these two fault splays may represent the most active surface trace of the PSFDS during the Quaternary.

This hypothesis is also supported by the fact that the 3 km-long 2009 coseismic rupture occurred along fault splay P3.

However, in the Paganica sector, the high-resolution shallow seismic profiling (Chapter 7) shows the presence of two buried SW-dipping fault splays (red dotted

lines in figure 8.5 and P0 and P1 in the map of figure 8.1) in the Paganica sector that involve bedrock and basin infill deposits with throw values of ~100 m and ~150 m.

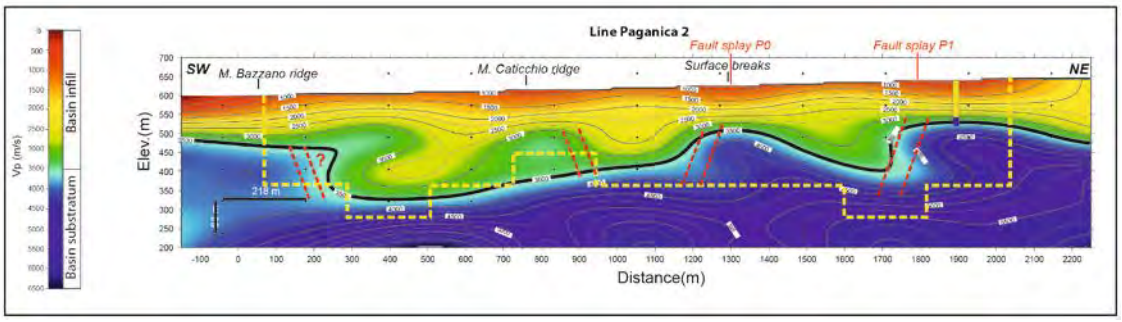

Figure 8.5 - Long wavelength Vp model of line p2. The figure also shows the location of the borehole reaching the bedrock at -78 m depth and the location of some of the discontinuous surface breaks reported in Chapter 3.

Interestingly, the surface projection of fault splay P0 coincides with the occurrence of some aligned but highly discontinuous 2009 coseismic surface ruptures (figure 8.6 – see also Chapter 3).

In this light, fault splay P3 may not be the only presently active trace within the narrow deformation zone of the Paganica sector, but we should also take into account the deformation accommodated by the 2 SW-dipping buried fault splays (P0 and P1). The latter splays do not show a clear morphological expression likely because of their location in the active hangingwall of the fault system and the high sedimentation rates.

The subsurface geometry in this sector of the PSDFS hangingwall appears therefore to be more complicated than expected from surface geomorphological and geological investigations.

8.4 Slip-rate

Vertical slip-rates were defined for different time intervals in the Quaternary on the basis of the integration of all the data resulting from paleoseismological, geomorphological, geophysical and geological investigation. Table 8.1 summarizes the results from each approach.

Paleoseismological investigations show evidence for the occurrence of repeated Late Pleistocene-Holocene surface faulting events and allowed for vertical slip-rate estimates at a very short time scale with respect to the whole ~2 Ma long time interval investigated. These data are available only for the Paganica sector of the PSDFS where we dug exploratory trenches after the April 6, 2009 shock. A Late Holocene (last 5 ka) vertical slip-rate was estimated by using the age and throws of individual paleoearthquakes recognized on the studied trench walls and resulted in an average value of 0.27-0.52 mm/yr.

Furthermore, a Late Holocene vertical slip-rate at Mo'Tretteca site of ~0.4 mm/yr was obtained for the past ~1000 years by means of high-resolution petrophysical

correlations and the age of the deposits, thus in good agreement with those obtained from the classical paleoseismological approach.
Furthermore, data from the trenches allowed us also to calculate a vertical slip-rate for the Late Pleistocene of 0.21-0.25 mm/yr for the Paganica sector of the PSDFS.
Geomorphological, geophysical and geological investigations were integrated to estimate long-term slip-rates for the PSDFS at different time intervals:
A) 1.8 Ma – 781 ka: Bottom of the Early Pleistocene;
B) 1.8 Ma – 781 ka: Top of the Early Pleistocene;
C) 781 - 561$\pm$2 ka: Bottom of the Middle Pleistocene;
D) 561$\pm$2 - 172$\pm$12 ka: Top of the Middle Pleistocene.
For each time interval we estimated vertical slip-rates across transects crossing most of the fault splays affecting the deposits belonging to that specific time-interval, being aware of the fact that we may have missed some deformation (lack of information, erosion, etc.). Transects are schematically represented in figure 8.6 as light shaded areas.
The slip-rates estimated across these transects can be considered as representative of the actual strain across the PSDFS. This is both because a common decrease of the slip from depth to surface, but also because, in this case, at the surface the strain tends to be distributed among parallel fault splays, whereas at depth it concentrates on a narrow zone (according to the modeling of the 2009 earthquake causative fault). Therefore, the strain accommodated by the PSDFS, should be derived by the sum of the relative contribution of each fault splay (i.e. transects) and represent a minimum.
Vertical slip-rates fall in the following ranges and are reported in bold in table 8.1:

- Period A: 0.1 - 0.54 mm/yr;
- Period B: 0.14 - 0.58 mm/yr;
- Period C: 0.15 - 0.54 mm/yr;
- Period D: 0.09 - 0.47 mm/yr;

When well-constrained throws and ages were available also for individual fault splays, we estimated vertical slip-rates associated with individual faults (see table 8.1 – regular fonts and figure 8. 6).
Although slip-rates shown in table 8.1 were estimated by means of methods operating at very different temporal resolutions and across different time intervals (i.e. paleoseismology vs. Quaternary geology), the obtained values are well comparable.
Given the consistency both in time and space among the vertical slip-rates across the system, to obtain an overall average Quaternary vertical slip-rate of 0.22 – 0.39 mm/yr for the PSDFS, we averaged the minimum and maximum values estimated from the transects that included most of the splays (bold values in table 8.1).
All the vertical slip-rates were converted into slip-rates on the fault plane and into extension-rates. This is done under the assumption that we are dealing with a simple regular structure and we know its dip angle. As for this latter parameter, taking into account all the information coming from subsurface geophysical imaging

(chapter 7) and geological investigations (chapter 6) as well as from the modeling of the 2009 earthquake causative fault (Chapter 3), we can assume an average 55° dipping fault plane as typical for the PSDFS. All the converted values are reported in table 8.1.

Following this procedure, the overall average Quaternary vertical slip-rate is converted into overall Quaternary slip-rate and extension-rate of 0.27 - 0.48 mm/yr and of 0.15 - 0.27 mm/yr, respectively.

Code	Site	Fault	Time interval	Vertical slip-rate min (mm/yr)	Vertical slip-rate max (mm/yr)	Slip-rate min (mm/yr)	Slip-rate max (mm/yr)	Extension min (mm/yr)	Extension max (mm/yr)
F	*Paganica trenches*	*P3*	*Late Holocene (last 5 ka)*	*0,27*	*0,52*	*0,33*	*0,63*	*0,19*	*0,36*
E	*Paganica trenches*	*P3*	*Late Pleistocene (30 ka)*	*0,21*	*0,25*	*0,26*	*0,30*	*0,15*	*0,17*
B1	*1 - Paganica*	*P3*	*Vall'Orsa unit - Early Pleistocene (1.8 Ma - 781 ka)*	*0,03*	*0,08*	*0,04*	*0,09*	*0,02*	*0,05*
A1	***2 - Pescomaggiore***	***P3 P2 P1 P0***	***San Nicandro unit - Early Pleistocene (1.8 Ma - 781 ka)***	***0,16***	***0,37***	***0,20***	***0,45***	***0,11***	***0,26***
B2	***2 – Pescomaggiore***	***P4 P3 P2 P1 P0***	***Vall'Orsa unit - Early Pleistocene (1.8 Ma - 781 ka)***	***0,17***	***0,38***	***0,20***	***0,47***	***0,12***	***0,27***
C1	***2 – Pescomaggiore***	***P3 P2***	***Valle Inferno unit - Middle Pleistocene (781 - 561 ka)***	***0,15***	***0,21***	***0,19***	***0,26***	***0,11***	***0,15***
A2	***3 – San Valentino***	***P1***	***San Nicandro unit - Early Pleistocene (1.8 Ma - 781 ka)***	***0,10***	***0,23***	***0,12***	***0,28***	***0,07***	***0,16***
B3	***3 – San Valentino***	***P4 P2 P1***	***Vall'Orsa unit - Early Pleistocene (1.8 Ma - 781 ka)***	***0,25***	***0,58***	***0,30***	***0,70***	***0,17***	***0,40***
B3a	*3 – San Valentino*	*P1*	*Vall'Orsa unit - Early Pleistocene (1.8 Ma - 781 ka)*	*0,11*	*0,26*	*0,14*	*0,31*	*0,08*	*0,18*
B3b	*3 – San Valentino*	*P4 P2*	*Vall'Orsa unit - Early Pleistocene (1.8 Ma - 781 ka)*	*0,14*	*0,32*	*0,17*	*0,39*	*0,10*	*0,22*
C2	***3 – San Valentino***	***P4 P2 P1***	***Valle Inferno unit - Middle Pleistocene (781 - 561 ka)***	***0,27***	***0,38***	***0,33***	***0,46***	***0,19***	***0,26***
C2a	*3 – San Valentino*	*P1*	*Valle Inferno unit - Middle Pleistocene (781 - 561 ka)*	*0,10*	*0,14*	*0,12*	*0,17*	*0,07*	*0,10*
D1	***3 – San Valentino***	***P1***	***San Mauro unit – Middle Pleistocene (561 - 172±12 ka)***	***0,09***	***0,31***	***0,11***	***0,38***	***0,06***	***0,22***
A3	***4 – Valle dell'Inferno***	***S10 - S2***	***San Nicandro unit - Early Pleistocene (1.8 Ma - 781 ka)***	***0,23***	***0,54***	***0,28***	***0,66***	***0,16***	***0,38***
A3a	*4 – Valle dell'Inferno*	*S6*	*San Nicandro unit - Early Pleistocene (1.8 Ma - 781 ka)*	*0,13*	*0,29*	*0,16*	*0,36*	*0,09*	*0,21*
A3b	*4 – Valle dell'Inferno*	*S10*	*San Nicandro unit - Early Pleistocene (1.8 Ma - 781 ka)*	*0,08*	*0,18*	*0,09*	*0,22*	*0,05*	*0,13*

B4	***4 – Valle dell'Inferno***	***S10 - S2***	***Vall'Orsa unit - Early Pleistocene (1.8 Ma - 781 ka)***	***0,14***	***0,33***	***0,18***	***0,41***	***0,10***	***0,23***
B4a	*4 – Valle dell'Inferno*	*S6*	*Vall'Orsa unit - Early Pleistocene (1.8 Ma - 781 ka)*	*0,12*	*0,27*	*0,14*	*0,33*	*0,08*	*0,19*
C3	***4 – Valle dell'Inferno***	***S10 - S5***	***Valle Inferno unit - Middle Pleistocene (781 - 561 ka)***	***0,38***	***0,54***	***0,47***	***0,65***	***0,27***	***0,38***
C3a	*4 – Valle dell'Inferno*	*S6*	*Valle Inferno unit - Middle Pleistocene (781 - 561 ka)*	*0,29*	*0,41*	*0,36*	*0,50*	*0,21*	*0,29*
C3b	*4 – Valle dell'Inferno*	*S10*	*Valle Inferno unit - Middle Pleistocene (781 - 561 ka)*	*0,05*	*0,07*	*0,06*	*0,09*	*0,04*	*0,05*
D2	***4 – Valle dell'Inferno***	***S5 - S1***	***San Mauro unit – Middle Pleistocene (561 - 172±12 ka)***	***0,34***	***0,47***	***0,42***	***0,57***	***0,24***	***0,33***
D2a	*4 – Valle dell'Inferno*	*S1*	*San Mauro unit (FLUVIAL) – Middle Pleistocene (561 - 172±12 ka)*	*0,19*	*0,31*	*0,23*	*0,38*	*0,13*	*0,22*
D2b	*4 – Valle dell'Inferno*	*S5*	*San Mauro unit (ALL. FAN)– Middle Pleistocene (561 - 172±12 ka)*	*0,13*	*0,19*	*0,15*	*0,23*	*0,09*	*0,13*

Table 8.1 - Slip-rate values for the whole Paganica-San Demetrio fault system.

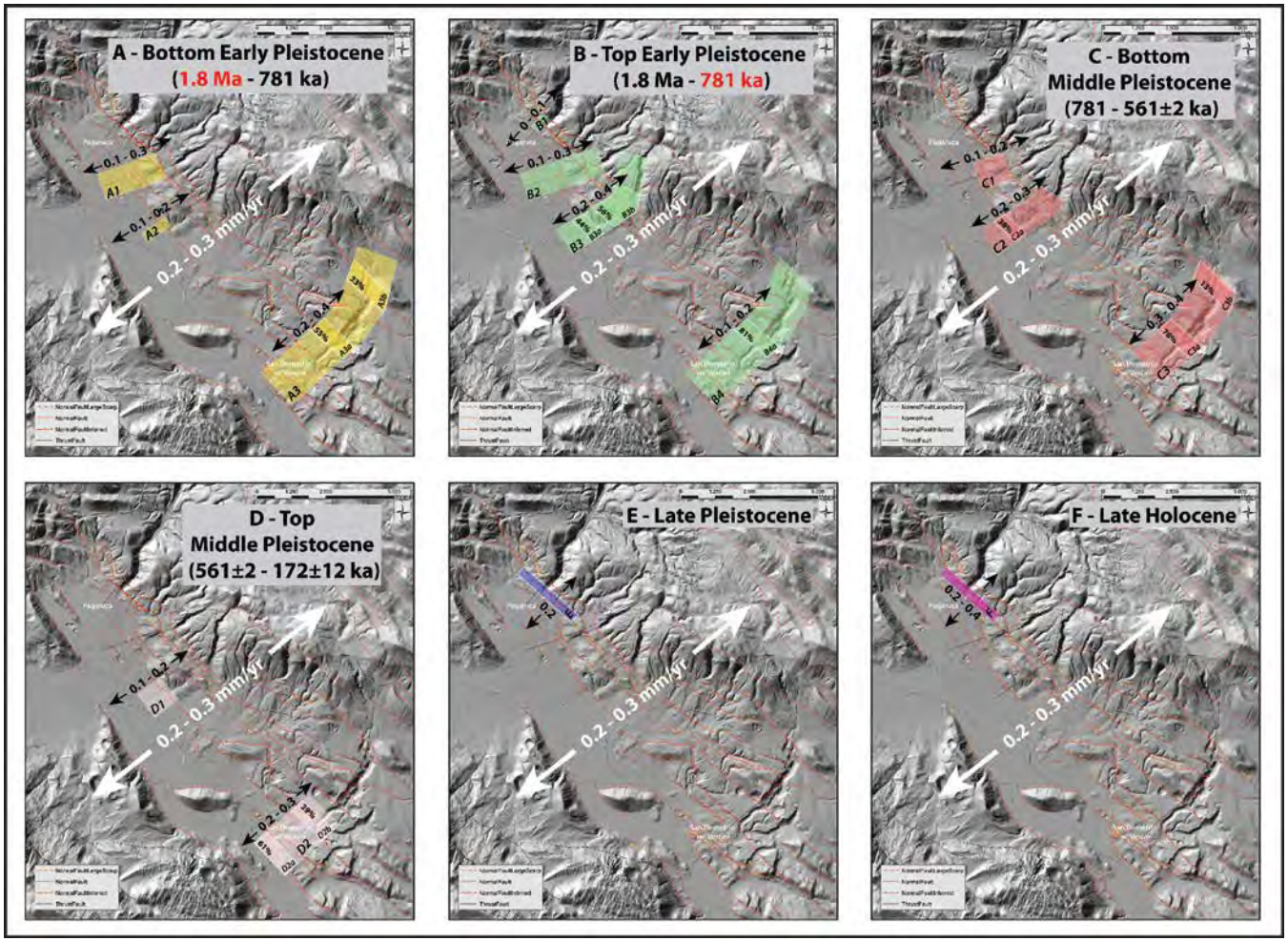

Figure 8.6 – Evolution in time and space of the extension-rates of the PSDFS. The overall average Quaternary extension-rate of the PSDFS is reported inside the white arrows and is used as a reference to analyze the relative contribution to the deformation of different sectors and splays. Light-shaded areas are the transects across which the extension-rates were estimated for each specific time-interval (keyed with a capital letter and a number that are the same in text and table 8.1). When available, individual contribution of single fault splays is reported as percentage of the extension-rate estimated in each transect(keyed with letters and a number that are the same in text and table8.1).

8.5 Slip-rates through time and space

Slip-rates were analyzed in different time windows so they are averaged from the oldest age of the displaced deposits to present. Following this approach, we identified six time intervals (table 8.1 and figure 8.6).

In the following discussion we refer to figure 8.6 and use extension-rates as representative of the component of deformation of normal faults in map view.

Taking into account all the uncertainties in the calculation of the extension rates (intrinsic in both vertical slip-rate values and average fault dip angle), in the following text and in figure 8.6 we rounded these values to the first decimal number. For example, the abovementioned overall average Quaternary extension-rate of 0.15 - 0.27 mm/yr for the whole PSDFS is reported as 0.2 - 0.3 mm/yr.

As already mentioned, because this latter value is considered as representative of the extension across the whole PSDFS (see previous section), we use it as a reference to analyze the relative contribution to the deformation of different sectors and splays. Figure 8.6 shows the specific transects where the data were collected and is subdivided in 6 boxes each one representing a different period.

Period A – Bottom of the Early Pleistocene (figure 8.6A) - In the Paganica sector the extension rates derived across transects A1 and A2 (both not including all the fault splays, e.g. P4) are slightly lower than the overall average Quaternary extension-rate. This suggests that also the splays not included in the transect were active in this period of time and thus that all the parallel splays (P0 to P4) were likely active.

In the San Demetrio sector, we note a general agreement between the overall average Quaternary extension-rate and the value estimated in transect A3 (including all the splays but S1). Moreover, taking into account the relative contribution of individual fault splays to the extension in the specific transect, we note that S6 (box A3a) and S10 (box A3b) account for 55% and 33%, respectively, that is for most of the deformation along this transect.

Period B - Top of the Early Pleistocene (figure 8.6B) - In the Paganica sector the extension-rate estimated across transects B3 and B2 is comparable to the overall average Quaternary value, suggesting that during this time interval the deformation continued to be accommodated by all the fault splays. Transect B1, crossing only a few splays, accounts only for part of the overall extension-rate, implicitly confirming the need for a contemporaneous activity of the all the fault splays. Moreover, transect B3 shows that most of the deformation is accommodated by the fault splays falling in box B3b (P2 and P4) and in box B3a (P1) accounting for 56% and 44%, respectively.

In the San Demetrio sector transect B4 (including all the splays but S1) can explain most of the overall deformation, although part of it may have already been taken by S1. Interestingly splay S6 (box B4a) contributes for the 81% of it, with a net increment with respect to the previous time interval.

Period C- Bottom of the Middle Pleistocene (figure 8.6C) - In the Paganica sector the extension-rate obtained from transect C2 (fault splays P1 – P2 and P4) is consistent

with the overall average Quaternary extension-rate whereas transect C1 (containing only P2 and P3) do not fully explain the overall extension, suggesting that all the fault splays in this sector have to be active. This is even more clear when we look at transect C2 where the individual contribution of fault splay P1 (box C2a) is 38% of the total.

In the San Demetrio sector, we note that transect A3 (including fault splays S5 to S10) satisfies the whole overall average Quaternary extension-rate. Moreover, the deformation appears to persist on fault splay S6 (box C3a) that accommodate a 78% whereas, fault splay S10 (box C3b) adjust only the 13%, reducing its importance within the system.

Period D - Bottom of the Middle Pleistocene (figure 8.6D) – In the Paganica sector there is only one extension-rate available (transect D1 containing only fault splay P1) that accounts only for part of the overall average Quaternary extension-rate, suggesting that some of the faults to the northeast continued to contribute to the extension in this period.

In the San Demetrio sector, transect D2 explains the whole overall average Quaternary extension-rate, highlighting that if the fault splays to the northeast are still active they contribute for a negligible part of the deformation. The relative contribution of individual fault splay S1 (box D2a) and S5 (box D2b) accommodated 61% and 39% of the extension, respectively, together accounting for all the deformation observed along this transect.

Period E - Late Pleistocene (figure 8.6E) – for this time interval only a rate from paleoseismology is available and only for fault splay P3 along the Paganica sector (box E). This falls in the lower part of the overall average Quaternary extension-rate, suggesting that other fault splays contributed to the extension.

Period F - Late Holocene (figure 8.6F) - similarly to time interval E, only a fault splay (P3) allows us estimating extension-rate. This latter is consistent with the overall average Quaternary extension-rate, suggesting that most of the extension is taken by P3. Consequently, fault splay P4 may be negligibly active; limited data do not allow to estimate the relative contribution of the southwestern splays (P0 and P1).

8.6 Strain migration

On the basis of the results of this work, starting from the understanding of the tectonic style and of the strain distribution on the PSDFS, we discuss the possible PSDFS evolution in time and space at the surface and discuss the possible meaning for the understanding of the fault at depth.

The distribution of the extension-rates in space and over the different time intervals shown in figure 8.6 highlight different strain distributions along the two sectors of the PSDFS during the Quaternary and suggests the occurrence of strain migration across the San Demetrio sector.

- In the Paganica sector the strain has been concentrated since Early Quaternary (~2 Ma) along the same fault zone, 1 to 2 km-wide, controlling

the basin evolution as well as the persistence of the depocenter location until present. Only during Late Holocene P4 activity may become negligible and P3, that is also the splay that ruptured in 2009, takes most of the extension.

- In the San Demetrio sector the strain at the surface has not been homogeneously distributed among all fault splays during the whole Quaternary. The presence of a wider Quaternary basin (~5 km) suggests that the inset of the deformation in Early Pleistocene occurred along the easternmost basin-bounding fault splay (S10), where the oldest tectonically displaced Quaternary deposits are found.

  With time, most of the extension migrated toward the southwestern splays. Since ~550 ka (Middle Pleistocene – figure 8.6D), most of the extension is taken by fault splays S1 to S5 and the activity of the former basin-bounding splay (S10) becomes negligible.

The fact that the Paganica sector appears mostly stationary through time and space and vice versa San Demetrio sector shows migration, finds support also by the along-strike plot of the morphological throws (figure 8.7).

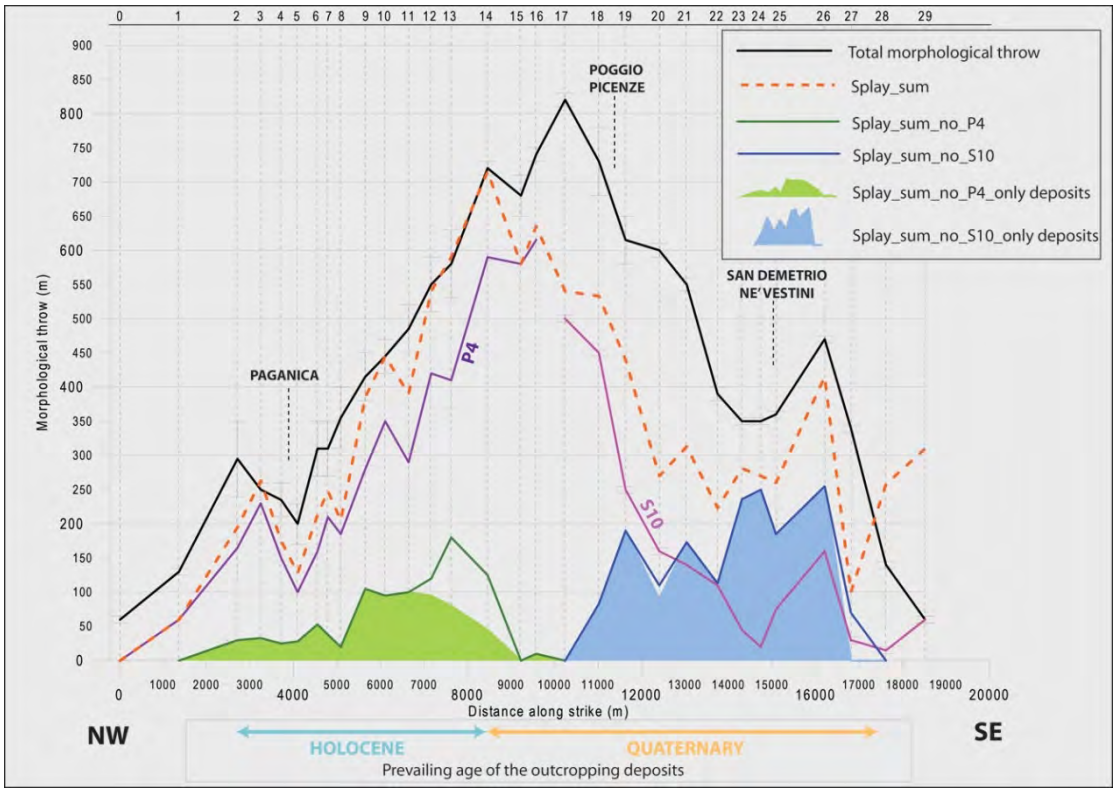

Figure 8.7 - Along-strike plot of all the morphological throw values measured from the topographic profiles. The orange dotted curve represents the sum of the relative contribution of each fault, while the green and the blue solid lines represent the sum of all the fault splays with exception of P4 and S10, respectively. Green and blue areas show the relative contribution of the splays displacing Quaternary sediments in the Paganica and San Demetrio sector, respectively.

In fact, the relative contribution to the total strain of the fault splays affecting only Quaternary deposits (green and blue areas in figure 8.7) is substantially smaller for the Paganica sector with respect to the San Demetrio sector. This is because in the

Paganica sector the deformation persisted on a narrow bend, creating a relatively small Quaternary basin, affected by few fault splays; differently, in the San Demetrio sector, the strain migration through time allowed an important deformation to be recorded by the Quaternary deposits.

8.7 Contribution to seismic hazard

As we wrote at the beginning of this thesis, the slip-rate of a fault represents a critical information for seismic hazard assessment of an area, because it describes the fault activity and its relevance with respect to nearby faults.

We estimated an overall Quaternary average slip-rate of the PSDFS of 0.27 - 0.48 mm/yr. This compares with the lower range of slip-rates observed in the area on nearby faults that is from 0.4 to 1.2 mm/yr, with intermediate values preferred, i.e. 0.6-0.8 mm/yr (Galadini and Galli, 2000; Galli et al., 2008 and references therein). This agreement suggests a similarity in behavior of the faults active in this area possibly related to a characteristic strength of the crust and of a homogeneous distribution of the extension in the area.

We can also attempt an interesting comparison between geologically and geodetically determined extension-rates.

GPS analyses of D'Agostino et al., 2011 show a contemporary deformation field over central Apennines characterized by a NE-SW oriented extension-rate of 2.7 ± 0.2 mm/yr, focused in coincidence of the belt axis.

We have seen that the overall Quaternary average slip-rate of the PSDFS (0.27 - 0.48 mm/yr) is in general agreement with the slip-rates observed in the area on nearby faults, and that this value can be translated into an extension-rate of 0.2 - 0.3 mm/yr.

Geological studies accomplished so far across central Apennines have shown the presence of 2, max 6 almost parallel active faults, with average Late Quaternary fault slip-rates estimates typically <0.5 mm/yr (Boncio et al., 2004; Roberts and Michetti, 2004; Galli et al., 2008). Only in some cases, they are slightly larger than 1 mm/yr (Pantosti et al., 1996; Galli et al., 2008).

Assuming GPS-derived extension-rates are representative and comparable over Quaternary time, and if the crustal extension is accommodated only by elastic strain distributed on several tectonic structures, to reconcile with geodetically determined rates each fault would have to accommodate 0.5–1.5 mm/yr of extension.

Thus, the extension-rate obtained by summing Late Quaternary fault displacements is generally not sufficient to accommodate the geodetic estimates.

This discrepancy may be related to different factors:

- A significant amount of elasto-plastic strain release;
- Strain produced by faults at depth that do not break at the surface (blind structures) or that produce small surface ruptures (commonly related to events with $M < 6.5$), characterized by a poor geomorphic signature (hidden structures), and thus difficult to recognize by means of geomorphological and paleoseismological investigations;

- A significant amount of strain accommodated by unknown/blind or estimated to be inactive major faults, even if such active structures usually have a clear geomorphic expression in central Italy;
- GPS data (years to decades long) may be unrepresentative of the long-term geological deformation rate.

Another key information for seismic hazard assessment is represented by the maximum expected magnitude on the fault. To obtain such information, we need to recognize and measure maximum slip per event and rupture lengths of seismogenetic faults. The overall long-term geomorphic expression of the PSDFS defines a ~19 km-long fault. The total length of the presently most active traces at surface (linking P3 and S6) reaches ~15 km (figure 8.4). Moreover, Wells and Coppersmith, 1994 indicated that surface rupture length typically is equal to 75% of the subsurface rupture length. This translates in a total fault length at depth of at least 20 km.

The fault length defined by 2009 coseismic seismologic and geodetic observations ranges from 15 to 18 km.

In summary, taking into consideration the data presented above, a ~20 km-long fault may well represent the maximum rupture length of the PSDFS.

Given this interpretation, and according to the empirical relationships among magnitude and surface rupture length (Wells and Coppersmith, 1994) we can hypothesize that the PSDFS may generate the contemporaneous rupture of the northwestern and southeastern fault splays, potentially producing a Mw≥ 6.3 earthquake.

It is worth nothing that from our paleoseismological investigations we observe that the amount and the style of deformation in past events (vertical displacement of 0.4 - 0.8 m, well-preserved colluvial wedges, large graben structures, intensive sheared zone, backtilting) suggest the occurrence of old earthquakes larger than the 2009 event (Cinti et al, 2011). The observed vertical displacements of 0.4 - 0.8 m can be converted to a slip per event on the fault plane of 0.5 – 1 m assuming an average 55° dipping fault plane as typical of the whole PSDFS. Assuming these values as representative of the average fault displacement they would account for moment magnitude earthquakes ranging between 6.5 and 6.8 (Wells and Coppersmith, 1994).

Thus, the different lengths of the PSDFS and the slip per event resulting from our paleoseismological investigations converge toward the possibility for the occurrence of past surface faulting earthquakes characterized by a moment magnitude between 6.3 and 6.8, notably larger than the 2009 event, and compatible with the M range observed in historical earthquakes in the area. The 2009 earthquake would be the smallest expected, opening the possibility that the same fault generates also more energetic events. This changes substantially the hazard of the area.

The understanding of the evolution of the PSDFS through time and space was critical to assess the seismic potential of the PSDFS. The overall picture deciphered so far highlighted the existence of a complex structural setting of the PSDFS at the surface, characterized by the presence of several parallel normal fault splays.
Looking at the geometry of the PSDFS, the identified segment boundaries and the step over separating Paganica from San Demetrio sectors, are likely related to inherited structures/discontinuities related to earlier tectonic phases.
In fact these may represent both geometrical and structural barriers to fault and slip propagation, thus influencing the development of the fault system.

Moreover, we have also shown that in the San Demetrio sector the strain has not been homogeneously distributed over time and space across the fault system and that, with time, most of the extension migrated toward the southwestern fault splays.
The abovementioned considerations are critical in terms of assessment of the seismic hazard of the area. The occurrence of strain migration, in particular, has a significant implication in terms of surface faulting hazard in the area. This topic is important because often it determines a substantial risk where urban areas and/or important infrastructures and facilities are developed or planned. This was actually the case of the 2009 L'Aquila earthquake, where buildings and lifelines located in coincidence (on top/near) of the observed coseismic surface ruptures suffered significant damages.

9 Conclusions

The L'Aquila Mw 6.3 April 6, 2009 earthquake causative fault was used as a test site to apply a multidisciplinary and multiscale-based strategy aimed at improving the normal faults seimogenic characterization, focusing mainly on slip-rate estimate as a measure of the fault activity.
This thesis integrated the application, testing, and refinement of traditional or innovative approaches aimed at providing a detailed knowledge in terms of location, geometry, and characterization of the 2009 L'Aquila earthquake source fault, and at developing a reference approach useful for extending these investigations to other seismogenetic normal faults.
In particular we performed a three steps approach:

1. paleoseismological, including a trenching and coring campaign with the excavation of 4 trenches and the realization of 2 boreholes;
2. geomorphological and geological, integrating field survey and dating of Quaternary layers by means of Optically Stimulated Luminescence (OSL), radiocarbon dating and tephrochronology together with LiDAR-derived high resolution DEM and air-photo analysis;
3. geophysical, including high resolution petrophysical correlations, electrical resistivity tomography (ERT) and shallow seismic profiling.

By a methodological point of view, the multidisciplinary and multiscale-based investigation strategy emphasizes the advantages of the joint application of different approaches and methodologies for active faults identification and characterization.
Our work suggests that each approach alone may provide sufficient information but only the application of a multidisciplinary strategy is effective in providing a proper framework of active faults and robust results. For the case of the PSDFS, the results obtained from this multidisciplinary approach are certainly unique for this portion of the Apennines.

The detailed multidisciplinary and scale-based investigations where crucial to provide a precise knowledge in terms of location, geometry and characterization of the 2009 L'Aquila earthquake source fault, that is the PSDFS.
The integration of geomorphology, geology as well as shallow geophysics, was essential to produce a geomorphological and geological map of the PSDFS and to define its tectonic style, arrangement, kinematics, extent, geometry and boundaries. A detailed geomorphological and geological map of the fault is reported in Chapter 6 and in appendix A.
At a basin-wide scale, the fault system is characterized by a complex structural setting at the surface, with several normal parallel fault splays frequently arranged in a quasi-fractal sequence of horsts and grabens of variable size. Moreover, our

investigations highlighted that the PSDFS is arranged in two main sectors: the Paganica sector to the NW and the San Demetrio sector to SE. The Paganica sector is characterized by a narrow deformation zone, with a relatively small (but deep) Quaternary basin affected by few fault splays. The San Demetrio sector is characterized by a strain distribution at the surface that is accommodated by several tectonic structures, with the system opening into a set of parallel, km-spaced fault traces that exhume and dissect the Quaternary basin.
Among the numerous tectonic structures that characterize the morphological expression of the PSDFS we were able to define a first-order hierarchy, identifying the different contribution of individual fault splays to the overall deformation across the fault system (Chapters 6 and 8). Most of the deformation of the PSDFS is accommodated by the two easternmost basin-bounding fault splays (P4 and S10) affecting mainly the bedrock. Among the fault splays affecting mainly the Quaternary deposits (last ~2Ma), an important contribution to the overall deformation is accommodated by fault splays P3 and S6.

On the basis of the long-term morphological expression of the fault system at surface and by analyzing the cumulative displacement distribution along strike, we set the fault boundaries and defined the actual extent of the PSDFS at the surface (chapter 8). This was one of the main questions raised by the occurrence of the 2009 earthquake. The resulting overall length of the PSDFS, from our multidisciplinary approach, approximates 19 km, and is in good agreement with the 15 to 18 km-long 2009 earthquake causative fault, as defined by coseismic seismologic and geodetic observations.

The integration of all the fault displacement data and age constraints resulting from paleoseismological, geomorphological, geophysical and geological investigation played a primary role in our estimate of the slip-rate of the active PSDFS. Although estimated by means of methods operating at very different temporal resolutions and across different time intervals (i.e. high-resolution petrophysical correlations vs. paleoseismology vs. Quaternary geology), the obtained slip-rates are quite comparable and thus represent a reliable dataset.
Slip-rates were estimated for different time intervals in the Quaternary, ranging from Early Pleistocene (1.8 Ma) to Late Holocene (last 5 ka) and resulted in an average Quaternary slip-rate for the PSDFS of 0.27 - 0.48 mm/yr.
This compares with the lower part of the range of slip-rates observed in the area on nearby faults that range from 0.4 to 1.2 mm/yr. This agreement suggests a similarity in behavior of the faults active in this area possibly related to a characteristic strength of the crust and of a homogeneous distribution of the extension in the area.

A part from slip-rate estimates, a further contribution of this work to the understanding of the PSDFS seismic behavior and thus of the local seismic hazard derives from estimate of the max expected magnitude for this fault on the basis of its

length and slip per event, and from the understanding of the evolution of the PSDFS through time and space for highlighting the presently active fault splays.
The length of the PSDFS as defined by its long-term geomorphological expression, as well as the slip per event resulting from our paleoseismological investigations converge toward the possibility for the occurrence on the PSDFS of past surface faulting earthquakes characterized by a moment magnitude between 6.3 and 6.8, notably larger than the 2009 event and compatible with the M range observed in historical earthquakes in the area. The 2009 earthquake would be the smallest expected, opening the possibility that the same fault generates also more energetic events. This changes substantially the hazard of the area.

On the basis of the slip-rate distribution over time and space and starting from the understanding of the tectonic style and of the strain partitioning on the PSDFS, we highlighted different strain distributions along the two sectors of the PSDFS during the Quaternary. Our results indicate that in the Paganica sector the strain has been concentrated since Early Quaternary (~2 Ma) along the same narrow fault zone, 1 to 2 km-wide, controlling the basin evolution as well as the persistence of the depocenter location until present; differently, in the San Demetrio sector, the strain at the surface has not been continuously distributed among all fault splays during the whole Quaternary. The presence of a wider Quaternary basin (~5 km) suggests the occurrence of strain migration through time, starting from the Early Pleistocene inset of the deformation along the easternmost basin-bounding fault splay and followed by a migration of the strain, with time, toward the southwestern splays. Since ~550 ka (Middle Pleistocene), most of the extension is taken by the fault splays located at the present Aterno river valley bottom and the activity of the former basin-bounding splays becomes negligible.
The understanding of the evolution of the PSDFS through time and space was critical to assess the seismic potential of the PSDFS. The occurrence of strain migration, in particular, has a significant implication in terms of surface faulting hazard in the area, because it can contribute defining the fault splays that have a higher potential to slip during future earthquakes along the PSDFS.
This topic is particularly important because often it determines a substantial risk where urban areas and/or important infrastructures and facilities are developed or planned. This was actually the case of the 2009 L'Aquila earthquake, where buildings and lifelines located in coincidence (on top/near) of the observed coseismic surface ruptures suffered significant damages (e.g. the Tempera aqueduct pipe broke because crossed by surface faulting).

In summary, the integration of traditional or innovative approaches, such as paleoseismology, geomorphology and geology, shallow geophysical investigations and high-resolution petrophysical correlations, gave compelling constraints to improve our knowledge in terms of location, geometry, and characterization of the

2009 L'Aquila earthquake source fault, and developed a reference approach useful for extending the investigation to other seismogenetic normal faults.

By a methodological point of view, this thesis was also thought to apply, test, and improve innovative methodologies and evaluate their strength or limitations. The most innovative methodology we applied, as an alternative paleoseismological tool, was based on core sampling (done at one trench site by collecting 4 cores just across the 2009 surface rupture) and laboratory analyses or also *in situ* measurements of physical properties. Applying the high-resolution petrophysical correlations method, we obtained a Late Holocene vertical slip-rate at Mo'Tretteca site of ~0.4 mm/yr. This slip-rate estimate is in good agreement with the slip-rates obtained for the same time interval from the classical paleoseismological approach. Moreover, the results from another test site (Fossa village) indicate that high-resolution petrophysical correlations were effective in reproducing the offset visible on the exposed stratigraphy, with a minimum variability with respect to the measurements performed with a conventional stratigraphic approach.
This approach seems to have a good potential for future investigations and can be an effective tool to investigate recent faulting in unconsolidated continental sediments and to estimate fault slip-rates, providing a viable alternative when sediment characteristics prevent reliable stratigraphic correlations and/or classical paleoseismological trenching is impractical and a less invasive approach is needed.

Electrical resistivity tomography (ERT) and shallow seismic profiling complemented the geomorphological and geological investigations and were effective in imaging the position and geometry of the faults splays and, in some cases, in estimating the fault throw.

Classical geomorphological and geological investigations took advantages of the availability of high-resolution (1 m) topographic data derived from the elaboration and analysis of an airborne LiDAR survey of the area. This sustantially increased our confidence to identify and map the numerous faults splays of the PSDFS through an enanched visualization of the morphological features related to faulting activity.

Moreover, the integration of Optically Stimulated Luminescence (OSL) dating with ^{14}C and tephrochronology, as well as with archeological evaluation of pottery shards, allowed us to develop a chronological framework and to obtain new and essential age constraints for the observed displacements/offsets.

References

- Adams, K. D. and S. G. Wesnousky (1999), Surficial characteristics, soil development and regional Shoreline correlation, Geomorphology 30: 357-392.
- Agenzia per la Protezione dell'Ambiente ed i servizi Tecnici (APAT), Servizio Geologico d'Italia (2006), foglio 359 L'Aquila. Carta Geologica d'Italia alla scala 1:50000. S.EL.CA., Firenze, Italy.
- Akinci, A., F. Galadini, D. Pantosti, M. Petersen, L. Malagnini and D. Perkins (2009), Effect of time dependence on probabilistic seismic-hazard maps and deaggregation for the central Apennines, Italy, Bull. Seismol. Soc. Am., 99, 585–610. doi:10.1785/0120080053.
- Akinci, A., L. Malagnini and F. Sabetta, F. (2010), Characteristics of the strong ground motions from the 6 April 2009 L' Aquila earthquake, Italy, *Soil Dynamics and Earthquake Engineering* 30, 320- 335.
- Anderson, E.M., The dynamics of faulting, Trans. Edinburgh Geol. Soc., 8 (3), 387-402, 1905.
- Anderson, E.M., The Dynamics of Faulting and Dyke Formation With Application to Britain, 2nd ed., 206 pp., Oliver and Boyd, Edinburgh, 1951.
- Angelier, J. (1994) Fault slip analysis and palaeostress reconstruction. In Hancock, P.L. (ed.) Continental Deformation, pp. 53– 100. Pergamon Press, Tarrytown, NY.
- Anzidei, M., E. Boschi, V. Cannelli, R. Devoti, A. Esposito, A. Galvani, D. Melini, G. Pietrantonio, F. Riguzzi, V. Sepe and E. Serpelloni (2009), Coseismic deformation of the destructive April 6, 2009 L'Aquila earthquake (central Italy) from GPS data, Geophys. Res. Lett., 36, L17307. doi:10.1029/2009GL039145.
- Amos, C. B., K. I. Kelson, D. H. Rood, D. T. Simpson and R. S. Rose (2010), Late Quaternary slip rate on the Kern Canyon Fault at Soda Spring, Tulare County, California, Lithosphere, 2(6):411-417.
- Arrowsmith, J. R., O. Zielke (2009). Tectonic geomorphology of the San Andreas Fault zone from high resolution topography: An example from the Cholame segment, Geomorphology, doi:10.1016/j.geomorph.2009.01.002.
- Atzori, S., I. Hunstad, M. Chini, S. Salvi, C. Tolomei, C. Bignami, S. Stramondo, E. Trasatti, and A. Antonioli (2009), Finite fault inversion of DInSAR coseismic displacement of the 2009 L'Aquila earthquake (central Italy), Geophys. Res. Lett., 36, L15305. doi:10.1029/ 2009GL039293.
- Bagnaia, R., A. D'Epifanio, and S. Sylos Labini (1992), Aquila and sub-aequan basins: an example of Quaternary evolution in central Apennines, Italy, Quat. Nova, II, 187–209.
- Begg, J. G. and V. Mouslopoulou (2010), Analysis of late Holocene faulting within an active rift using lidar, Taupo Rift, New Zealand. Journal of Volcanology and Geothermal Research, 190, 152–167, doi:10.1016/j.jvolgeores.2009.06.001.
- Bertini T., Bosi C. (1993). La tettonica quaternaria della conca di Fossa (L'Aquila). Il Quaternario (Italian Journal of Quaternary Science) 6, 293- 314.
- Boncio, P., G. Lavecchia and B. Pace (2004), Defining a model of 3D seismogenic sources for Seismic Hazard Assessment applications: the case of central Apennines (Italy), J. Seismol., 8(3), 407–425.

- Boncio, P., A. Pizzi, F. Brozzetti, G. Pomposo, G. Lavecchia, D. Di Naccio and F. Ferrarini (2010), Coseismic ground deformation of the 6 April 2009 L'Aquila earthquake (central Italy, Mw6.3), Geophys. Res. Lett., 37, L06308, doi:10.1029/2010GL042807.
- Boschi, E., D. Giardini, D. Pantosti, G. Valensise, R. Arrowsmith, P. Basham, R. Bürgmann, A.J. Crone, A. Hull, R.K. McGuire, D. Schwartz, K. Sieh, S.N. Ward and R.S. Yeats (1996). New trends in active faulting studies for seismic hazard assessment. Annali di Geofisica, XXXIX, 1301-1307.
- Bronk Ramsey, C. (2008). Deposition models for chronological records. Quaternary Science Reviews, 27(1-2), 42-60.
- Brunori, C.A., Civico, R., Cinti, F.R., Ventura, G., (2012), Characterization of active fault scarps from LiDAR data: a case study from Central Apennines (Italy), submitted to International Journal of Geographical Information Science
- Burbank, D. W., & Anderson, R. S. (2001). Tectonic Geomorphology. Oxford: Blackwell Science, 274 p.
- Caputo, R., S. Piscitelli, A. Oliveto, E. Rizzo and V. Lapenna (2003), The use of electrical resistivity tomographies in active tectonics: Examples from the Tyrnavos Basin, Greece, *J. Geodyn.*, *36*, 19–35, doi:10.1016/S0264-3707(03)00036-X.
- Cartwright, J.A., Trudgill, B.D., Mans®eld, C.S., 1995. Fault growth by segment linkage Ð an explanation for scatter in maximum displacement and trace length data from the Canyonlands grabens of SE Utah. Journal of Structural Geology 17, 1319±1326.
- Caskey, S. J., S. G. Wesnousky, P. Zhang and D. B. Slemmons (1996), Surface faulting of the 1954 Fairview Peak (MS 7.2) and Dixie Valley (MS 6.8) earthquakes, central Nevada, Bulletin of the Seismological Society of America, Jun 1996; 86: 761 – 787.
- Cheloni, D., N. D'Agostino, E. D'Anastasio, A. Avallone, S. Mantenuto, R. Giuliani, M. Mattone, S. Calcaterra, P. Gambino, D. Dominici, F. Radicioni and G. Fastellini (2010), Coseismic and initial post-seismic slip of the 2009 Mw6.3 L'Aquila earthquake, Italy, from GPS measurements, Geophys. J. Int, 181, 1539-1546, doi:10.1111/j.1365-246x.2010.04584.x.
- Chiarabba, C., L. Jovane and R. Di Stefano (2005), A new view of Italian seismicity using 20 years of instrumental recordings, Tectonophysics, 395, 251–268, doi:10.1016/j.tecto.2004.09.013.
- Chiarabba, C., A. Amato, M. Anselmi, P. Baccheschi, I. Bianchi, M. Cattaneo, G. Cecere, L. Chiaraluce, M. G. Ciaccio, P. De Gori, G. De Luca, M. Di Bona, R. Di Stefano, L. Faenza, A. Govoni, L. Improta, F. P. Lucente, A. Marchetti, L. Margheriti, F. Mele, A. Michelini, G. Monachesi, M. Moretti, M. Pastori, N. Piana Agostinetti, D. Piccinini, P. Roselli, D. Seccia and L. Valoroso (2009), The 2009 L'Aquila (central Italy) Mw6.3 earthquake: main shock and aftershocks, Geophys. Res. Lett., 36, L18308, doi:101029/2009GL039627.
- Cinti, F. R., L. Faenza, W. Marzocchi and P. Montone (2004), Probability map of the next large earthquakes in Italy, G Cubed, 5, 1. doi:10.1029/2004GC000724.
- Cinti, F.R., Pantosti, D., De Martini, P.M. Pucci, S., Civico, R., Pierdominici, S., Cucci, L., Brunori, C.A., Pinzi, S. and Patera, A., (2011), Evidence for surface faulting events along the Paganica fault prior to The 6 April 2009 L'Aquila Earthquake Central Italy. J. Geophys. Res, 116, B07308, doi:10.1029/2010jb007988.
- Cirella, A., A. Piatanesi, M. Cocco, E. Tinti, L. Scognamiglio, A. Michelini, A. Lomax and E. Boschi (2009), Rupture history of the 2009 L'Aquila (Italy) earthquake from non-linear

joint inversion of strong motion and GPS data, Geophys. Res. Lett., 36, L19304. doi:10.1029/2009GL039795.
- Collettini C., Sibson R.H. 2001, Normal faults, normal friction?: Geology, v. 29,p. 927–930, doi: 10.1130/0091-7613(2001)029<0927:NFNF>2.0.CO;2.
- CPTI Working Group (2004), Catalogo Parametrico dei Terremoti Italiani, versione 2004 (CPTI04), INGV, Bologna. Available at: http://emidius.mi.ingv.it/CPTI04/.
- Cunningham, D., S. Grebby, K. Tansey, A. Gosar and V. Kastelic (2006) Application of airborne LiDAR to mapping seismogenic faults in forested mountainous terrain, southeastern Alps, Slovenia, Geophys. Res. Lett., 33, L20308, doi:10.1029/2006GL027014.
- Davis, G.H., and Reynolds, S.J., 1996, Structural Geology of Rocks and Regions (2nd Edition): New York, John Wiley and Sons, Inc., 776 p
- D'Addezio, G., E. Masana, D. Pantosti (2001), The Holocene paleoseismicity of the Aremogna-Cinque Miglia Fault (central Italy), J. Seismol., 5, 181-205.
- Nicola D'Agostino, Sergio Mantenuto, Elisabetta D'Anastasio,Roberta Giuliani, Maurizio Mattone, Stefano Calcaterra, Piera Gambino, and Luciano Bonci, (2011) Evidence for localized active extension in the central Apennines (Italy) from global positioning system observationsGeology, April 2011, v. 39, p. 291-294, doi:10.1130/G31796.1
- DeLong, S. B., G. E. Hilley, M. J. Rymer and C. Prentice (2010). Fault zone structure from topography: Signatures of en echelon fault slip at Mustang Ridge on the San Andreas Fault, Monterey County, California, Tectonics, 29, TC5003, doi:10.1029/2010TC002673.
- Dietrich W. E., D. Bellugi and R. R. Asua (2001), Validation of the Shallow Landslide Model, SHALSTAB, for Forest Management. In Land Use and Watershed: Human Influence on Hydrology and Geomorphology in Urban Forest Areas. Water Science Application. AGU Vol., 2, 195-227.
- Dorsey,R. J., B. A. Housen, S. U. Janecke, C.M. Fanning and A. L.F. Spears (2011), Stratigraphic record of basin development within the San Andreas fault system: Late Cenozoic Fish Creek–Vallecito basin, southern California, Geological Society of America Bulletin, May 2011, v. 123, no. 5-6, p. 771-793, doi:10.1130/B30168.1
- Doser, D. I. (1986), Earthquake processes in the Rainbow Mountain-Fairview Peak-Dixie Valley, Nevada region 1954-1959, J. Geophys. Res., 91, 12,572-12,586.
- Dramis, F. (1983), Morfogenesi di versante nel Pleistocene superiore in Italia: i depositi detritici stratificati, Geografia Fisica e Dinamica Quaternaria, 6, 180-182.
- Dramis, F., A. M. Blumetti (2005), Some considerations concerning seismic geomorphology and paleoseismology, Tectonophysics, 408, 1-4, 177-191, doi:10.1016/j.tecto.2005.05.032.
- Emergeo Working Group (2010), Evidence for surface rupture associated with the Mw 6.3 L'Aquila earthquake sequence of April 2009 (central Italy), Terra Nova, 22, 1, 43-51, doi: 10.1111/j.1365-3121.2009.00915.x.
- Falcucci, E., S. Gori, E. Peronace, G. Fubelli, M. Moro, M. Saroli, B. Giaccio, P. Messina, G. Naso, G. Scardia, A. Sposato, M. Voltaggio, P. Galli and F. Galadini (2009), The Paganica Fault and surface coseismic ruptures caused by the 6 April 2009 earthquake (L'Aquila, central Italy), Seism. Res. Lett, 80, 6, 940-950.
- Frankel, K. L., J. F. Dolan, R. C. Finkel, L. A. Owen and J. S. Hoeft (2007). Spatial variations in slip rate along the Death Valley-Fish Lake Valley fault system determined from LiDAR topographic data and cosmogenic 10Be geochronology, Geophys. Res. Lett., 34, L18303, doi:10.1029/2007GL030549.

- Friedrich, A., et al., Comparison of geodetic and geologic data from the Wasatch region, Utah, and implications for the spectral character of Earth deformation at periods of ten to ten million years, J. Geophys. Res., 108, doi:10.1029/2001JB000682, in press, 2003.
- Gabriel, A. K., R. M. Goldstein, and H. A. Zebker (1989), Mapping small elevation changes over large areas: Differential interferometry, J. Geophys. Res., 94, 9183–9191, doi:10.1029/JB094iB07p09183.
- Galadini, F. and P. Galli (1999), The Holocene paleoearthquakes on the 1915 Avezzano earthquake faults (central Italy): implications for active tectonics in the central Apennines, Tectonophysics, 308, 1-2, 143-170, doi:10.1016/S0040-1951(99)00091-8.
- Galadini F., Galli P. (2000). Active tectonics in the central Apennines (Italy) Input data for seismic hazard assessment. Nat Hazards 22, 225-270.
- Galadini, F. and P. Galli (2003), Paleoseismology of silent faults in the Central Apennines (Italy): the Mt. Vettore and Laga Mts. Faults, Ann. Geophys., 46, n. 5, 815-836.
- Galadini, F., P. Galli and M. Moro (2003), Paleoseismology of silent faults in the Central Apennines (Italy): the Campo Imperatore Fault (Gran Sasso Range Fault System), Ann. Geophys., 46, 793–813.
- Galli, P., F. Galadini, M. Moro and C. Giraudi (2002), New paleoseismological data from the Gran Sasso d'Italia area (central Apennines), Geophys. Res. Lett., 29, 38.1–38.4. doi:10.1029/ 2001GL013292.
- Galli P., Galadini F., Pantosti D. (2008). Twenty years of paleoseismology in Italy. Earth-Science Rev. 88, 89-117.
- Galli, P. and R. Camassi, eds. (2009), Report on the effects of the Aquilano earthquake of 6 April 2009; Dipartimento della Protezione Civile Istituto Nazionale di Geofisica e Vulcanologia QUEST Team, http://www.mi.ingv.it/eq/090406/quest_eng.html.
- Galli, P., B. Giaccio, P. Messina (2010), The 2009 central Italy earthquake seen through 0.5 Myr-long tectonic history of the L'Aquila faults system, Quaternary Science Reviews, 29, 3768-3789, doi:10.1016/j.quascirev.2010.08.018.
- Gasperini, P., G. Vannucci, D. Tripone and E. Boschi (2010), The location and sizing of historical earthquakes using the attenuation of macroseismic intensity with distance, Bull. Seism. Soc. Am., 100, 5A, 2035-2066, doi:10.1785/0120090330.
- Glenn, N. F., D. R. Streutker, D. J. Chadwick, G. D. Thackray, S. J. Dorsch (2006), Analysis of LiDAR-derived topographic information for characterizing and differentiating landslide morphology and activity, Geomorphology, Volume 73, Issues 1-2, Pages 131-148, ISSN 0169-555X, 10.1016/j.geomorph.2005.07.006.
- Gruppo di Lavoro M.P.S. (2004), Redazione della mappa di pericolosità sismica prevista dall'Ordinanza PCM del 20 marzo 2003, Rapporto Conclusivo per il Dipartimento della Protezione Civile, INGV, Aprile 2004, 65pp. + 5 appendici. Available at: http://zonesismiche.mi.ingv.it/.
- Haugerud, R. A., D. J. Harding, S. Y. Johnson, J. Harless, C. S. Weaver and B. L. Sherrod, (2003), High-resolution lidar topography of the Puget Lowland, Washington - A bonanza for earth science: GSA Today, v. 13, no. 6, p. 4–10.
- Hasegawa, H., H. P. Sato and J. Iwahashi (2007), Continuous Caldera Changes in Miyakejima Volcano after 2001. Bulletin of the GSI, 54, 60-64.
- Hilley, G. E., S. DeLong, C. Prentice, K. Blisniuk and J. R. Arrowsmith (2010), Morphologic dating of fault scarps using airborne laser swath mapping (ALSM) data, Geophys. Res. Lett., 37, L04301, doi:10.1029/2009GL042044.

- Improta, L., L. Ferranti, P. M. De Martini, S. Piscitelli, P. P. Bruno, P. Burrato, R. Civico, A. Giocoli, M. Iorio, G. D'addezio and L. Maschio (2010), Detecting young, slow-slipping active faults by geologic and multidisciplinary high-resolution geophysical investigations: A case study from the Apennine seismic belt, Italy. J. Geophys. Res., 115, B11307, doi:10.1029/2010JB000871.
- Jackson J.A., White N.J. 1989, Normal faulting in the upper continental crust: Observations from regions of active extension: Journal of Structural Geology, v.11, p. 15–36, doi: 10.1016/0191-8141(89)90033-3.
- Jackson, J. and Blenkinsop, T. (1993). The Malawˆi earthquake of March 10, 1989: Deep faulting within the east African rift system. Tectonics 12(5): doi: 10.1029/93TC01064. issn: 0278-7407.
- Jackson, J., and T. Blenkinsop (1997), The Bilila-Mtakataka fault in Malaŵi: An active, 100-km long, normal fault segment in thick seismogenic crust, Tectonics, 16(1), 137–150, doi:10.1029/96TC02494.
- Kondo, H., S. Toda, K. Okumura, K. Takada and T. Chiba (2008), A fault scarp in an urban area identified by LiDAR survey: A Case study on the Itoigawa–Shizuoka Tectonic Line, central Japan, Geomorphology, Volume 101, Issue 4, 1, Pages 731-739, ISSN 0169-555X, 10.1016/j.geomorph.2008.02.012.
- Loke, M.H., I. Acworth and T. Dahlin (2003), A comparison of smooth and blocky inversion methods in 2D electrical imaging surveys. Exploration Geophysics, 34, 182-187.
- Nederbragt, A.J., Thurow, J.W., Russell B. M., in Lyle, M., Koizumi, I., Richter, C., and Moore, T.C., Jr. (Eds.), 2000, Proceedings of the Ocean Drilling Program, Scientific Results, Vol. 167.
- Mariucci M.T., Montone P., Pierdominici S., 2010. Present-day stress in the surroundings of 2009 L'Aquila seismic sequence (Italy). Geophys. J. Int., 182 (2), 1096-1102. doi: 10.1111/j.1365-246X.2010.04679.x
- Marzocchi, W., J. Selva, F. R. Cinti, P. Montone, S. Pierdominici, R. Schivardi and E. Boschi (2009), On the recurrence of large earthquakes: new insights from a model based on interacting faults embedded in a realistic tectonic setting, J. Geophys. Res., Vol. 114, B01307, doi:10.1029/2008JB005822.
- Mattson, A., R. L. Bruhn and G. T. Schuster (2003), Beneath the trench: High-resolution seismic tomograms and sediment cores applied to paleoseismology, Mercur, Utah, paper presented at Annual Meeting, Geol. Soc. of Am., Seattle, Wash., 2 –5 Nov.
- Messina, P., P. Galli, B. Giaccio and E. Peronace (2009), Quaternary tectonic evolution of the area affected by the Paganica fault (2009 L'Aquila earthquake), 29th GNGTS Conference, Extended abstract Volume, pp. 47-50, Trieste (Italy), November 2009.
- Michetti, A. M., F. Brunamonte, L. Serva and E. Vittori (1996), Trench investigations of the 1915 Fucino earthquake fault scarps (Abruzzo, central Italy): Geological evidence of large historical events, J. Geophys. Res., 101(B3), 5921–5936, doi:10.1029/95JB02852.
- Montone, P., Amato, A. & Pondrelli, S., 1999. Active stress map of Italy, Journal of Geophysical Research., 104, 25 595–25 610.
- Moro, M., V. Bosi, F. Galadini, P. Galli, B. Giaccio, P. Messina and A. Sposato (2002), Analisi paleosismologiche lungo la faglia del M. Marine (alta valle dell'Aterno): Risultati preliminari, Il Quaternario, 15, 267–278.

- Nguyen, F., S. Garambois, D. Jongmans, E. Pirard and M. H. Loke (2005), Image processing of 2D resistivity data for imaging faults, *J. Appl. Geophys.*, *57*, 260–277, doi:10.1016/j.jappgeo.2005.02.001.
- Operto, S., C. Ravaut, L. Improta, J. Virieux, A. Herrero and P. Dell'aversana (2004), Quantitative imaging of complex structures from dense wide-aperture seismic data by multiscale traveltime and waveform inversions: a case study. Geophys. Prospect., 52, 625–651, doi:10.1111/j.13652478.2004.00452.x.
- Pace, B., L. Peruzza, G. Lavecchia and P. Boncio (2006), Layered seismogenic source model and probabilistic seismic hazard analyses in central Italy, Bull. Seismol. Soc. Am., 96, 107–132.
- Pantosti, D., G. D'Addezio and F. R. Cinti (1996), Paleoseismicity of the Ovindoli-Pezza fault, central Apennines, Italy: a history including a large, previously unrecorded earthquake in the Middle Ages (860–1300 A.D.), J. Geophys. Res., 101 (B3) 5937–5959.
- Papanikolaou, I. D., M. Foumelis, I. Parcharidis, E. L. Lekkas, and I. G. Fountoulis (2010), Deformation pattern of the 6 and 7 April 2009, MW=6.3 and MW=5.6 earthquakes in L'Aquila (Central Italy) revealed by ground and space based observations, Nat. Hazards Earth Syst. Sci., 10, 73-87, doi:10.5194/nhess-10-73-2010.
- Pino, N. A. and F. Di Luccio (2009), Source complexity of the 6 April 2009 L'Aquila (central Italy) earthquake and its strongest aftershock revealed by elementary seismological analysis, Geophys. Res. Lett., 36, L23305, doi:10.1029/2009GL041331.
- Pondrelli, S., S. Salimbeni, A. Morelli, G. Ekström, M. Olivieri and E. Boschi (2010), Seismic moment tensors of the April 2009, L'Aquila (Central Italy), earthquake sequence, Geophys. J. Int. doi:10.111/j.1365-246X.2009.04418.x.
- Reid, H.F. (1910), On mass-movements in tectonic earthquakes. The California earthquake of April 18, 1906. Report of the state earthquake investigation commission: Carnegie Institute of Washington, D.C.
- Reimer, P. J., M. G. Baillie, E. Bard, A. Bayliss, J. W. Beck, C. J. H. Bertrand, P.G. Blackwell, C. E. Buck, G. S. Burr, K. B. Cutler, P. E. Damon, R. L.Edwards, R. G. Fairbanks, M. Friedrich, T. P. Guilderson, A. G. Hogg, K. A. Hughen, B. Kromer, F. G. McCormac, S. W. Manning, C. B. Ramsey, R. W. Reimer, S. Remmele, J. R. Southon, M. Stuiver, S. Talamo, F. W. Taylor, J. van der Plicht and C. E. Weyhenmeyer, (2004), IntCal04 Terrestrial radiocarbon age calibration, 26 - 0 ka BP, Radiocarbon 46, 1029-1058.
- Roberts, G.P., P. Cowie, I. Papanikolaou and A. M. Michetti (2004), Fault scaling relationships, deformation rates and seismic hazards: an example from the Lazio–Abruzzo Apennines, central Italy, J. Struct. Geol., 26, 377–398.
- Sallenger, A.H., W. Krabill, J. Brock, R. Swift, M. Jansen, S. Manizade, B. Richmond, M. Hampton and D. Eslinger (1999), Airborne laser study quantifies El Niño-induced coastal change: Eos (Transactions American Geophysical Union), v. 80, p. 89, 92–93.
- Salvi, S., F. R. Cinti, L. Colini, G. D'Addezio, F. Doumaz and E. Pettinelli (2003), Investigation of the active Celano–L'Aquila fault system, Abruzzi, Geophys. J. Int., 155, 805–818.
- Scholz, C.H., The Mechanics of Earthquakes and Faulting, 439 pp., Cambridge Univ. Press, New York, 1990.
- Schwartz, D. P. and K. J. Coppersmith (1984), Fault Behavior and Characteristic Earthquakes: Examples From the Wasatch and San Andreas Fault Zones, J. Geophys. Res., 89(B7), 5681–5698, doi:10.1029/JB089iB07p05681.

- Sherrod, B.L., T. M. Brocher, C. S. Weaver, R. C. Bucknam, R. J. Blakely, H. M. Kelsey, A. R. Nelson, R. Haugerud (2004), Holocene fault scarps near Tacoma, Washington, USA, Geology 32: 9-12.
- Shimazaki, K. and T. Nakata (1980), Time-predictable recurrence model for large earthquakes, Geophys. Res. Lett., 7, 279–282.
- Silberling, N.J., and Wallace, R.E., 1967, Geologic map of the Imlay quadrangle, Pershing County, Nevada: U.S. Geological Survey Geologic quadrangle Map GQ-666, scale 1:62,500
- Slemmons, D.B., 1957, Geological effects of the Dixie Valley-Fairview Peak, Nevada, earthquakes of December 16, 1954: Seismol. Soc. America Bull., v. 47, no. 4, p. 353-375.
- Slemmons, D.B., and De Polo C.M., 1986: Evaluation of active faulting and associated hazards, in: Geophysics Study Committee: Active Tectonics; National Academy Press, Washington D.C.
- Stewart, I.S. and P. L. Hancock (1990), What is a fault scarp? Episodes 13, pp. 256–263.
- Suzuki, K., S. Toda, K. Kusunoki, Y. Fujimitsu, T. Mogi and A. Jomori (2000), Case studies of electrical and electromagnetic methods applied to mapping active faults beneath the thick quaternary, *Eng. Geol. Amsterdam*, *56*, 29–45, doi:10.1016/S0013-7952(99)00132-5.
- Tertulliani, A., A. Rossi, L. Cucci and M. Vecchi (2009), L'Aquila (Central Italy) earthquakes: the predecessors of the April 6, 2009 event, Seism. Res. Lett., 80, 6, 1008-1013.
- Thorarinsson S. (1974), The terms tephra and tephrochronology, in Westgate, J.A. and Gold, C.M., eds., World bibliography and index of Quaternary tephrochronology: University of Alberta, p. xix – xxi.
- Trasatti, E., C. Kyriakopoulos and M. Chini (2011), Finite element inversion of DInSAR data from the Mw 6.3 L'Aquila earthquake, 2009 (Italy),*Geophys. Res. Lett.*, *38*, L08306, doi:10.1029/2011GL046714.
- Vezzani, L. and F. Ghisetti (1998), Carta Geologica dell'Abruzzo, Scala 1:100,000. S.EL.CA., Firenze.
- Wallace, R.E., Tatlock, D.B., Silberling, N.J., and Irwin, W.P., 1969, Geologic map of the Unionville quadrangle, Pershing County, Nevada: U.S. Geological Survey Geologic quadrangle Map GQ-820, scale 1:62,500.
- Wallace, R. E. (1977), Profiles and ages of young fault scarps, north-central Nevada. Geological Society of America Bulletin 88, 1267-1281.
- Wallace, R. E. (1987), Grouping and migration of surface faulting and variation in slip rates on faults in the Great Basin province, Bull. Seismol. Soc. Am., 77, 868– 877.
- Walters, R. J., J. R. Elliott, N. D'Agostino, P. C. England, I. Hunstad, J. A. Jackson, B. Parsons, R. J. Phillips and G. Roberts (2009), The 2009 L'Aquila earthquake (central Italy): A source mechanism and implications for seismic hazard, Geophys. Res. Lett., 36, L17312, doi:10.1029/2009GL039337.
- Wells, D.L. and K.J. Coppersmith (1994), New empirical relationships among Magnitude, rupture length, rupture width, rupture area, and surface displacement, Bull. Seismol. Soc. Am., 84, 974-1002.
- Wesnousky, S. G. (2005), Active faulting in the Walker Lane, *Tectonics*, *24*, TC3009, doi:10.1029/2004TC001645.
- Wise, D. J., J. Cassidy and C. A. Locke (2003), Geophysical imaging of the Quaternary Wairoa North Fault, New Zealand: A case study, *J. Appl. Geophys.*, *53*, 1–16, doi:10.1016/S0926-9851(03)00013-2.

APPENDIX A

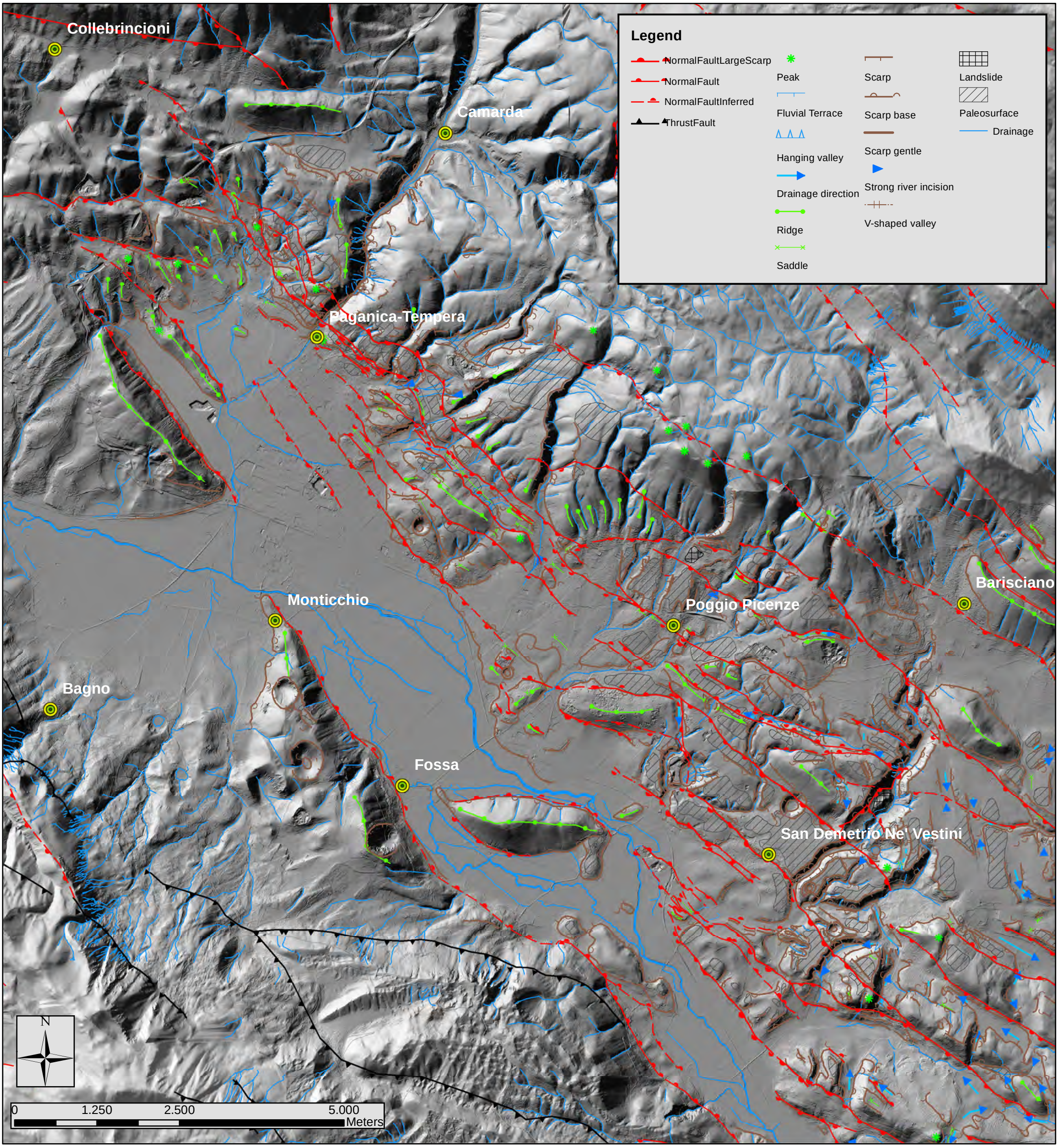
Collebrincioni
Camarda
Paganica-Tempera
Monticchio
Bagno
Fossa
Poggio Picenze
Barisciano
San Demetrio Ne' Vestini
Legend
NormalFaultLargeScarp
NormalFault
NormalFaultInferred
ThrustFault
Peak
Fluvial Terrace
Hanging valley
Drainage direction
Ridge
Saddle
Scarp
Scarp base
Scarp gentle
Strong river incision
V-shaped valley
Landslide
Paleosurface
Drainage
N
0
1.250
2.500
5.000
Meters

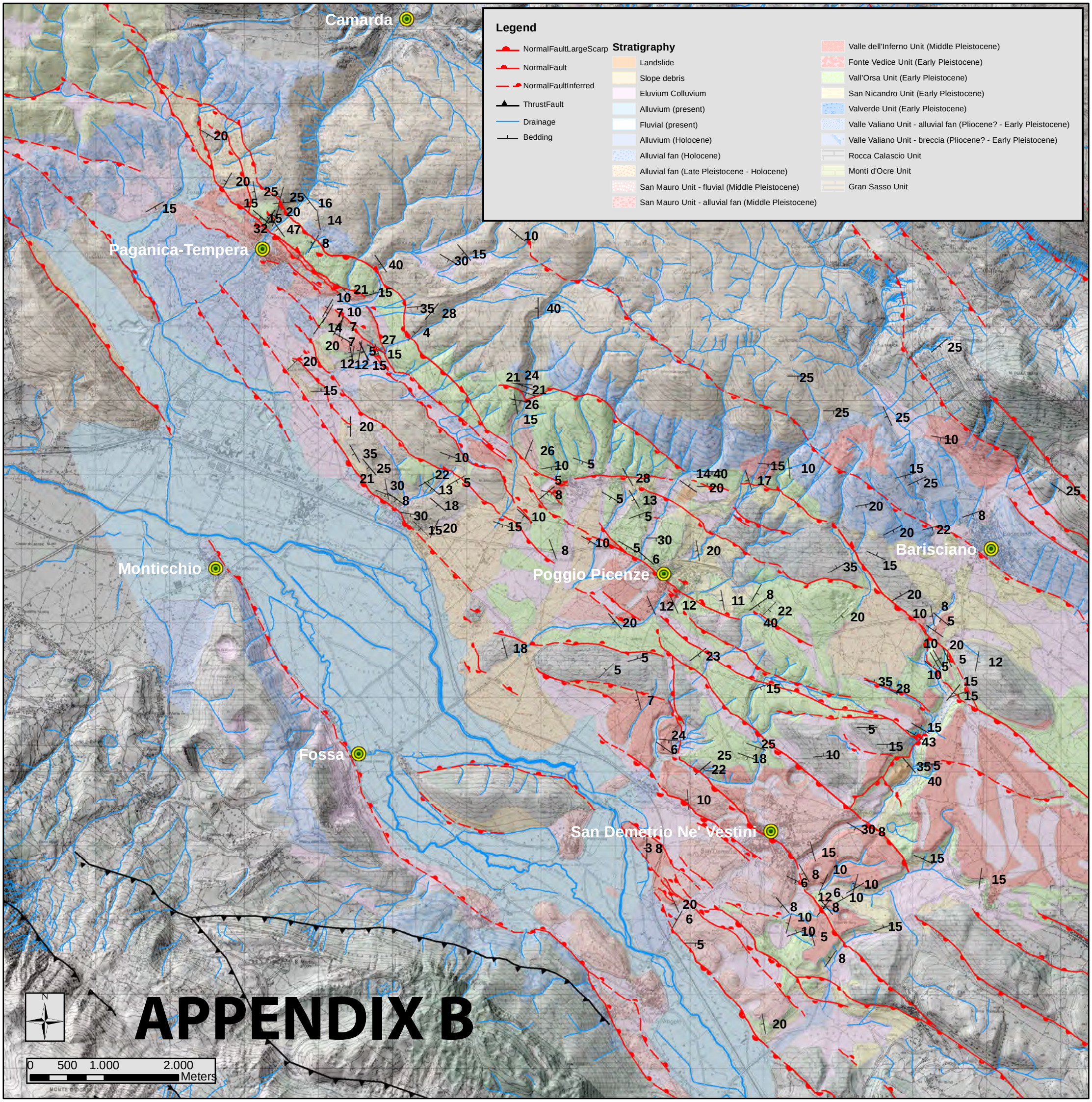
Legend
NormalFaultLargeScarp
NormalFault
NormalFaultInferred
ThrustFault
Drainage
Bedding
Stratigraphy
Landslide
Slope debris
Eluvium Colluvium
Alluvium (present)
Fluvial (present)
Alluvium (Holocene)
Alluvial fan (Holocene)
Alluvial fan (Late Pleistocene - Holocene)
San Mauro Unit - fluvial (Middle Pleistocene)
San Mauro Unit - alluvial fan (Middle Pleistocene)
Valle dell'Inferno Unit (Middle Pleistocene)
Fonte Vedice Unit (Early Pleistocene)
Vall'Orsa Unit (Early Pleistocene)
San Nicandro Unit (Early Pleistocene)
Valverde Unit (Early Pleistocene)
Valle Valiano Unit - alluvial fan (Pliocene? - Early Pleistocene)
Valle Valiano Unit - breccia (Pliocene? - Early Pleistocene)
Rocca Calascio Unit
Monti d'Ocre Unit
Gran Sasso Unit
Camarda
Paganica-Tempera
Monticchio
Poggio Picenze
Barisciano
Fossa
San Demetrio Ne' Vestini
APPENDIX B
0 500 1.000 2.000
Meters

APPENDIX C

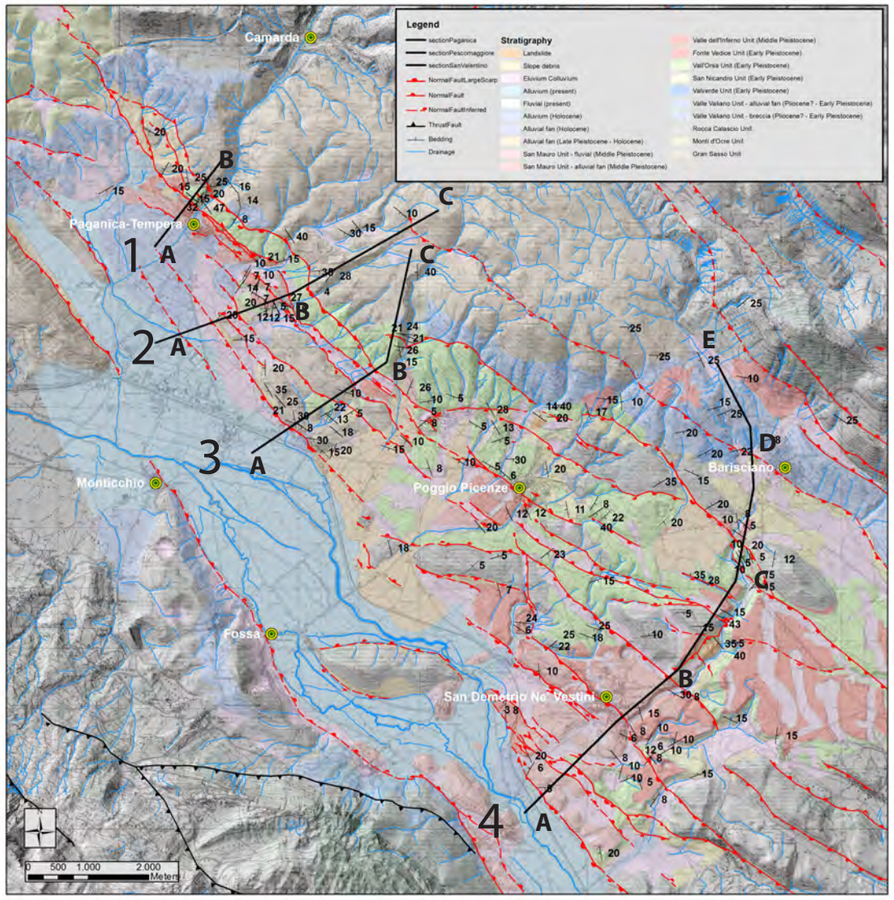
Legend
sectionPaganica
sectionPescomaggiore
sectionSanValentino
NormalFaultLargeScarp
NormalFault
NormalFaultInferred
ThrustFault
Bedding
Drainage
Stratigraphy
Landslide
Slope debris
Eluvium Colluvium
Alluvium (present)
Fluvial (present)
Alluvium (Holocene)
Alluvial fan (Holocene)
Alluvial fan (Late Pleistocene - Holocene)
San Mauro Unit - fluvial (Middle Pleistocene)
San Mauro Unit - alluvial fan (Middle Pleistocene)
Valle dell'Inferno Unit (Middle Pleistocene)
Fonte Vedice Unit (Early Pleistocene)
Vall'Orsa Unit (Early Pleistocene)
San Nicandro Unit (Early Pleistocene)
Valverde Unit (Early Pleistocene)
Valle Veliano Unit - alluvial fan (Pliocene? - Early Pleistocene)
Valle Veliano Unit - breccia (Pliocene? - Early Pleistocene)
Rocca Calascio Unit
Monti d'Ocre Unit
Gran Sasso Unit
Camarda
Paganica-Tempera
Monticchio
Fossa
Poggio Picenze
Bariscano
San Demetrio Ne' Vestini
0 500 1.000 2.000 Meters

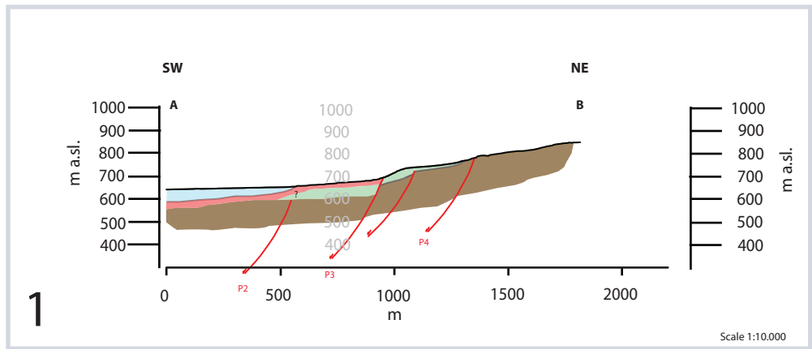
SW
NE
A
B
m a.s.l.
1000
900
800
700
600
500
400
P2
P3
P4
0
500
1000
1500
2000
m
1
Scale 1:10.000

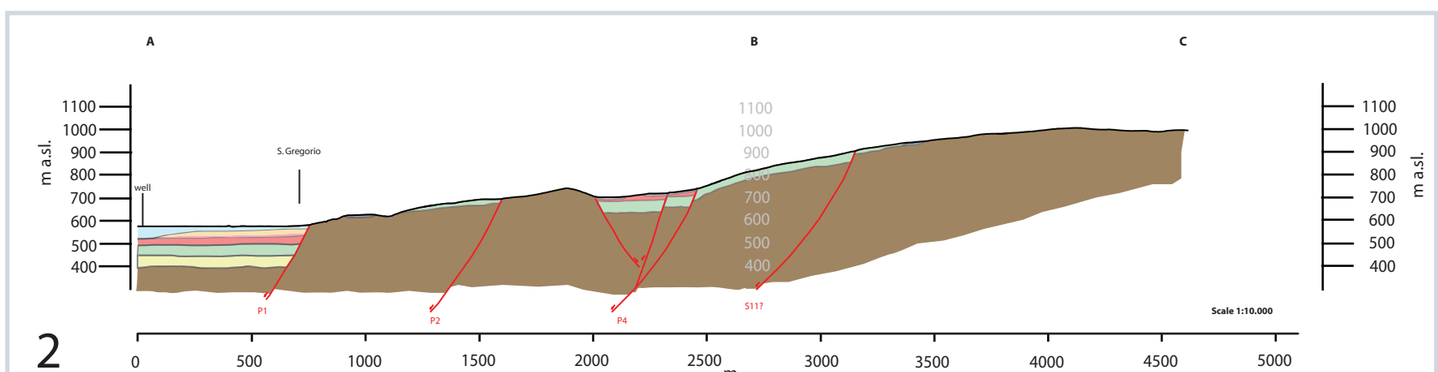
A
B
C
m a.s.l.
1100
1000
900
800
700
600
500
400
well
S.Gregorio
P1
P2
P4
S11?
0
500
1000
1500
2000
2500
3000
3500
4000
4500
5000
m
2
Scale 1:10.000

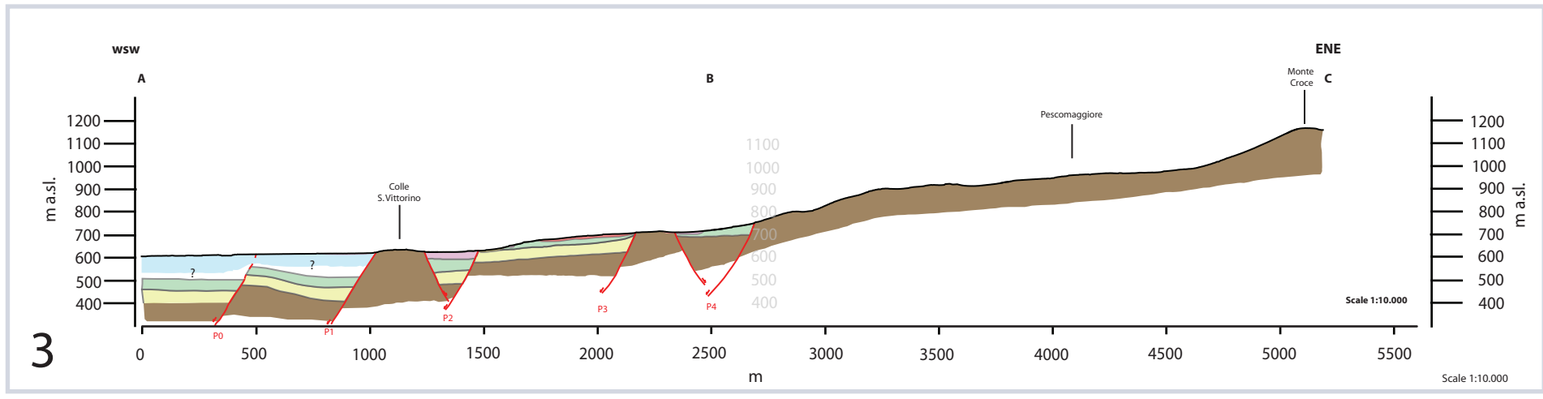
wsw
ENE
A
B
C
m a.s.l.
1200
1100
1000
900
800
700
600
500
400
Colle
S. Vittorino
Pescomaggiore
Monte
Croce
?
P0
P1
P2
P3
P4
0
500
1000
1500
2000
2500
3000
3500
4000
4500
5000
5500
m
3
Scale 1:10.000

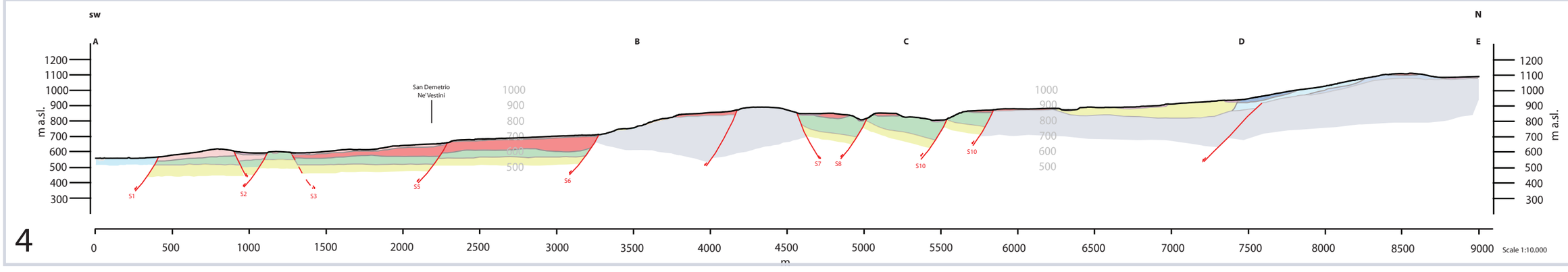
sw
N
A
B
C
D
E
m a.s.l.
1200
1100
1000
900
800
700
600
500
400
300
San Demetrio
Ne' Vestini
S1
S2
S3
S5
S6
S7
S8
S10
S10
0
500
1000
1500
2000
2500
3000
3500
4000
4500
5000
5500
6000
6500
7000
7500
8000
8500
9000
m
4
Scale 1:10.000

APPENDIX D1 - TOPOGRAPHIC PROFILES 0 - 7

SW NE

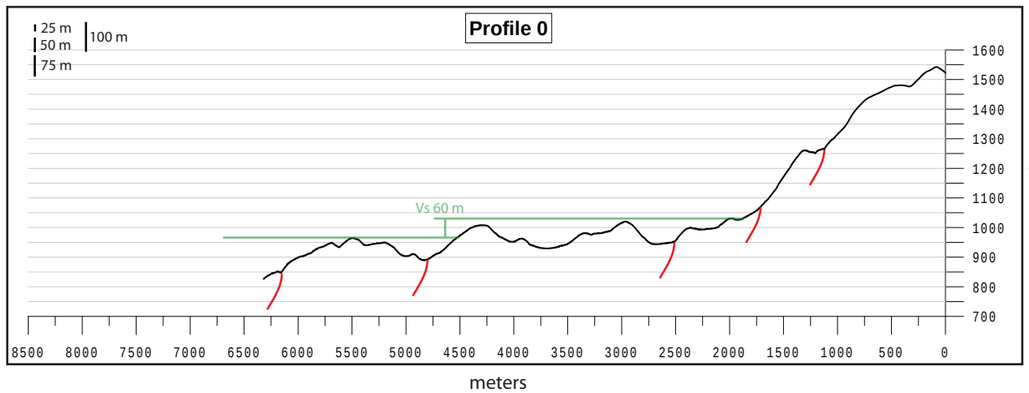

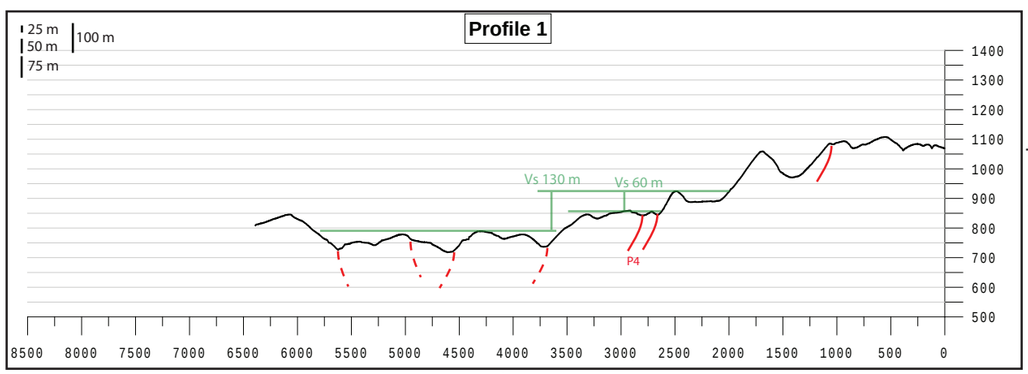

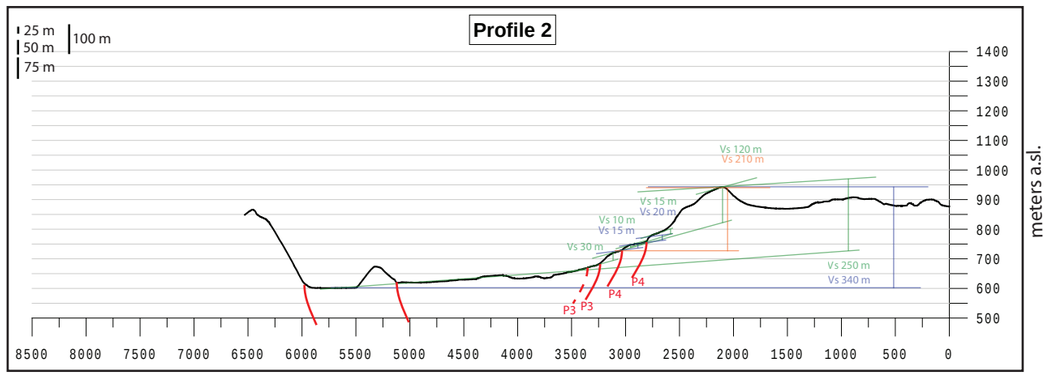

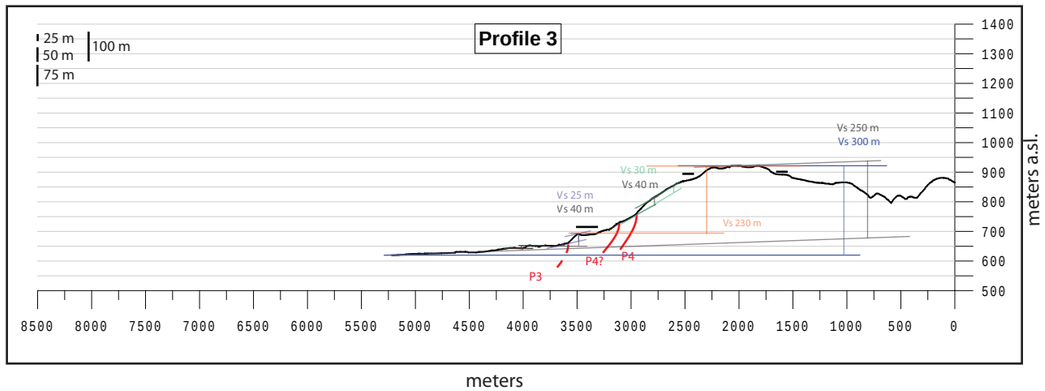

SW NE

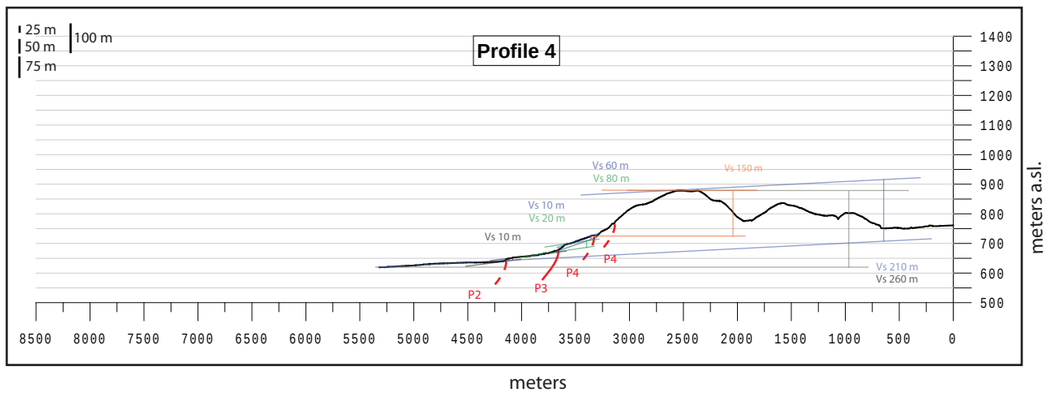

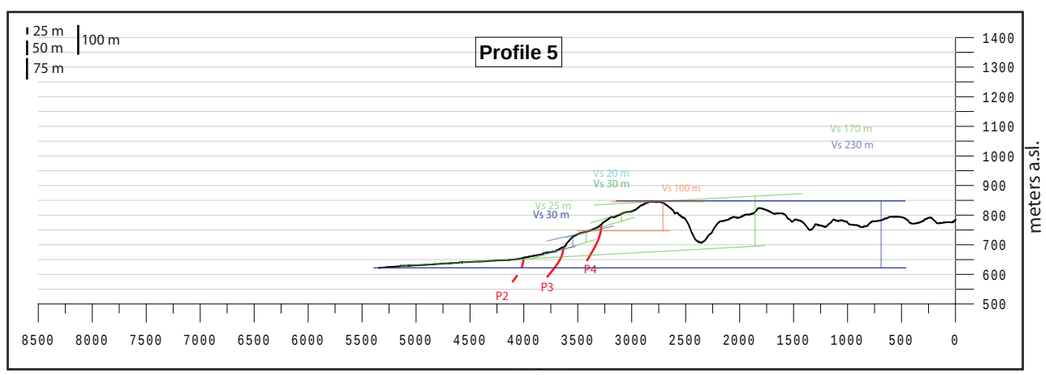

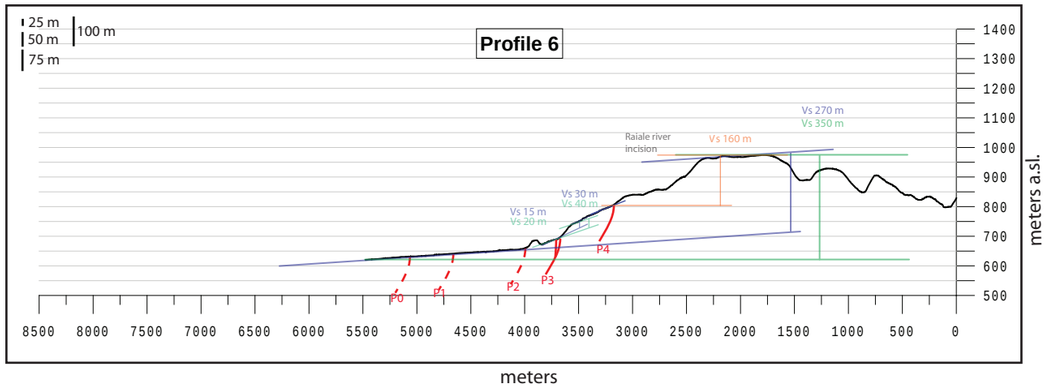

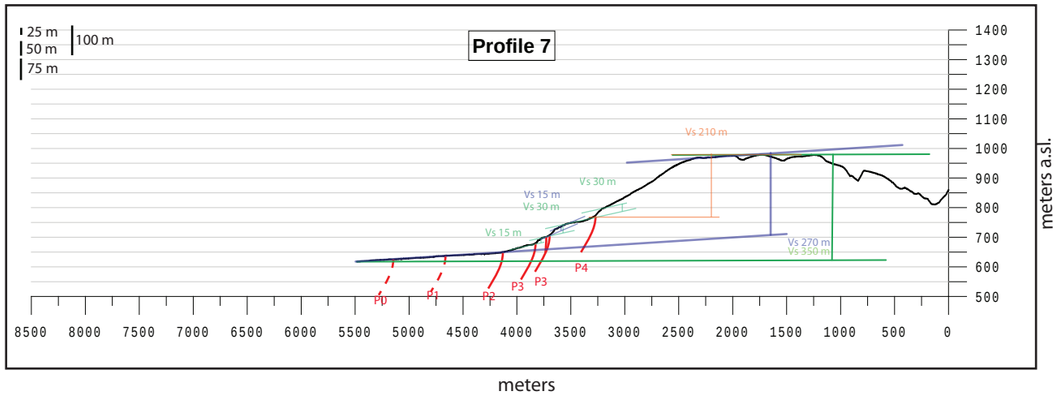

APPENDIX D2 - TOPOGRAPHIC PROFILES 8 - 15

SW NE

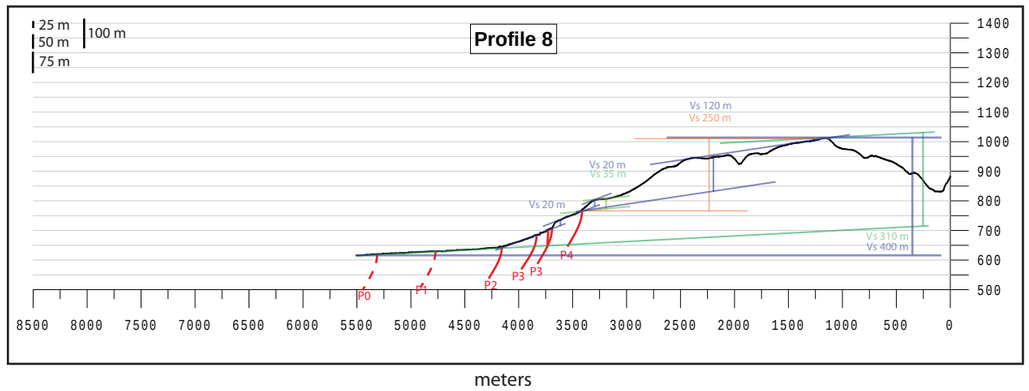

SW NE

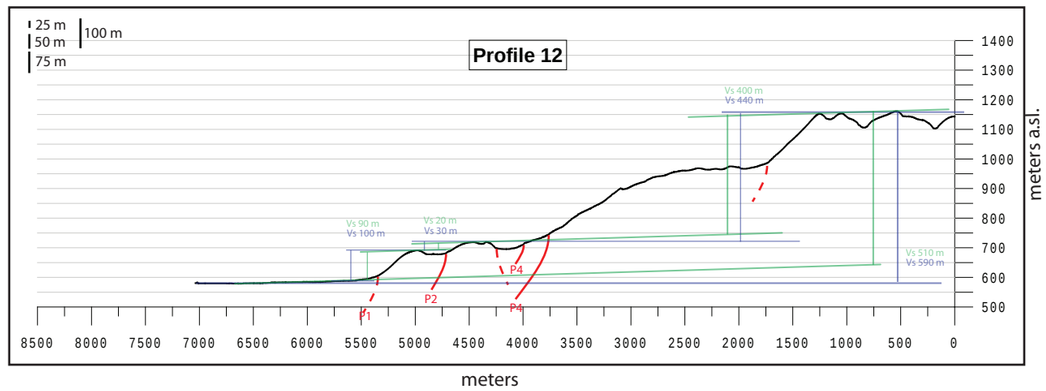

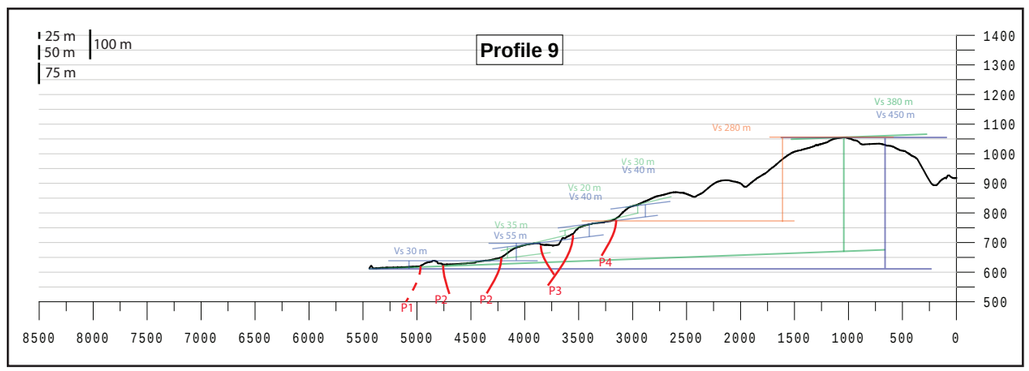

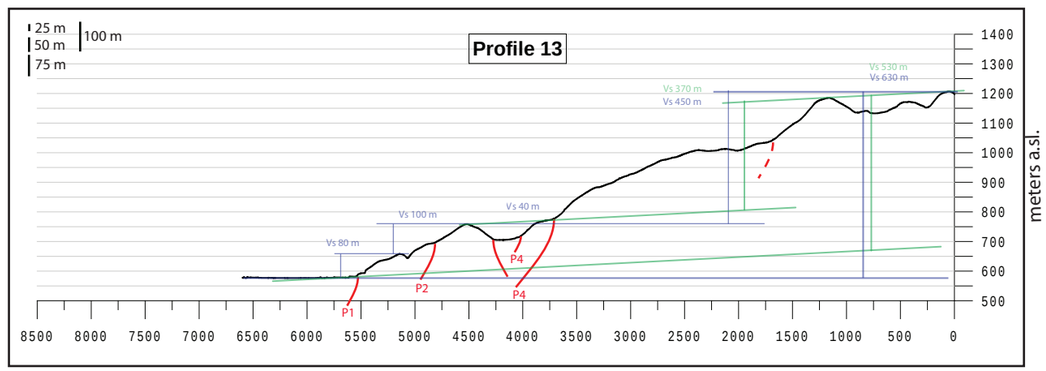

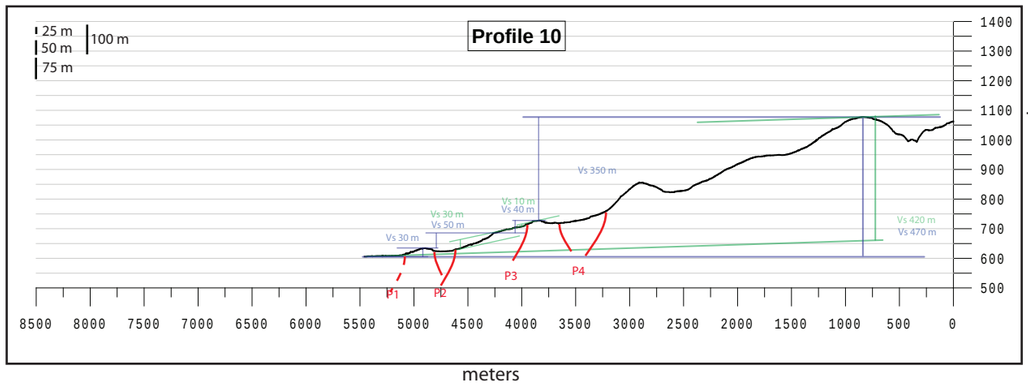

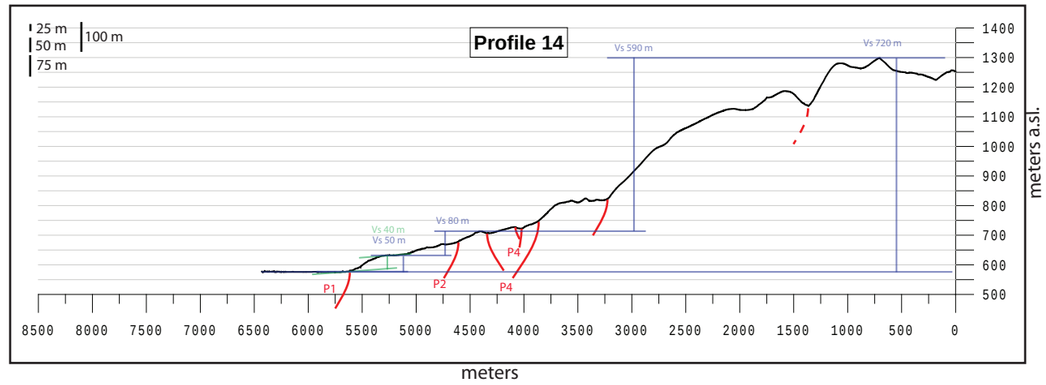

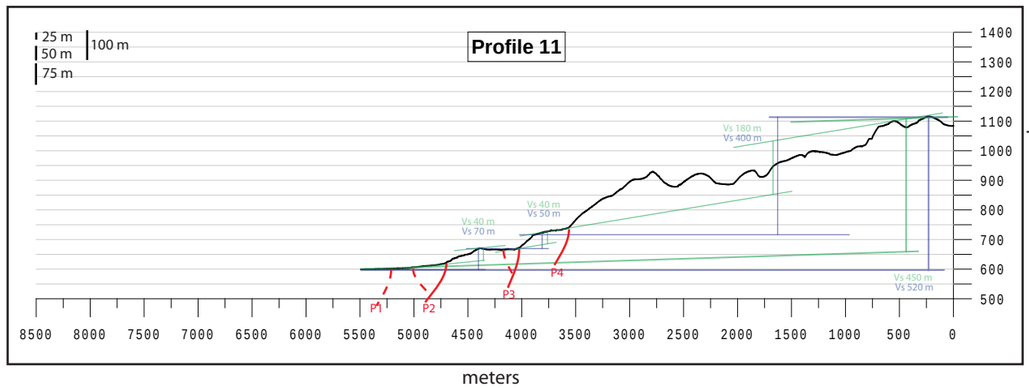

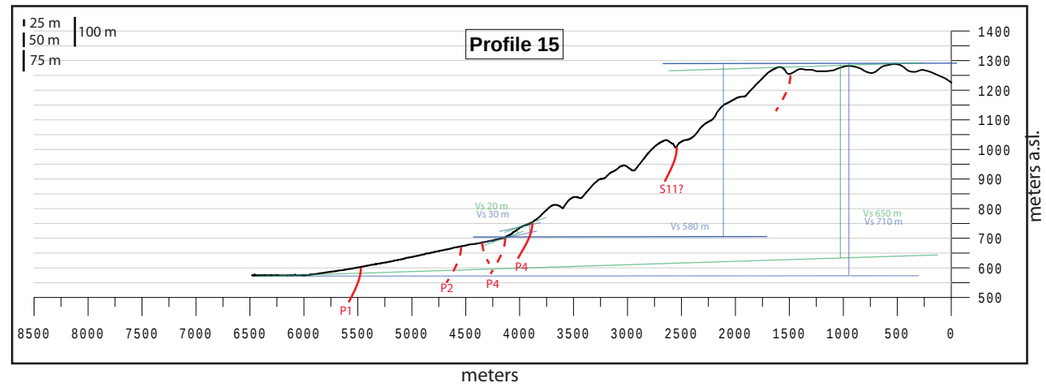

APPENDIX D3 - TOPOGRAPHIC PROFILES 16 - 23

SW NE

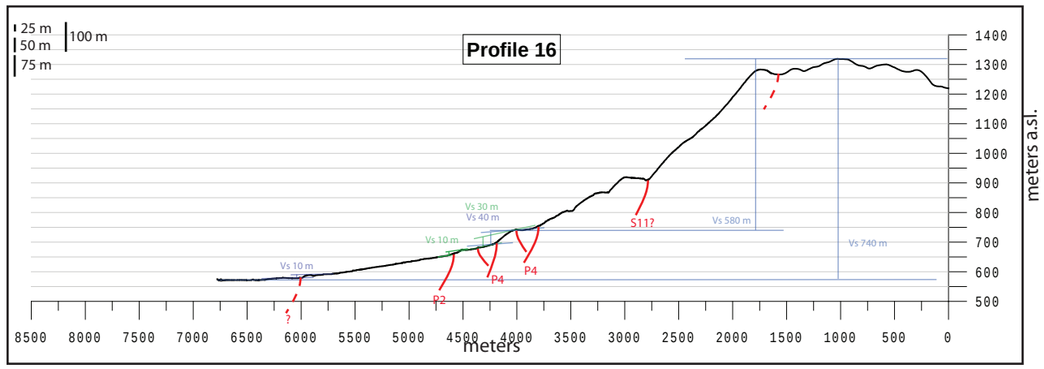

SW NE

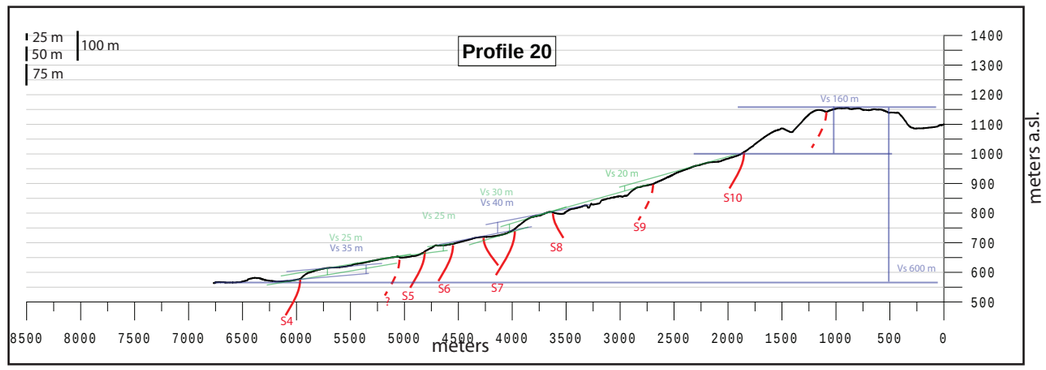

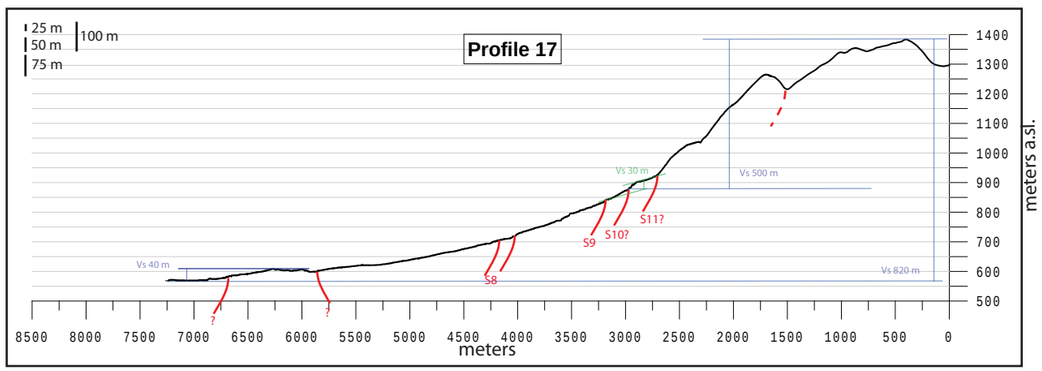

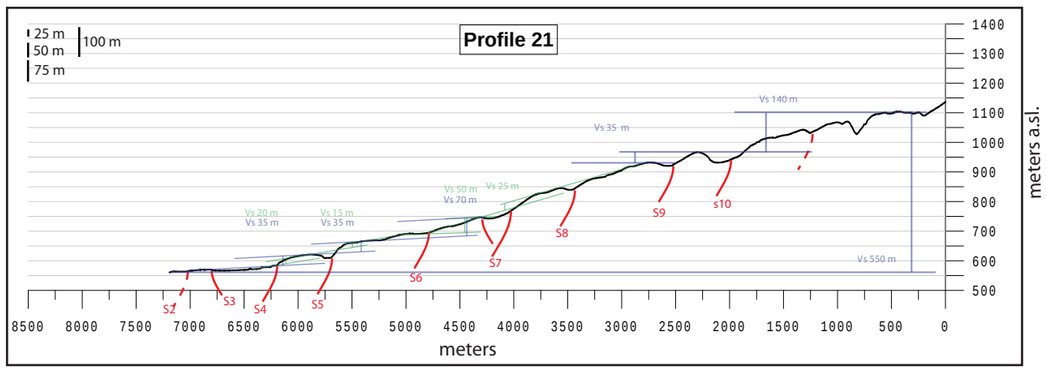

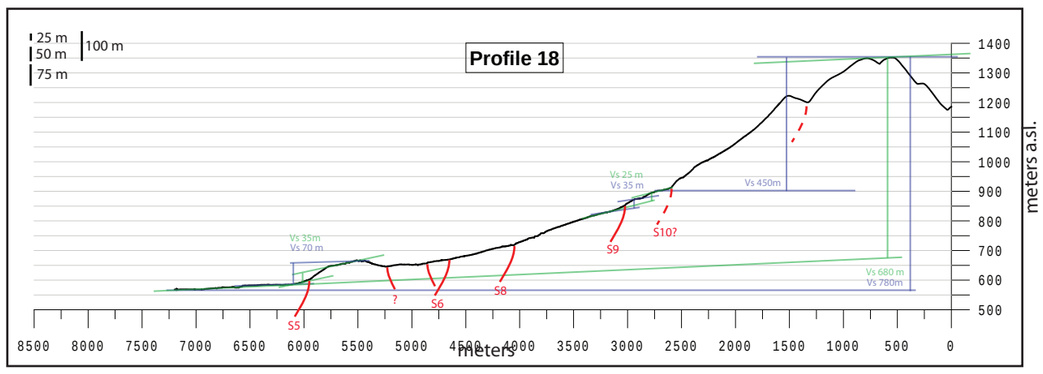

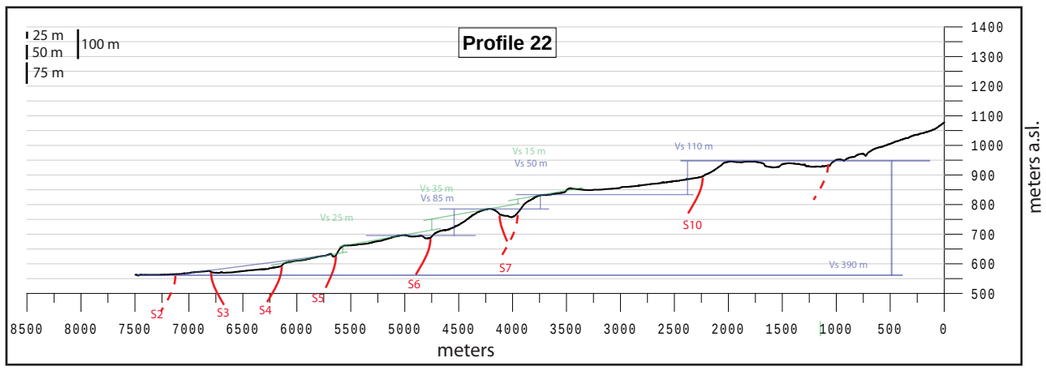

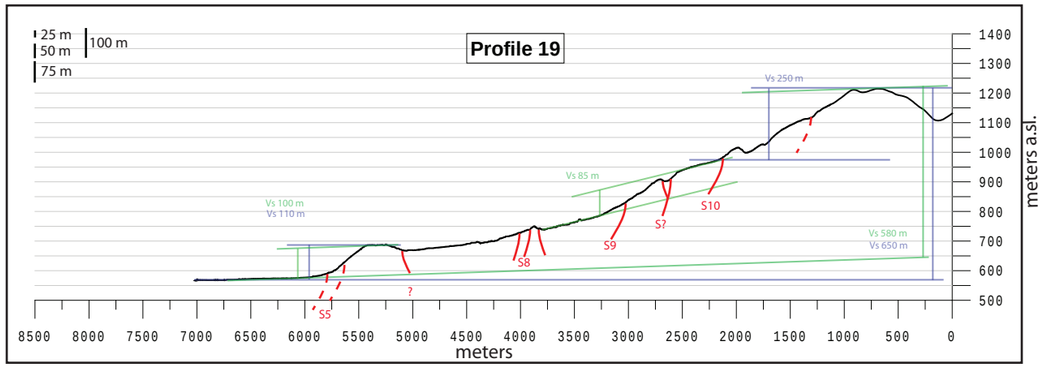

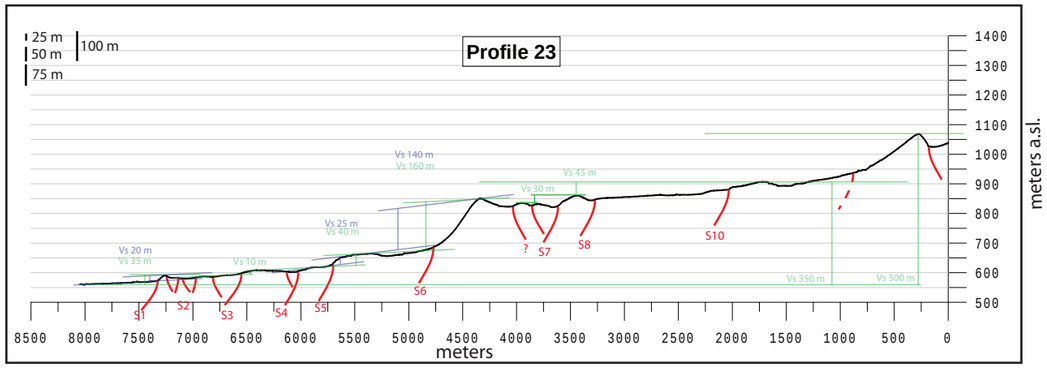

APPENDIX D4 - TOPOGRAPHIC PROFILES 24 - 29

SW NE

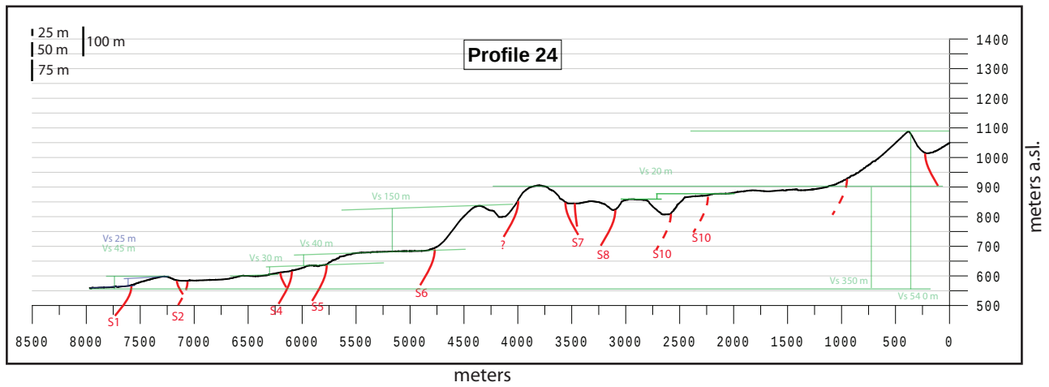

SW NE

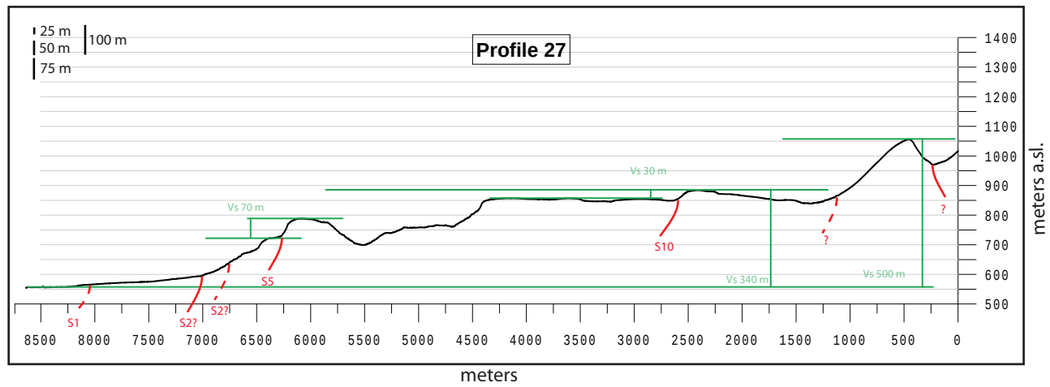

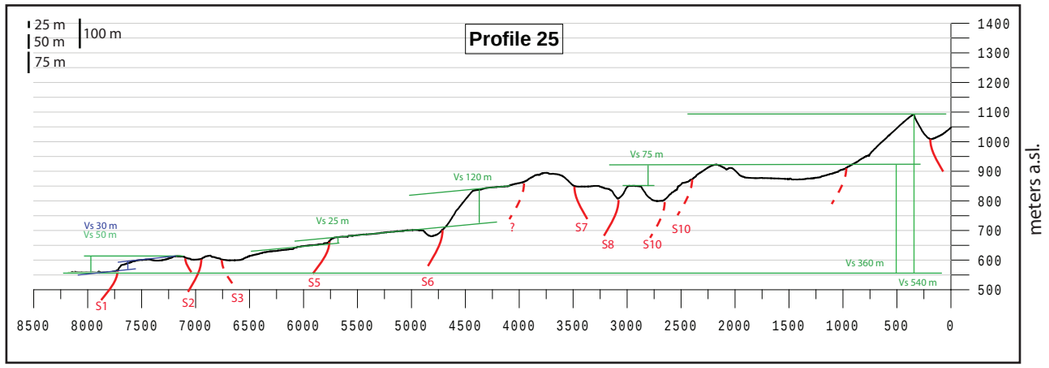

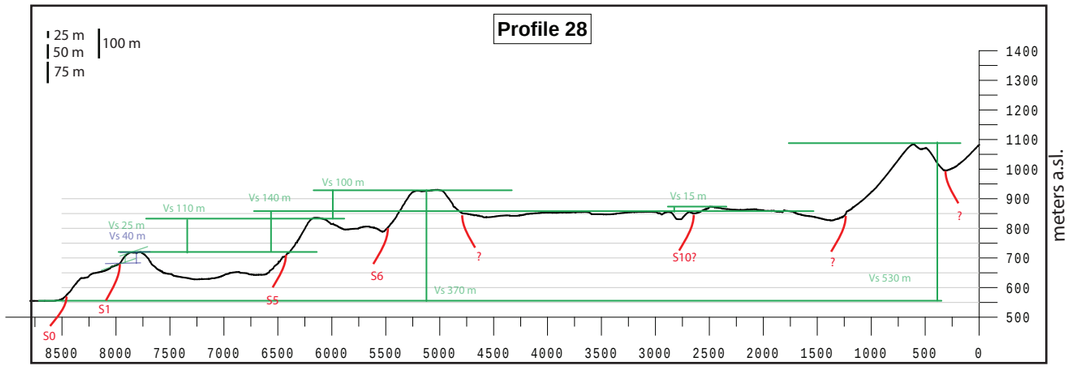

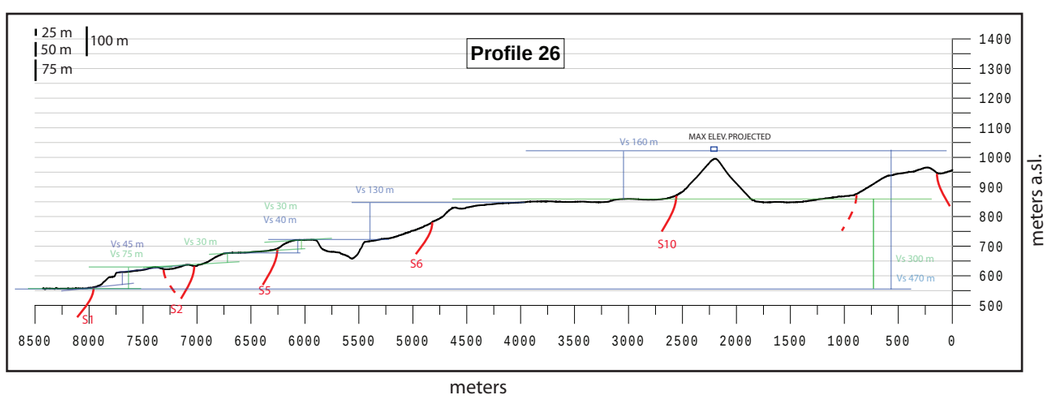

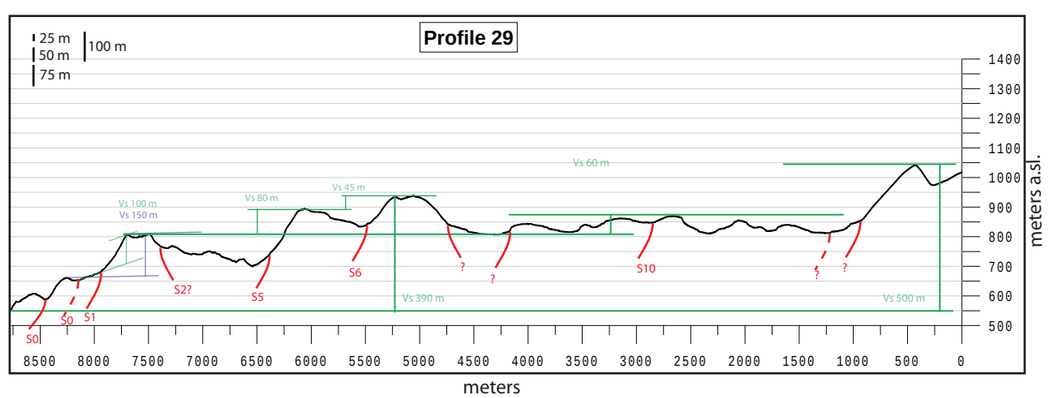

APPENDIX E

Total morphological throw

Bedrock/bedrock

Bedrock/deposit

Deposit/deposit

POGGIO PICENZE

SAN DEMETRIO NE' VESTINI

PAGANICA

P1 P2 P3 P4

S1 S2 S4 S5 S6 S7 S9 S10

Morphological throw (m)

Distance along strike (m)

NW

SE

HOLOCENE

QUATERNARY

Prevailing age of the outcropping deposits

- APPENDIX F - Emergeo Working Group (2010), *Evidence for surface rupture associated with the Mw 6.3 L'Aquila earthquake sequence of April 2009 (central Italy),* Terra Nova, 22, 1, 43-51, doi: 10.1111/j.1365-3121.2009.00915.x.

doi: 10.1111/j.1365-3121.2009.00915.x

Evidence for surface rupture associated with the Mw 6.3 L'Aquila earthquake sequence of April 2009 (central Italy)

EMERGEO Working Group*

Istituto Nazionale di Geofisica e Vulcanologia, Via di Vigna Murata, 605, 00143 Rome, Italy

ABSTRACT

An earthquake of Mw = 6.3 struck L'Aquila town (central Italy) on 6 April 2009 rupturing an ~18-km-long SW-dipping normal fault. The aftershock area extended for a length of more than 35 km and included major aftershocks on 7 and 9 April and thousands of minor events. Surface faulting occurred along the SW-dipping Paganica fault with a continuous extent of ~2.5 km. Ruptures consist of open cracks and vertical dislocations or warps (0.1m maximum throw) with an orientation of N130°–140°. Small triggered slip and shaking effects also took place along nearby synthetic and antithetic normal faults. The observed limited extent and small surface displacement of the Paganica ruptures with respect to the height of the fault scarps and vertical throws of palaeo-earthquakes along faults in the area put the faulting associated with the L'Aquila earthquake in perspective with respect to the maximum expected magnitude and the regional seismic hazard.

Terra Nova, 22, 43–51, 2010

Introduction

At 01.32 GMT on 6 April 2009, an earthquake of Mw = 6.3 occurred in the central Apennines (Abruzzi region). It caused heavy damage in the town of L'Aquila (73 000 inhabitants) and surrounding villages and resulted in about 300 fatalities and thousands of injured. The epicentre was located close to L'Aquila and was followed by two large aftershocks on 7 April (Mw = 5.6) and 9 April (Mw = 5.4). The seismic sequence was confined to the upper 10–12 km, with the exception of 7 April hypocenter at about 15 km depth (Fig. 1). The focal mechanisms of the main events (Fig. 1) show NW-striking normal faulting (Pondrelli *et al*., 2009) consistent with the NE–SW trending extensional regime (Patacca and Scandone, 1989; Galadini *et al*., 2000; Montone *et al*., 2004; D'Agostino *et al*., 2008). The aftershocks occurred in three distinct zones: (1) the area of the mainshock (Fig. 1, section AB), where seismicity is clearly confined within the Aterno river valley and images a ~50° SW-dipping fault; (2) the area hit by 7 April aftershock; and (3) the Campotosto area hit by 9 April aftershock, which occurred on a SW-dipping fault north-east of the mainshock (Fig. 1, section CD).

The region is part of the central Apennines (Fig. 2) characterized by Quaternary extension superimposed on a NE-verging Neogene fold and thrust belt (i.e. Cipollari and Cosentino, 1995; Ghisetti and Vezzani, 1999; Meletti *et al*., 2000). On the basis of their geomorphic expression and age of faulted sediments and geomorphic features, many workers have identified a large number of active normal faults (Figs. 1 and 3), mostly NW-trending, up to 15-km-long, 50°–70° SW-dipping, with a smaller number of NE-dipping faults (Lavecchia *et al*., 1994; Vezzani and Ghisetti, 1998; Barchi *et al*., 2000; Galadini and Galli, 2000 and reference therein; Foglio CARG 2009). Many historical earthquakes have hit the region (Fig. 1); however, none of them could be clearly attributed to one of the mapped active faults. Palaeoseismological studies on several faults (Pantosti *et al*., 1996; Galli *et al*., 2002; Galadini *et al*., 2003; Salvi *et al*., 2003) indicate average recurrence intervals for M = 6.5–7 earthquakes of 1000–3000 years and average slip rates lower than 1 mm yr^{-1}. Based on historical seismicity, the presence of active faults and evidence of large surface-faulting palaeo-earthquakes, the L'Aquila region was considered a high hazard seismic zone (Cinti *et al*., 2004; Gruppo di Lavoro M.P.S, 2004; Pace *et al*., 2006; Akinci *et al*., 2009).

We present the data collected during the post-earthquake campaigns by the Emergeo team (http://portale.ingv.it/real-time-monitoring/emergeo/; Emergeo Working Group, 2009) and a preliminary tectonic interpretation.

The geological co-seismic ruptures

Co-seismic surface effects were recognized during the field survey within the epicentral area with observations recorded at about 400 sites (Fig. 3). Most of these are fractures arranged with consistent trends that cross-cut soft and hard rocks, paved and unpaved roads and different types of man-made features. Most of the fractures occur along pre-existing fault traces. Among these, the Paganica ones most likely represent the primary rupture associated with the mainshock. The small, localized slip along the other tectonic structures (Fig. 4) may represent triggered slip or shaking effects.

We describe the most prominent tectonic ruptures along the Paganica fault, two antithetic fault strands (the Bazzano and the Monticchio-Fossa faults) and other minor features along other faults, as well as the most

Correspondence: Paola Montone, Istituto Nazionale di Geofisica e Vulcanologia, Via di Vigna Murata, 605, 00143 Rome, Italy. Tel.: +39 0651860419; fax: +39 0651860507; e-mail: paola.montone@ingv.it

*G. Alessio, L. Alfonsi, C.A. Brunori, F.R. Cinti, R. Civico, L. Cucci, G. D'Addezio, R. De Ritis, E. Falcucci, U. Fracassi, A. Gasparini, S. Gori, A. Lisi, S. Mariano, M.T. Mariucci, P. Montone, R. Nappi, D. Pantosti, A. Patera, S. Pierdominici, M. Pignone, S. Pinzi, S. Pucci, P. Vannoli, A. Venuti, F. Villani. EMERGEO INGV Prompt Geological Survey Team – http://portale.ingv.it/real-time-monitoring/emergeo/.

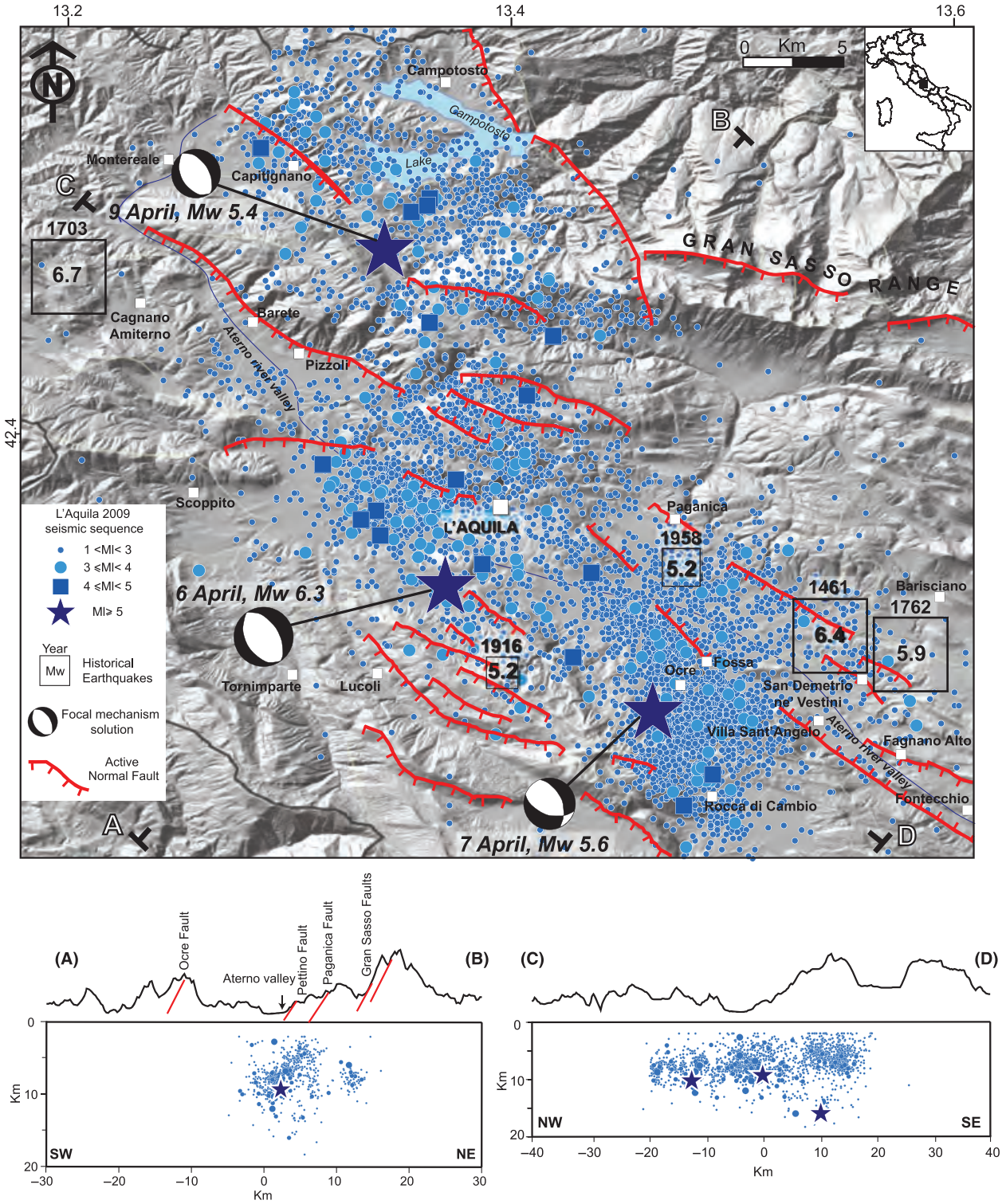

Fig. 1 Seismicity map of the L'Aquila region from 6 April to 11 May 2009 (http://portale.ingv.it/primo-piano-1/news-archive/2009-news/april-6-earthquake/copythe-l-aquila-seismic-sequence-april-2009/view?set_language=en). The historical earthquakes (CPTI Working Group, 2004) are scaled by magnitude and the main active faults are from Galli *et al.* (2008) and references therein. The two cross-sections below (locations shown on the map), perpendicular (AB) and parallel (CD) to the belt axis, define the aftershock distribution and the mainshock location at depth. The location of faults along the topographic profile is approximate.

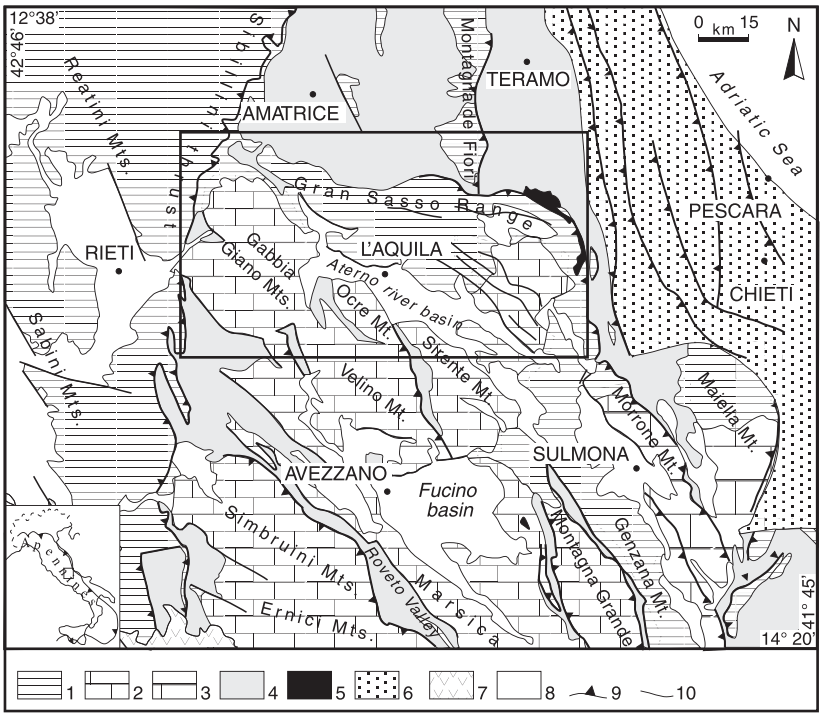

Fig. 2 Geological and structural map of the central Apennines, modified from Speranza *et al*. (2003). Legend: 1. Mesozoic–Cenozoic slope-basin sediments; 2. Mesozoic–Cenozoic Latium–Abruzzi shelf carbonates; 3. Mesozoic–Cenozoic Apulian shelf carbonates; 4. upper Miocene–lower Pliocene foredeep siliceous turbidites; 5. Messinian–lower Pliocene thrust-top sediments; 6. buried Pliocene marine sediments; 7. middle–upper Pleistocene volcanics; 8. Pliocene–Pleistocene and Holocene marine and continental deposits; 9. thrusts; 10. undifferentiated faults. The rectangular area includes the 2009 earthquake sequence.

noticeable local shaking-induced features. No evidence for surface ruptures was observed in the Campotosto area (9 April aftershock).

The Paganica fault

The Paganica fault is represented by a morphological scarp formed by the tectonic juxtaposition of Pliocene–middle Pleistocene with late Pleistocene alluvial deposits (Bagnaia *et al*., 1992; Vezzani and Ghisetti, 1998; Boncio *et al*., 2004; Foglio CARG, 2009). Co-seismic tectonic ruptures along and close to the NW-trending, SW-dipping, Paganica normal fault were found: the most clear of which coincide with the most prominent of its long-term geomorphic expression (Fig. 5). The ruptures are confined to a maximum distance of 30 m from the base of the scarp. They extend to about 2.5 km (Fig. 5) and consist of vertical dislocations or warps (~40%) and open cracks (~60%), with a persistent orientation of N130°–140° (Fig. 6). The envelope of these ruptures describes a surface trace that occurs regardless of slope angle, the type of deposits crossed or the type of manmade features. Individual ruptures are a maximum of 25 m long, and are commonly organized as up to −2.0 m left-steps (with rare secondary right steps), but with no overlap (Fig. 6). Many of the ruptures are associated with southwest-side down vertical throw reaching a maximum of about 0.1 m, sometimes with a slight (few millimetres) dextral component. Conversely, where open cracks are common, the vertical displacement is expressed as a ground flexure with a comparable amount of separation. Locally, the open cracks branch into a zone of deformation with a maximum width of 15 m (e.g. at the outlet of the Raiale stream, in Holocene fluvial deposits), with no appreciable vertical deformation along individual elements (Fig. 5). The amount of vertical separation and SW–NE widening of the ruptures increased slightly (twice at a few sites) in the days subsequent to the mainshock, suggesting the occurrence of afterslip on the primary fault plane. Both to the north and south of the 2.5 km alignment of ruptures along the Paganica fault, other discontinuous and sporadic breaks occurred with a trend ranging from N120° to N170°. If these features belong to the Paganica surface rupture, the total length of surface faulting may exceed 6 km (inset in Fig. 5).

The Mt. Bazzano fault

The north-east dipping Mt. Bazzano fault (antithetic to the Paganica fault) is clearly expressed by a bedrock fault plane along a NW–SE 3-km-long limestone ridge, located between L'Aquila and the Paganica alluvial fan (Fig. 3). At the base of the bedrock fault plane, we observed a whitish fault ribbon (Fig. 7a) with a constant height of about 50 mm. Fresh north-east facing scarps are present in the unconsolidated slope deposits at the foot of a main 1.5–3.0 m high pre-existing scarp. These discontinuous scarps extend for about 1 km with an average strike of N320°, suggesting co-seismic vertical displacements of 0.1–0.3 m (Fig. 7b).

The Monticchio-Fossa fault

The north-east dipping Monticchio-Fossa fault runs along the eastern slope of the Mt. Ocre ridge (Foglio CARG, 2009) and is aligned with the south-eastward continuation of the Mt. Bazzano fault (Fig. 3). The long-term surface expression of the Monticchio-Fossa fault consists of a fault scarp in cemented breccias, with a more recent, parallel scarp running along the base of the slope. Surface ruptures at least 300 m long occurred on and close to the recent geomorphic scarp, particularly near Fossa village. Here, an excavation across the scarp exposed part of the fault zone in unconsolidated colluvial and slope wash deposits, with evidence of dip-slip palaeo-offset (NE side down). At this site, newly formed 10–20 mm wide fissures, without appreciable vertical displacement, had formed along the pre-existing fault planes (Fig. 8a).

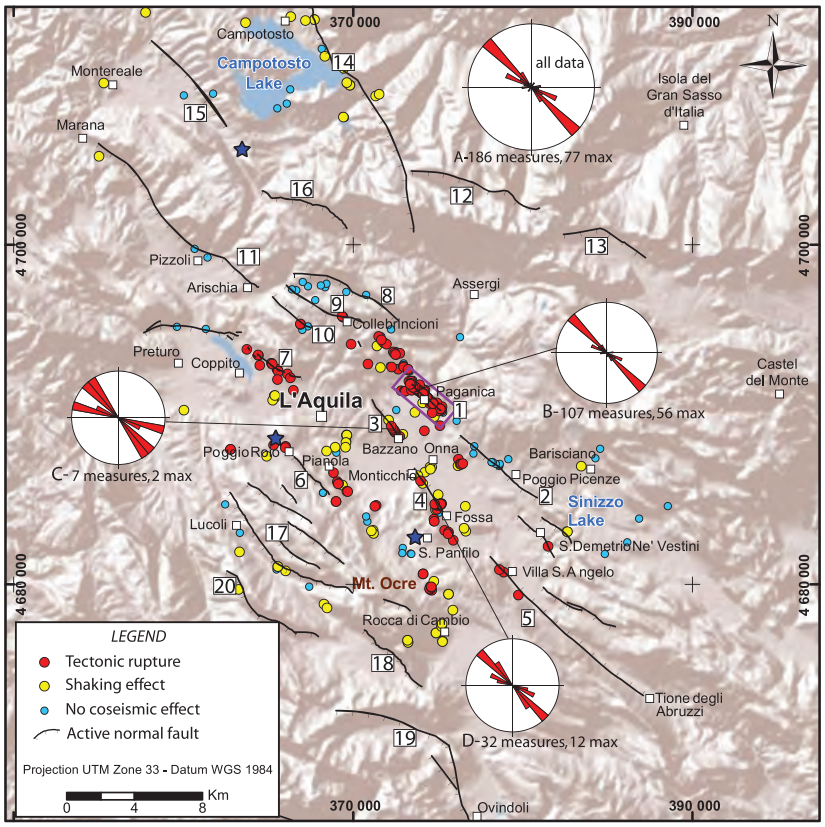

Fig. 3 Map of the surveyed co-seismic effects. Sites of measurements are distinguished between tectonic ruptures and shaking effects. The purple box includes the Paganica ruptures, which are interpreted to be primary surface faulting (shown in detail in Fig. 5). We also show the sites along faults where no ruptures or other effects were observed. Stars indicate the three main events. Rose diagrams of the tectonic surface ruptures: (A) total data; (B) Paganica fault; (C) Mt. Bazzano fault and (D) Monticchio-Fossa fault. We do not report rose diagrams when the data are less than five measurements. Active normal faults are numbered as follow: 1 – Paganica, 2 – Poggio Picenze-S. Demetrio, 3 – Mt. Bazzano, 4 – Monticchio-Fossa, 5 – S. Angelo-Tione, 6 – Roio-Canetra, 7 – Mt. Pettino, 8 – Mt. Stabiata, 9 – Colle Praticciolo, 10 – Valle del Macchione, 11 – Mt. Marine, 12 – Gran Sasso-Mt. Corvo, 13 – Campo Imperatore, 14 – Mt. Laga, 15 – SW-Campotosto, 16 – Mt. S. Franco, 17 – Mt. Ocre system, 18 – Campo Felice, 19 – Ovindoli-Pezza, 20 – Mt. Orbetello.

Along the lower scarp at the base of the ridge, we mapped N130° striking left-stepping fractures, with 50–150 mm of north-east facing vertical offset at some locations (Fig. 8b).

The Roio-Canetra, Colle Praticciolo, Valle del Macchione and Mt. Pettino faults

Ruptures with small offsets and of limited and discontinuous extent were observed along other faults within the area (Fig. 3). A fresh free-face scarp with a constant height up to 30 mm, associated with local fissuring and detachment of the soil and loose debris, was mapped along the bedrock plane of the SW-dipping Roio-Canetra fault (Fig. 9a), for a minimum length of 1 km. A 10-mm free-face scarp was also observed along the SW-dipping Colle Praticciolo fault, in the vicinity of Collebrincioni (Fig. 9b). Local ground ruptures occur along the NE-dipping Valle del Macchione fault extending for about 100 m at the base of a pre-existing scarp. Similarly, vertical offsets in soil and debris of 0.1–0.2 m, mostly parallel to the slope, were observed along the SW-dipping Mt. Pettino fault (Fig. 9c) on discontinuous strands, each with a length of several tens of metres.

Shaking effects

Within the Aterno River valley, there were many features that we interpret as being induced by the intense seismic shaking, not associated with tectonic structures, but related to gravitational or differential compaction phenomena

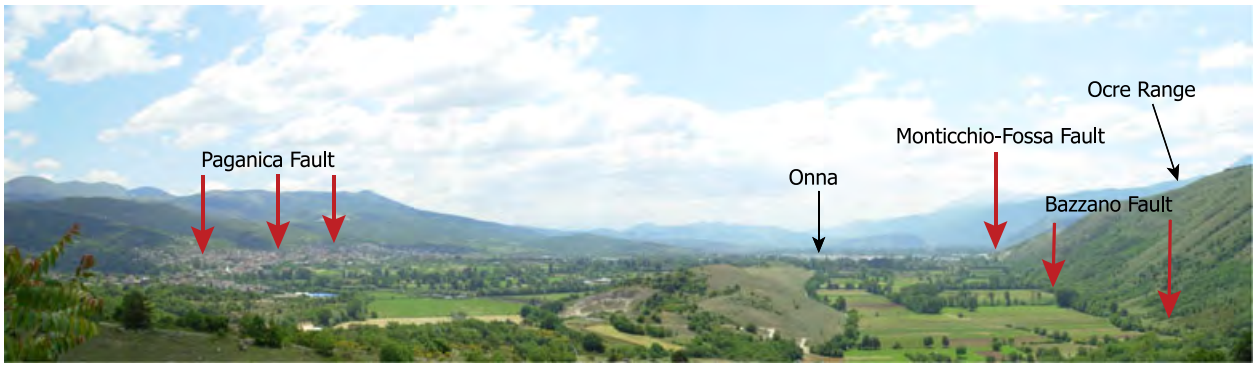

Fig. 4 View from the NW of the eastern side of the Middle Aterno valley. The Paganica and Bazzano faults are in the foreground of the picture, the Monticchio-Fossa fault is in the background. Onna is the village most damaged by the 6 April earthquake (10 on the MCS scale). The distance between the Paganica and the Bazzano faults is ~2.5 km.

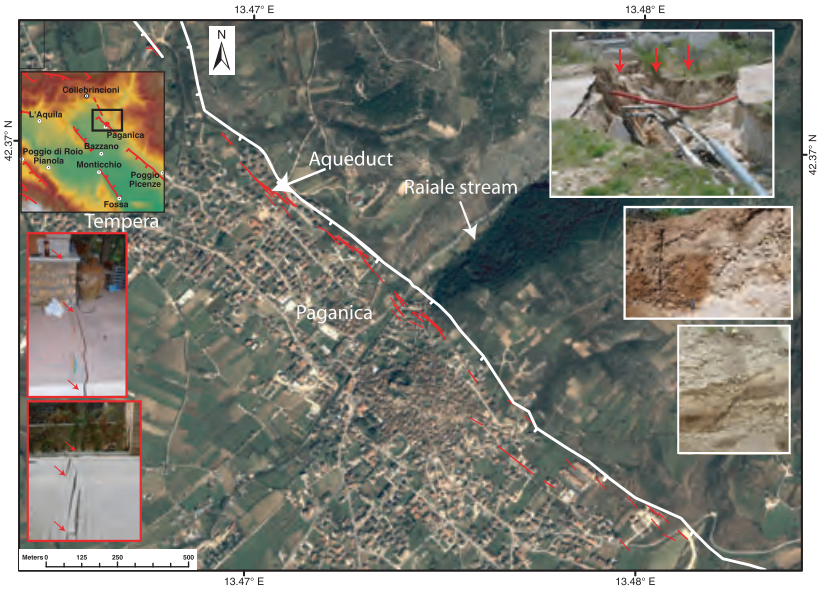

Fig. 5 Details of the Paganica surface faulting. Red lines are the mapped rupture strands (see purple box in Fig. 3 for location), and the white line is the long-term Paganica fault trace. The inset in the upper left shows the fault setting in this sector of the Aterno valley (dashed red line is the inferred NW-prolongation of the surface ruptures). Photos with white frame show details of the long-term expression and displacements of the Paganica fault. In particular, a natural trench originated by collapse of a major aqueduct in the village of Paganica which exposed a complex fault structure. The upper photo is the aqueduct excavation before repair where the cutting exposed the Paganica fault zone (red arrows point to faults). Photos with the red frame show details of the April ruptures (red arrows) crossing man-made features in the urbanized area.

(Fig. 3). Among the significant failures and sediment compaction features was a 150 m long, NW–SE striking, set of open cracks affecting the alluvial sediments near Onna Village (Fig. 10a). Also, numerous ruptures occurred parallel to the youngest terrace risers in the alluvial plain of the Vetoio stream (west of L'Aquila) (Fig. 10b). The karstic Sinizzo lake, near S. Demetrio ne' Vestini village, was affected by a large collapse expressed by open failures encircling the shore (Fig. 10c). The highly fractured and weathered bedrock in the epicentral area and the steep fault-related slopes contributed to the formation of seismically induced small-scale gravitational failures as along the steepest slopes of the Mt. Ocre range (Fig. 10d). Landslides of medium size, debris slides and broken trees occurred in the area of the Campotosto Lake (Fig. 10e) and along the SW-Campotosto and Mt. Laga faults, which were strongly shaken by the 9 April aftershock (Fig. 1).

Fig. 6 Surface ruptures along the Paganica fault. The breaks consist of vertical dislocations or warps and open cracks, with a persistent orientation of N130°–140°. The ruptures cross different types of deposits and man-made features.

Discussion

We found evidence of co-seismic tectonic ruptures in the epicentral area. The alignment of ruptures along the Paganica fault shows a spatial continuity not observed along any other structure within the area. These ruptures are located at the base of the most evident long-term geomorphic expression of the Paganica fault and are particularly clear along an ~2.5 km section of the scarp. To the north and to the south, they fade out and are difficult to follow. The Paganica fault ruptures cut across loose and cemented deposits, buildings and structures, always with a constant N130°–140° strike and irrespective of local slope direction.

The continuity and the consistency of the ruptures lead us to interpret them as the surface rupture of the fault responsible for the Mw 6.3 earthquake. This interpretation is in agreement with the seismological data as well as with GPS and DInSar modelling (Fig. 11, Anzidei *et al.*, 2009; Atzori *et al.*, 2009; Chiarabba *et al.*, 2009). Seismicity recorded by INGV permanent and temporary stations shows that the 9-km-deep mainshock and the aftershocks (generally deeper than 2 km) clearly image a ~50° SW-dipping normal fault the projection of which to the surface coincides with the Paganica fault (Fig. 1). Moreover, based on seismological and geodetic models, the most shallow slip patch (with ~1 m of displacement) is located below the 2.5-km-long surface ruptures (Atzori *et al.*, 2009; Cirella *et al.*, 2009). Thus, we interpret the main 2.5-km-long Paganica fault ruptures to represent the propagation to the surface of the slip at depth on the mainshock fault. The ruptures observed along the Bazzano and Fossa antithetic faults can be interpreted as triggered slip considering: (1) their geometrical

Fig. 7 Surface ruptures along the Mt. Bazzano fault: (a) free-face at the base of the bedrock fault plane; (b) NE-facing scarp in slope deposits.

Fig. 8 Surface ruptures along the Monticchio-Fossa fault: (a) newly open crack along pre-existing fault plane; (b) fractures with cm-scale north-east facing vertical offset (red arrows).

Fig. 9 Surface ruptures on: (a) Roio-Canetra fault, showing fresh free-face and soil detachment on the bedrock fault plane and fissuring in the loose debris (red arrows); (b) Colle Praticciolo fault, showing fresh free-face along the bedrock fault plane; (c) Mt. Pettino fault, with soil and debris offset along the fault scarp.

arrangement, these faults are shallow-rooted on the Paganica fault, accommodating the extension on its hanging-wall without reaching seismogenic depth; (2) their regular throw, and that ruptures are consistent with the long-term fault expression; (3) they occur both on gentle and steep slopes thus independently from gravitational effects; and (4) they currently contribute to the graben growth along with the Paganica fault as suggested by its long-term geomorphic expression. All the other ruptures appear to be related to shaking or gravitational movement.

The small surface displacement observed on the Paganica fault associated with Mw 6.3 earthquake raises questions about the range of seismogenic behaviour of the fault. On the Paganica fault itself, on the antithetic Monticchio-Fossa fault, and also on other faults in the region (e.g. Mt. Marine, Campo Imperatore, Cerasitto-Campo Felice–Ovindoli-Pezza faults – see Galli *et al.*, 2008 and references therein), there is evidence for large cumulative displacements (average scarp heights of several m) and for individual events of surface faulting with vertical throws of 0.25–1.0 m (Fig. 5). Historical seismicity in the region has also recorded earthquakes in the $M\sim7$ range the latest of which occurred in 1915 ~40 km to the south. Thus, if during previous events the Paganica fault has ruptured with larger displacement at the surface, and assuming that surface displacement is scaled with earthquake magnitudes, then this fault may have produced events with larger magnitude than the 2009 event. The dense array of surface ruptures associated with the L'Aquila earthquake also begs the question of the connectivity of the surface faults at seismogenic depth. Do they connect at depth so that the surface array represents active splays of the 2009 seismogenic plane, or are the surface faults merely accommodating the deformation induced by the deep fault? The complex surface deformation observed recently requires us to reconsider the seismogenic model built for this region on the basis of historical and palaeoseismological evidence.

Conclusion

The 2009 earthquake sequence was associated with an extensive and com-

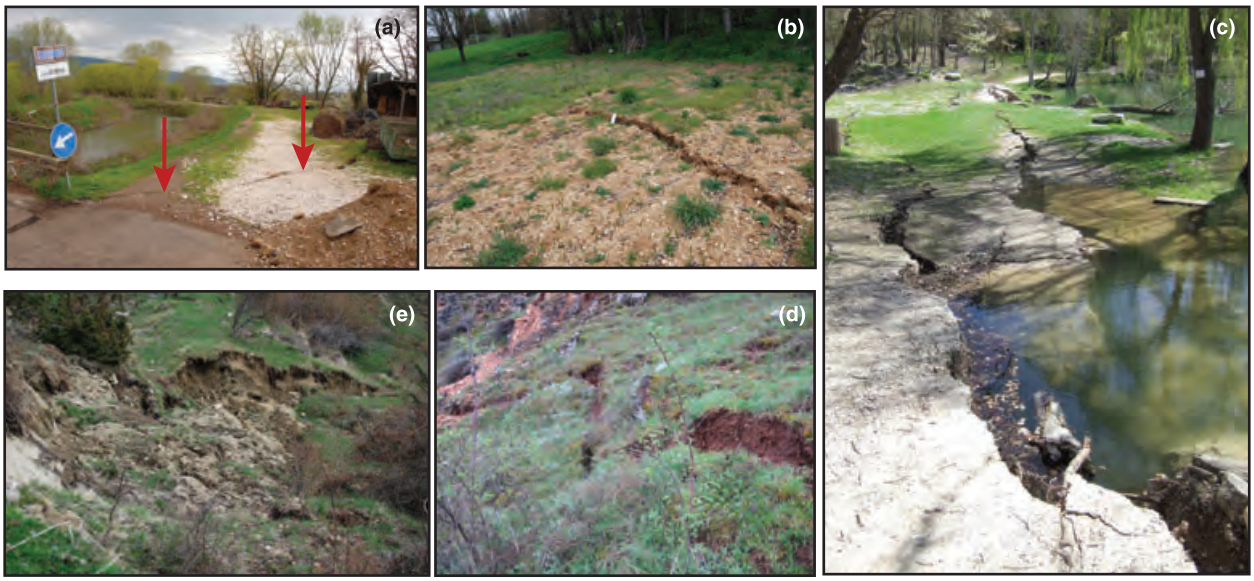

Fig. 10 Shaking effects: (a) open cracks (red arrow) in alluvial sediments beside the Aterno River, close to the village of Onna; (b) ruptures in the alluvial plain of the Vetoio stream (west of L'Aquila); (c) open fissures (up to 2.0 m wide, and up to 1.5 m deep) in the banks of the Sinizzo Lake; (d) landslide surface of detachment along the eastern slope of Mt. Ocre range; (e) landslide in slope deposits in the Campotosto area.

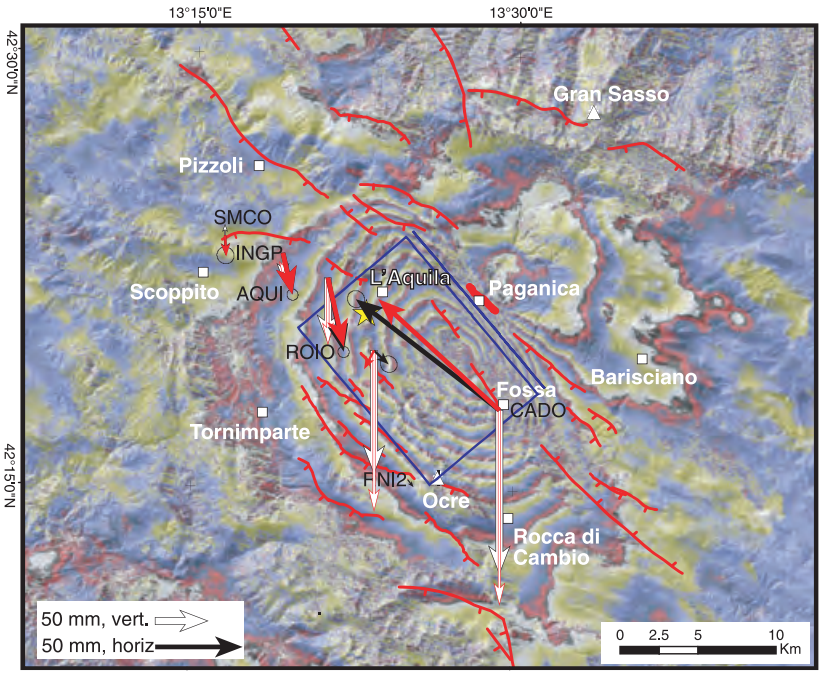

Fig. 11 GPS and DInSar data modelling with respect to the active faults of the area. The arrows represent the GPS data (Anzidei *et al.*, 2009): black and white arrows are the observed horizontal and vertical displacements, respectively; red arrows are the modelled horizontal and vertical displacements. A blue box marks the surface projection of the modelled source. DInSar data (Atzori *et al.*, 2009): the different colour fringes define the displacement field (almost vertical) because of the earthquake from the ENVISAT Interferogram. The maximum lowering is about 0.25 m between L'Aquila and Fossa village (each fringe corresponds to 25 mm). The heavy red line shows the envelope of the surface fractures identified in the field.

plex set of surface features. A NW–SE orientation of the ruptures is persistent throughout the whole area (Fig. 3: see rose diagram A), with a particularly consistent trend of N130°–140° along the Paganica, Bazzano, Monticchio-Fossa faults (Fig. 3: rose diagrams B–D).

The continuity of the ruptures, the consistency between the average trend of these ruptures and focal plane solutions, seismicity distribution, geodetic and DInSar observations and the coincidence of the ruptures with the late Quaternary trace of the Paganica fault, lead us to interpret these ruptures as the surface expression of the seismogenic fault. Our data indicate that rupture of the Paganica fault to produce the Mw 6.3 earthquake propagated to reach the surface, causing minor, but detectable surface faulting. The limited extent and the small throw of the surface rupture, in comparison with the cumulate size of late Quaternary Paganica fault scarp, and with other well-expressed active faults in the region, suggests that the Paganica fault is capable of rupture with a larger maximum magnitude earthquake than the 2009, Mw 6.3 event. Thus, although the L'Aquila earthquake and associated faulting

caused major damage and loss of life, it does not fully characterize the seismic hazard associated in this area.

Acknowledgements

Special thanks to the local people who, despite their tragedy, have been always collaborative and kind, giving also indications on ruptures even when crossing their damaged property. We are grateful to all the colleagues belonging to the Emergeo team (INGV prompt geological survey team) during the survey, to the Department of Civil Protection for providing the helicopter flight for aerial recognition. Special thanks also to David P. Schwartz for the careful review of the field work and the manuscript. Kelvin Berryman and an anonymous reviewer provided thorough reviews that substantially helped in improving the manuscript. A photo gallery is available at http://portale.ingv.it/produzione-scientifica/quaderni-di-geofisica/quaderni-di-geofisica-2009 (Emergeo Working Group, 2009).

References

Akinci, A., Galadini, F., Pantosti, D., Petersen, M., Malagnini, L. and Perkins, D., 2009. Effect of time dependence on probabilistic seismic-hazard maps and deaggregation for the central Apennines, Italy. *Bull. Seismol. Soc. Am.*, **99**, 585–610. Doi:10.1785/0120080053.

Anzidei, M., Boschi, E., Cannelli, V., Devoti, R., Esposito, A., Galvani, A., Melini, D., Pietrantonio, G., Riguzzi, F., Sepe, V. and Serpelloni, E., 2009. Coseismic deformation of the destructive April 6, 2009 L'Aquila earthquake (central Italy) from GPS data. *Geophys. Res. Lett.*, **36**, L17307. Doi:10.1029/2009GL039145.

Atzori, S., Hunstad, I., Chini, M., Salvi, S., Tolomei, C., Bignami, C., Stramondo, S., Trasatti, E. and Antonioli, A., 2009. Finite fault inversion of DInSAR coseismic displacement of the 2009 L'Aquila earthquake (central Italy). *Geophys. Res. Lett.*, **36**, L15305. Doi:10.1029/2009GL039293.

Bagnaia, R., D'Epifanio, A. and Sylos Labini, S., 1992. Aquila and sub-aequan basins: an example of Quaternary evolution in central Apennines, Italy. *Quat. Nova*, **II**, 187–209.

Barchi, M., Galadini, F., Lavecchia, G., Messina, P., Michetti, A.M., Peruzza, L., Pizzi, A. and Tondi, E. (eds), 2000. *Sintesi delle conoscenze sulle faglie attive in Italia Centrale: parametrizzazione ai fini della caratterizzazione della pericolosità sismica*. GNDT, Gruppo Nazionale per la Difesa di terremoti, Special Publication, Roma, 62 pp.

Boncio, P., Lavecchia, G. and Pace, B., 2004. Defining a model of 3D seismogenic sources for Seismic Hazard Assessment applications: the case of central Apennines (Italy). *J. Seismol.*, **8/3**, 407–425.

Chiarabba, C., Amato, A., Anselmi, M., Baccheschi, P., Bianchi, I., Cattaneo, M., Cecere, G., Chiaraluce, L., Ciaccio, M.G., De Gori, P., De Luca, G., Di Bona, M., Di Stefano, R., Faenza, L., Govoni, A., Improta, L., Lucente, F.P., Marchetti, A., Margheriti, L., Mele, F., Michelini, A., Monachesi, G., Moretti, M., Pastori, M., Piana Agostinetti, N., Piccinini, D., Roselli, P., Seccia, D. and Valoroso, L., 2009. The 2009 L'Aquila (central Italy) Mw6.3 earthquake: main shock and aftershocks. *Geophys. Res. Lett.*, **36**, L18308. Doi:101029/2009GL039627.

Cinti, F.R., Faenza, L., Marzocchi, W. and Montone, P., 2004. Probability map of the next large earthquakes in Italy. *G Cubed*, **5**, 1. Doi:10.1029/2004GC000724.

Cipollari, P. and Cosentino, D., 1995. Miocene unconformities in the Central Apennines: geodynamic significance and sedimentary basin evolution. *Tectonophysics*, **252**, 375–389.

Cirella, A., Piatanesi, A., Cocco, M., Tinti, E., Scognamiglio, L., Michelini, A., Lomax, A. and Boschi, E., 2009. Rupture history of the 2009 L'Aquila (Italy) earthquake from non-linear joint inversion of strong motion and GPS data. *Geophys. Res. Lett.*, **36**, L19304. Doi:10.1029/2009GL039795.

CPTI WORKING Group, 2004. *Catalogo Parametrico dei Terremoti Italiani, versione 2004 (CPTI04)*. INGV, Bologna. Available at: http://emidius.mi.ingv.it/CPTI04/.

D'Agostino, N., Mantenuto, S., D'Anastasio, E., Avallone, A., Barchi, M., Collettini, C., Radicioni, F., Stoppini, A. and Fastellini, G., 2008. Contemporary crustal extension in the Umbria– Marche Apennines from regional CGPS networks and comparison between geodetic and seismic deformation. *Tectonophysics*, **476**, 1–2, 3–12. Doi:10.1016/j.tecto.2008.09.033.

Emergeo Working Group, 2009. Field geological survey in the epicentral area of the Abruzzi (central Italy) seismic sequence of April 6th, 2009. *Quad. Geofis.*, **70**. Istituto Nazionale di Geofisica e Vulcanologia, ISSN 1590-2595. Available at: http://portale.ingv.it/produzione-scientifica/quaderni-di-geofisica/quaderni-di-geofisica-2009.

Foglio CARG 1:50,000, 2009. *Cartografia Geologica Ufficiale*. Foglio CARG 1:50,000 N. 359, L'Aquila.

Galadini, F. and Galli, P., 2000. Active tectonics in the Central Apennines (Italy)-input data for Seismic Hazard Assessment. *Nat. Hazards*, **22**, 225–270.

Galadini, F., Meletti, C. and Rebez, A. (eds), 2000. *Le ricerche del GNDT nel campo della pericolosità sismica (1996–1999)*. CNR-Gruppo Nazionale per la Difesa dai Terremoti, Roma, 397 pp.

Galadini, F., Galli, P. and Moro, M., 2003. Paleoseismology of silent faults in the Central Apennines (Italy): the Campo Imperatore Fault (Gran Sasso Range Fault System). *Ann. Geophys.*, **46**, 793–813.

Galli, P., Galadini, F., Moro, M. and Giraudi, C., 2002. New paleoseismological data from the Gran Sasso d'Italia area (central Apennines). *Geophys. Res. Lett.*, **29**, 38.1–38.4. Doi:10.1029/2001GL013292.

Galli, P., Galadini, F. and Pantosti, D., 2008. Twenty years of paleoseismology in Italy. *Earth Sci. Rev.*, **88**, 89–117. Doi:10.1016/j.earscirev.2008.01.001.

Ghisetti, F. and Vezzani, L., 1999. Depth and modes of Pliocene–Pleistocene crustal extension of the Apennines (Italy). *Terra Nova*, **11**, 67–72.

Gruppo di Lavoro M.P.S., 2004. *Redazione della mappa di pericolosità sismica prevista dall'*Ordinanza PCM del 20 marzo 2003. Rapporto Conclusivo per il Dipartimento della Protezione Civile, INGV, Milano/Roma, Aprile 2004, 65 pp. + 5 appendici. Available at: http://zonesismiche.mi.ingv.it/.

Lavecchia, G., Brozzetti, F., Barchi, M., Menichetti, M. and Keller, J.V.A., 1994. Seismotectonic zoning in east-central Italy deduced from an analysis of the Neogene to present deformations and related stress fields. *Geol. Soc. Am. Bull.*, **106**, 1107–1120.

Meletti, C., Patacca, E. and Scandone, P., 2000. Construction of a seismotectonic model: the case of Italy. *Pure Appl. Geophys.*, **157**, 11–35.

Montone, P., Mariucci, M.T., Pondrelli, S. and Amato, A., 2004. An improved stress map for Italy and surrounding regions (central Mediterranean). *J. Geophys. Res.*, **109**, B10410. Doi:10.1029/2003JB002703.

Pace, B., Peruzza, L., Lavecchia, G. and Boncio, P., 2006. Layered seismogenic source model and probabilistic seismic-hazard analyses in central Italy. *Bull. Seismol. Soc. Am.*, **96**, 107–132.

Pantosti, D., D'Addezio, G. and Cinti, F.R., 1996. Paleoseismicity of the Ovindoli-Pezza fault, central Apennines, Italy: a history including a large, previously unrecorded earthquake in the Middle Ages (860–1300 A.D.). *J. Geophys. Res.*, **101** (B3) 5937–5959.

Patacca, E. and Scandone, P., 1989. Post-Tortonian mountain building in the Apennines; the role of the passive sink-

ing of a relic lithospheric slab. In: *The Lithosphere in Italy. Advances in Earth Science Research* (A. Boriani, M. Bonafede, G.B. Piccardo and G.B. Vai, eds). *Atti Conv. Lincei*, **80**, 157–176.

Pondrelli, S., Salimbeni, S., Morelli, A., Ekström, G., Olivieri, M. and Boschi, E., 2009. Seismic moment tensors of the April 2009, L'Aquila (Central Italy), earthquake sequence. *Geophys. J. Int.* Doi:10.111/j.1365-246X.2009.04418.x. (in press).

Salvi, S., Cinti, F.R., Colini, L., D'Addezio, G., Doumaz, F. and Pettinelli, E., 2003. Investigation of the active Celano–L'Aquila fault system, Abruzzi. *Geophys. J. Int.*, **155**, 805–818.

Speranza, F., Adamoli, L., Maniscalco, R. and Florindo, F., 2003. Genesis and evolution of a curved mountain front: paleomagnetic and geological evidence from the Gran Sasso range (central Apennines, Italy). *Tectonophysics*, **362**, 183–197.

Vezzani, L. and Ghisetti, F., 1998. *Carta Geologica dell'*Abruzzo, Scala 1:100,000. S.EL.CA., Firenze.

Received 16 June 2009; revised version accepted 6 October 2009

- APPENDIX G - Cinti, F.R., Pantosti, D., De Martini, P.M., Pucci, S., **Civico, R.**, Pierdominici, S., Cucci, L., Brunori, C.A., Pinzi, S., Patera, A. (2011), *Evidence for surface faulting events along the Paganica Fault prior to the April 6, 2009 L'Aquila earthquake (Central Italy).* J. Geophys. Res., 116, B07308, doi:10.1029/2010JB007988.

Evidence for surface faulting events along the Paganica fault prior to the 6 April 2009 L'Aquila earthquake (central Italy)

F. R. Cinti,[1] D. Pantosti,[1] P. M. De Martini,[1] S. Pucci,[1] R. Civico,[1] S. Pierdominici,[1] L. Cucci,[1] C. A. Brunori,[1] S. Pinzi,[1] and A. Patera[1]

Received 10 September 2010; revised 20 April 2011; accepted 29 April 2011; published 29 July 2011.

[1] We performed paleoseismological investigations at four sites across the normal Paganica fault (PF) (source of the 2009 Mw 6.3 L'Aquila earthquake), with the goal of reconstructing the rupture history and of contributing to the evaluation of the maximum event expected along the PF. We recognized five distinct surface faulting earthquakes (including the 2009) in the trenches. The age of the penultimate event is consistent with the 1461 earthquake; the third event back occurred around 1000 AD. The two oldest events have larger uncertainties and occurred in the interval 760 BC–670 AD and 2900–760 BC, respectively. The along-strike vertical displacement for each paleoevent has a limited variability consistently with the fairly homogeneous slip observed in 2009 along the northern part of the rupture. Conversely, the throws change between distinct events and range between 0.15 m in 2009 (maximum estimate) and close to 0.4 (lower bound estimate) in earlier events. These paleorecords and the high fault escarpments imply that earthquakes larger than 2009 occurred on the PF, with implications for the level of hazard. Recurrence intervals also reflect a change with time, the average interval before ~1000 AD is longer compared to that after this date. Two events occurred in the 2000–4000 years preceding ~1000 AD, while three events occurred since ~1000 AD. The age uncertainties affecting the interpreted events prevent the evaluation of a unique value for interevent interval; the older events appear closely spaced in time or far apart depending on the upper or lower boundary of the age interval. We tentatively assign an average interevent time of ~500 years for the three youngest events, whereas the time elapsed between the previous ones could be larger, in the order of 1000–2000 years. We calculate a late Pleistocene dip-slip rate for the PF of 0.2–0.4 mm/yr, consistent with 0.25–0.5 mm/yr for the early Pleistocene. Using age and throw of individual events, we calculate a similar late Holocene average dip-slip rate of ~0.3–0.4 mm/yr. This suggests that the portion of the PF where the 2009 continuous surface faulting occurred has fairly a constant average slip release since late Pleistocene. Finally, we discuss different rupture scenarios and alternative models of occurrence compatible with our data and their variability.

Citation: Cinti, F. R., D. Pantosti, P. M. De Martini, S. Pucci, R. Civico, S. Pierdominici, L. Cucci, C. A. Brunori, S. Pinzi, and A. Patera (2011), Evidence for surface faulting events along the Paganica fault prior to the 6 April 2009 L'Aquila earthquake (central Italy), *J. Geophys. Res.*, *116*, B07308, doi:10.1029/2010JB007988.

1. Introduction

1.1. The 2009 Earthquake and the Historical Seismicity of the L'Aquila Area

[2] The L'Aquila 6 April 2009 (01:32 UTC) Mw 6.3 earthquake struck the Apennines portion of the Abruzzi region and was felt in a wide part of central Italy (inset in Figure 1). The earthquake killed more than 300 people and devastated the town of L'Aquila (~73,000 inhabitants) as well as several nearby villages, leaving 60,000 homeless. The Mw 6.3 main shock originated in the upper crust at a depth of 9.5 km, within the typical seismogenic thickness of central Apennines [*Chiarabba et al.*, 2009]. The main shock was the apex of a 4 month long seismic sequence that progressively alarmed the population, especially after the largest foreshock (Ml 4.1) occurred on 30 March. Seven Mw 5+ and numerous Mw 4+ events occurred in the two weeks following the 6 April main shock, and a total of >30,000 seismic events were recorded during the aftershock sequence (Figure 1). The seismicity distribution [*Chiarabba et al.*, 2009], the focal mechanism of the main shock [*Pondrelli et al.*, 2010], and GPS, DinSar, and strong motion

[1]Istituto Nazionale di Geofisica e Vulcanologia, Rome, Italy.

0148-0227/11/2010JB007988

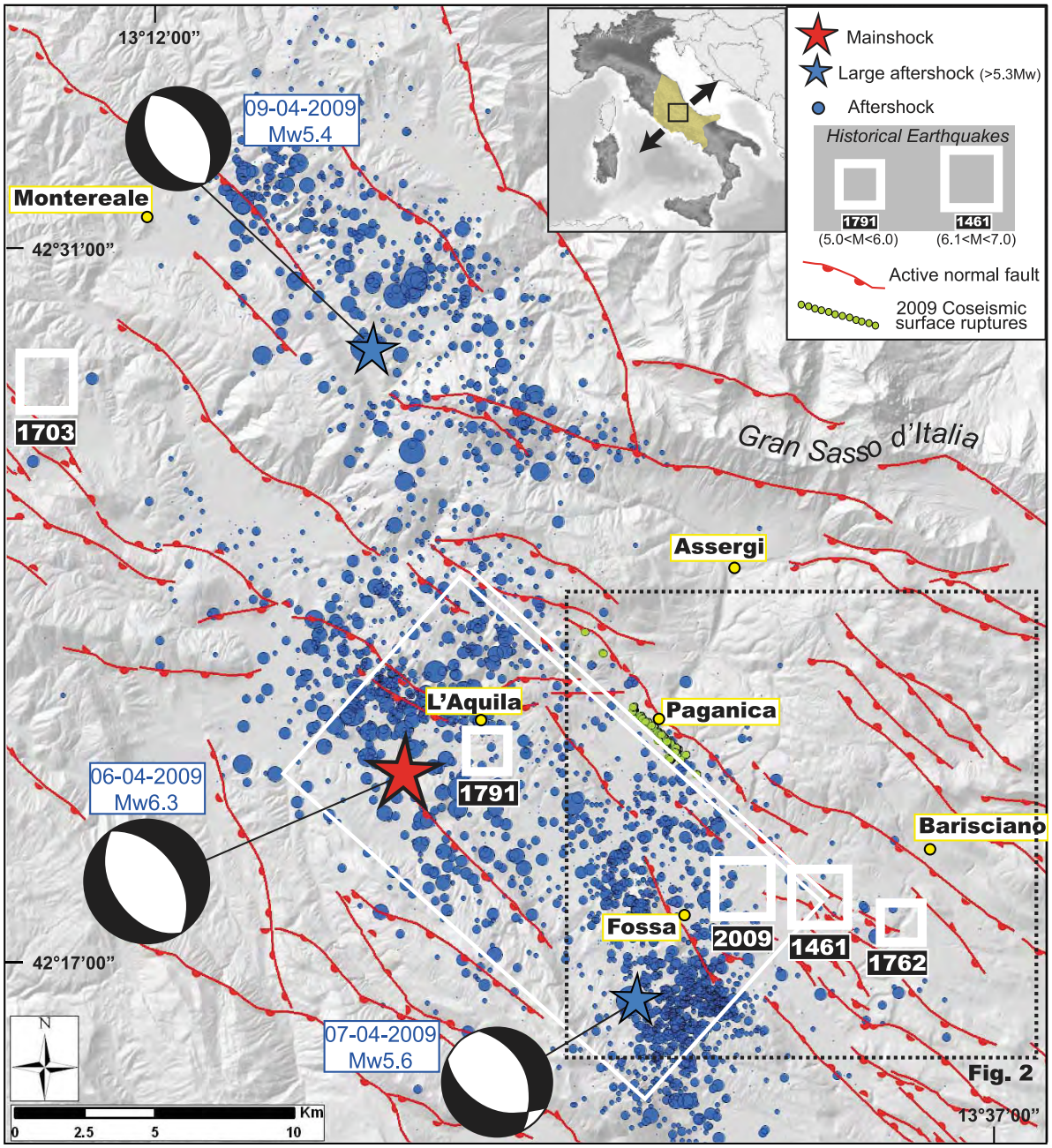

Figure 1. The 2009 L'Aquila earthquake sequence as recorded by the INGV Italian National Seismic Network [*Chiarabba et al.*, 2009]. Focal mechanisms of the main shock and of the two largest aftershocks [*Pondrelli et al.*, 2010], historical seismicity (M > 5.0; http://emidius.mi.ingv.it/CPTI04), and active faults are shown. The macroseismic epicentral location (from damage and felt reports) of the 2009 event was computed using the code Boxer 4.0 [*Gasperini et al.*, 2010] and is shown for comparison with seismic intensity of historical earthquakes. The white box is the projection to the surface of the ~18 km long fault according to the model of *Cirella et al.* [2009]; the white line is the expected emergence of the fault at the surface. The green dots highlight the 3 km long undebated portion of surface faulting [*Falcucci et al.*, 2009; *Boncio et al.*, 2010; *Emergeo Working Group*, 2010]. The dashed box to the lower right encloses the area of Figure 2. The inset in the upper right shows the direction of extension across the central Apennines and the regional felt area for the 6 April main shock (in yellow from http://www.haisentitoilterremoto.it/repository/2206496920/2206496920mcs.jpg).

modeling [*Anzidei et al.*, 2009; *Atzori et al.*, 2009, *Cheloni et al.*, 2010; *Cirella et al.*, 2009] concur to image a 15–18 km long, 50°SW dipping normal fault, coinciding with the Paganica fault (referred to also as PF) as the source of the earthquake. Surface ruptures were observed along at least 3 km of the Paganica fault [*Falcucci et al.*, 2009; *Boncio et al.*, 2010; *Emergeo Working Group*, 2010] (see the following section for a description).

[3] According to the 2004 national seismic hazard map [*Gruppo di Lavoro M.P.S.*, 2004; see also *Cinti et al.*, 2004] and regional time-dependent hazard studies [*Pace et al.*, 2006; *Akinci et al.*, 2009], a high seismic hazard characterizes this region. In fact, as reported in the Italian historical records, the Abruzzi region has been repeatedly hit by large magnitude, destructive earthquakes. Among these were the 1349, 1703, and 1915 events, all having $M \geq 6.5$ and $I > 10$ MCS (Mercalli-Cancani-Sieberg scale) (http://emidius.mi.ingv.it/CPTI04) and occurring within 35 km of the 2009 epicenter. The historical earthquakes closest to the town of L'Aquila have $M < 6.5$ and are the 1791 Maw 5.4, 1762 Maw 5.9 and the 1461 Maw 6.4 events (Maw = average weighted Magnitude derived from macroseismic intensities (http://emidius.mi.ingv.it/CPTI04) (Figure 1). Strong similarities in the distribution of intensities and in the temporal pattern of foreshock and aftershock activity between the 2009 and 1461 earthquakes suggest that these two events may be possibly "twins" produced by the same structure [*Tertulliani et al.*, 2009]. The historical record in the 2009 epicentral area seems to describe only moderate size seismicity, with earthquakes less energetic than in the surrounding region. However, this difference may be only apparent, since from paleoseismological studies we learn that the average recurrence time for $M > 6.5$ earthquakes in the region is on the order of one or more millennia [*Michetti et al.*, 1996; *Pantosti et al.*, 1996; *Galadini and Galli*, 1999; *D'Addezio et al.*, 2001; *Galli et al.*, 2002; *Moro et al.*, 2002; *Galadini et al.*, 2003; *Salvi et al.*, 2003]. This uncertainty raises critical questions about the true seismic potential of this area.

1.2. The Paganica fault and the 6 April 2009 Surface Rupture

[4] The central Apennines are part of a thrust and fold mountain belt dissected by intense extensional tectonics that, since late Pliocene time, have led to the formation of intramountain basins controlled by NW–SE trending normal faults such as the Paganica fault. Several different maps of the PF were published both before [e.g., *Bagnaia et al.*, 1992; *Vezzani and Ghisetti*, 1998; *Boncio et al.*, 2004; *Italian Geological Cartography*, 2009] and after the L'Aquila earthquake [*Falcucci et al.*, 2009; *Boncio et al.*, 2010]. Before the earthquake only the portion of the PF in proximity of the alluvial fan of the Raiale stream (Figures 2 and 3) was consistently reported and its seismic potential recognized [*Pace et al.*, 2006].

[5] A detailed geological and geomorphic analysis of the Paganica fault system and of the Quaternary depositional setting of the area was recently achieved by *Civico et al.* [2010] and is synthesized in Figure 2. Together with antithetic faults that bound the southwestern side of the Middle Aterno valley, the PF system forms a graben that controls the Holocene depocenter (Figure 2). Along the northern portion of the fault, between Collebrincioni and Paganica villages, the deformation is localized on a few closely spaced splays (in a 0.5 km wide band). To the south, the fault system opens into a set of parallel, km-spaced elements (Figure 2). These strands dissect the Quaternary basin and produce a staircase landform with paleosurfaces separated by scarps on deposits that are progressively younger and less elevated toward the present Aterno River valley. The preservation, the continuity, and the height of the escarpments were used by *Civico et al.* [2010] to define a first-order hierarchy among the numerous NW trending, SW and NE dipping fault strands. A possible interpretation of this complex setting is shown in the sketch in the inset of Figure 2. In this interpretation, the Paganica normal fault is seen as a complex fault system that has a zone of overlap and stepover with the Barisciano and Middle Aterno fault systems. Based on the tectonic and geomorphic expression, the northern boundary of the PF system is interpreted to be near Collebrincioni, where a series of WNW trending, right, en echelon splays occur. The southern boundary of the system is set within the zone of extremely distributed deformation at about the latitude of S. Demetrio nè Vestini village (almost coinciding with the southernmost boundary of the 2009 modeled earthquake source, see Figure 1). Given this interpretation, the length of the PF system is about 15–16 km. On the basis of offset early Pleistocene lacustrine deposits, *Civico et al.* [2010] estimate a minimum vertical slip rate of ca. 0.25–0.5 mm/yr across the Paganica fault system within the overlap zone between S. Demetrio nè Vestini and Barisciano.

[6] During the 2009 Mw 6.3 L'Aquila earthquake, unquestionable surface faulting occurred along the northwestern part of the Paganica fault system, coincident with the long-term, morphological scarp (Figure 2) [*Falcucci et al.*, 2009; *Boncio et al.*, 2010; *Emergeo Working Group*, 2010]. There, a 3 km long zone of coseismic ruptures was observed, consisting of vertical or flexural scarps, with a maximum of 0.15 m down to the SW throw, along with extensional cracks or open fissures. The ruptures have clear continuity and a persistent orientation of N130°–140° (Figure 3). The southern part of the ruptures zone includes a ~0.5 km long parallel splay. Whereas the main coseismic rupture runs along the base of a cumulative tectonic scarp that bounds the northeast side of the village of Paganica, this splay follows a younger, less prominent tectonic scarp in middle-late Pleistocene alluvial and colluvial deposits that should accommodate part of the deformation. Both to the north and south of these continuous sections of the rupture and along the same trend, discontinuous open fissures occurred, following mapped long-term splays of the PF [*Bagnaia et al.*, 1992; *Vezzani and Ghisetti*, 1998; *Boncio et al.*, 2004, 2010; *Civico et al.*, 2010], (Figure 2). The patchy ruptures in Holocene deposits south of the village of Paganica may reflect a buried structure. Depending on whether or not these discontinuous fissures are interpreted as evidence of coseismic slip on the PF at depth, the total length of the 6 April surface faulting is between 3 and 13 km [*Falcucci et al.*, 2009; *Boncio et al.*, 2010; *Emergeo Working Group*, 2010]. The geometry and kinematics of the 2009 surface ruptures are consistent with other coseismic data sets [*Anzidei et al.*, 2009; *Atzori et al.*, 2009; *Chiarabba et al.*, 2009]. Also, the location of the 3 km long zone of

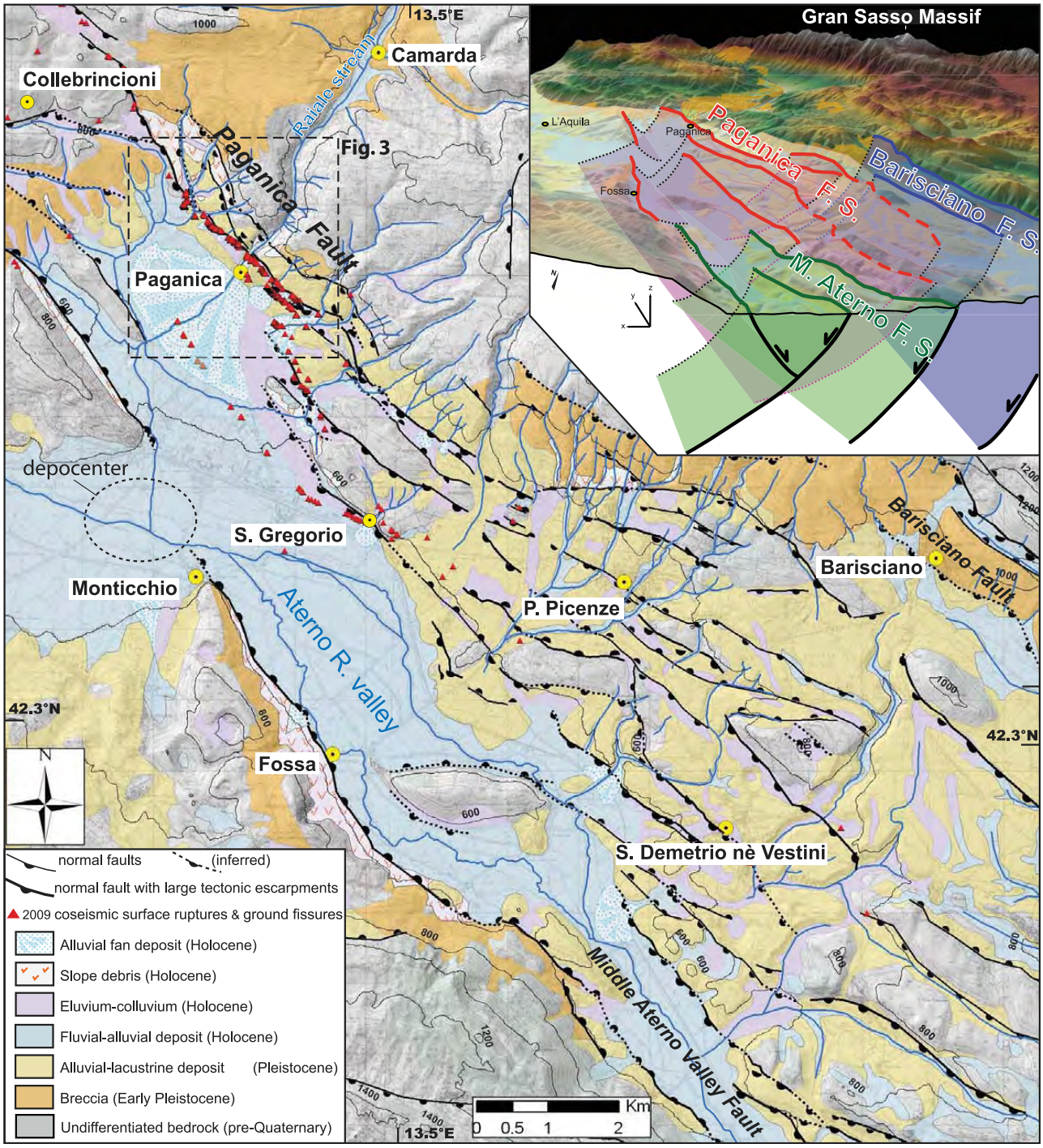

Figure 2. Active normal faults and Quaternary deposits of the Middle Aterno valley (modified from *Civico et al.* [2010]; location in Figure 1) and observations of 2009 coseismic surface rupture (red triangles) from *Falcucci et al.* [2009], *Boncio et al.* [2010], and *Emergeo Working Group* [2010]. Continuous ruptures were mapped for about 3 km in proximity of the Raiale stream alluvial fan. The dashed box encloses the area of Figure 3. The inset presents a possible 3D interpretation of the complex setting of this part of the Aterno Valley with three main overlapping fault systems: Paganica (red), Barisciano (blue) and Middle Aterno (green) [modified from *Civico et al.*, 2010].

surface faulting coincides with the patch of maximum slip released, imaged through the joint inversion of GPS and strong motion data [*Cirella et al.*, 2009].

1.3. Open Question Raised by the 2009 Earthquake

[7] The length of the seismogenic fault, as defined by coseismic seismologic and geodetic observations (15–18 km, see section 1.1), and the length of the long-term expression

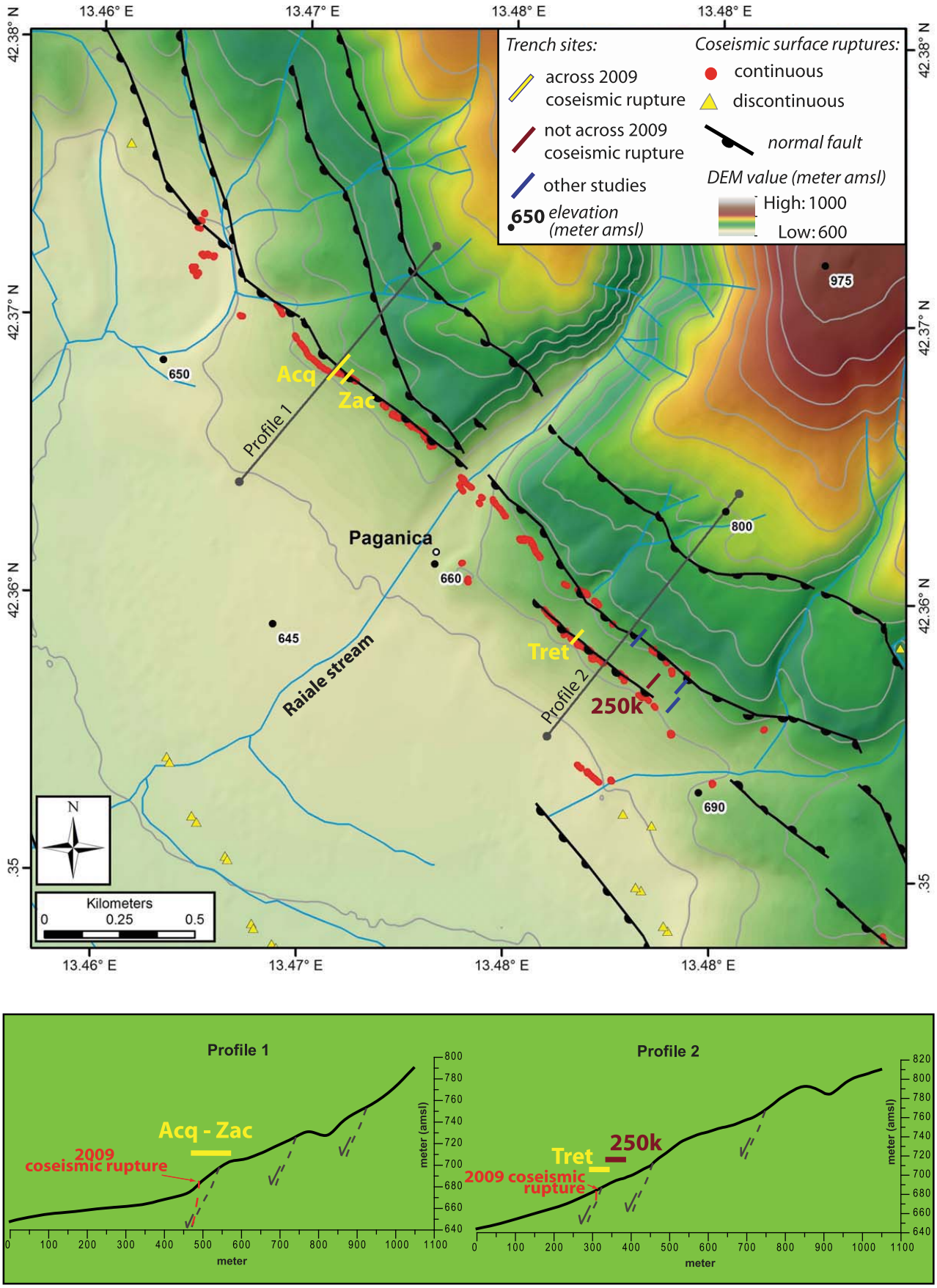
13.46° E
13.47° E
13.48° E
13.48° E
42.38° N
42.37° N
42.36° N
.35
Trench sites:
across 2009 coseismic rupture
not across 2009 coseismic rupture
other studies
650 elevation (meter amsl)
Coseismic surface ruptures:
continuous
discontinuous
normal fault
DEM value (meter amsl)
High: 1000
Low: 600
975
650
Acq
Zac
Profile 1
Paganica
660
800
645
Raiale stream
Tret
Profile 2
250k
690
N
Kilometers
0 0.25 0.5
Profile 1
Acq - Zac
2009 coseismic rupture
meter (amsl)
meter
Profile 2
Tret
250k
2009 coseismic rupture
meter (amsl)
meter

Figure 3

of the Paganica fault system, as defined on the basis of geomorphic, geologic and structural considerations by different works [*Falcucci et al.*, 2009; *Boncio et al.*, 2010; *Civico et al.*, 2010] are consistent. This agreement is congruent with the concept that the long-term expression of a fault is the result of the accumulation of repeated coseismic displacements. However, the 2009 surface ruptures that had measurable displacement, clearly reactivated only 3 km of the PF system (Figure 2). Moreover, the centimetric throw (max 0.15 m near Paganica) that occurred in 2009 can hardly contribute to the growth of the fault escarpment which is ~20 m high. In fact, in order to compete with erosional and depositional processes, surface displacements substantially larger than those in 2009 are needed. For comparison, vertical throws of at least 0.5–1 m have been observed in paleoseismological trenches on other faults in the same region, with scarps greater than 10 m [e.g., *Pantosti et al.*, 1996; *Galli et al.*, 2002; *Salvi et al.*, 2003].

[8] Given these considerations, a critical question for evaluating the seismic hazard of the area and for the broader understanding of fault behavior is whether the PF is capable of earthquakes larger than Mw 6.3. To address this question and thus to contribute to seismic hazard evaluations for the L'Aquila area, we started paleoseismological investigations across the PF. We identify and date paleosurface faulting events to build a history of Paganica fault slip, both in time and space. These results will be integrated with ongoing and future studies from other sites and faults of the area.

[9] From a global perspective, paleoseismological recognition of small surface faulting earthquakes is a critical problem for many intraplate regions (i.e., most part of Europe). Because these types of events can be infrequent and produce poor geomorphic signatures, they are difficult to study. However, in densely populated regions like Europe, they may produce disasters such as it occurred in L'Aquila. Very few paleoseismological studies find evidence of such surface faulting events [e.g., *Pavlides*, 1996; *Vanneste et al.*, 2001; *Pantosti et al.*, 2004; *Chatzipetros et al.*, 2005; *Villamor et al.*, 2007] and hence, this work can provide a case study for comparison to other areas.

2. Paleoseismological Trenching

[10] We studied in detail four artificial exposures across the portion of the PF system where the 2009 surface ruptures were continuous and considered to be the direct evidence of fault displacement at depth (Figure 3) [*Falcucci et al.*, 2009; *Boncio et al.*, 2010; *Emergeo Working Group*, 2010]. We also drilled several cores to a maximum depth of 4.5 m, with the aim of checking stratigraphy and measuring the vertical separation of correlative deposits. Because in this area surface faulting intercepts the Paganica village, the high concentration of residential buildings made difficult the selection of the trench sites. Two trenches were newly excavated (Zaccagnini and Mo'Tretteca sites, hereinafter Zac and Tret), whereas the other two took advantage of artificial cuts: one preearthquake created for a building construction (250K site) and the other produced by water escaping from an aqueduct pipeline that broke during the 6 April earthquake (Aqueduct site, hereinafter Acq) (Figure 3). While the Acq, Zac, and Tret exposures cross the 2009 coseismic surface ruptures, the 250K site is located a few meters upslope from the rupture. Because the main goal of this work is to reconstruct the recent paleoseismological history of the PF, we studied the exposures where middle-to-late Pleistocene alluvial and colluvial deposits are buried by Holocene colluvium.

[11] All the studied exposures are located at the base of the main fault escarpment (Figure 3) and share a similar stratigraphic history. In particular, the lowermost deposits common to all the trench walls are middle-late Pleistocene carbonate gravels of an alluvial braidplain, generally clast supported in a fine-grained sandy matrix (numbered as unit 100 at all sites). The top of this deposit is abruptly truncated by an erosional surface on which developed brown to dark brown paleosols that predate the Last Glacial Maximum in the region (LGM, ~18 ka) [*Dramis*, 1983]. Slope deposits overlie the paleosols and are truncated by a second erosional surface associated with the LGM. This surface is overlain by a series of Holocene fine- to coarse-grained alluvial and slope-derived deposits. Human settlements and economic ascent in the area (the town of L'Aquila was founded in 1229 AD) since ~1000 AD are the cause for the high level of modification of the local deposits that were used as a mining source for building material. A reference chronological framework was developed based on 27 radiocarbon dates (Table 1), integrated with archeological evaluation of pottery shards (Table 2). Because detrital charcoal is quite rare in the stratigraphy, we also dated bulk sediments.

[12] The trench walls (a total area of ~120 m by 2.5 m) were logged at a scale of 1:20, photographed, and mosaicked (Figures 4–7). In the logs, we use the same color for units that are correlated from one trench to another (e.g., unit Zac 94 correlated to Acq 91). For unit 100, which has been recognized at all sites at the base of the exposed stratigraphic sequence, we used the same color and the same number. Vertical throws measured in the trenches are rounded to the nearest 0.05 m. Sample for age dating is reported with the trench site acronym as a prefix (e.g., 250K-B2). The same rule applies to faulting events (e.g., Acq-E1), although the fault zone name also may be included to differentiate among multiple zones of faulting (e.g., 250K-F2E1). In the following, we discuss the observations and interpretations from each trench site, from NW to SE (Figure 3).

3. The Aqueduct Site

[13] The 2009 coseismic surface ruptures along the PF crossed and broke apart the Gran Sasso water pipeline (Figure 4a). The ejected overpressured water (25 atm, Ing. Stefano Pacitti, Gran Sasso Acqua S.p.A. personal communication, 2010) deeply scoured the ground for a length of

Figure 3. Detail of the area of the 3 km long continuous surface ruptures along the escarpment bounding the Paganica village, location of trench sites, and topographic profiles crossing the range front (lower box). Besides the four sites from the present study (Acq, Zac, Tret, and 250k), three sites are from *Galli et al.* [2010] and M. Moro et al. (personal communication, 2010). Topographic color ramp and profiles are derived from a 5 m resolution DEM. Contour lines interval is 25 m.

Table 1. Measured and Calibrated Ages of the Samples Collected

Site	Unit	Sample, Lab Code[a]	Type	Conventional Age BP[b]	Calibrated Age[c]	Probability Distribution
ACQ	90	ACQ-B3, Beta-273363	bulk	31370 ± 260	36490–35150 BP	1.000
ACQ	93	ACQ-B4, Beta-273364	bulk	24600 ± 150	30050–28920 BP	1.000
ACQ	82	ACQ-B5, Beta-273365	bulk	7500 ± 50	6440–6250 BC	1.000
ACQ	93	ACQ-B7, Beta-273366	bulk	25560 ± 160	30850–30170 BP	0.934
					30010–29730 BP	0.066
ZAC	80	ZAC-B2, Poz-33712	bulk	14810 ± 90	18510–18230 BP	0.365
					18150–17680 BP	0.635
ZAC	50	ZAC-B4, Poz-33711	bulk	4440 ± 40	3330–3210 BC	0.341
					3190–3160 BC	0.069
					3130–2930 BC	0.589
ZAC	38	ZAC-B5, Poz-33710	bulk	1410 ± 35	580–670 AD	1.000
ZAC	35	ZAC-C1, Beta-273371	charcoal	1400 ± 40	570–680 AD	1.000
TRET	60	TRET-B50, Poz-33714	bulk	1330 ± 30	650–720 AD	0.814
					740–770 AD	0.186
TRET	80	TRET-C805, Poz-33716	charcoal	755 ± 35	1220–1290 AD	1.000
TRET	81	TRET-C300, Poz-33720	charcoal	1205 ± 30	690–700 AD	0.005
					710–750 AD	0.091
					770–890 AD	0.904
TRET	81	TRET-C1, Beta-266355	bulk	1330 ± 40	650–770 AD	1.000
TRET	80	TRET-C31, Poz-33719	charcoal	1025 ± 30	900–920 AD	0.029
					970–1040 AD	0.945
					1100–1120 AD	0.023
					1140–1150 AD	0.004
TRET	80	TRET-C4, Poz-33718	charcoal	1035 ± 30	900–920 AD	0.056
					950–960 AD	0.009
					960–1040 AD	0.935
TRET	90	TRET-C2, Poz-33721	charcoal	2020 ± 35	150–140 BC 110	0.020
					BC–60 AD	0.980
TRET	90	TRET-C11, Poz-33722	charcoal	1130 ± 30	780–790 AD	0.008
					810–840 AD	0.054
					860–990 AD	0.939
TRET	210	TRET-B10, Poz-33715	bulk	2460 ± 35	760–680 BC	0.265
					670–410 BC	0.735
TRET	200	TRET-C30, Beta-266356	charcoal	2510 ± 40	790–510 BC	0.987
					440–420 BC	0.013
TRET	90	TRET-B20, Beta-273368	bulk	1070 ± 40	890–1020 AD	1.000
TRET	302	TRET-S1a, Beta-273370	bulk	22210 ± 130	27570–27210 BP	0.104
					27110–26170 BP	0.896
250K	62	250K-B1, Poz-32265	bulk	2605 ± 30	820–760 BC	0.985
					680–670 BC	0.015
250K	70	250K-B2, Poz-32266	bulk	6010 ± 40	5000–4800 BC	1.000
250K	60	250K-B3, Poz-32267	bulk	2535 ± 35	800–720 BC	0.360
					690–540 BC	0.640
250K	90	250K-B30, Beta-273359	bulk	23500 ± 140	28610–27920 BP	1.000
250K	80	250K-B50, Beta-273360	bulk	15520 ± 70	18870–18580 BP	1.000
250K	65	250K-B70, Beta-273361	bulk	4200 ± 40	2900–2830 BC	0.286
					2820–2660 BC	0.702
					2650–2640 BC	0.012
250K	50	250K-C101, Beta-273362	charcoal	20 ± 40	1690–1730 AD	0.216
					1810–1920 AD	0.717
					1950–1955[d] AD	0.067

[a]Lab code: Beta, Beta Analytics Inc. (Florida) laboratory; Poz, Poznan Radiocarbon Laboratory (Poland).
[b]Measured radiocarbon age corrected for isotopic fractionation, calculated using the delta 13C. It is not calendar calibrated.
[c]Age dendrochronologically corrected for the C^{12}/C^{14} changes in the atmosphere according to Calib Rev 6.0.0 [*Stuiver and Reimer*, 1993; *Reimer et al.*, 2009] and rounded to the nearest decade. Holocene ages are given as AD/BC, and Pleistocene ages as BP. 2σ range.
[d]Denotes influence of nuclear testing C14.

about 80 m and a depth of up to 4 m. This excavation provided an exceptional exposure of sediments and fault structures across the ~20 m high compound scarp of the PF. Soon after repair of the pipeline, this site was studied by several groups of geologists [e.g., *Falcucci et al.*, 2009; *Boncio et al.*, 2010; *Emergeo Working Group*, 2010; *Galli et al.*, 2010]. To improve the analysis of the stratigraphic and structural relations, three months after the earthquake we deepened (1 to 2 m) and rectified the NW wall in the lower part of the trench (Figure 4a). This deepening, together with exploratory cores, allowed us to expose the graben architecture that characterizes the main fault zones, and to estimate the long-term slip rate by correlating units. Moreover, we were able to better understand ambiguous contacts, initially interpreted as faults but actually of artificial origin (e.g., at horizontal meter 22 in Figure 4b, where below a man-made subvertical cut unit 100 is continuous and unfaulted).

[14] At this site, the 2009 ruptures occurred at the base of the scarp on the fields and tarmac road adjacent to the pipeline. The surface trace of the coseismic cracks showed a prevailing left-stepping en echelon arrangement with throw

Table 2. Evaluation of Pottery Fragments

Sample	Unit	Age Interval[a]
250K-P4	61	XI–XIII century
TRET-PY	50	XIV–XV century
TRET-P3	50	XIII–XIV century
TRET-P2	90	XI–XIII century
TRET-P10	90	XI–XIII century
TRET-P200	90	XI–XIII century
ACQ-P2	10	XII–XIII century
ACQ-P1	81	<XII–XIII century

[a]Expert evaluation of archeologists: Enrico Cirelli and Hermann Borghesi.

(both as vertical separation and subtle warping) and opening ranging between 0 and 0.1 m [*Emergeo Working Group*, 2010].

[15] Because the excavation is long, the stratigraphy and setting are quite variable and complicated (Figure 4). The upper portion of the excavation (meters 36 to 78.5, Figure 4b) exposed the deposits that underlie the upper surface (unit 200) and that, according to *Messina et al.* [2009], are of Middle Pleistocene age. These comprise calcareous conglomerate with whitish, fine-grained silty/sandy matrix and interbedded layers of brown clayish silt that belong to an alluvial braidplain. These deposits are affected by several high-angle (50°–70°), mostly SW dipping, normal faults that are highlighted by clast reorientation along the shearing direction and are locally cemented or fault gouge supported. At m 35–36 a fault (F in Figure 4b) marks the separation between unit 200 and a younger sequence of alluvial braidplain deposits composed by calcareous conglomerate with fine-grained sandy matrix, possibly of late Pleistocene age (unit 100).

[16] From m 0 to 36, unit 100 is the lowermost unit exposed in the trench and is overlain by colluvial, alluvial, and slope wash deposits (units 70 to 95). This portion of the exposure is characterized by two main fault zones: fault zone 1 (FZ1) at m 25–36 and fault zone 2 (FZ2) at m 3–13 (Figure 4). The two fault zones share a similar graben-like structure formed by closely spaced, high-angle, SW and NE dipping normal faults and show clear evidence of repeated events. Although not completely exposed because of modification due to the pipeline repair and wall collapse, fault F appears to bound the northeast side of FZ1. The synthetic splays of FZ2 are characterized by intense fissuring, faulting, sheared infilling, and clasts reorientation. Both fault zones involve the same depositional sequence which is composed of carbonate cemented, sandy gravelly, scarp-derived colluvium (units 90–92), and finer grained colluvial deposits of organic-rich, brown clayey silt with carbonate veins (units 93–95). The latter units appear to be backtilted within the graben and in angular discordance with the capping deposits. A borehole at meter 7 (Figure 4c) within the FZ2 graben confirms that unit 100 is capped by the same set of organic-rich layers that fills the base of the FZ1 graben (units 93–94, Figure 4d). This correlation is also supported by radiocarbon ages of ~30 kyr from unit 93 in both graben (ACQ-B4 and ACQ-B7 in Table 1 and Figures 4b and 4c).

[17] The antithetic faults that bound the graben terminate below unit 90. This is particularly clear at FZ2 (Figure 4c). Radiocarbon dating of unit 90 (sample ACQ-B3) provided an age older than samples ACQ-B4 and ACQ-B7, both from the stratigraphically older unit 93. This age reversal is likely due to the presence of calcium carbonate-rich matrix and caliche veins within the strongly cemented deposit of unit 90. Therefore, we are not using the age of sample ACQ-B3. An erosional contact at the top of unit 90 is interpreted to be associated with the LGM in the region. This and the correlation of unit 90 with deposits in the nearby trench at Zaccagnini site (see following section) suggest that unit 90 shortly predates the LGM (~18 kyr).

[18] The youngest units at Acq consist of loose colluvium with varying organic content (units 82–70). An erosional contact truncates the top of unit 82 (deposits dated at ~6300 cal yr BC, sample ACQ-B5, Table 1 and Figure 4c). This unconformity (contact 82/81, dotted thick line in Figure 4c) appears to be due to man-made modification, probably quarrying of the gravel exposed in the scarp. The deposits on top of this contact are both scarp-derived and man-made fill; these are composed of loose fine sandy silt containing sparse gravel and pottery shards (units 10, 70, 80, 81). The shards were evaluated as being from the XII–XIII centuries (Acq-P1 and Acq-P2, Table 2 and Figures 4b and 4c). The complexity and the instability of the wall in the upper portion of the trench made it difficult the tracing of this contact.

[19] FZ2 extends up into the youngest deposits (at m 9.5–10.5) and shows the most recent activity, that is in 2009. In 2009 some of the preexisting fault strands were reactivated as fractures that produced voids, and propagated upward into units 80 and 70 as newly formed cracks (Figures 4c and 4e). Projecting in the wall the 2009 cracks observed on the open field at the western side of the exposure, these are associated with the subvertical faults that extend only as high as units 100 and 81 (m 12–14). As a consequence, the width of the rupture zone indicated in Figure 4c results from the en echelon style of the 2009 ruptures. On the basis of a flexure along the contact between the units 80 and 70 near m 10, we measured a vertical throw of 0.1–0.15 m for the 2009 earthquake (Acq-E1). The penultimate event (Acq-E2) is well defined by upward fault terminations and displacements at the top of colluvium 81. This unit is downthrown to the southwest a total 0.35–0.4 m. By subtracting the 2009 throw from this amount, we quantify the vertical displacement produced by Acq-E2 as 0.2–0.3 m. This value is possibly a minimum because units 80–82 are missing at FZ1. The erosional unconformity at the base of unit 81 (Figure 4c) prevents us from recognizing previous older events.

[20] The age of Acq-E2 is not well constrained. A pottery fragment in unit 81 evaluated as dating from the XII–XIII centuries or later (ACQ-P1, Table 2) suggests the event occurred after this period. Therefore, Acq-E2 could be associated with the 1461 earthquake or a later one (see section 1.1. and Figure 1).

[21] There is evidence of multiple faulting events in the late Pleistocene. According to the style and magnitude of the deformational structures related to these previous events, such as graben structures (e.g., sharp vertical contact of unit 90 at m 10), possible scarp-derived colluvial wedge (unit 92 at FZ1), intensive sheared zone (faults at m 10), backtilting (both FZ1 and FZ2), the size of these surface faulting events was likely much larger than 2009, with throws on the order of 0.5 m or larger (Figure 4).

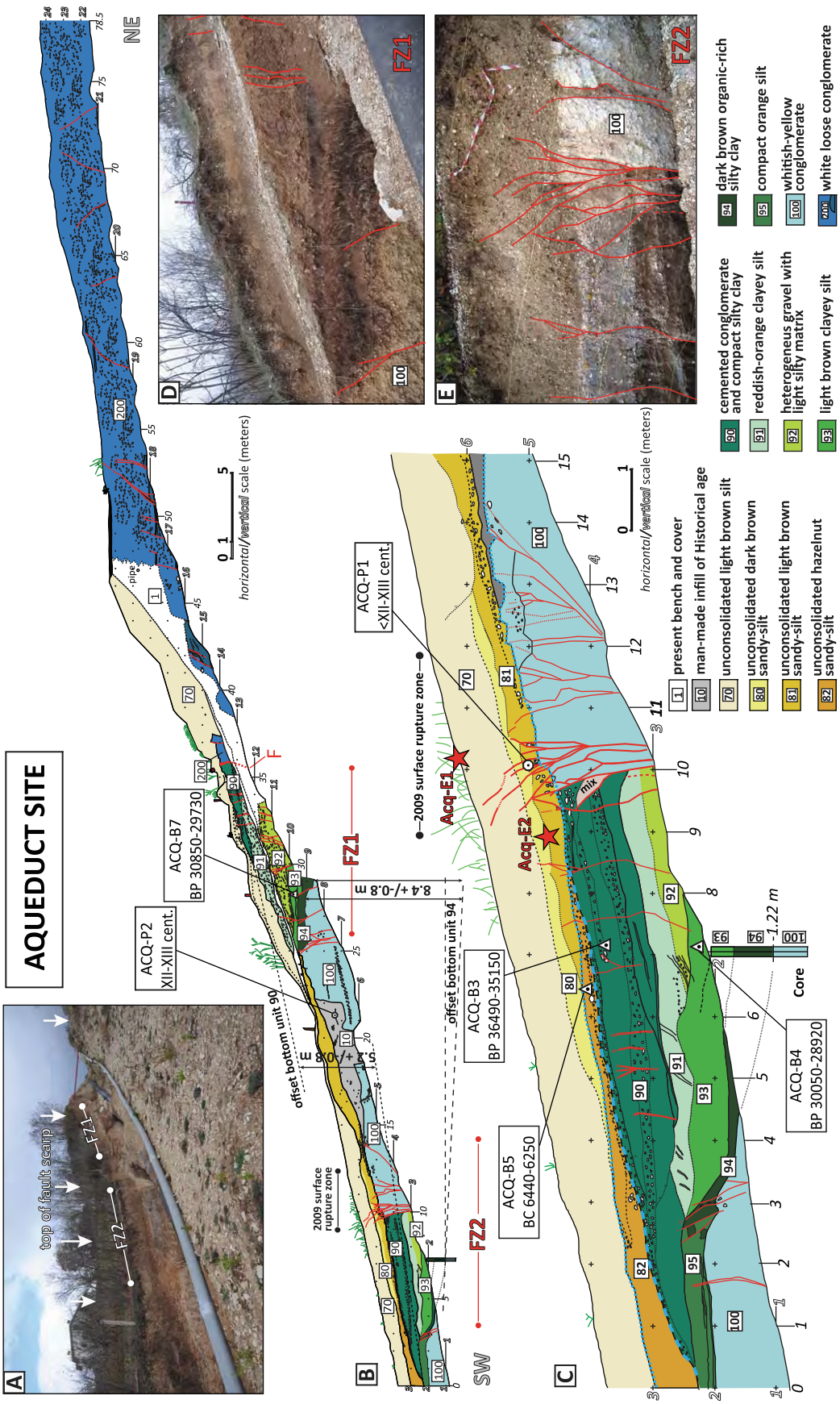

Figure 4. Acq site. (a) View of the excavation along the water pipeline where it crosses the 20 m high cumulative scarp. (b) Simplified log of the NW wall (average orientation N40°E) from a 1:20 scale survey. Triangles indicate dated radiocarbon samples (Table 1); circles indicate evaluated pottery shards (Table 2). Dashed gray lines show correlations of units for long-term vertical slip rate evaluation. Dashed and dotted blue thick lines mark erosional contacts associated with the LGM and with probable medieval quarrying, respectively. (c) Enlargement of fault zone FZ2. Symbols are the same as in Figure 4b; red stars indicate location of event horizons (ground surfaces at the time of surface faulting earthquakes). (d) View of the graben associated with fault zone FZ1 approximately between m 25 and 33. (e) View of the active fault traces of fault zone FZ2 approximately between m 8 and 12. In this zone the 2009 ruptures produced diffuse deformation accompanied both by cracking and warping.

[22] A minimum late Pleistocene-Holocene vertical slip rate can be estimated by measuring the minimum amount of vertical separation of late Pleistocene deposits across FZ2 (Figure 4b). Vertical separation is measured by taking different original attitudes of the contacts and introducing in the calculation the largest uncertainties. The total offset recorded at the base of unit 90 is of 5.2 ± 0.8 m. This provides a rate of about 0.15–0.33 mm/yr since 18–30 kyr (the age of unit 90, see discussion above). This estimate is a minimum for the site because unit 90 does not cross fault F. We may also use the apparent offset at the base of unit 94 (oldest unit tectonically preserved into the graben structures) across FZ2, between the borehole at m7 (Figure 4b) and the FZ1 graben, to roughly estimate a total throw of 8.4 ± 0.8 m. Using the ages from unit 93, we obtain a vertical slip rate for FZ2 of 0.25–0.3 mm/yr since 30 kyr. This value is less constrained because we are not considering the net value across FZ1 and FZ2.

4. The Zaccagnini Site

[23] The Zaccagnini (Zac) trench is located ~30 m SE of the Aqueduct site (Figure 3); at this location the 2009 coseismic surface ruptures consist of a SW facing free face with a throw of about 0.10 ± 0.05 m, locally accompanied by ground warping. The geomorphic situation is the same as at the Acq site, with the 2009 ruptures running along the base of the main scarp. However, here the man-made scarp modification is even more pronounced, with greater removal of deposits in the hanging wall. The trench strikes N40°E and has a peculiar geometry due to previous excavations at this site: the NW wall is 12 m long, whereas the SE one is only 4 m long (Figure 5a). A prominent N130° striking and 50°–55° SW dipping main normal fault and a 4 m wide zone of subvertical hanging wall faults, which includes the 2009 ruptures, are exposed in both trench walls (Figures 5a and 5b). This geometry is very similar to that of FZ2 at the Acq site.

[24] The primary fault juxtaposes late-middle Pleistocene white alluvial gravel (unit 100) against a ~3 m thick sequence of alluvial and colluvial deposits (units 94 to 38, Figure 5), mainly consisting of gravels, silts and silty clays with varying organic content including different size carbonatic clasts, more abundant in the younger units. Based on their sedimentological and stratigraphical characteristics, some of these deposits can be correlated with those exposed at the nearby Acq site (i.e., unit Zac 94 with unit Acq 91, unit Zac 90 with unit Acq 90, and unit Zac 40 with unit Acq 82; Figures 4 and 5). Repeated faulting of units 94 to 50 in Zac has produced intense disruption, shearing, and the tectonic juxtaposition of distinct packages of stratigraphy. The youngest deposits in the Zac trench, units 30, 35, and 38, are separated from the older units by an erosional contact (bottom of 38 and 35) and consist of white to gray silty colluvium with rounded, mainly carbonatic clasts. Although a one-to-one correlation between the youngest units at Zac site and Acq site (Acq 70, 80, and 81) is not possible, these units are likely correlative as units packages (Figures 4 and 5). Constraints on the ages of the deposits exposed are provided by four radiocarbon dates (Table 1) on three bulk sediment samples (ZAC-B2 from unit 80, 18510–17680 years BP; ZAC-B4 from the upper part of unit 50, 3320–2930 years BC; ZAC-B5 from unit 38, 580–670 AD) and on one small piece of charcoal (ZAC-C1 from unit 35, 570–680 AD). These ages integrate well with those from the Acq site and, provided our stratigraphic correlations are correct, units Zac 90 and Acq 90 predate the LGM and postdate 30 kyr, and the upper units (Zac 38, 35, and 30 and Acq 70, 80 and 81) belong to the historical period. The sequence Zac 80–50 (bracketed between 18 and 3 kyr), which is preserved only in the V-shaped depression in front of the main fault, is missing at Acq site, likely due to erosion after the LGM. The assumption that the units Zac 50 and 40 are correlative among them and with Acq 82 (are at the same stratigraphic positions; Figures 4 and 5), is not confirmed by dating. This is possibly due to contamination of Acq 82 sample, as also hypothesized for Acq 90 (see section 2). A further difference between the ages of the youngest units at the two sites is also recorded. The historical deposits at Zac appear to be several hundreds years older than at Acq, either because of reworked organic material in the samples or because gravel mining at Zac was shallower than at Acq (this is also suggested by the lack of pottery in Zac trench).

[25] The 2009 event (Zac-E1) is evidenced on both walls of the trench by open fractures and by about 0.1 m slip along a secondary subvertical splay of the main fault plane clearly visible as a free face at the surface. Tectonic structures and stratigraphic relations such as increasing displacements with depth, upward-terminating faults and colluvial wedge provide evidence for at least two paleoearthquakes.

[26] Evidence for the penultimate event (Zac-E2) can be found only on the NW wall because the youngest units on the SE wall have been almost completely removed due to modern modification. Zac-E2 is recognized because of a 0.1–0.15 m displacement of unit 38 along a subvertical upward-terminating fault, which is sealed by unit 30 (m 4–5 in Figure 5d). Further evidence for Zac-E2 is a gentle warp (or at least part of it) of unit 38 coincident with two upward-terminating faults at m 2. Therefore, we set the Zac-E2 horizon at the top of unit 38 (Figure 5d).

[27] The occurrence of a previous paleoevent (Zac-E3) is set on both walls by infilled V-shaped fissures and upper terminations of faults at the base of unit 38 (Figure 5). Moreover, the geometry and texture of unit 38 (limited lateral extent, no clear sedimentary structure, concentration of clasts in the lowermost part) suggest that it can be interpreted as a colluvial wedge that postdates Zac-E3. On the NW wall the base of unit 38 shows a cumulative offset of ~0.6 m that, if the Zac-E1 and E2 throws are subtracted, yields a Zac-E3 offset of 0.25–0.3 m (Figure 5d). Because part of the deformation zone is missing on the SE wall, we can estimate only a minimum displacement of 0.15 m.

[28] Intense faulting and shearing of units 90 to 60, pervasive faulting within this sequence and the larger offset of older units across the main fault with respect to the younger units, are evidence that multiple faulting events occurred prior to Zac-E3, and suggest the possibility of events larger than 2009. Unfortunately, we could not define individual events in this older section.

[29] Time constraints for the occurrence of the paleoearthquakes are quite limited in the Zac trench. Zac-E2 is younger than 580–670 AD (sample ZAC-B5, Table 1 and Figure 5) and is therefore compatible with any of the historical events discussed in section 1.1. The occurrence of

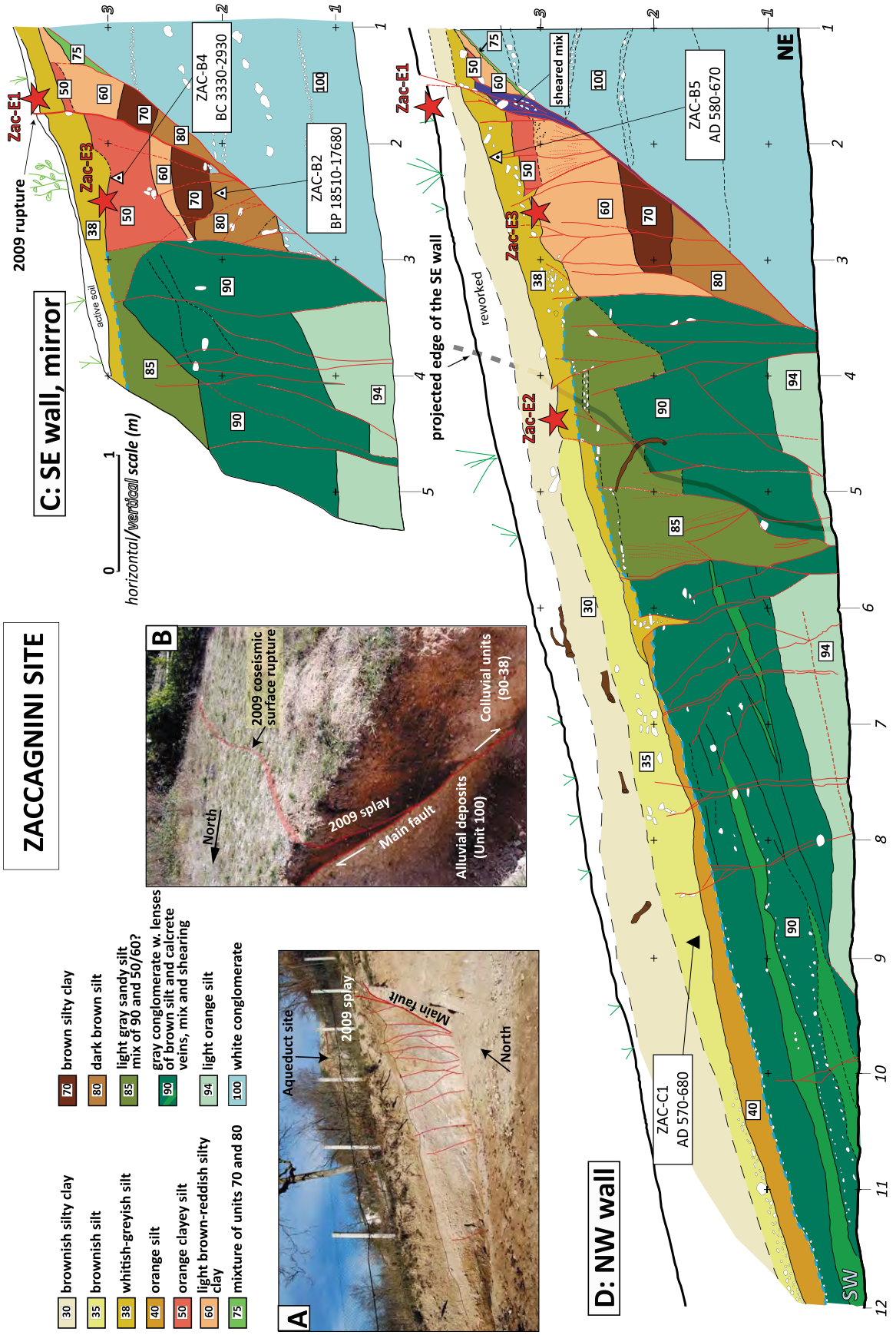

Figure 5. Zac site. (a) View of the NW trench wall. (b) View of the shorter SE trench wall. (c) Simplified log of the SE wall (average orientation N40°E) from a 1:20 scale survey. Triangles indicate dated radiocarbon samples (Table 1), red stars indicate location of event horizons, dashed thick blue line marks the erosional contact associated with the LGM. (d) Simplified log of the NW wall, symbols are the same as in Figure 5c.

Zac-E3 is constrained between the ages of units 50 and 38 (3330 BC and 670 AD, Table 1 and Figure 5), with the younger part of the interval preferred.

5. The Mo'Tretteca Site

[30] The Mo'Tretteca (Tret) trench crossed the secondary splay of the 2009 coseismic rupture occurred along the ~5 m high, southwest facing minor scarp of the PF (Figure 3). Here, the 2009 rupture displayed up to 0.1 m of vertical throw, a few cm of warping, and up to 0.05 m of opening. The trench was N60°E oriented, about 20 m long and up to 3 m deep and wide and was cut across an abandoned alluvial fan surface. It was possible to survey only the SE wall because the other wall collapsed soon after excavation (Figure 6).

[31] The sedimentary sequence exposed in the trench is composed of partially cemented whitish alluvial gravel within a yellow sandy matrix (unit 100) buried under a layered colluvial sequence characterized by silty to silty clay deposits with abundant, small, mainly angular, carbonatic clasts (units 220–40, Figure 6). The thickness of this sequence increases downslope. Coincident with the 2009 surface rupture, the trench wall shows a single, 2 m wide, V-shaped fault zone composed of a main fault plane and several synthetic splays (Figure 6). The vertical offset of the deposits across the fault zone increases with depth, suggesting the occurrence of repeated surface faulting events.

[32] Twelve radiocarbon ages and some pottery fragments provide constraints on the ages of the deposits (Figure 6, Tables 1 and 2). Pottery was found both in units 50 and 90 and provides ages of XIII–XV centuries and XI–XIII centuries, respectively (Table 2). Radiocarbon ages range between 1220 and 1290 AD for unit 80 (TRET-C805) and 790–420 BC for unit 200 (TRET-C30) (Table 1). In the following discussion the ages of some samples collected from unit 60, unit 81 and unit 90 (samples TRET-B50, TRET-C1, TRET-C300, and TRET-C2) are not used because they are older than stratigraphically expected and are also excluded by the Oxcal 4.1 analysis for age-depth model because the program rejected them as out of sequence. In general, the radiocarbon ages and archeological evaluations of material from the trenches show an internal stratigraphic coherence indicating that all the exposed colluvial units were deposited during the past 3 millennia (Tables 1 and 2).

[33] With the aim of finding deposits correlative with the oldest ones exposed on the footwall (units 95 and 100), we cored the hanging wall to a depth of 7.6 m (Figure 6). The core intercepted the gravel from unit 100 between m −7.38 and −7.60 (although we cannot preclude that this material may be reworked and that the in situ unit 100 is deeper). Taking into account the dip of unit 100 from the trench wall and assuming limited erosion of the footwall, we estimate a minimum throw of about 4.7 ± 0.1 m. A bulk sample collected in the core a meter above unit 100 (Figure 6), resulted in a calibrated age of 27570–26180 BP (TRET-S1a, Table 1) and provides a minimum age constraint for approximately estimating a maximum late Pleistocene vertical slip rate of 0.15–0.2 mm/yr for this splay of the PF.

[34] The penultimate earthquake at this site (Tret-E2) is recognized from the observation that the top of unit 80 shows a vertical offset of up to 0.3 m, at least twice as large as the deposits above. The event horizon may be at the top of unit 80 or more likely is within the lower part of unit 70, because of the subtle thickness change across the fault zone (about 0.1 m) and the presence of a couple of fault splays that die out in this unit. By removing the 2009 throw from that recorded by unit 80, Tret-E2 vertical throw is about 0.15–0.2 m. A previous event, Tret-E3, is recognized at the bottom of unit 81/top of 90 from the observation that the top of unit 90 shows a vertical offset that is about 0.1–0.2 m larger than the deposits above and a corresponding increase in thickness across the fault zone.

[35] Unit 200 is interpreted to be a colluvial wedge from an older event (Tret-E5) and it is strongly sheared along fault splays between meters 6 and 5 (Figure 6). The complexity and style of deformation of unit 200 is not common for a normal fault. Moreover, unit 200 is apparently thrusted over unit 210 and this is difficult to explain simply with the occurrence of Tret-E3. This observation suggests the occurrence of an additional event, Tret-E4 which may have had a significant component of lateral slip. The event horizon for Tret-E4 is set in the middle of unit 90, where some fault splays seem to die out (Figure 6a). To roughly estimate the vertical throw for this event, we attempted a reconstruction of the original shape of the wedge (unit 200) and calculated an apparent vertical separation of about 0.3–0.45 m (potentially including the slip associated with Tret-E3). The event horizon for Tret-E5 is placed at the top of unit 220 and the minimum vertical throw in this event is estimated by considering the thickness of the colluvial wedge. However, because this unit is highly sheared, we use its thickness (~0.35 m) on the part that appears the least disturbed but is furthest from the bounding fault, thus the actual throw in this event may be greater.

[36] On the basis of the available chronological constraints (Tables 1 and 2, Figure 6), Tret-E2 postdates 1220–1290 AD (sample TRET-C805) and predates the XIII–XV century (TRET-PY and TRET-P3 in Unit 50) and, therefore, is consistent with the 1461 earthquake. Tret-E3 is constrained between 890 and 1020 AD (sample TRET-B20, and TRET-P200, TRET-P2, TRET-P10 from unit 90) and 900–1150 AD (sample TRET-C31 from unit 80). Tret-E4 age constraints are the same as for Tret-E5, thus between 760 and 410 BC (sample TRET-B10 from unit 210) and 890–1020 AD (sample TRET-B20 and TRET-P200, TRET-P2, TRET-P10 from unit 90). Based on stratigraphic considerations, Tret-E4 would be expected to have occurred closer to the age of sample TRET-B20, whereas Tret-E5 should be slightly older than 760–410 BC (Figure 6a).

[37] To refine these time windows and provide the most probable ages at least for the youngest events, we used a P sequence based on a Bayesian model of deposition [*Bronk Ramsey*, 2008], implemented by the computer software OxCal 4.1 [*Bronk Ramsey*, 2009]. The P sequence depositional model takes into account the uncertainties in the variation of the sedimentation rates by regarding sedimentation as an inherently random process. The resulting age model reflects increasing uncertainties with the distance from the calibrated sample ages. To run the P sequence model we input the uncalibrated C^{14} ages and their corresponding sampling depths, changes in sedimentation expressed as unit boundaries, and an age of the ground surface fixed at year

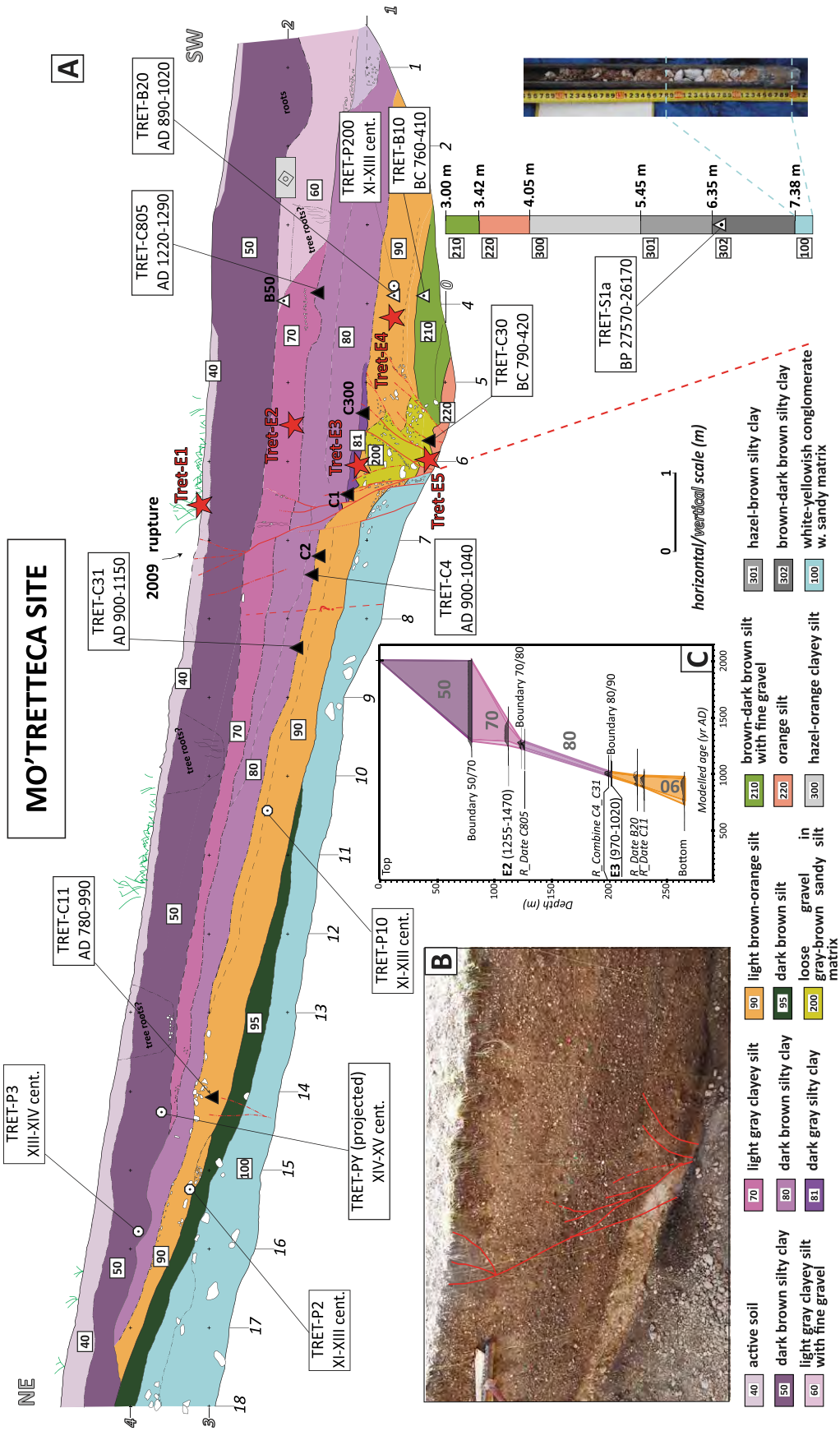

Figure 6. Tret site. (a) Simplified log of the SE wall (average orientation N60°E) from a 1:20 scale survey. Triangles indicate dated radiocarbon samples (Table 1), circles indicate evaluated pottery shards location (Table 2), red stars indicate location of event horizons. (b) Photo of the fault zone approximately between m 4 and 8. (c) Age-depth model obtained for units 90 to 50 using a P sequence from OxCal v4.1.5 [*Bronk Ramsey*, 2008, 2009]. The best estimate of the age ranges of events Tret-E2 and Tret-E3 are derived from this model.

2009. In this model, the regularity of the sedimentation process is determined by factor k, with higher values of k reflecting smaller variations in sedimentation rate. We chose the highest possible values of k, to allow the modeled ages to fit all the individual calibrated sample ages. By using $k = 10$ we obtained the 68% and 95% probability ranges, the latter being plotted in the calibrated age versus depth model (Figure 6c).

[38] Based on this model, the age of Tret-E2 is 1255–1470 AD, and of Tret-E3 is 970–1020 AD (Figure 6). This estimate further confirms that the pre-2009 surface faulting earthquake is likely the 1461 historical event.

6. The 250K Site

[39] A NE-SW cut in a building yard located in between the two 2009 rupture splays was logged in detail because it contained faulted late Pleistocene and Holocene deposits (Figures 3 and 7). This ~15 m long wall exposed a set of colluvia overlying the white late-middle Pleistocene alluvial gravel found also at the other sites (unit 100). Units 90, 80, 70, and 69, which extend across most of the exposure, consist mainly of sandy silt with varying organic concentrations, contain rare clasts, and are infiltrated by carbonate veins. In the SW part of the exposure (m 13–14) a wedge of brown colluvium, composed of layers with varying clast content and matrix (unit 65), lies against unit 90 and is capped by fine gravelly orange silt (unit 62). The two youngest units, 60 and 50, are comprised of brownish sand and silt, contain lenses of clasts, and are crossed by roots and bioturbation. Units 50 and 60–62 have sharp erosional contacts at their base, indicating a relevant material removal. Near m 11 a pocket of clean limestone cobbles of anthropic origin (stones removed from agricultural plough were commonly stored in holes below the ground surface, unit 51) is inset within units 80/90.

[40] Pottery shards and six radiocarbon dates provide constraints on the age of the exposed deposits (Tables 1 and 2). Radiocarbon ages span from 28610 BP to 540 BC. These ages, along with the pottery shards within unit 51, evaluated at XI–XIII centuries (250K-P4), indicate that the upper part of the faulted sequence (above unit 80) is of Holocene age and that units 50, 51, and 60 were deposited during the past 2–3 millennia.

[41] Two main normal fault zones displace the entire sequence (Figure 7). Fault zone 1 (FZ1) is composed of a set of subvertical splays that merges in a single plane in unit 100. This fault zone is faced by a ~ 6 m wide graben formed by a set of synthetic and antithetic fault splays that is the same style of deformation observed at the Acq site. Units 100, 90, 80, and 70 are strongly affected by the graben faults; unit 69 lies in the graben but does not extend far enough to show relations to graben-bounding faults. While the intragraben faults terminate within or below unit 70, the outermost faults (m 9–11 and 4–5) show evidence of reactivation after the deposition of unit 70. Fault zone 2 (FZ2, Figure 7a) is exposed at the SW edge of the wall as a set of subvertical, normal, down to the SW splays that juxtapose colluvial units 65 and 90 and penetrate up into units 62 and 50. Unfortunately, the record on the hanging wall side of this fault zone has been destroyed and so the relation of faulting at this site to the 2009 rupture mapped about 15 m southwest is unclear (Figure 3). Projecting the top of unit 100 across FZ1 and FZ2, and assuming no erosion in the footwall, the net vertical offset is up to 2 m. However, because this site does not cross the entire zone of deformation (Figure 3), this value is a minimum.

[42] In addition to the cumulative deformation represented by the graben, we recognize at least two discrete young faulting events on FZ1 and FZ2. The most recent event (250k-F1E1) on fault zone 1 is expressed by a 0.25–0.35 m displacement of unit 60 and possibly of the base of unit 50 (FZ1, meters 10 and 11). Because the human modification (i.e., digging for trees planting) at this fault zone, we are not able to confidently identify the event horizon. However, the presence of clasts concentrated at the base of unit 50 above the fault zone, which may represent scarp colluvium, and the lack of clear fault traces within unit 50, suggest that the event horizon is located close to the base of unit 50. A fissure mapped at the base of unit 50 at m 10 is a further evidence of an event at this horizon. Evidence of a previous event comes from a deposit comprised of bedded clasts with a wedge shape (unit 68) at the top of unit 70 (250k-F1E2). If this is a scarp-derived colluvial wedge, the minimum slip related to this event, on the main fault-bounding FZ1, is ~0.3 m, equal to the thickness of the wedge (Figure 7).

[43] The most recent event at fault zone 2 (250k-F2E1) is responsible for the displacement of the whole sequence up to the lower part of unit 50. Layer 62 is clearly displaced ~0.15 m, much less than the underlying deposits. A previous event (250k-F2E2) is defined not only by the larger displacement of the older deposits but also by the presence of a possible scarp-derived colluvial wedge (unit 65). The ~0.5 m thickness of this unit provides an estimate of the minimum vertical separation related to this event at FZ2 (Figure 7).

[44] Given their similar stratigraphic positions, events 250k-F1E1 and 250k-F2E1 may represent a single surface faulting earthquake (Figure 7c) that occurred after 800 BC (samples 250K-B1 and 250K-B3) and before the XI–XIII centuries (sample 250K-P4 whose age is likely close to that of the lower part of unit 50; Tables 1 and 2). Event 250k-F2E2 was closely followed by the deposition of the colluvial wedge, unit 65; a bulk soil sample from this unit is dated at 2900–2640 BC (250K-B70). Because unit 65 is likely derived from material eroded from the scarp, this age may be older than the faulting event by an unknown amount. By using the date from unit 62 as an upper constraint on the age of faulting (sample 250K-B1), 250k-F2E2 occurred before 670 BC and perhaps also before 2900 BC. Finally, the age of event 250k-F1E2 is constrained between 5000 BC and 540 BC (see ages of samples 250K-B2 and 250K-B3 in Figure 7 and Table 1). Although this age interval is very broad, we tentatively correlate this event with 250k-F2E2.

7. Surface Faulting Events Along the Paganica Fault

[45] The four excavations discussed in the previous sections are an important paleoseismological data set as they are located within a distance of only ~1.5 km, and thus account for the earthquake history of this portion of the PF (Figure 3). Two more paleoseismological excavations located on the same main escarpment of Acq and Zac sites were investigated by *Galli et al.* [2010] and M. Moro et al.

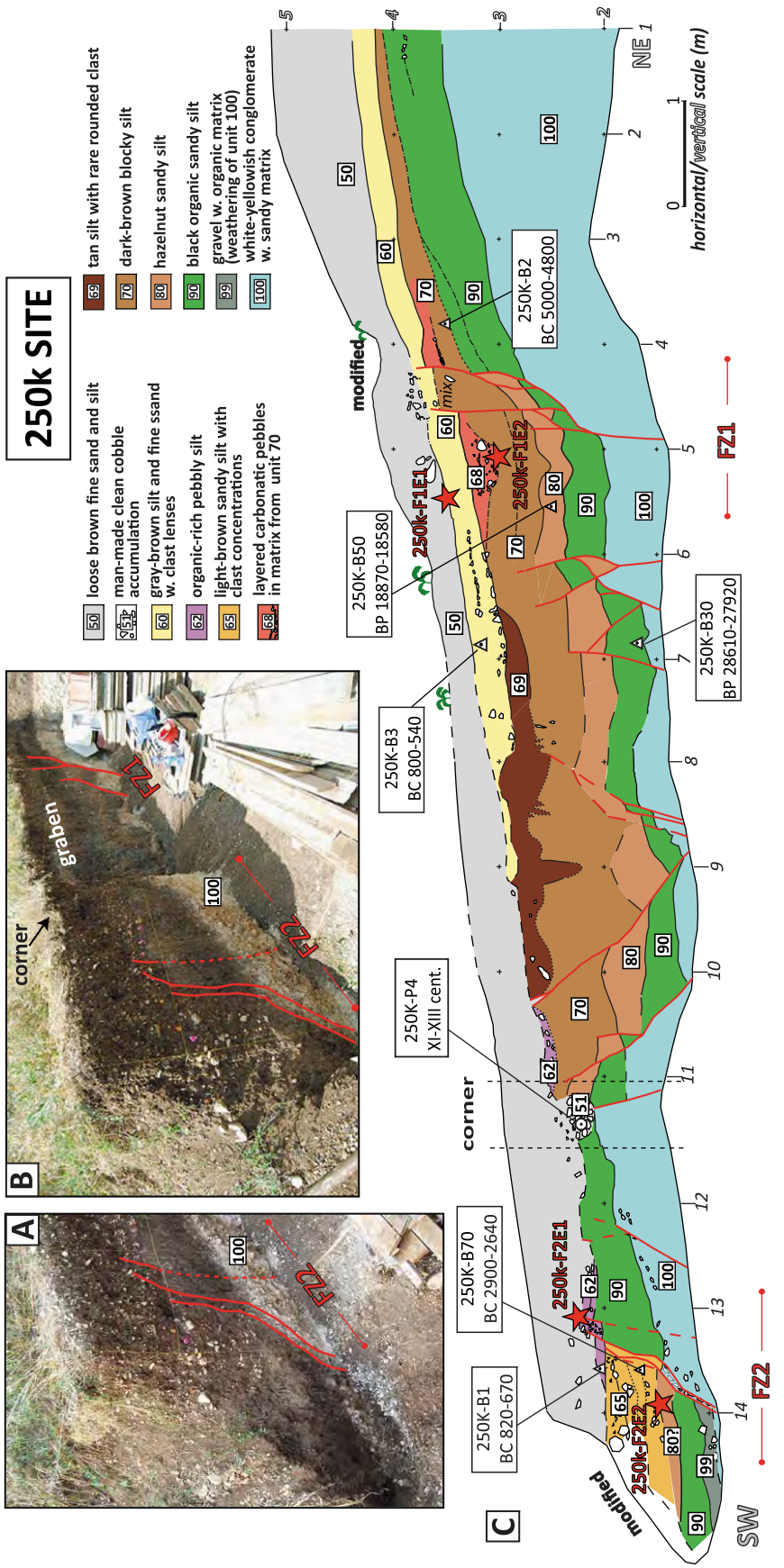

Figure 7. The 250k site. (a) View of fault zone FZ2 on the NW wall of the excavation juxtaposing the colluvial wedge unit 65 (on the right) with unit 90. (b) View of the NW wall of the excavation (average orientation N35°E). The two fault zones FZ1 and 2 and part of the FZ1 graben are visible; the wall is not rectilinear but forms a corner between m 12 and 11. (c) Simplified log of the NW wall from a 1:20 scale survey. Triangles indicate dated radiocarbon samples (Table 1), circles indicate evaluated pottery shards location (Table 2), red stars indicate location of event horizons. Notice that because of the corner in the wall between m 11 and 12, the distance between these two reference lines exceeds 1 m.

(personal communication, 2010) (Figure 3). These trenches do not intersect the 2009 rupture but do show evidence of repeated decimetric Holocene faulting events.

[46] The fact that in 2009, and likely in previous events, the fault ruptured to the surface along at least two parallel strands, and that anthropic modification removed large portions of the stratigraphy, complicates the correlation among surface faulting events at the different sites. As a consequence of the discontinuous sedimentation and of the possible presence of reworked material, the available chronological constraints provide fairly wide age ranges, especially for the oldest events. Figure 8 synthesizes the paleoseismological results discussed above and reports a tentative correlation among the paleoevents recognized in the trenches. We conclude that a minimum of 5 surface faulting earthquakes ruptured at least the studied part of the PF in the late Holocene. These events are referred to as PF1-PF5 and the preferred correlation among sites is shown by colored shaded bands in Figure 8.

[47] PF1 is the 2009 earthquake and is recognized at all the sites with exception of trench 250K, which shows evidence only for events older than XIII century. Measured throws for PF1 range between 0.1 and 0.15 m. The age of the penultimate event PF2, which is recognized at Tret, Acq, and Zac, is consistent with the 1461 earthquake. Therefore, taking into account also the damage distribution of this historical earthquake [*Tertulliani et al.*, 2009], we consider it highly probable that the 1461 earthquake ruptured the same portion of the PF as the 2009 earthquake. Minimum throw in PF2 at the three sites ranges between 0.15 and 0.3 m. Our PF2 interpretation diverges from the analysis by *Galli et al.* [2010], who assign the historical earthquake of 1703 to the penultimate event along the PF (Figure 1). This divergence is based on a different interpretation of a sharp vertical contact at Acq site that *Galli et al.* [2010] performed before the deepening of the wall presented in this work (horizontal meter 22 in Figure 4b, see also section 3).

[48] A previous event PF3 occurred around 1000 AD and appears to be recorded (or resolved) only at Tret (Tret-E3), although this event has a partial age overlap with 250K-E1 and Zac-E2. For stratigraphic considerations (see section 5), we discard both these possible correlations. PF3 throw at Tret is 0.1–0.2 m. The lack of evidence of this event in the other trenches may be related to the mining activity in the area started in the ~1000 AD, and/or to a rupture pattern different than that in 2009.

[49] Event PF4 derives from the correlation of 250k-E1 with Tret-E4 and Zac-E3 and, if correct, the event appears to have occurred between 760 BC and 670 AD. Throws estimated for PF4 range between 0.25 and 0.5 m, opening the possibility that PF4 was larger than the subsequent events. An older event, PF5, is recognized at the 250K site (250K-E2) and the Tret site (Tret-E5) and occurred 2900–670 BC, possibly 790–670 BC. Because the uncertainty in the correlation of oldest events at different sites and the limited dating available, we prefer to consider the widest age interval of occurrence for PF5 with respect to the very narrow one. A rough estimated throw for PF5 varies between 0.35 and 0.8 m.

[50] The observed vertical displacement for each paleoevent at each of the trench site has a low variability, consistently with the fairly homogeneous slip observed in 2009 along the same portion of the PF. Conversely, the throws vary between events at the same site and range between 0.15 m (maximum) in 2009 and 0.4–0.8 m in earlier events. This translates into dip-slip fault displacement (assuming a fault dip of 50°–60°) of ~0.2 and ~0.5–1 m, respectively. Whether the fault displacement is in the lower or higher part of this range, it makes a large difference in terms of possible paleoearthquake magnitude. Assuming these values are representative of the fault average displacement, they would account for moment magnitudes ranging between 6.2 and 6.8 [*Wells and Coppersmith*, 1994].

[51] The 2009 earthquake and, likely, also the 1461 event suggest that the PF can produce events in the lower end of this magnitude interval. However, greater slip is associated with earthquakes in the past, and we observe a general progression of increasing slip with age (Figure 8). These data robustly converge to different size of the rupture and more energetic earthquakes occurring in the past on the PF. Such single-event displacement variability associated to complex and variable pattern of the rupture is also recognized in other parts of the world [e.g., *Vanneste et al.*, 2001; *Yoong and Okada*, 2005; *Maruyama et al.*, 2007].

[52] Assuming our events correlations are correct, recurrence intervals also reflect a change with time. In fact, the average interval before ~1000 AD is longer compared to that after this date. Two events, PF4-PF5, occurred in the 2000–4000 years preceding ~1000 AD, while three events, PF3-PF2-PF1, occurred since ~1000 AD. The age uncertainties affecting the interpreted older events prevent the evaluation of a unique value for interevent intervals; these events appear closely spaced in time or far apart depending on the upper or lower boundary of the age interval. We may only tentatively assign an average interevent time considering the midpoints in the age interval or, when available, our preferred time of occurrence (Figure 8). The resulting frame is that PF1, PF2, PF3 events seem to be spaced ~500 years, whereas the time elapsed between the previous ones can be 1000–2000 years (PF4 and PF5 occurred between 2900 BC and 670 AD). Merging this possibility with the observation of the greater slip for older events, we obtain suggestion for clustered smaller events separated by longer time intervals during which larger events

Figure 8. Summary of the results obtained from each paleoseismological site. Vertical bars refer to the range of observed throws (all minimum values except those of the 2009 event), whereas horizontal bars indicate age uncertainties. Arrows on the horizontal bars point to the preferred portion of the age interval; filled circles indicate our preferred time of occurrence of the events or the 2009, while empty circles indicate the midpoint in the age interval. For the 250k site dashed, bleached lines and dots represent alternative interpretations that we do not use in the final synthesis. Colored vertical bands represent preferred correlations among the events at the different sites (assumed to have ruptured the PF at least for a length comparable to 2009) that are named PF1-PF5 starting from the 2009. Average interevent time considering the midpoint in the age interval or preferred age of each correlated event is reported on top and represented with gray dashed arrows.

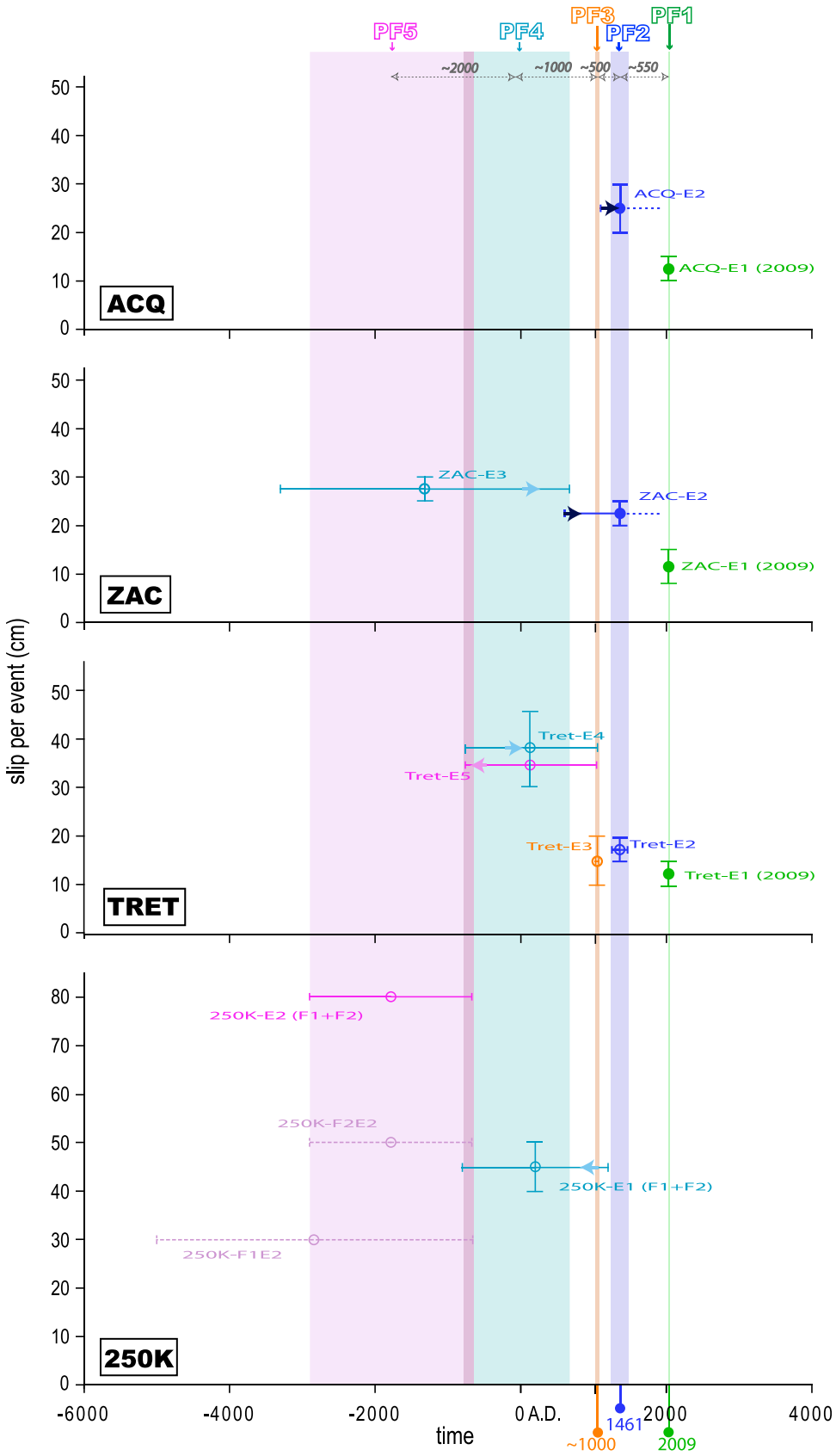
PF5
PF4
PF3
PF2
PF1
~2000
~1000
~500
~550
ACQ-E2
ACQ-E1 (2009)
ACQ
ZAC-E3
ZAC-E2
ZAC-E1 (2009)
ZAC
Tret-E4
Tret-E5
Tret-E3
Tret-E2
Tret-E1 (2009)
TRET
250K-E2 (F1+F2)
250K-F2E2
250K-E1 (F1+F2)
250K-F1E2
250K
slip per event (cm)
time
-6000
-4000
-2000
0 A.D.
2000
4000
1461
~1000
2009

Figure 8

occur. Different distributions of recurrence time on faults embedded in a complex network (such in our case) could be explained by fault interaction processes, even though the tectonic stressing rate may be constant in time and space, as evidenced by *Marzocchi et al.* [2009] on the basis of numerical modeling. A further process impacting the recurrence of faults is played by fluids in the fault failure process; fluids migration may trigger, anticipate or delay earthquakes on a fault and then affects its recurrence time. The role of fluid migration was observed in the nucleation and evolution of the L'Aquila earthquake sequence [*Di Luccio et al.*, 2010; *Lucente et al.*, 2010] and 1997 Colfiorito sequence [*Miller et al.*, 2004]. Data from the trenches allow us also to calculate a slip rate for the late Pleistocene to Holocene. Late Pleistocene dip-slip rates for Acq (see section 3) and Tret (see section 5) of 0.2–0.4 and 0.2–0.3 mm/yr, respectively, are obtained by assuming a 50°–60° dipping fault. These estimates are consistent with the 0.25–0.5 mm/yr early Pleistocene slip rate estimated by *Civico et al.* [2010] farther south across the fault zone. Late Holocene slip rates can be calculated by using the age and throw of individual events and result in an average dip-slip rate at each site of ~0.3–0.4 mm/yr, in agreement with the late Pleistocene estimates. This leads to the conclusion that the portion of the PF system, where deformation is concentrated and the 2009 continuous surface faulting occurred, has a constant average rate of slip release since late Pleistocene, and perhaps throughout the Quaternary.

8. Discussion

[53] Although not the largest earthquake to hit Italy in the past century, the 6 April 2009 L'Aquila event had strong psychological and social impact. Once again, the community directly faced the high vulnerability of our country, where the huge damage to artistic, historical, and residential buildings is mostly caused by unreinforced buildings, and also by the location of urban centers on shaking sensitive geologic sites. There is a strong need for systematic prevention plans based on detailed local seismic hazard evaluations. Therefore, the L'Aquila earthquake should be thoroughly studied to shed light on the seismogenic potential of this area of high tectonic complexity and eventually export this knowledge to nearby similar areas. When we started this paleoseismological work we aimed to collect all the information to answer the main open question derived by the study of the 2009 coseismic ruptures and of the tectonic and geologic setting of the area (see section 1.3): Is the Paganica fault also capable of generating earthquakes larger than Mw 6.3? A key point for maximum magnitude prediction on a fault is to understand the largest earthquakes that occurred in the past. This information is generally obtained by the analysis of the long-term surface expression of the fault and by the recognition and measurement of displacements and rupture lengths related to paleoearthquakes. The complexity and long-term expression of the PF is discussed in section 1.2, where we highlight the inconsistency between the extent and the cumulative escarpment of the PF relative to the length and the throw of the continuous 2009 surface rupture. From the trenches we observe that the amount and the style of deformation in past events (notably, well-preserved colluvial wedges, large graben structures, intensive sheared zone, backtilting) point to earthquakes larger than 2009. Thus, our paleoseismogical results coupled with the long-term expression of the PF allow the possibility for the occurrence of larger surface faulting earthquakes in the past ($M > 6.5$) producing longer surface rupture and larger throw, which likely will recur in the future. Following this reasoning, there are different scenarios we can picture for the occurrence of the large events hypothesized and the large throws observed, alternated to less energetic events (2009-type earthquakes): (1) Larger magnitude events were produced along the PF by the linkage of the PF system with adjacent structures bordering the Aterno valley (e.g., Middle Aterno fault system, Figure 2, see also *Roberts et al.* [2004]). (2) The larger magnitude events result from the variability of the distribution in the coseismic fault slip at depth along the ~16 km long PF system, i.e., rupture of different size asperities and at shallower depth with respect to the 2009 event.

[54] The data collected in this work also allow for comment on a further issue on the seismic behavior of the Paganica fault: Is the 2009 Mw6.3 earthquake characteristic for this fault (CEQ, sensu *Schwartz and Coppersmith* [1984])? Paleoseismological results show variability of the slip per event at the same site with coefficient of variation (standard deviation divided by the mean) of 0.4–0.5. According to *Hecker and Abrahamson* [2004] this average variation is observed worldwide and is consistent with the CEQ model. However, a noncharacteristic behavior for the PF can be invoked as alternative, given that even the largest values at site are minimum estimates (because of possible additional throws on different splays). In this case variability in earthquake size may be larger than that expected for CEQ model. The tectonic complexity of the area may result in the rupture of different slip patches on the same fault, and result in "variable" slip behavior. The distinction between the CEQ and the variable slip model is debated and not rigorously defined yet; we need a larger amount of data and reduced uncertainties to favor one of the two models for the PF.

[55] Moreover, based on the L'Aquila paleoseismological case we may also add some comments on the general applicability of paleoseismology: Are we able with "traditional" paleoseismology to recognize small slip events (similar to 2009) or are they overprinted by larger ones? Based on paleoseismological analysis, we were able to locate in the exposures the deformation produced by 2009-type or slightly larger paleoearthquakes (0.1–0.3 m throw per event). This is not a novelty as few more examples of trenching studies that recognize such a small amount of slip are reported in literature [e.g., *Pavlides*, 1996; *Vanneste et al.*, 2001; *Pantosti et al.*, 2004; *Chatzipetros et al.*, 2005; *Villamor et al.*, 2007], but represents an additional insight on the potential for paleoseismological research also in areas of moderate seismicity such as central Europe.

[56] Given that with this study we have verified that small throw events can be recognized in paleoseismological trenches, it seems unusual that if we look at other paleoseismological studies along nearby active faults within the Abruzzi region [*Michetti et al.*, 1996; *Pantosti et al.*, 1996; *Galadini and Galli*, 1999; *D'Addezio et al.*, 2001; *Galli et al.*, 2002; *Moro et al.*, 2002; *Galadini and Galli*, 2003; *Salvi et al.*, 2003], the paleoearthquakes recognized in the trench walls are always associated with larger throws (>0.30 m).

This would mean that these faults produce only M > 6.5 earthquakes. However, on the basis of the 2009 experience, we should also consider the possibility that older small throws occurred but, because of the overprinting from larger events, they may not have been noticed (e.g., would we still see the 2009 throws if a 0.5 m throw earthquake occur on the PF?). What is interpreted as slip in a discrete event may actually be cumulative slip in more than one event. Back to our trench data for the Paganica fault, we record a general increasing of the slip with time and the smallest slip is the most recent. Of course, we cannot definitively rule out the possibility that some of the recognized older events may be multiples of smaller displacement events, occurred close in time. Moreover, the tectonic geomorphology produced by normal active faults, as the PF, is typically characterized by a steep slope coupled with a basin. This setting causes intense erosion of the footwall and the older beds may contain incomplete records because of an increasing possibility of having experienced erosional phases. However, this prospect seems to be remote on the basis of several evidence in the walls, such as the presence of scarp-derived well-preserved wedges, formation of wide graben, as well as the high escarpments at surface, which certainly favor the large event interpretation. Moreover, the comparable values of the slip rates obtained for different time intervals (late Holocene to early Pleistocene rates, section 7) imply that we are not missing additional small events in the oldest part of the record.

[57] We know that small primary rupture does occur on the PF (2009), but just for the sake of completeness we also mention about the possibility that some of the slip events in our trenches could represent triggered slip from earthquakes on other nearby faults. This is an additional possibility to consider in paleoseismological analysis particularly within areas of moderate seismicity with a dense array of faults.

[58] The seismic history of other Abruzzi faults may be more complicated than hypothesized and even if the energy involved is smaller, the L'Aquila earthquake dramatically showed how damaging can be a Mw 6.3 earthquake. Therefore, for a correct seismic hazard assessment, the local faults seismic history needs to include or exclude also possible 2009-type events. Under this light, a future commitment for the local paleoseismologists should be the systematic review of the paleoseismic interpretation of the Abruzzi faults.

9. Conclusions

[59] On the basis of paleoseismological investigations, including trenching and coring, conducted at four artificial exposures across the portion of the Paganica fault that ruptured at the surface in 2009 (Figure 3), we obtained a preliminary reconstruction of the seismic history of the 6 April 2009 L'Aquila earthquake causative fault. We estimated timing and throw for each event, correlated events among trench sites and obtained late Pleistocene and Holocene slip rates.

[60] The main results of this study can be summarized in the following points:

[61] 1. The 2009 Paganica surface rupture coincides with mainly normal, high-angle dipping, fault planes at depth and is directly related to the coseismic movement along these planes. Four distinct paleoevents were recognized on the same fault zones, characterized by a similar style of deformation, with different scale structures organized in well defined and recurrent geometries (e.g., grabens, V-shaped faults).

[62] 2. The timing of the events at the trenching sites suggests that contemporary rupture at the surface along at least two parallel strands recurred also in the past earthquakes (no observation for PF3), like in 2009. The vertical displacement for each paleoevent along the investigated part of the fault has a low variability consistently with the fairly homogeneous slip observed in 2009 only in the northern portion of the rupture.

[63] 3. Chronological constraint and measured slip suggest that the penultimate event that ruptured the PF is the 1461 earthquake, already considered a predecessor of the 2009 earthquake on the basis of historical reports.

[64] 4. The measured throws associated to each of the five events vary between 0.15 m in 2009 (maximum estimate) and close to 0.4 (lower bound estimate) in earlier events. A general progression of increasing slip with age is observed and the paleoseismological results, along with the long-term expression of the PF, converge to more energetic earthquakes occurring in the past on the PF.

[65] 5. The overall average recurrence of surface faulting along the northern portion of the PF is in the range of about 700–1250 years (5 events since 2900–760 BC). The average interval before ~1000 AD is longer compared to that after this date (two events in the 2000–4000 years preceding ~1000 AD, while three events since ~1000 AD).

[66] 6. The late Holocene and late Pleistocene dip-slip rates for the investigated portion of the fault are consistent, and range between 0.2 and 0.4 mm/yr.

[67] Although we are aware that the trenching data are punctual and are limited to a restricted section of the PF, that are affected by broad uncertainties on the older events, and that other trenching analysis are needed both on parallel scarps and on the nearby fault systems to fully characterize the fault behavior, these results are the first at this level of detail for the area and should be seen as a useful starting point.

[68] **Acknowledgments.** We are grateful to the Gran Sasso Acque S.p.A. for permitting the deepening of the Acq trench and also for supplying the backhoe for the Zac trench. Thanks to Enzo Zaccagnini and his family and Ubaldo Bontempo for their kindness and for having allowed the trenching of their private land. We wish to thank Alessandra Smedile, Enrico Cirelli, and Hermann Borghesi for the useful discussions and contribution about the dating of the stratigraphy and age estimates of pottery shards. We thank the Editor Tom Parsons, and we are particularly grateful to Suzanne Hecker for the constructive suggestions and comments that strongly improved the paper and to an anonymous reviewer. Many thanks also to anyone occasionally involved during the survey. This work was partially funded by the Italian Dipartimento della Protezione Civile in the frame of the 2007–2009 Agreement with Istituto Nazionale di Geofisica e Vulcanologia (INGV).

References

Akinci, A., F. Galadini, D. Pantosti, M. Petersen, L. Malagnini, and D. Perkins (2009), Effect of time dependence on probabilistic seismic-hazard maps and deaggregation for the central Apennines, Italy, *Bull. Seismol. Soc. Am.*, *99*, 585–610, doi:10.1785/0120080053.

Anzidei, M., et al. (2009), Coseismic deformation of the destructive April 6, 2009 L'Aquila earthquake (central Italy) from GPS data, *Geophys. Res. Lett.*, *36*, L17307, doi:10.1029/2009GL039145.

Atzori, S., I. Hunstad, M. Chini, S. Salvi, C. Tolomei, C. Bignami, S. Stramondo, E. Trasatti, and A. Antonioli (2009), Finite fault inversion of DInSAR coseismic displacement of the 2009 L'Aquila earthquake (central Italy), *Geophys. Res. Lett.*, *36*, L15305, doi:10.1029/2009GL039293.

Bagnaia, R., A. D'Epifanio, and S. Sylos Labini (1992), Aquila and sub-aequan basins: An example of Quaternary evolution in central Apennines, Italy, *Quat. Nova*, *II*, 187–209.

Boncio, P., G. Lavecchia, and B. Pace (2004), Defining a model of 3D seismogenic sources for seismic hazard assessment applications: The case of central Apennines (Italy), *J. Seismol.*, *8*, 407–425, doi:10.1023/B:JOSE.0000038449.78801.05.

Boncio, P., A. Pizzi, F. Brozzetti, G. Pomposo, G. Lavecchia, D. Di Naccio, and F. Ferrarini (2010), Coseismic ground deformation of the 6 April 2009 L'Aquila earthquake (central Italy, Mw6.3), *Geophys. Res. Lett.*, *37*, L06308, doi:10.1029/2010GL042807.

Bronk Ramsey, C. (2008), Deposition models for chronological records, *Quat. Sci. Rev.*, *27*(1–2), 42–60, doi:10.1016/j.quascirev.2007.01.019.

Bronk Ramsey, C. (2009), Bayesian analysis of radiocarbon dates, *Radiocarbon*, *51*, 337–360.

Chatzipetros, A., S. Kokkalas, S. Pavlides, and I. Koukouvelas (2005), Paleoseismic data and their implication for active deformation in Greece, *J. Geodyn.*, *40*, 170–188, doi:10.1016/j.jog.2005.07.005.

Cheloni, D., et al. (2010), Coseismic and initial post-seismic slip of the 2009 Mw6.3 L'Aquila earthquake, Italy, from GPS measurements, *Geophys. J. Int.*, *181*, 1539–1546, doi:10.1111/j.1365-246x.2010.04584.x.

Chiarabba, C., et al. (2009), The 2009 L'Aquila (central Italy) Mw6.3 earthquake: Main shock and aftershocks, *Geophys. Res. Lett.*, *36*, L18308. doi:10.1029/2009GL039627.

Cinti, F. R., L. Faenza, W. Marzocchi, and P. Montone (2004), Probability map of the next large earthquakes in Italy, *Geochem. Geophys. Geosyst.*, *5*, Q11003, doi:10.1029/2004GC000724.

Cirella, A., A. Piatanesi, M. Cocco, E. Tinti, L. Scognamiglio, A. Michelini, A. Lomax, and E. Boschi (2009), Rupture history of the 2009 L'Aquila (Italy) earthquake from non-linear joint inversion of strong motion and GPS data, *Geophys. Res. Lett.*, *36*, L19304, doi:10.1029/2009GL039795.

Civico, R., et al. (2010), Long-term expression of the Paganica Fault vs. 2009 L'Aquila earthquake surface ruptures: Looking for a better understanding of its seismic behavior, *Geophys. Res. Abstr.*, *12*, EGU2010–12775–1.

D'Addezio, G., E. Masana, and D. Pantosti (2001), The Holocene paleoseismicity of the Aremogna-Cinque Miglia Fault (central Italy), *J. Seismol.*, *5*, 181–205, doi:10.1023/A:1011403408568.

Di Luccio, F., G. Ventura, R. Di Giovambattista, A. Piscini, and F. R. Cinti (2010), Normal faults and thrusts reactivated by deep fluids: The 6 April 2009 Mw 6.3 L'Aquila earthquake, central Italy, *J. Geophys. Res.*, *115*, B06315, doi:10.1029/2009JB007190.

Dramis, F. (1983), Morfogenesi di versante nel Pleistocene superiore in Italia: I depositi detritici stratificati, *Geogr. Fis. Din. Quat.*, *6*, 180–182.

Emergeo Working Group (2010), Evidence for surface rupture associated with the Mw 6.3 L'Aquila earthquake sequence of April 2009(central Italy), *Terra Nova*, *22*(1), 43–51, doi:10.1111/j.1365-3121.2009.00915.x.

Falcucci, E., et al. (2009), The Paganica Fault and surface coseismic ruptures caused by the 6 April 2009 earthquake (L'Aquila, central Italy), *Seismol. Res. Lett.*, *80*(6), 940–950, doi:10.1785/gssrl.80.6.940.

Galadini, F., and P. Galli (1999), The Holocene paleoearthquakes on the 1915 Avezzano earthquake faults (central Italy): Implications for active tectonics in the central Apennines, *Tectonophysics*, *308*, 143–170, doi:10.1016/S0040-1951(99)00091-8.

Galadini, F., and P. Galli (2003), Paleoseismology of silent faults in the central Apennines (Italy): The Mt. Vettore and Laga Mts. faults, *Ann. Geophys.*, *46*, 815–836.

Galadini, F., P. Galli, and M. Moro (2003), Paleoseismology of silent faults in the central Apennines (Italy): The Campo Imperatore Fault (Gran Sasso Range Fault System), *Ann. Geophys.*, *46*, 793–813.

Galli, P., F. Galadini, M. Moro, and C. Giraudi (2002), New paleoseismological data from the Gran Sasso d'Italia area (central Apennines), *Geophys. Res. Lett.*, *29*(7), 1134, doi:10.1029/2001GL013292.

Galli, P., B. Giaccio, and P. Messina (2010), The 2009 central Italy earthquake seen through 0.5 Myr-long tectonic history of the L'Aquila faults system, *Quat. Sci. Rev.*, *29*, 3768–3789, doi:10.1016/j.quascirev.2010.08.018.

Gasperini, P., G. Vannucci, D. Tripone, and E. Boschi (2010), The location and sizing of historical earthquakes using the attenuation of macroseismic intensity with distance, *Bull. Seismol. Soc. Am.*, *100*, 2035–2066, doi:10.1785/0120090330.

Gruppo di Lavoro, M. P. S. (2004), Redazione della mappa di pericolosita` sismica prevista dall'Ordinanza PCM del 20 marzo 2003, Rapp. Conclusivo per il Dipartimento della Protezione Civile, 65 pp., Inst. Naz. di Geofis. e Vulcanol., Milan, Italy. (Available at http://zonesismiche.mi.ingv.it/).

Hecker, S., and N. A. Abrahamson (2004), Low slip-at-a-point variability: Implications for earthquake-size distribution, fault rupture hazard, and ground-motion modelling, paper presented at Basin and Range Seismic Hazards Summit II, Western States Seismic Policy Council, Reno-Sparks, Nevada, 16–19 May.

Italian Geological Cartography (2009), Cartografia Geologica Ufficiale. Foglio CARG 1:50,000 N. 359, L'Aquila.

Lucente, F. P., P. De Gori, L. Margheriti, D. Piccinini, M. Di Bona, C. Chiarabba, and N. Piana Agostinetti (2010), Temporal variation of seismic velocity and anisotropy before the 2009 MW 6.3 L'Aquila earthquake, Italy, *Geology*, *38*(11), 1015–1018, doi:10.1130/G31463.1.

Maruyama, T., K. Iemura, T. Azuma, T. Yoshioka, M. Sato, and R. Miyawaki (2007), Paleoseismological evidence for non-characteristic behavior of surface rupture associated with the 2004 Mid-Niigata Prefecture earthquake, central Japan, *Tectonophysics*, *429*, 45–60, doi:10.1016/j.tecto.2006.09.008.

Marzocchi, W., J. Selva, F. R. Cinti, P. Montone, S. Pierdominici, R. Schivardi, and E. Boschi (2009), On the recurrence of large earthquakes: New insights from a model based on interacting faults embedded in a realistic tectonic setting, *J. Geophys. Res.*, *114*, B01307, doi:10.1029/2008JB005822.

Messina, P., P. Galli, B. Giaccio, and E. Peronace (2009), Quaternary tectonic evolution of the area affected by the Paganica Fault (2009 L'Aquila earthquake), paper presented at 29th Congresso Nazionale del Gruppo Nazionale di Geofisica della Terra Solida, Trieste, Italy.

Michetti, A. M., F. Brunamonte, L. Serva, and E. Vittori (1996), Trench investigations of the 1915 Fucino earthquake fault scarps (Abruzzo, central Italy): Geological evidence of large historical events, *J. Geophys. Res.*, *101*(B3), 5921–5936, doi:10.1029/95JB02852.

Miller, S. A., C. Collettini, L. Chiaraluce, M. Cocco, M. Barchi, and B. J. P. Kaus (2004), Aftershocks driven by a high-pressure CO2 source at depth, *Nature*, *427*, 724–727, doi:10.1038/nature02251.

Moro, M., V. Bosi, F. Galadini, P. Galli, B. Giaccio, P. Messina, and A. Sposato (2002), Analisi paleosismologiche lungo la faglia del M. Marine (alta valle dell'Aterno): Risultati preliminari, *Il Quaternario*, *15*, 267–278.

Pace, B., L. Peruzza, G. Lavecchia, and P. Boncio (2006), Layered seismogenic source model and probabilistic seismic hazard analyses in central Italy, *Bull. Seismol. Soc. Am.*, *96*, 107–132, doi:10.1785/0120040231.

Pantosti, D., G. D'Addezio, and F. R. Cinti (1996), Paleoseismicity of the Ovindoli-Pezza fault, central Apennines, Italy: A history including a large, previously unrecorded earthquake in the Middle Ages (860–1300 A.D.), *J. Geophys. Res.*, *101*(B3), 5937–5959, doi:10.1029/95JB03213.

Pantosti, D., P. M. De Martini, I. Koukouvelas, L. Stamatoupulos, N. Palyvos, S. Pucci, F. Lemeille, and S. Pavlides (2004), Palaeoseismological investigations of the Aigion Fault (Gulf of Corinth, Greece), *C. R. Geosci.*, *336*, 4–5, 385–393.

Pavlides, S. (1996), First paleoseismological results from Greece, *Ann. Geofis.*, *39*(3), 545–555.

Pondrelli, S., S. Salimbeni, A. Morelli, G. Ekström, M. Olivieri, and E. Boschi (2010), Seismic moment tensors of the April 2009, L'Aquila (central Italy), earthquake sequence, *Geophys. J. Int.*, *180*, 238–242, doi:10.1111/j.1365-246X.2009.04418.x.

Reimer, P. J., et al. (2009), IntCal09 and Marine09 radiocarbon age calibration curves, 0–50,000 years cal BP, *Radiocarbon*, *51*, 1111–1150.

Roberts, G. P., P. Cowie, I. Papanikolaou, and A. M. Michetti (2004), Fault scaling relationships, deformation rates and seismic hazards: An example from the Lazio–Abruzzo Apennines, central Italy, *J. Struct. Geol.*, *26*, 377–398, doi:10.1016/S0191-8141(03)00104-4.

Salvi, S., F. R. Cinti, L. Colini, G. D'Addezio, F. Doumaz, and E. Pettinelli (2003), Investigation of the active Celano–L'Aquila fault system, Abruzzi, *Geophys. J. Int.*, *155*, 805–818, doi:10.1111/j.1365-246X.2003.02078.x.

Schwartz, D. P., and K. J. Coppersmith (1984), Fault behavior and characteristic earthquakes: Examples from the Wasatch and San Andreas Fault zones, *J. Geophys. Res.*, *89*(B7), 5681–5698, doi:10.1029/JB089iB07p05681.

Stuiver, M., and P. J. Reimer (1993), Extended C-14 data-base and revised calib 3.0 C-14 age calibration program, *Radiocarbon*, *35*, 215–230.

Tertulliani, A., A. Rossi, L. Cucci, and M. Vecchi (2009), L'Aquila (central Italy) earthquakes: The predecessors of the April 6, 2009 event, *Seismol. Res. Lett.*, *80*(6), 1008–1013, doi:10.1785/gssrl.80.6.1008.

Vanneste, K., K. Verbeeck, T. Camelbeeck, E. Paulissen, M. Meghraoui, F. Renardy, D. Jongmans, and M. Frechen (2001), Surface-rupturing history of the Bree fault scarp, Roer Valley graben: Evidence for six events since the late Pleistocene, *J. Seismol.*, *5*, 329–359, doi:10.1023/A:1011419408419.

Vezzani, L., and F. Ghisetti (1998), Carta Geologica dell'Abruzzo, Scala 1:100,000, SELCA, Florence, Italy.

Villamor, P., R. Van Dissen, B. V. Alloway, A. S. Palmer, and N. Litchfield (2007), The Rangipo fault, Taupo rift, New Zealand: An example of temporal slip-rate and single-event displacement variability in a volcanic environment, *Geol. Soc. Am. Bull.*, *119*, 529–547, doi:10.1130/B26000.1.

Wells, D. L., and K. J. Coppersmith (1994), New empirical relationships among Magnitude, rupture length, rupture width, rupture area, and surface displacement, *Bull. Seismol. Soc. Am.*, *84*, 974–1002.

Yoong, K. H., and A. Okada (2005), Surface deformations associated with the October 2004 Mid-Niigata earthquake: Description and discussion, *Earth Planets Space*, *57*, 1093–1102.

C. A. Brunori, F. R. Cinti, R. Civico, L. Cucci, P. M. De Martini, D. Pantosti, A. Patera, S. Pierdominici, S. Pinzi, and S. Pucci, Istituto Nazionale di Geofisica e Vulcanologia, Via di Vigna Murata 605, I-00143 Rome, Italy. (francesca.cinti@ingv.it)

- APPENDIX H - Improta, L., Villani, F., Bruno, P.P., Castiello, A., De Rosa, D., Varriale, F., Punzo, M., Brunori, C.A., **Civico, R.**, Pierdominici, S., Berlusconi, A., Giacomuzzi, G. (2011), *High-resolution controlled-source seismic tomography across the Middle Aterno basin in the epicentral area of the 2009, Mw 6.3, L'Aquila earthquake (central Apennines, Italy).* In press on the Italian Journal of Geosciences.

Italian Journal of Geosciences
Bollettino della
Società Geologica Italiana
e del Servizio Geologico d'Italia

High-resolution controlled-source seismic tomography across the Middle Aterno basin in the epicentral area of the 2009, Mw 6.3, L'Aquila earthquake (central Apennines, Italy)

Journal:	*Italian Journal of Geosciences*
Manuscript ID:	IJG-2011-0108.R2
Manuscript Type:	Original Article
Date Submitted by the Author:	n/a
Complete List of Authors:	Improta, Luigi; Istituto Nazionale di Geofisica e Vulcanologia, Sezione Roma 1 Villani, Fabio; Istituto Nazionale di Geofisica e Vulcanologia, Sezione Roma 1 Bruno, Pier Paolo; Istituto Nazionale di Geofisica e Vulcanologia, Sezione Osservatorio Vesuviano Castiello, Antonio; Istituto Nazionale di Geofisica e Vulcanologia, Sezione Osservatorio Vesuviano De Rosa, Dario; Istituto Nazionale di Geofisica e Vulcanologia, Sezione Osservatorio Vesuviano Varriale, Francesco; Istituto Nazionale di Geofisica e Vulcanologia, Sezione Osservatorio Vesuviano Punzo, Michele; Istituto Nazionale di Geofisica e Vulcanologia, Sezione Osservatorio Vesuviano Brunori, Carlo Alberto; Istituto Nazionale di Geofisica e Vulcanologia, Sezione Centro Nazionale Terremoti Civico, Riccardo; Istituto Nazionale di Geofisica e Vulcanologia, Sezione Roma 1 Pierdominici, Simona; Istituto Nazionale di Geofisica e Vulcanologia, Sezione Roma 1 Berlusconi, Andrea; Università dell'Insubria, Facoltà di Scienze MM.FF.NN. Giacomuzzi, Genny; Istituto Nazionale di Geofisica e Vulcanologia, Sezione Centro Nazionale Terremoti
Keywords:	Non-linear Tomography, L'Aquila Earthquake, Normal Fault System, Middle Aterno basin, Central Apennines, Italy

High-resolution controlled-source seismic tomography across the Middle Aterno basin in the epicentral area of the 2009, Mw 6.3, L'Aquila earthquake (central Apennines, Italy)

Indagini di tomografia sismica ad alta risoluzione nel bacino della Media Valle del Aterno nell'area epicentrale del terremoto de L'Aquila (Mw 6.3) del 2009 (Appennino centrale, Italia)

Improta Luigi [1], Villani Fabio [1]*, Bruno Pier Paolo [2], Castiello Antonio [2], De Rosa Dario [2], Varriale Francesco [2], Punzo Michele [2], Brunori Carlo Alberto [3], Civico Riccardo [1], Pierdominici Simona [1], Berlusconi Andrea [4], Giacomuzzi Genny [3]

1 – Istituto Nazionale di Geofisica e Vulcanologia, Sezione Roma 1; via di Vigna Murata 605 – 00143 Roma

2 – Istituto Nazionale di Geofisica e Vulcanologia, Sezione Osservatorio Vesuviano; Via Diocleziano, 328 - 80124 Napoli

3– Istituto Nazionale di Geofisica e Vulcanologia, Sezione Centro Nazionale Terremoti; via di Vigna Murata 605 – 00143 Roma

4 – Università dell'Insubria, Facoltà di Scienze MM.FF.NN.; via Valleggio 11 – 22100 Como

* corresponding author: telephone: +390651860747; fax: +390651860507; e-mail: fabio.villani@ingv.it

Abstract

We present high-resolution Vp models of the Middle Aterno basin obtained by multi-scale non-linear controlled-source tomography. Seismic data have been collected along four dense wide-aperture profiles, that run SW-NE for a total length of ~ 6 km in the hangingwall of the Paganica - S. Demetrio Fault, source of the 6th April 2009 (M_w 6.3) L'Aquila normal-faulting earthquake. Seismic tomography expands the knowledge of the basin with high spatial resolution and depth penetration (> 300 m), illuminating the Meso-Cenozoic substratum that corresponds to high-Vp regions (Vp > 3500-4000 m/s). Low Vp (1500-2000 m/s) lacustrine sediments (Early Pleistocene in age) are imaged only in the SW sector of the basin, where they are up to 200 m thick and lie below coarse fluvial and alluvial fan deposits. The overall infill consists of Early to Late Pleistocene alluvial fan and fluvial sediments between the Paganica Fault and the Bazzano ridge, with Vp reaching 3000 m/s for the oldest conglomeratic bodies. The substratum has an articulated topography. The main depocenter, ~ 350 m deep, is in the SW sector of the basin south of the Bazzano ridge. Remarkably, this depocenter and the overlying thick lacustrine body match the area of maximum coseismic subsidence observed after the 2009 earthquake. In the Paganica area, Vp images unravel large steps in the substratum related to two unreported SW-dipping buried strands, synthetic to the Paganica Fault, with ~ 250 m associated total vertical throw. This finding has important implications on the long-term history of the Paganica – S. Demetrio Fault system, whose total vertical displacement has been previously underestimated. An additional ~ 250 m vertical offset along this complex Quaternary extensional structure should therefore be considered.

Key words

Non-linear Tomography, L'Aquila Earthquake, Normal Fault System, Middle Aterno basin, Central Apennines, Italy.

Riassunto

In questo lavoro vengono presentati dei modelli di velocità delle onde P (Vp) ad alta risoluzione del bacino della Media Valle dell'Aterno ottenuti mediante inversione tomografica non-lineare di dati di sismica attiva. I dati sono stati acquisiti con tecnica dense wide aperture lungo quattro profili orientati SW-NE per una lunghezza totale di ~ 6 km nell'hangingwall della Faglia di Paganica – S. Demetrio, sorgente del terremoto de L'Aquila del 6 aprile 2009 (M_w 6.3). L'indagine tomografica migliora la conoscenza della struttura del bacino grazie ad una elevata risoluzione spaziale e profondità del modelli di velocità (> 300 m), illuminando il substrato Meso-Cenozoico che corrisponde a regioni di alta Vp (> 3500-4000 m/s). Terreni a bassa Vp (1500-2000 m/s) riferibili a sedimenti lacustri del Pleistocene Inferiore sono stati riconosciuti soltanto nel settore SW del bacino, dove raggiungono uno spessore di 200 m e si ritrovano alla base di depositi grossolani alluvionali e di conoide. Il riempimento complessivo del bacino, tra la Faglia di Paganica e la dorsale di Bazzano, consiste invece di depositi alluvionali grossolani e di conoide del Pleistocene Inferiore-Superiore con Vp che raggiungono i 3000 m/s nei termini conglomeratici più antichi. Il depocentro principale del bacino, profondo ~ 350 m, si trova nel settore SW della Media Valle dell'Aterno, a sud della dorsale di Bazzano. È importante evidenziare che questo depocentro e i sovrastanti sedimenti lacustri sono ubicati in corrispondenza dell'area di massima subsidenza cosismica osservata dopo il terremoto del 2009. Nell'area di Paganica, i modelli di Vp rivelano dei considerevoli gradini nel substrato riferibili a due segmenti sepolti immergenti a SW, sintetici rispetto alla Faglia di Paganica e non riportati precedentemente in letteratura, con rigetto

cumulato di ~ 250 m. Ciò ha importanti implicazioni sulla storia di dislocazione di lungo termine del sistema di faglie Paganica – S. Demetrio, il cui rigetto complessivo è stato in passato sottostimato. Pertanto, a tale valore andrebbero aggiunti altri ~ 250 m cumulati dai due segmenti sintetici della Faglia di Paganica.

Parole chiave

Tomografia Non-lineare, Terremoto de L'Aquila, Sistema di Faglie Normali, Bacino della Media Valle dell'Aterno, Appennino Centrale, Italia.

1. Introduction

The 2009 L'Aquila seismic sequence that culminated with the 6th April 2009 M_w 6.3 mainshock (CHIARABBA *et alii*, 2009; GALLI *et alii*, 2009) is the last of a long series of destructive earthquakes occurred in the central Apennines extensional belt (TERTULLIANI *et alii*, 2009). This sequence is related to a ~ 40 km long, NW-trending and SW-dipping normal fault system (CHIARABBA *et alii*, 2009) and is coherent with the structural framework of this sector of the central Apennines (see a review in: ROBERTS *et alii*, 2010 and GALLI *et alii*, 2010). Particularly, the long-term activity of normal faulting systems during the Quaternary generated several intramontane fault-bounded basins which, together with other active faults, now give rise to a typical tectonic-controlled basin and range landscape. Among these depressions, the Middle Aterno River Valley (BOSI & BERTINI, 1970; BERTINI *et alii*, 1989; BERTINI & BOSI, 1993; GALADINI & GALLI, 2000; BOSI *et alii*, 2003) is the result of the Quaternary activity of a fault system that includes the source of the 2009 mainshock (e.g.: Paganica – S. Demetrio Fault System, hereinafter PSDFS according to GALLI *et alii*, 2010).

Prior to the 2009 L'Aquila earthquake, the geometry and activity of the PSDFS were not defined univocally (see GALLI *et alii*, 2010 for a review). After the earthquake, a wealth of new field investigations have provided a detailed picture of the geometry, length and segmentation of the PSDFS (EMERGEO WORKING GROUP, 2009; FALCUCCI *et alii*, 2009; GALLI *et alii*, 2009; BONCIO *et alii*, 2010). In addition, paleoseismological trenches allow defining the short-term displacement history (< 24 ka) of the faults activated during the seismic sequence (GALLI *et alii*, 2010; CINTI *et alii*, 2011), particularly of the Paganica Fault (PF), which is related to the causative source of the 2009 mainshock because it exhibits the clearest coseismic surface ruptures (EMERGEO WORKING GROUP, 2009) and accommodated maximum coseismic slip (CIRELLA *et alii*, 2009). On the other hand, the long-term evolution (< 500 ka) of the PSDFS has been reconstructed by GALLI *et alii* (2010) by integrating stratigraphical and morphological analyses with new tephrochronological data.

Conversely, the subsurface geometry and internal architecture of the Middle Aterno fault system and related basins are still poorly known mainly because seismic exploration data are lacking. No commercial reflection profile is available in the mainshock area and the PSDFS is not investigated by shallow seismic surveys. As a consequence, long-term reconstruction of the fault system and basins evolution still suffers from the absence of seismic constraints.

To overcome this drawback, we carried out a high-resolution shallow seismic experiment across the Middle Aterno River Valley in the Paganica – Bazzano area in 2010 (Fig. 1). Seismic data were collected with the innovative dense wide aperture acquisition geometry (OPERTO *et alii*, 2004), which allows the use of both seismic tomography and seismic reflection techniques. Our primary goal was to yield reliable images of the Middle Aterno basin which could shed light on the relations between the large-scale basin architecture and Quaternary faults.

In this paper we present the seismic experiment and multi-scale Vp images obtained by non-linear traveltime tomography along four profiles for a total length of ~ 6 km (Fig. 1). Vp models define the basin structure down to 300-350 m depth, reaching the pre-Quaternary substratum, and provide valuable information for the reconstruction of the basin architecture and long-term evolution. In addition, high-resolution shallow Vp images unravel unknown buried splays of the PSDFS likely activated during the seismic sequence.

2. Geological and geomorphological setting

The 2009 L'Aquila sequence (CHIARABBA *et alii*, 2009) struck a portion of the central Apennines which underwent thrusting during Miocene-Pliocene times and was affected by Quaternary extension (PATACCA *et alii*, 1990). The chain backbone is made of Mesozoic-Tertiary carbonate and marly ridges separated by fault valleys hosting Miocene-Pliocene siliciclastic deposits (BOSI & BERTINI, 1970; CENTAMORE *et alii*, 2006). The structural setting is characterized by inherited Jurassic-Cretaceous normal faults, which are cross-cut by NW-trending Miocene-Pliocene thrusts; finally, Quaternary extension generated a network of NW- to W-striking normal fault systems that at some places reactivated older structures (GALADINI, 1999; GALADINI & GALLI, 2000; GALADINI & MESSINA, 2001, 2004; PIZZI & GALADINI, 2009). These normal faults consist of generally SW-dipping, 5-15 km long individual strands which generated several intramontane basins and, together with the Quaternary climatic fluctuations and large-scale uplift of the chain, controlled their long-term evolution (PIZZI *et alii*, 2002; BOSI *et alii*, 2003; MESSINA *et alii*, 2001, 2003, 2007; GALADINI *et alii*, 2003). Late Pleistocene – Holocene activity of some of these faults was ascertained before the 2009 earthquake (see a review in: GALADINI & GALLI, 2000; GALLI *et alii*, 2008): among them, the study area comprises the so called Upper and Middle Aterno River Fault System, which created a set of tectonic depressions late Pliocene-Quaternary in age (Fig. 1; BERTINI *et alii*, 1989; BOSI & MESSINA, 1991; BAGNAIA *et alii*, 1992; BERTINI & BOSI, 1993; VEZZANI & GHISETTI, 1998).

Coseismic surface breaks (EMERGEO WORKING GROUP, 2009; FALCUCCI *et alii*, 2009; BONCIO *et alii*, 2010; GALLI *et alii*, 2010) and geodetic analysis of ground displacement related to the 2009 earthquake (ANZIDEI *et alii*, 2009; ATZORI *et alii*, 2009; WALTERS *et alii*, 2009; STRAMONDO *et alii*, 2011) depict a complex deformation pattern that is coherent with the Quaternary tectonic setting (GALLI *et alii*, 2010). In fact, the earthquake activated at least three main right-stepping fault segments associated to coseismic ground faulting and fracturing (Fig. 1; see BONCIO *et alii*, 2010) belonging to the SW-dipping PSDFS, whose hangingwall hosts part of the Middle Aterno basin where the maximum coseismic subsidence (about 0.25 m; ATZORI *et alii*, 2009) is observed. The majority of surface breaks occurred along fault strands often coupled with scarps in their footwall (see a review in: GALLI *et alii*, 2010; ROBERTS *et alii*, 2010). The hangingwall of the PSDFS hosts important antithetic structures, such as the Bazzano and Monticchio NE-dipping normal faults, and small substratum salients (Fig. 1; CENTAMORE *et alii*, 2006), which suggest a quite complex topography of the pre-Quaternary substratum.

The complexity of the fault system activated during the seismic sequence is confirmed by aftershocks distribution (CHIARABBA *et alii*, 2009). The causative fault of the mainshock is imaged by a main hypocenter alignment from 2 to 9 km depth, whose geometry is compatible with the surface trace of the PF. Conversely, in the uppermost crust aftershocks spread in a wide volume beneath the whole Middle Aterno basin in the hangingwall of PF. This suggests that shallow deformation was accommodated by numerous, minor structures (VALOROSO *et alii*, 2011).

Our seismic investigation targets the northwestern sector of the Middle Aterno Valley that can be roughly subdivided by the Bazzano-Monticchio ridge into two sub-basins (Fig. 1). The

western sub-basin (Bazzano sub-basin), bounded by the Bazzano ridge to the east, is locally emplaced on Miocene turbidites (sandstones, marls, marly limestones), which in turn cover Meso-Cenozoic limestones (CENTAMORE *et alii*, 2006). The eastern sub-basin (Paganica sub-basin), bounded by the PSDFS and the Bazzano fault, is emplaced on Meso-Cenozoic carbonates of slope to basin sequences (Fig. 1).

Continental deposits exposed in this area can be referred to two main cycles (BOSI & BERTINI, 1970; BERTINI & BOSI, 1993): 1) a lower (Early Pleistocene) fluvio-lacustrine cycle, > 200 m thick, including lacustrine silts (S. Nicandro Fm.), etheropic with deltaic and alluvial fan deposits (Vall'Orsa, Valle dell'Inferno, Valle Valiano and Fonte Vedice Fm.); 2) an upper fluvio-lacustrine cycle (Middle Pleistocene), carved in the former one and consisting of sands rich of volcanic ashes and gravels (S. Mauro Fm.). All these deposits are covered by Late Pleistocene-Holocene fluvial sediments, mainly related to the Aterno River, and by slope debris (BERTINI & BOSI, 1993). A detailed picture of the Quaternary stratigraphy in the Paganica sub-basin is provided by GALLI *et alii*, 2010. The authors recognize seven main sedimentary units covering the pre-Quaternary substratum, being affected by a total amount of vertical offset ~ 250 m across the PSDFS near Paganica and ~ 400 m near S. Demetrio (BERTINI & BOSI, 1993). The stratigraphic sequence spans the last 1 Ma time interval, with fluvial and alluvial fan depositional events alternated with long phases of geomorphic stability and pedogenesis, which gave rise to distinct, regional pedo-markers. The oldest sediments (PAG-7 Unit in GALLI *et alii*, 2010) are related to the Early Pleistocene fluvial gravels (Vall'Orsa and Valle dell'Inferno Fm.) proposed by BERTINI & BOSI (1993). Units PAG4 (450 ± 100 ka; ~ 50 m thick) and PAG2 (< 110 ka; 20-25 m thick) instead represent two distinct stages of the alluvial fan accretion at the NE border of the Middle Aterno basin (GALLI *et alii*, 2010).

The shallow subsurface of the two sub-basins was investigated by numerous boreholes, drilled for civil engineering purposes, and by several Electrical Resistivity Tomographies (ERT) performed after the 2009 earthquake (GRUPPO DI LAVORO MS-AQ, 2010; GIOCOLI *et alii*, 2011). These surveys seldom exceed 50-100 m depth and reach the pre-Quaternary substratum only along the eastern margin of the Paganica sub-basin. The large-scale structure of the Middle Aterno basin was investigated by BALASCO *et alii* (2011) by means of a Deep Electrical Resistivity Tomography (DERT), that complemented a crustal magnetotelluric survey. The resistivity section, ~ 1000 m deep, defines in the Paganica sub-basin a conductive alluvial filling ~ 200 m thick above an articulated high-resistivity carbonate substratum. On the other hand, the geometry of the Bazzano sub-basin is poorly constrained because the substratum includes conductive Miocene turbidites and fractured Cenozoic carbonates with high water content (BALASCO *et alii*, 2011).

3. The seismic surveys

Seismic surveys focus on the Paganica and Bazzano sub-basins characterized by coseismic surface ruptures and maximum coseismic subsidence, respectively (EMERGEO WORKING GROUP, 2009; ATZORI *et alii*, 2009; STRAMONDO *et alii*, 2011). The survey geometry was preliminary designed based on the analysis of aerial photos and geologic maps and on results of geologic investigations carried out after the earthquake (EMERGEO WORKING GROUP, 2009; BONCIO *et alii*, 2010; GRUPPO DI LAVORO MS-AQ, 2010). However, unfavorable logistic and environmental conditions posed significant difficulties. Main factors hampering seismic profiling were a railway, a national road and the Aterno river, which parallel the valley, as well as the high urbanization with widespread anthropic sources of seismic noise. As result, we traced 5 seismic profiles representing the best compromise between geologic targets and logistic/environmental difficulties (Fig. 1). The

profiles had a total length of 6800 m and were acquired during a two-weeks-long experiment in 2010. Noteworthy, data acquisition required closing to traffic main roads.

All profiles trend SW-NE and, as a whole, they define a transect across the Aterno River valley (Fig. 1). This seismic transect follows the DERT profile of BALASCO *et alii* (2011) in the Bazzano sub-basin (Lines B1 and B2), while it is shifted 400-800 m to the NW in the Paganica sub-basin (Line P2). Lines B1 and B2 cross the south-western and central portions of the Bazzano sub-basin, between the eastern slopes of the Mt. Ocre calcareous massif and the western slope of the Bazzano ridge. These profiles run above recent fluvial sediments for a length of 1075 m and 1498 m, respectively. Line B3 is 963 m long and crosses the buried threshold of the Bazzano-Monticchio ridge. Line P2 covers the western portion of the Paganica sub-basin in the hangingwall of the PF, running for 2095 m over Late Pleistocene-Holocene alluvial fan deposits. The SW end of line P2 abuts against the Bazzano fault-bounded ridge, while the NE end is ~ 200 m apart from the lower splay of the PF reported by GALLI *et alii* (2010).

The seismic experiment is complemented by line P1 that crosses the PF (Fig. 1). Because this line was acquired in the Paganica village, it suffers from a crooked acquisition geometry and strong cultural noise which deserve a complicated and long data processing. For this reason, this profile is not included in the paper.

A 216-channel, 10-Hz geophone array with a 5 m spacing between individual sensors was used to record dense sources (5-10 m spaced) provided by a high-resolution vibrating source (IVI-Minivib). The used dense geophone spread is 1075 m long, that is 3-4 times larger than the presumed depth of the basin substratum (300-400 m). This field setup, namely dense wide-aperture geometry (OPERTO *et alii*, 2004), differs from typical common midpoint reflection profiling. It allows collecting not only multi-fold reflection data but also highly redundant first P pulses corresponding to shallow direct waves and deep-penetrating turning waves and critical refractions, which are basic ingredients for multi-scale traveltime tomography (IMPROTA & BRUNO, 2007).

4. First Arrivals Picking and Tomographic Method

Overall, common-shot-gather (CSG) sections exhibit a good signal-to-noise ratio and clear first P pulses even for far offsets traces (Fig. 2 a). First arrivals were handpicked on raw CGSs taking advantage of the redundant reciprocity relationships between CSGs. In some cases, band-pass filtered (25-100 Hz) data were used to facilitate the picking of far offset noisy traces. A summary of the data set used for traveltime tomography, including picking uncertainty, is reported in Table A.

CSGs often show evident shadow zones at intermediate-large offsets on all three profiles (Fig. 2 a). This suggests low-Vp bodies and strong lateral heterogeneities inside the basin, for which a traditional linearized inversion could be improper. We overcame this problem by a non-linear multi-scale tomographic technique that does not require a starting model and is able to cope with strong lateral Vp changes. This technique, specifically implemented for crustal targets (IMPROTA *et alii*, 2002; IMPROTA & CORCIULO, 2006), is very effective for shallow imaging of basins and faults (IMPROTA *et alii*, 2003; IMPROTA & BRUNO, 2007; BRUNO *et alii*, 2010a, BRUNO *et alii*, 2010b, IMPROTA *et alii*, 2010). Traveltimes are computed by a finite-difference Eikonal solver. The multi-scale inversion consists in a succession of inversion runs performed by gradually reducing the spacing of the velocity grid. At each run, the best-fit model is searched by a non-linear algorithm that combines global random (Monte Carlo) with local (Simplex) search. This procedure allows the dense sampling of the model space with affordable computational costs, thus strongly decreasing the risk of falling into secondary minima of the cost function. The multi-scale inversion defines first the large-scale structure of the basin and subsequently illuminates the

near-surface with an increased spatial resolution. The gradual improvement in spatial resolution is achieved run by run, but at the cost of a progressive limitation in resolution depth. For this reason, two stopping criteria are used to halt the multi-scale inversion: the decrease of RMS traveltime residual and the decrease in resolution depth estimated run by run by *a posteriori* checkerboard tests.

5. Tomographic models and interpretation

For each profile we show two Vp models, together with resolution tests, obtained at different steps of the multi-scale inversion: a long-wavelength model, representative of the large-scale basin structure, complemented by a short-wavelength model that pictures the shallow structure with a higher spatial resolution. We interpret the tomographic models based on a simplified Vp-lithology association (Table B), derived by similar investigations of intramontane basins in the Apennines (IMPROTA *et alii*, 2003; BRUNO *et alii*, 2010a, BRUNO *et alii*, 2010b IMPROTA *et alii*, 2010), and on stratigraphic schemes proposed by several authors for the study area (see Section 2). Some intrinsic limitations to our interpretations are due to the lack of accurate borehole data, and to the uncertainty in correlating outcropping formations with possible equivalents in the subsurface. Also the unclear role of the Bazzano-Monticchio ridge threshold in separating two different sub-basins during Early-Middle Pleistocene may hamper correlation of their respective sedimentary units.

Bazzano1 line (B1)

The multi-scale inversion consisted in 11 inversion runs. Both the long-wavelength model (Fig. 3 a) and the short-wavelength model (Fig. 3 c) reveal evident lateral heterogeneities below a very low Vp (< 1500 m/s) near-surface layer ~ 30-50 m thick. The most noticeable feature, captured since the first inversion runs, is the pronounced low-Vp region extending between 500 and 900 m distance and 100-300 depth (hereinafter depths are relative to the ground surface) (Fig. 3 a). Here, a low Vp (1500-2000 m/s) body is found below two higher Vp wedges (Vp ~ 2500 m/s, Fig. 3 c). The low Vp anomaly overlies a high Vp (3500-4000 m/s) region imaged at the bottom of the long-wavelength model between 250 and 350 m depth (Fig. 3 a). This high Vp region dips towards NE and rapidly rises on the SW side of the model (Fig. 3 a).

The near-surface layer may be related to Late Pleistocene-Holocene unconsolidated alluvia of the Aterno River and to older fluvial deposits similar to the Middle Pleistocene fluvial gravels and sands outcropping at the northern border of the basin (S. Mauro Fm., BERTINI & BOSI, 1993). This shallow layer also includes to the SW alluvial fan deposits fed by Mt. Ocre. The two bodies with Vp ~ 2500 m/s (Fig. 3 c) can be related to coarse fluvial sediments similar to the Early Pleistocene cycle described for the Middle Aterno basin so far (see Section 2). Anyway, the SW wedge could also define an older, thick alluvial fan fed by the mountains behind, buried beneath the basin. The ~ 200 m thick low Vp (1500-2000 m/s) body responsible for the strong velocity inversion in the middle of the section is reasonably related to lacustrine and palustrine silts and clays of the Early Pleistocene cycle (equivalent to the S. Nicandro Fm., BERTINI & BOSI, 1993), which lie below coarse fluvial deposits of the subsequent depositional stage (PAG-7 Unit of GALLI *et alii*, 2010). As regards the deep high Vp body (Vp ~ 3500-4000 m/s), it is interpreted as the Meso-Cenozoic substratum (limestones and thin remnants of Miocene sandstones) that crops out close to Bagno village. Thus, the band marked by a strong vertical gradient, with Vp increasing from 3500 m/s to 4000 m/s, can be considered as representative of the top of the pre-Quaternary substratum. This interpretation is based on the analysis of ray paths relative to critical refractions and on subsurface constraints (see the next two paragraphs and Fig. 2 a-b). Moreover, it is

coherent with previous tomographic imaging of intramontane basins in the Apennines (IMPROTA *et alii*, 2003, BRUNO *et alii*, 2010a, BRUNO *et alii*, 2010b, IMPROTA *et alii*, 2010). Thus, the infill thickness in this sector of the Bazzano sub-basin may range between ~ 100-150 m at the SW margin, close to the Mt. Ocre mountainside, and ~ 300-350 m in the NE part of the profile. This is the deeper depocenter of the Middle Aterno basin along the investigated transect.

Bazzano2 line (B2)

The multi-scale inversion consisted in 12 inversion runs. The near-surface is characterized by very low Vp (< 1500 m/s) deposits, ~ 30-50 m thick, which thin at the NE end of the line (Fig. 4 c). In the central sector of the long-wavelength model (Fig. 4 a), a thick region approximately homogenous with velocities around 3000 m/s extends down to 200-250 m depth. A high Vp (3500-4500 m/s) body is found below. The 3500-4000 m/s contours describe a slightly bumpy geometry (Fig. 4 a). The high Vp body is ~ 180-200 m deep at 300-800 m distance, ~ 250 m deep at 900-1100 m distance, and abruptly rises from 200 m to 100 m depth on the NE side of the model in correspondence of an evident lateral heterogeneity (~ 1300 m distance).

The short-wavelength model provides relevant details on the basin infill (Fig. 4 c). A weak vertical velocity inversion characterizes the central portion of the model. Here, an upper layer with Vp in the 2500-2750 m/s range lies on lower velocity deposits (Vp ~ 2250 m/s), which in turn laterally grade into a well-resolved low Vp (1500-2000 m/s) region located between 250-500 m distance. This low Vp region is similar to the one imaged beneath the line B1 at a comparable depth range (75-150 m; Fig. 4 c). Anyway the low Vp body of line B2 is located above a shallower substratum, evidenced by a well-resolved high Vp (3500-4500 m/s) structure, whose top can be set to 180-220 m depth based on ray paths of critical refractions (Fig. 2 a).

Model interpretation is similar to the line B1. The near-surface includes recent alluvia of the Aterno River and fluvial deposits (possibly equivalent to the S. Mauro Fm.; BERTINI & BOSI, 1993), while the upper layer (Vp ~ 2500-2750 m/s), ~ 50-75 m thick, can be related to coarse, dense fluvial gravels and conglomerates of the Early Pleistocene cycle (Vall'Orsa Fm., Valle dell'Inferno Fm. of BERTINI & BOSI 1993). A main difference with respect to line B1 is the reduced extension of the low Vp (1500-2000 m/s) body relatable to fine lacustrine sediments (equivalent to the S. Nicandro Fm. of BERTINI & BOSI 1993). The weak vertical velocity inversion imaged at ~ 100 m depth may be indicative of finer alluvial deposits (Vp ~ 2250 m/s), which pass south-westward to etheropic lacustrine deposits (Fig. 4 c).

The pre-Quaternary substratum is shallower with respect to line B1, being at 180-250 m depth. It rapidly rises at ~ 100 m depth at the NE end of the line (Fig. 4 a, Fig. 4 c), coherently with the presence of the nearby Bazzano ridge, where thin Miocene turbidites and Meso-Cenozoic carbonates crop out (Fig. 1). The deepening of the substratum between 900-1100 m distance may be related to a paleo-valley morphology, since no displacement may be inferred from tomographic results alone. The substratum is poorly defined at the SW end of the models affected by a low resolution. Thus, the drowning of the 3500-4000 m/s contours between 0-300 m distance down to ~ 300 m depth (Fig. 4 c) is uncertain, even if this depth value agrees with the depth range of the substratum illuminated beneath the NE side of line B1 (Fig. 3 a).

Bazzano3 line (B3)

The multi-scale inversion consisted in 13 inversion runs. The long-wavelength model is quite regular (Fig. 5 a). In the shallow part, seismic velocity rapidly increases with depth from 1000 m/s to 3000 m/s. The vertical Vp gradient is lower in the central part (~ 100-200 m depth), where velocity increases from 3000 m/s to 3500 m/s. Below, the 3750-4000 m/s contours depict a regular very-high Vp body (Vp up to 4500 m/s) gently dipping to the NE. Near-surface low Vp (<

1500 m/s) deposits are 20-40 m thick and thin to the NE (Fig. 5 c). The short-wavelength model shows significant lateral heterogeneities in the 100-200 m depth range (Fig. 5 c). The 2000-2750 m/s contours define three small thickened zones at 150 m, 500 m and 750 m distance, which bound two evident high-velocity bumps, with Vp exceeding 3750 m/s. These bumps merge downwards into the very-high Vp region (Vp > 4000 m/s).

As for lines B1 and B2, we relate the shallow layers with Vp < 2750 m/s to a stack of recent alluvia and Middle-Late Pleistocene fluvial and alluvial fan deposits (possibly equivalent to the S. Mauro Fm., BERTINI & BOSI, 1993 and to units PAG-1, PAG-2 and PAG-4 of GALLI *et alii*, 2010) overlying ancient coarse fluvial and alluvial fan sediments, probably Early Pleistocene in age (Valle dell'Inferno Fm. of BERTINI & BOSI 1993; Unit PAG-7 of GALLI *et alii*, 2010). This interpretation is constrained by a 130 m deep borehole, located ~ 350 m to the SE of the profile (Fig. 1 and Fig. 5 c). The well drilled ~ 40 m of loose to dense fluvial and alluvial fan gravels with silty intercalations and then conglomerates down to the bottom, without reaching the pre-Quaternary substratum (GRUPPO DI LAVORO MS-AQ, 2010). We relate Vp values higher than 3250-3500 m/s to Meso-Cenozoic rocks. In particular, the 3250-3750 m/s Vp range may be attributed to Miocene turbidites exposed in the Mt. Bazzano ridge, while higher velocities could correspond to the underlying Meso-Cenozoic limestones.

B3 line is located in the middle of the valley cutting through the Bazzano-Monticchio ridge, but it does not show strong lateral Vp variations clearly diagnostic of the antithetic fault on the NE side. The profile, that abuts against a railway and a national road, is likely too short to illuminate the fault hangingwall. About half of line B3 (~ 450 m) overlaps the NE portion of line B2, with a lateral offset of ~ 450-650 m. In the overlap section, the velocity images are quite different. Along line B2 the high-Vp substratum (Vp > 3250-3500 m/s) is deeper and rapidly rises north-eastward from ~ 200-250 m to ~ 120 m depth (Fig. 4 a, Fig. 4 c). Along line B3 the high-Vp substratum is ~ 100-200 m deep but defines a culmination (Fig. 5 c). We believe that line B3 intercepts the SE-plunging culmination of the Mt. Bazzano ridge along the threshold, whereas line B2 illuminates only the SW buried flank of this structure. Moreover, we infer that the saddle in the substratum found at ~ 450 m distance along line B3 (Fig. 5 c) may represent a former incision of the Miocene turbidites.

Paganica2 line (P2)

The multi-scale inversion consisted in 10 inversion runs. Since the first inversion runs, Vp models display strong lateral Vp variations, which delineate at least three main high velocity (Vp > 3250 m/s) bumps at 800, 1300 and 1900 m distance (Fig. 6 a). The strongest variations occur between 1100-1300 m and 1700-1900 m distance, revealed by an abrupt SW deepening of the 3250-4000 m/s contours showing ~ 100 m and ~ 150 m of vertical separation, respectively. These contours define two major steps in the high Vp region. Concurrently, two thick wedges with Vp ranging from 2250-2500 m/s to 2750-3000 m/s develop above the western and eastern steps respectively. On the western side of section, the high Vp (3500-4000 m/s) region gently dips SW between 300-600 m distance reaching ~ 250 m depth. Then, it rises at the end of the line in correspondence of a deep lateral Vp change.

The short-wavelength model displays significant thickness changes of the near surface low Vp (500-1500 m/s) layer (Fig. 6 c). It is thicker (up to 50 m) between 1200-1400 m and 1700-2000 m distance and thinner (< 20 m) around 1100 and 1600 m distance. The near-surface contours gently dip to SW at the western end of the section.

We relate the shallow low Vp layer to Middle-Late Pleistocene gravels and sands of alluvial fan systems fed by the Raiale Torrent (PAG-4 and PAG-2 units in GALLI *et alii*, 2010) plus more recent fan flood sediments and colluvial deposits (PAG-1 unit in GALLI *et alii*, 2010). The bodies

with Vp > 2250 m/s, which cover the high Vp substratum with a variable thickness (up to 200 m to the NE of the Mt. Bazzano fault), can be related to conglomerates of the Early Pleistocene fluvial cycle (PAG-7 Unit, GALLI *et alii*, 2010). Along this profile there is no evidence of very low Vp bodies relatable to old lacustrine sediments (i.e.: S. Nicandro Fm.), contrary to what observed along lines B1 and B2.

The 3250-3500 m/s contours can be taken as a proxy for the top of the Meso-Cenozoic carbonate substratum (Fig. 6 a). This interpretation is based on the analysis of ray paths of critical refractions (Fig. 2 b) and it is constrained by a deep borehole and ERT data collected close to the NE end of the line (see location in Fig. 1; GIOCOLI *et alii*, 2011). The projection of the substratum drilled at 78 m depth onto line P2 line falls around the 3250-3500 m/s contours (Fig. 6 c), which are reliable velocities for the shallow fractured limestones and marly limestones penetrated by the well. The nearby ERT also defines a resistive carbonate substratum between 80-100 m depth in the hangingwall of the lower splay of the PF (GIOCOLI *et alii*, 2011). The carbonate nature of the substratum all along line P2 is also documented by the DERT section (see the next paragraph, BALASCO *et alii,* 2011).

The substratum is characterized by an articulated geometry (Fig. 6 a). The two evident high Vp steps found at ~ 1200 m and ~ 1700 m distance are good candidates for previously unknown SW-dipping synthetic segments of the PSDFS that juxtapose limestone against ancient fluvial and alluvial fan coarse deposits. Based on the offset of the 3500-4000 m/s contours, the down-thrown of the substratum can be set to ~ 100 m and ~ 150 m for the western and eastern segments, respectively. The two wedges developed above the downthrown side of the presumed faults at 1200 m and 1700 m distance likely denote syn-tectonic thickening. This interpretation also agrees with the thickening of shallow low Vp layer (< 1000 m/s) between 1200-1400 m (Fig. 6 c), which can be related to recent colluvial and fan deposits filling the hangingwall as a response to ongoing subsidence.

The high Vp bump at ~ 800 m distance suggests a further rise of the substratum. This structure corresponds to the southern prolongation of the small carbonate ridge (Monte Caticchio Ridge in Fig. 6 a), that crops out to the NW of the line (Fig. 1) and is limited eastward by a normal (antithetic) fault and westward by a reverse fault. The intense rock fracturing due to faulting may explain the lower velocities (Vp ~ 3000-3250 m/s), which make the imaging of this structure less clear. The rise of the substratum at the beginning of the line (Fig. 6 a) is in agreement with the presence of the nearby Bazzano carbonate ridge bounded by the antithetic fault (Fig. 1). The substratum reaches ~ 250 m depth in the fault hangingwall (Fig. 6 a) that is mainly filled by high velocity (2500-3000 m/s; Fig. 6 c) deposits referable to ancient conglomerates (PAG-7 Unit, GALLI *et alii*, 2010). Noteworthy, recent activity of the Bazzano fault is suggested by near-surface velocity contours that dip SW at the beginning of the line (Fig. 6 c).

6. Discussions and conclusions

Seismic tomography expands the knowledge of the Middle Aterno basin with unprecedented spatial resolution. Indeed, the comparison of Vp models with the DERT section (BALASCO *et alii*, 2011) reveals the lower spatial resolution of the resistivity image due to a 400 m averaging spacing among measurement stations (Fig. 7). For instance, the two evident steps in the high-Vp substratum in the model P2 correspond to undulation of the high-resitivity substratum (Fig. 6 a, Fig. 7). Nevertheless, the comparison puts constraints on the geologic interpretation of both surveys.

In the Paganica sub-basin, where the two surveys are 400-800 m apart (Fig. 1), the DERT corroborates the interpretation of the high-Vp region (Vp > 3500 m/s) as the limestone

substratum because it corresponds to very-high resistivity values (> 500 Ω∗m). Our interpretation of the high-Vp infill in the hangingwall of the Bazzano fault as ancient coarse deposits (up to 250 m thick) agrees with the ~ 200 m thick wedge with intermediate resistivity values (150-200 Ω∗m) imaged above the limestone substratum.

In the Bazzano sub-basin, where the DERT does not constrain the basin geometry (BALASCO *et alii*, 2011), seismic tomography is crucial to discriminate between a conductive pre-Quaternary substratum and the continental filling (Fig. 3, Fig. 4 and Fig. 7). Along line B2, the DERT defines a low-to-moderate resistivity layer (50-200 Ω∗m), 800-1000 m thick, above a high resistivity (> 500 Ω∗m) region. By integrating velocity and resistivity images, we can reasonably relate the basin substratum to high-Vp (Vp > 3250-3500 m/s) but conductive rocks consisting of Miocene turbidites and fractured Meso-Cenozoic carbonates with high water content. These latter may correspond to the deep regions with Vp above 4000 m/s (Fig. 4 c). Moreover, the presence of a thick body of fine lacustrine deposits along line B1 (Fig. 3 a-c) agrees with the very low resistivity (< 25 Ω∗m) region defined in the shallow part of the DERT section between 1600 m and 2400 m distance (Fig. 7).

As regards stratigraphic information, Vp images provide proxies for some outcropping Quaternary continental formations, which leads to a reliable first-order model interpretation. We found evidence of lacustrine deposits (reasonably equivalent to the S. Nicandro Fm., Early Pleistocene in age, BERTINI & BOSI, 1993) only in the SW portion of the Bazzano sub-basin, where they are up to 200 m thick (Fig. 3, Fig. 4). Conversely, the overall infill of the Paganica sub-basin mainly consists of Early to Late Pleistocene alluvial fan and fluvial sediments (PAG-7, PAG-4, PAG-2 units in GALLI *et alii*, 2010), with Vp reaching ~ 3000 m/s for the deepest and oldest bodies (Fig. 6).

Regarding the large-scale geometry of the basin, we found that the 3250-4000 m/s contours can be considered as a proxy for the articulated topography of the pre-Quaternary substratum. The velocity contours delineate a broad (~ 2.3 km wide) and smooth depocenter in the SW sector of the Bazzano sub-basin, with a depth exceeding 300 m (~ 250-275 m a.s.l.) beneath the NE end of line B1 (Fig. 3). The substratum is shallower and rises towards NE along line B2 (Fig. 4), while it has a complex morphology along line B3, where a culmination likely represents the SE plunge of the Bazzano ridge ~ 100 m deep (Fig. 5 c).

In the Paganica sub-basin, strong lateral heterogeneities and steps in the substratum evidence important faults (Fig. 6). We first envisage the role of the Bazzano fault in creating a narrow but up to ~ 250 m deep depocenter in its hangingwall, with a syn-tectonic thickening of coarse deposits mainly referable to the PAG-7 unit of GALLI *et alii* (2010). This amount of local subsidence in the Bazzano fault hangingwall must have been enhanced by the concurrent displacement along two unreported SW-dipping faults (at 1200 m and 1700 m along line P2) belonging to the PSDFS (Fig. 6 a). The fault at 1700 m is ~ 500 m apart from the lower splay of the PF described by GALLI *et alii* (2010).

Tomographic evidence of these two fault segments is coherent with the local structural setting. The fault at 1700 m may be regarded as a fourth synthetic splay of the PF, buried by recent sediments. Alternatively, it could be a high-angle relay structure with a dominant normal component, located in the overlap zone of the PF and S. Demetrio (SDF) right-stepping faults.

On the other hand, we relate the fault at 1200 m to the northwestern prolongation of the SDF (*S. Gregorio fault zone* in BONCIO *et alii*, 2010). Our interpretation is corroborated by surface data from BONCIO *et alii* (2010), who report coseismic open fissures without slip in unconsolidated sediments (Fig. 1) matching the surface projection of the fault at 1200 m (Fig. 6 a; *S. Gregorio fault zone*). The authors interpreted these fissures as due to near-surface tensional stresses above the tip of a blind coseismic fault located at depth of 100-250 m. Noteworthy, the hypothesis of a blind fault agrees with the lack of appreciable offset of near-surface low-Vp layers (Fig. 6 c), while evidence of displacement of the high-Vp substratum (Fig. 6 a) and of the overlying

Early-Middle Pleistocene deposits (Vp ~ 2250-2500 m/s; Fig. 6 c) constraints the fault tip in the 50-100 m depth range.

Summarizing: 1) line P2 intercepts the buried SDF at ~ 1200 m (namely *S. Gregorio fault zone* of BONCIO *et alii*, 2010); 2) a further high-angle SW-dipping fault is defined at 1700 m along P2 in the hangingwall of the PF; 3) the fault at 1700 m could be a fourth synthetic splay of the PF or a subsidiary normal fault in the relay zone between the PF and SDF.

Along the P2 section, the two unknown SW-dipping faults total up ~ 100 m and ~ 150 m vertical throw affecting the pre-Quaternary substratum (Fig. 6 a). Therefore, at this location the SDF has still ~ 100 m of cumulative vertical displacement. If the fault at 1700 m is a synthetic splay of the PF, it would add ~ 150 m vertical throw to the PF along this transect, with relevant implications on the long-term displacement history of the PSDFS. In fact, GALLI *et alii* (2010) evaluated ~ 250 m long-term cumulative vertical displacement along the PF and ~ 400 m along the SDF. In conclusion, if our interpretation is correct, PSDFS totals up an additional ~ 250 m vertical offset along our transect, with ~ 100 m being partitioned on the SDF and ~ 150 m on the PF.

The complex architecture of the PSDFS evidenced by line P2 is also coherent with results of VALOROSO *et alii* (2011), which invoked the presence of numerous slip surfaces at shallow depths (< 2 km) to explain the pattern of aftershocks spreading in a wide volume in the hangingwall of PF.

By merging Vp models of our seismic lines (notwithstanding they are not perfectly aligned and have small gaps in between) we show a simplified NE-trending geological cross-section of the Bazzano and Paganica sub-basins (Fig. 8). This picture summarizes our inferences about the deep structural and stratigraphic framework of this sector of the Middle Aterno Basin discussed so far.

Our tomographic images suggest that the local structural setting may be explained by long-term extension and a temporal continuity of tectonic style, which reflect in the correspondence between active faults evidenced by Vp lateral changes and coseismic surface breaks. Moreover, the area of maximum coseismic subsidence experienced after the 2009 earthquake (Fig. 9, ATZORI *et alii*, 2009; STRAMONDO *et alii*, 2011) matches thick lacustrine sediments revealed by a very-low velocity and conductive body (< 25 Ω∗m, see Fig. 7), this latter located above the deepest depocenter of the Middle Aterno basin (Fig. 3; Fig. 8). This once more highlights the coherence of deformation style of the normal-faulting earthquakes that struck this portion of the Apennines and the long-term tectonic evolution of the Middle Aterno basin.

In conclusion, this tomographic study represents a first step towards a better comprehension of the structure the Middle Aterno basin and related Quaternary normal faults. The reflectivity images that will be determined by CDP processing of reflection data recorded along the four profiles presented in this paper and the analysis of profile P1 (Fig. 1) will yield additional information on the internal architecture of the PSDFS and related basins, particularly along the PF.

Acknowledgements

This work was financially supported by the Project INGV-DPC 2007-2009, S5 Task 4 (UR 8, resp. Luigi Improta).

Authors would like to express deep thanks to the Associate Editor, Agata Siniscalchi and Paolo Galli for their useful and constructive reviews of the manuscript. Field work of Bruna Perniola is kindly acknowledged. We thank AMRA s.c.a.r.l that provided part of the instrumentation and Vincenzo Rizzo and Alessandro Giocoli which made the ERT models available. Data acquisition in urban areas was possible thanks to the kind assistance of the L'Aquila Municipality Police. Finally, a special thank to Daniela Pantosti for her continuous encouragement and support.

References

ANZIDEI M., BOSCHI E., CANNELLI V., DEVOTI R., ESPOSITO A., GALVANI A., MELINI D., PIETRANTONIO G., RIGUZZI F., SEPE V., SERPELLONI E. (2009) - *Coseismic deformation of the destructive April 6, 2009 L'Aquila earthquake (central Italy) from GPS data*. Geophys. Res. Lett., **36**, L17307, doi: 10.1029/2009GL039145.

ATZORI, S., HUNSTAD I., CHINI M., SALVI S., TOLOMEI C., BIGNAMI C., STRAMONDO S., TRASATTI E., ANTONIOLI A., BOSCHI E. (2009) - *Finite fault inversion of DInSAR coseismic displacement of the 2009 L'Aquila earthquake (central Italy)*. Geophys. Res. Lett., **36**, L15305, DOI: 10.1029/2009GL039293.

BAGNAIA R., D'EPIFANIO A., SYLOS LABINI S. (1992) - *Aquila and subaequan basins: an example of Quaternary evolution in Central Apennines, Italy*. Quaternaria Nova, **2**, 187-209.

BALASCO M., GALLI P., GIOCOLI A., GUEGUEN E., LAPENNA V., PERRONE A., PISCITELLI S., RIZZO E., ROMANO G., SINISCALCHI A., VOTTA M., (2011) -. *Deep geophysical electromagnetic section across the middle Aterno Valley (central Italy): preliminary results after the April 6, 2009 L'Aquila earthquake*. Boll. Geofis. Teor. Appl., doi: 10.4430/bgta0028

BERTINI T. & BOSI C. (1993*). La tettonica quaternaria della conca di Fossa (L'Aquila)*. Il Quaternario **6**, 293–314.

BERTINI T., BOSI C., GALADINI F., (1989) - *La conca di Fossa-S. Demetrio dei Vestini*. In: C.N.R., Centro di Studio per la Geologia Tecnica & ENEA, P.A.S.: *Elementi di tettonica pliocenico-quaternaria ed indizi di sismicità olocenica nell'Appennino laziale abruzzese*, Soc. Geol. It., 26-58.

BONCIO, P., PIZZI A., BROZZETTI F., POMPOSO G., LAVECCHIA G., DI NACCIO D., FERRARINI F. (2010) - *Coseismic ground deformation of the 6 April 2009 L'Aquila earthquake (central Italy, Mw6.3)*. Geophys. Res. Lett., **37**, L06308, doi:10.1029/2010GL042807.

BOSI C. & BERTINI T. (1970) - *Geologia della media valle dell'Aterno*. Mem. Soc. Geol. It. **9**, 719 - 777.

BOSI C., GALADINI F., GIACCIO B., MESSINA P., SPOSATO A. (2003) - *Plio-Quaternary continental deposits in the Latium-Abruzzi Apennines: the correlation of geological events across different intermontane basins*. Il Quaternario, **16** (1Bis), 55-76.

BOSI C. & MESSINA P. (1991) - *Ipotesi di correlazione fra successioni morfo-litostratigrafiche plio-pleistoceniche nell'Appennino Laziale-Abruzzese*. Studi Geol. Cam., Special Volume 1991/**2**, 257-263.

BRUNO P.P., IMPROTA L., CASTIELLO A., VILLANI F., MONTONE P. (2010a) - *The Vallo di Diano Fault System: new evidence for an active range-bounding fault in southern Italy using shallow, high-resolution seismic profiling*. B. Seismol. Soc. Am., Short Notes, **100, 2**, doi: 10.1785/0120090210.

BRUNO, P.P., CASTIELLO A., IMPROTA L. (2010b) - *Ultrashallow seismic imaging of the causative fault of the 1980, M6.9, southern Italy earthquake by pre‐stack depth migration of dense wide‐aperture data*. Geophys. Res. Lett., **37**, L19302, doi:10.1029/2010GL044721.

CENTAMORE E., CRESCENTI U., DRAMIS F., BIGI S., FUMANTI F., RUSCIADELLI G., COLTORTI M., CHIOCCHINI M., DIDASKALOU P., MANCINELLI A., MATTEUCCI R., MICARELLI A., POTETTI M., PIGNATTI J.S., RAFFI I., SIRNA G., CONTE G. E PETITTA M. (2006) – *Note illustrative della*

Carta Geologica d'Italia alla scala 1:50.000, Foglio 359 "L'Aquila". APAT – Servizio Geologico d'Italia e Regione Abruzzo – Servizio Difesa del Suolo, S.EL.CA., Firenze, 2006, 128 pp.

CHIARABBA C., AMATO A., ANSELMI M., BACCHESCHI P., BIANCHI I., CATTANEO M., CECERE G., CHIARALUCE L., CIACCIO M.G., DE GORI P., DE LUCA G., DI BONA M., DI STEFANO R., FAENZA L., GOVONI A., IMPROTA L., LUCENTE F.P., MARCHETTI A., MARGHERITI L., MELE F., MICHELINI A., MONACHESI G., MORETTI M., PASTORI M., PIANA AGOSTINETTI N., PICCININI D., ROSELLI P., SECCIA D., VALOROSO L. (2009) - *The 2009 L'Aquila (central Italy) M_W6.3 earthquake: Main shock and aftershocks*. Geophys. Res. Lett., **36**, L18308, doi: 10.1029/2009GL039627.

CINTI, F. R., PANTOSTI D., DE MARTINI P. M., PUCCI S., CIVICO R., PIERDOMINICI S., CUCCI L., BRUNORI C. A., PINZI S., PATERA A. (2011) - *Evidence for surface faulting events along the Paganica Fault prior to the 6 April 2009 L'Aquila earthquake (central Italy)*. J. Geophys. Res., **116**, B07308, doi:10.1029/2010JB007988.

CIRELLA, A., PIATANESI A., COCCO M., TINTI E., SCOGNAMIGLIO L., MICHELINI A., LOMAX A., BOSCHI E. (2009) - *Rupture history of the 2009 L'Aquila (Italy) earthquake from non-linear joint inversion of strong motion and GPS data*. Geophys. Res. Lett., **36**, L19304, doi: 10.1029/2009GL039795.

CIVICO R., et alii (2010) - Long-term *expression of the Paganica Fault vs.1185 2009 L'Aquila earthquake surface ruptures: Looking for a better understanding of its seismic behavior*. Geophys. Res. Abstr., **12**, EGU2010 12775−1.

EMERGEO WORKING GROUP (2009) - *Evidence for surface rupture associated with the Mw 6.3 L'Aquila earthquake sequence of April 2009 (central Italy)*. Terra Nova, doi: 10.1111/j.1365-3121.2009.00915.x

FALCUCCI E., GORI S., PERONACE E., FUBELLI G., MORO M., SAROLI M., GIACCIO B., MESSINA P., NASO G., SCARDIA G., SPOSATO A., VOLTAGGIO M., GALLI P., GALADINI F., PANTOSTI D. (2009) - *Surface faulting due to the L'Aquila earthquake of April 6th 2009*. Seismol. Res. Lett. **80, 6**, doi: 10.1785/gssrl.80.6.940

GALADINI F. (1999) - *Pleistocene change in the central Apennine fault kinematics, a key to decipher active tectonics in central Italy*. Tectonics, **18**, 877-894.

GALADINI F. & GALLI P. (2000) - *Active tectonics in the central Apennines (Italy) - input data for seismic hazard assessment*. Nat. Haz. **22**, 225–270.

GALADINI F. & MESSINA P. (2001) - *Plio-Quaternary changes of the normal fault architecture in the central Apennines (Italy)*. Geodinamica Acta **14**, 321–344.

GALADINI F. & MESSINA P. (2004) - *Early-middle Pleistocene eastward migration of the Abruzzi Apennine (central Italy) extensional domain*. J. Geodyn. **37**, 57–81.

GALADINI F., MESSINA P., GIACCIO B., SPOSATO A. (2003) - *Early uplift history of the Abruzzi Apennines (central Italy): available geomorphological constraints*. Quatern. Int., **101/102**, 125-135.

GALLI P., GALADINI F., PANTOSTI D. (2008) - *Twenty years of paleoseismology in Italy*. Earth-Sci. Rev., **88**, 89–117, doi: 10.1016/j.earscirev.2008.01.001

GALLI, P., CAMASSI, R., AZZARO, R., BERNARDINI, F., CASTENETTO, S., MOLIN, D., PERONACE, E., ROSSI, A., VECCHI, M., TERTULLIANI, A., (2009) - *Il terremoto aquilano del 6 aprile 2009: rilievo macrosismico, effetti di superficie ed implicazioni sismotettoniche*. Il Quaternario **22**, 235-246.

GALLI P., GIACCIO B., MESSINA P., (2010) – *The 2009 central Italy earthwuake seen through 0.5 Myr-long tectonic history of the L'Aquila faults system*. Quaternary Sci. Rev., **29**, 27-28, 3768-3789, doi:10.1016/j.quascirev.2010.08.018

GIOCOLI, A., GALLI, P., GIACCIO, B., LAPENNA, V., MESSINA, P., PERONACE, E., PISCITELLI, S., ROMANO, G. (2011) - *Electrical Resistivity Tomography across the Paganica-San Demetrio fault system (L'Aquila 2009 earthquake)*. Bollettino di Geofisica Teorica ed Applicata, 52, 2011.

GRUPPO DI LAVORO MS–AQ (2010) - *Microzonazione sismica per la ricostruzione dell'area aquilana.* Regione Abruzzo – Dipartimento della Protezione Civile, L'Aquila.

IMPROTA, L., ZOLLO, A., HERRERO, A., FRATTINI, M., VIRIEUX, J., DELL'AVERSANA, P., (2002) - *Seismic imaging of complex structures by non-linear traveltime inversion of dense wide-angle data: Application to a thrust belt*. Geophys. J. Int., **151**, 264–278, doi: 10.1046/j.1365-246X.2002.01768.x.

IMPROTA, L., ZOLLO A., BRUNO P.P., HERRERO A., VILLANI F. (2003) - *High resolution seismic tomography across the 1980 (Ms 6.9) southern Italy earthquake fault scarp*. Geophys. Res. Lett., **30(10)**, 1494, doi: 10.1029/2003GL017077.

IMPROTA, L., & CORCIULO M. (2006) - *Controlled source non-linear tomography: A powerful tool to constrain tectonic models of the Southern Apennines orogenic wedge, Italy*. Geology, **34(11)**, 941−944, doi: 10.1130/G22676A.1.

IMPROTA, L., & BRUNO P.P. (2007) - *Combining seismic reflection with multifold wideaperture profiling: An effective strategy for high-resolution shallow imaging of active faults*. Geophys. Res. Lett., **34**, L20310, doi: 10.1029/2007GL031893.

IMPROTA, L., FERRANTI L., DE MARTINI P. M., PISCITELLI S., BRUNO P. P., BURRATO P., CIVICO R., GIOCOLI A., IORIO M., D'ADDEZIO G., MASCHIO L. (2010) - *Detecting young, slow‐slipping active faults by geologic and multidisciplinary high-resolution geophysical investigations: A case study from the Apennine seismic belt, Italy*. J. Geophys. Res., **115**, B11307, doi: 10.1029/2010JB000871.

MESSINA P., BOSI C., MORO M. (2003) - *Sedimenti e forme quaternari nell'alta valle dell'Aterno (L'Aquila)*. Il Quaternario, **16 (2)**, 231-239.

MESSINA P., DRAMIS F., GALADINI F., FALCUCCI E., GIACCIO B., GORI S., MORO M., SAROLI M., SPOSATO A. (2007) - *Quaternary tectonics of the Abruzzi Apennines (Italy) inferred from integrated geomorphological-stratigraphic data*. Epitome. . **2**, 235-236 ISSN: 1972-1552.

MESSINA P., MORO M., SPERANZA F. (2001) - *Primi risultati di stratigrafia magnetica su alcune formazioni continentali dell'alta valle dell'Aterno (Italia centrale)*. Il Quaternario, **14**, 167-172.

OPERTO, S., C. RAVAUT, L. IMPROTA, J. VIRIEUX, A. HERRERO, DELL'AVERSANA P. (2004) - *Quantitative imaging of complex structures from dense wide‐aperture seismic data by multiscale traveltime and waveform inversions: a case study*. Geophys. Prospect., **52**, 625–651, doi: 10.1111/j.1365-2478.2004.00452.x

PATACCA E., SARTORI R., SCANDONE P., (1990) - *Tyrrhenian Basin and Apenninic Arcs: kinematic relations since Late Tortonian times*, Memorie della Società Geologica Italiana, 1990, **45**, 1, 425-451.

PIZZI A., CALAMITA F., COLTORTI M., PIERUCCINI P. (2002). *Quaternary normal faults, intramontane basins and seismicity in the Umbria-Marche-Abruzzi Apennine ridge (Italy): contribution of neotectonic analysis to seismic hazard assessment*. Boll. Soc. Geol. It., Spec. Publ., **1**, 923–929.

PIZZI A. & GALADINI F., (2009) - *Pre-existing cross-structures and active fault segmentation in the northern-central Apennines (Italy)*. Tectonophys. **476**, 304–319, doi: 10.1016/j.tecto.2009.03.018

PONDRELLI, S., SALIMBENI S., MORELLI A., EKSTRÖM G., OLIVIERI M., BOSCHI E. (2010) - *Seismic moment tensors of the April 2009, L' Aquila (central Italy), earthquake sequence*, Geophys. J. Int., **180**, 238−242, doi:10.1111/j.1365-246X.2009.04418.x.

ROBERTS G. P., B. RAITHATHA, SILEO G., PIZZI A., PUCCI S., WALKER J.F., WILKINSON M., MCCAFFREY K., PHILLIPS R. J., MICHETTI A.M., GUERRIERI L., BLUMETTI A.M., VITTORI E., COWIE P., SAMMONDS P., GALLI P., BONCIO P., BRISTOW C., R. WALTERS (2010) - *Shallow subsurface structure of the 2009 April 6 Mw 6.3 L'Aquila earthquake surface rupture at Paganica, investigated with ground-penetrating radar*. Geophys. J. Int. **183,** 774–790, doi: 10.1111/j.1365-246X.2010.04713.x

STRAMONDO S., CHINI M., BIGNAMI C., SALVI S., ATZORI S. (2011) - *X-, C-, and L-band DInSAR investigation of the April 6, 2009, Abruzzi earthquake*. IEEE Geoscience and Remote Sensing Letters, v. 8, p. 49–53.

TERTULLIANI, A., ROSSI, A., CUCCI, L. & VECCHI, M., (2009) - *L'Aquila (Central Italy) earthquakes: the predecessors of the April 6, 2009 event*. Seismol. Res. Lett., **80**(6), 1008.

VALOROSO, L., CHIARALUCE L., DI STEFANO R., PICCININI D., SCHAFF D. P., WALDHAUSER F. (2011) - *Can seismicity image the complexity of fault architecture? A radiography of the 2009 MW 6.1 L'Aquila normal fault system (Central Italy)*. EGU Meeting Abstract, Wien 5-9 April 2011.

VEZZANI L. & GHISETTI, F. (1998) - Carta Geologica dell'Abruzzo, scale 1:100,000. S.EL.CA., Firenze.

WALTERS, R. J., ELLIOTT J. R., D'AGOSTINO N., ENGLAND P. C., HUNSTAD I., JACKSON J. A., PARSONS B., PHILLIPS R. J., ROBERTS G. (2009) - *The 2009 L'Aquila earthquake (central Italy): A source mechanism and implications for seismic hazard*. Geophys. Res. Lett., **36**, L17312, doi: 10.1029/2009GL039337.

Table A: picked CSGs and picking error for the four seismic lines.

Line	length (m)	picked CSGs	picked traces	picking error (ms)	RMS picking error (ms)
Bazzano1 (B1)	1075	107	21298	2.5-16.1	3.03
Bazzano2 (B2)	1497.5	94	16049	2.5-7.4	2.54
Bazzano3 (B3)	962.5	75	12336	2.5-7.5	2.68
Paganica2 (P2)	2095	131	19504	2.5-14.0	2.80

Table B: Vp-lithology associations and their possible equivalent formations used for the interpretation of tomographic models.

Vp range	lithology	type of deposits (with inferred age)	possible equivalent formations
500-1500 m/s	clays, sands and gravels	colluvial deposits; loose fluvial and alluvial fan deposits (Late Pleistocene – Holocene)	recent deposits of the Aterno River and alluvial fan deposits of the Raiale Torrent and Mt. Ocre; PAG-1, PAG-2 units (GALLI *et alii*, 2010)
1500-2000 m/s	clays, silts and sands	lacustrine and palustrine deposits (Early-Middle Pleistocene)	S. Nicandro Fm. (BERTINI & BOSI, 1993)
2250-3000 m/s	sands and conglomerates, breccias	dense/cemented fluvial and alluvial fan deposits; slope breccias (Early-Middle Pleistocene)	PAG-4, PAG-7 units (GALLI *et alii*, 2010); S. Mauro, Vall'Orsa, Valle dell'Inferno, Valle Valiano, Fonte Vedice Fms. (BERTINI & BOSI 1993)
> 3250-3500 m/s	sandstones, marly limestones, fractured limestones	turbidites (Miocene), slope to basin carbonate sequences (Mesozoic-Tertiary)	pre-Quaternary substratum
> 4000 m/s	limestones	slope to basin carbonate sequences (Mesozoic-Tertiary)	pre-Quaternary substratum

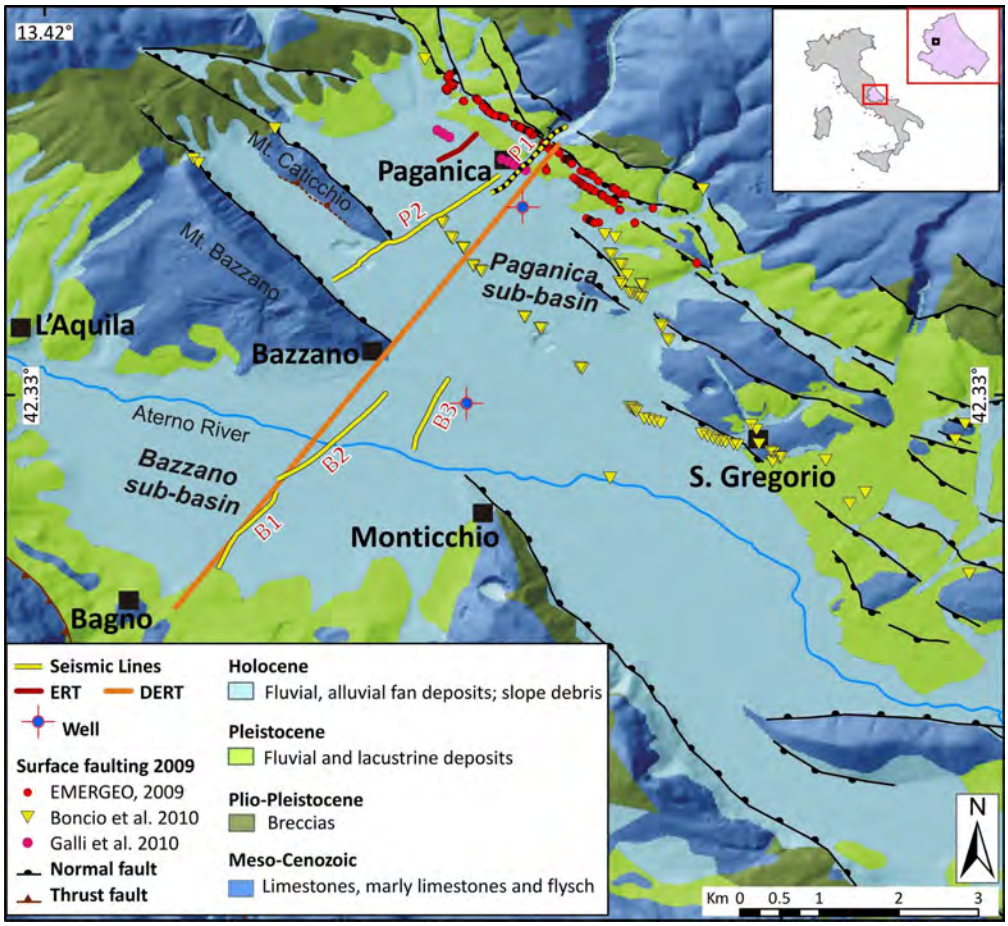

Figure 1:
Simplified geological map of the Middle Aterno basin (modified after: CIVICO et alii, 2010; CINTI et alii, 2011) with location of the seismic lines discussed in this work and coseismic surface breaks (after: EMERGEO WORKING GROUP, 2009; BONCIO et alii, 2010; GALLI et alii, 2010). Seismic lines are named as follows: Bazzano 1 (B1); Bazzano 2 (B2); Bazzano 3 (B3); Paganica 1 (P1, dashed line); Paganica 2 (P2). Location of the ERT (after GIOCOLI et alii, 2011) and DERT (after BALASCO et alii, 2011) surveys and of the two boreholes used to constrain the northern end of line P2 and line B3 is also reported. Black squares indicate main towns. See details in the text.
182x167mm (300 x 300 DPI)

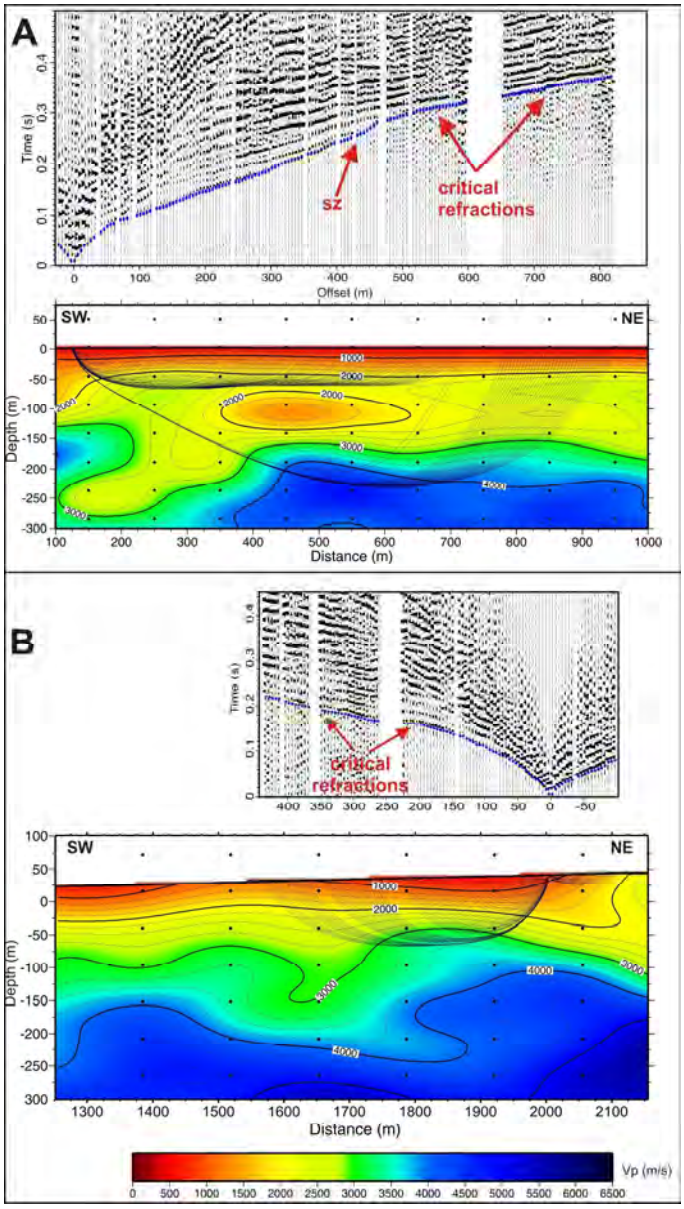

Figure 2:
Examples of common shot gathers with picked first P-pulses (blue dots) and corresponding ray-paths in the Vp models obtained by tomography. A) Band-pass filtered record section (f=30-100 Hz) for a shot at the western end of line B2. Red arrows outline a shadow zone (sz) and large offset post-critical refractions. The former, evidenced by an abrupt decrease of both amplitude and apparent velocities of first P-pulses, is generated by the low-Vp body at about 100 m depth. Post-critical refractions (head-waves) originate at the top of the high-Vp body that corresponds to the Mezo-Cenozoic substratum. B) Zoom on a band-pass filtered record section (f=40-120 Hz) for a shot at the eastern end of line P2. The red arrow outlines post-critical refractions travelling at the top of the high-Vp substratum.
246x437mm (300 x 300 DPI)

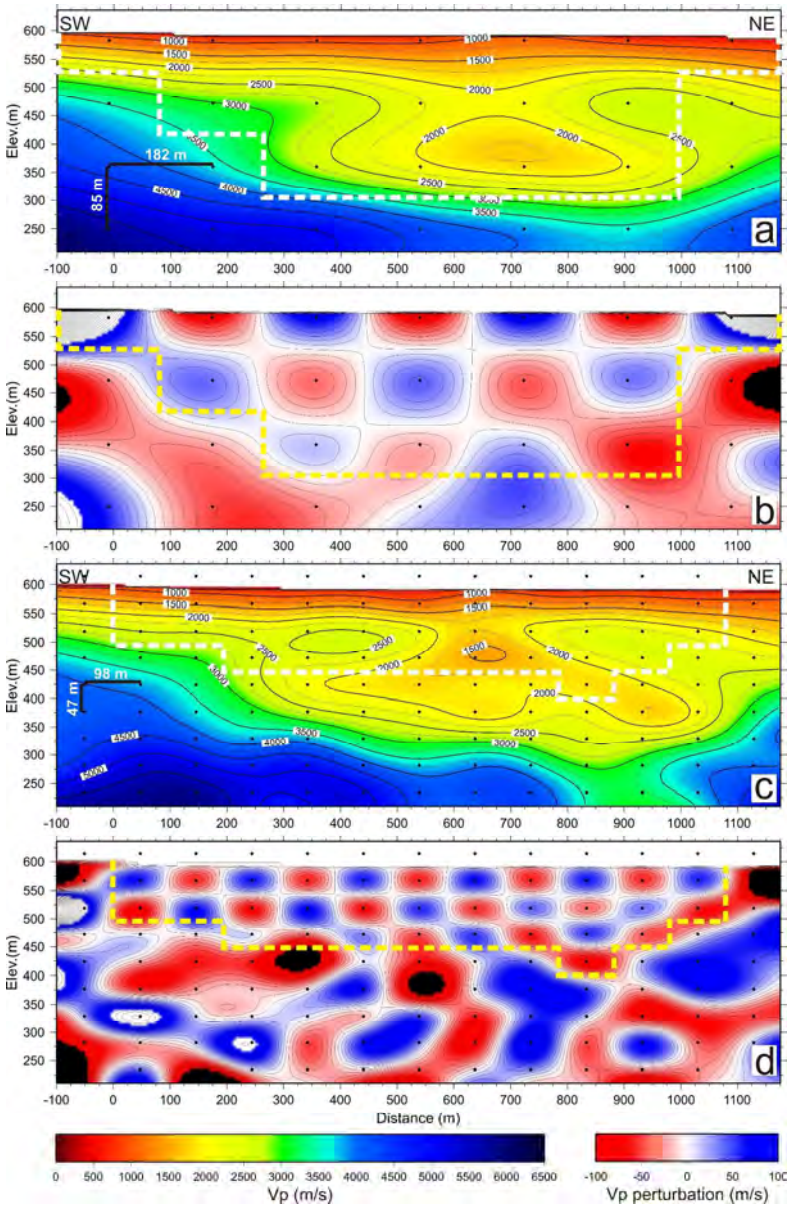

Figure 3:
Vp models of line Bazzano 1 (B1): a) Long-wavelength Vp model; b) Result of the resolution test with the retrieved checkerboard perturbation for the long-wavelength model; c) Short-wavelength Vp model; d) Result of the resolution test with the retrieved checkerboard perturbation for the short-wavelength model. Dashed lines define resolution depth inferred from checkerboard tests. Black circles depict nodes of the velocity grid (model parameters). No vertical exaggeration.
243x374mm (300 x 300 DPI)

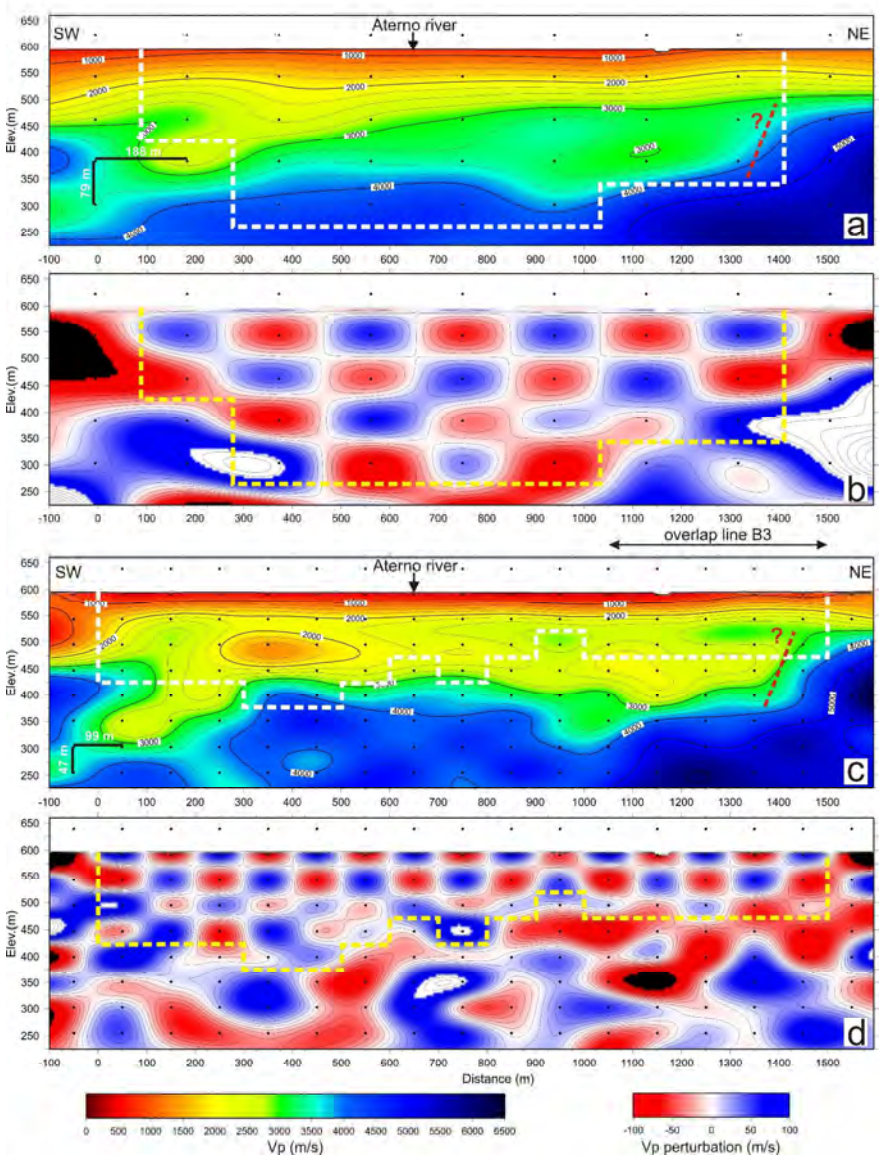

Figure 4:
Vp models of line Bazzano 2 (B2): a) Long-wavelength Vp model; b) Retrieved checkerboard perturbation for the long-wavelength model; c) Short-wavelength Vp model; d) Retrieved checkerboard perturbation for the short-wavelength model. Yellow and white dashed lines outline resolution depth. Black circles depict nodes of the velocity grid. The red dashed line outlines a strong lateral Vp variation that may indicate a possible normal fault affecting the substratum. No vertical exaggeration. Overlap section with line B3 is shown in Fig. 4 c. See details in the text.
260x359mm (300 x 300 DPI)

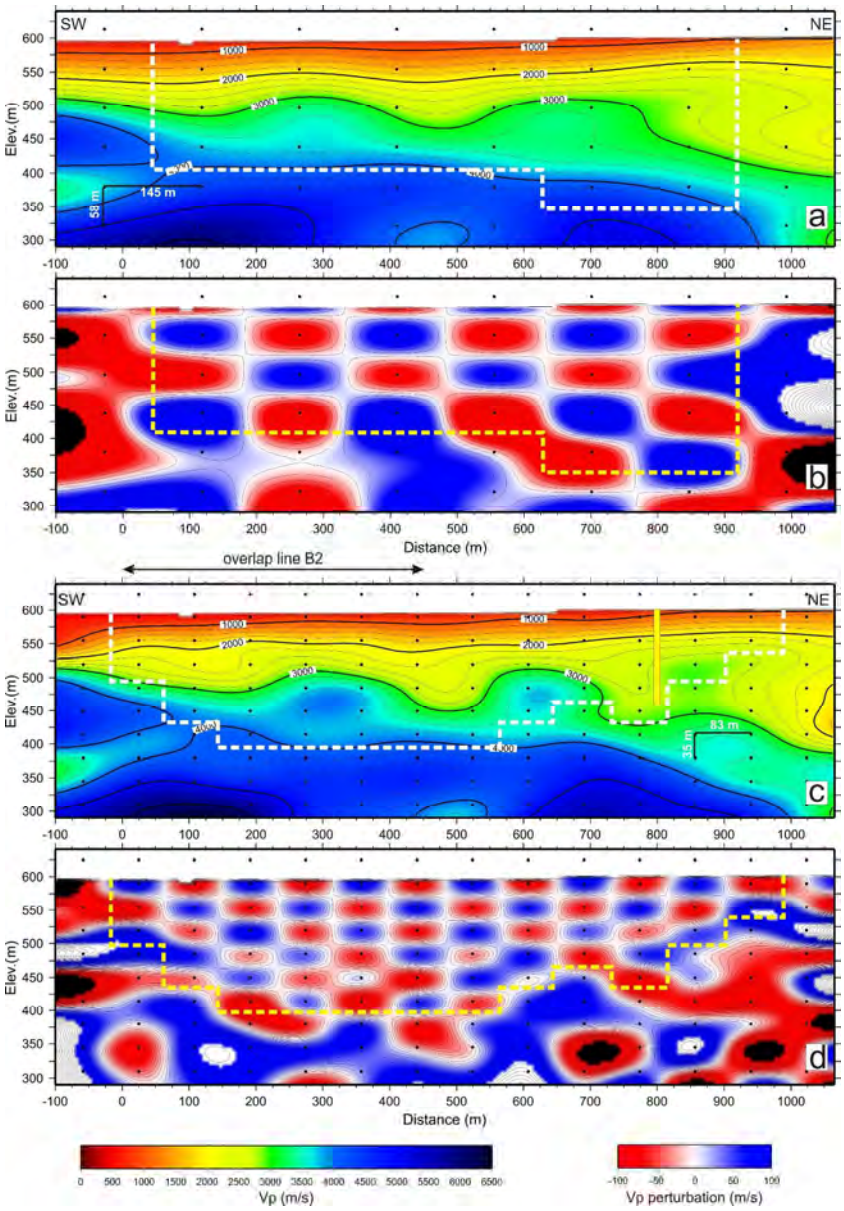

Figure 5:
Vp models of line Bazzano 3 (B3): a) Long-wavelength Vp model; b) Retrieved checkerboard perturbation for the long-wavelength model; c) Short-wavelength Vp model; d) Retrieved checkerboard perturbation for the short-wavelength model. Yellow and white dashed lines outline resolution depth. Black circles depict nodes of the velocity grid. No vertical exaggeration. Overlap section with line B2 and a well described in GRUPPO DI LAVORO MS-AQ (2010) and projected ~ 350 m from the SE are shown in Fig. 5 c. See details in the text.
243x349mm (300 x 300 DPI)

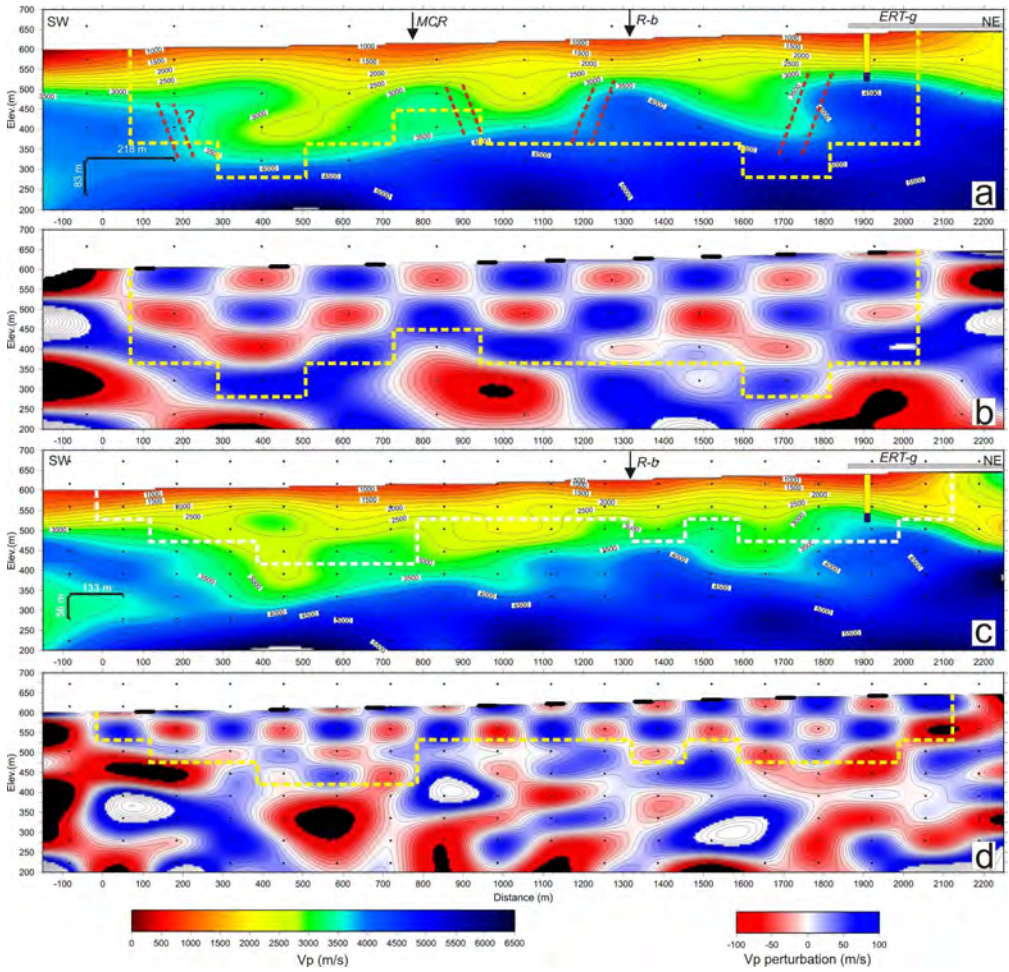

Figure 6:
Vp models of line Paganica 2 (P2): a) Long-wavelength Vp model; b) Retrieved checkerboard perturbation for the long-wavelength model; c) Short-wavelength Vp model; d) Retrieved checkerboard perturbation for the short-wavelength model. Yellow dashed lines outline resolution depth. Black circles depict nodes of the velocity grid. Red dashed lines outline clear steps in the high-Vp substratum caused by synthetic or antithetic fault splays. Location of the small carbonate ridge (Mt. Caticchio Ridge, MCR) and of the surface breaks (R-b; see BONCIO et alii, 2010) are outlined by black arrows. The figure also shows location of the ERT survey that partially overlaps the seismic line (grey box; ERT-g) and the borehole presented by GIOCOLI et alii (2011). Continental deposits and limestone drilled by the borehole are shown in yellow and blue, respectively. No vertical exaggeration. See details in the text.
178x171mm (300 x 300 DPI)

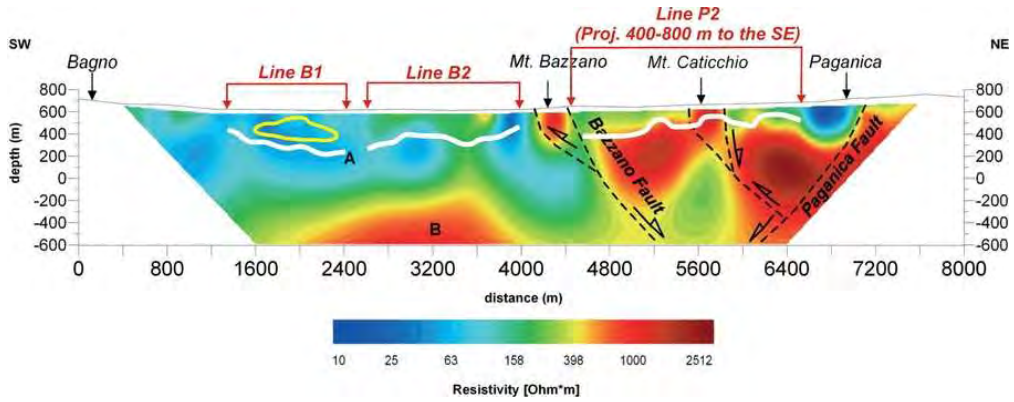

Figure 7:
DERT resistivity section with red arrows outlining location of the seismic profiles P2 (projected), B1 and B2 (modified from BALASCO et alii, 2011). We do not include line B3 because it runs ~ 1 km to the SE in a different geologic environment. The thick white line corresponds to the 3250-3750 m/s iso-velocity contours and defines the presumed pre-Quaternary substratum. The thick yellow line corresponds to the 1750-2000 m/s contours and roughly defines the thick lacustrine deposits found along profile B1 (see Fig. 3 a-c). Location of the seismic profiles and DERT is reported in Fig. 1.
76x29mm (300 x 300 DPI)

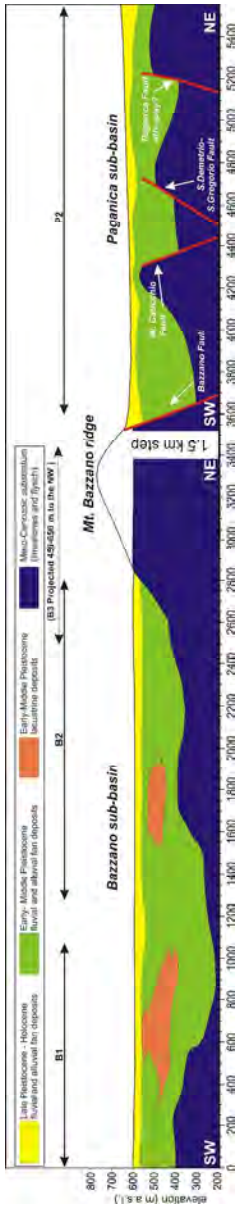

Figure 8:
Simplified geological cross-section with topography of the Middle Aterno basin from merging of seismic lines B1, B2 and P2. No vertical exaggeration. Length and location of profiles are shown by double arrows. Line B3 is dashed because its interpretation is not reported in this ideal cross-section due to the ~ 1.5 km step between B3 and P2 and their different features close to the Mt. Bazzano ridge. The main sedimentary bodies of the basin infilling, the pre-Quaternary substratum and the inferred faults are shown. See details in the text.
273x1427mm (300 x 300 DPI)

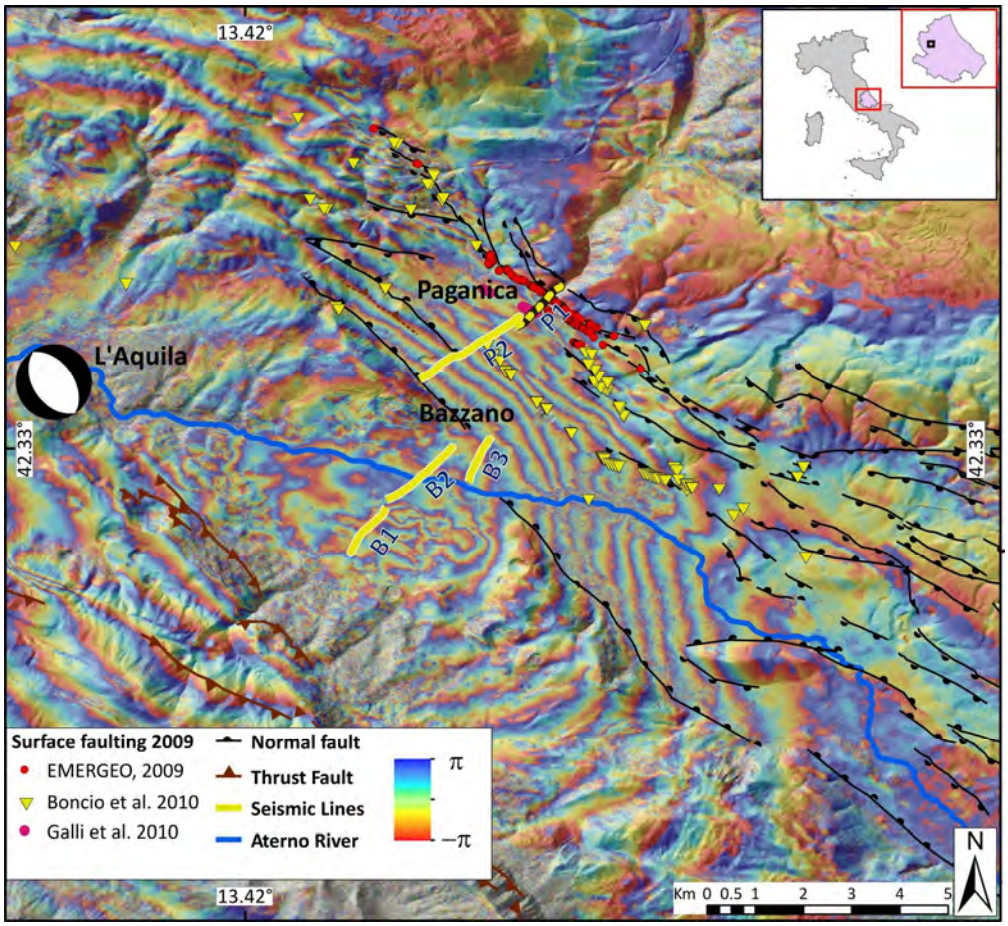

Figure 9:
Shaded relief topography of the Middle Aterno basin superimposed on the "wrapped" differential interferogram from the COSMO-SkyMed ascending orbit (pre-event 4th April, and post event 12th April 2009) (modified after: STRAMONDO et alii, 2011): one full-color cycle (blue-red-yellow-blue, from -π to +π) represents 1.5 cm of ground shift away from satellite along the radar line of sight. The resulting interferogram shows a NW-SE concentric fringe pattern that is composed of 12 fringes, the maximum ground displacement measured along the satellite LOS (i.e. ~36◦ from nadir) reaches 18 cm in correspondence of the seismic lines B1, B2 and B3. Remarkably, the maximum coseismic subsidence (~ 0.25 m) area is crossed by the NE part of line B1, where seismic tomography unravels the main depocenter of the basin (about 2 km wide and 350 m deep) and thick lacustrine deposits (see details in the text). The figure also shows main faults, coseismic surface ruptures (see also Fig. 1), location of the epicentre and the focal mechanism of the 6th April 2009 mainshock (after PONDRELLI et alii, 2010).
182x167mm (300 x 300 DPI)

- APPENDIX I - Brunori, C.A., **Civico, R.**, Cinti, F.R., Ventura, G. (2011), *Characterization of active fault scarps from LiDAR data: a case study from Central Apennines (Italy).* Submitted to the International Journal of Geographic Information.

Characterization of active fault scarps from LiDAR data: a case study from Central Apennines (Italy)

Journal:	*International Journal of Geographical Information Science*
Manuscript ID:	IJGIS-2011-0452.R1
Manuscript Type:	Special Issue Paper
Keywords:	Terrain analysis < Keywords Relating to Theory, Geomorphology < Keywords Relating to Application, Geological mapping and modelling < Keywords Relating to Application

Abstract. LiDAR data are used to construct a 1 m x 1 m DEM with the aim to capture the tectonic and erosive elements of the geometry of the Pettino fault, a well-known active, normal fault in Central Apennines (Italy). Four 90 to 280 m long fault scarp segments are selected and the surface between the base and the top of the scarps is analyzed through the statistical analysis of the following parameters: altitude, height of the fault scarp, distance along strike, slope and aspect. The results evidence the occurrence of fresh faces (slope=35°-45°) and degraded (<35°) scarps; slope is between 40° and 34° and aspect between 223° and 238°. An estimate of the long-term slip rate (0.6-1.1 mm/yr) of the Pettino fault is also provided based on the scarp height (12 to 19 m) and age of major erosional phase in the area. The combined analysis of the DEM derived parameters allow us to (a) define the 3D scarp geometry, (b) decipher its geomorphological significance, (c) recognize and interpret the tectonic pattern, (d) estimate the long-term slip rate.

Keywords: LiDAR; Fault scarp; Morphology; Pettino fault (Abruzzi)

1. Introduction

High-resolution topographic data such as LiDAR (Light Detection and Ranging)-derived digital elevation models (DEMs) allow us to qualitatively and quantitatively analyze landscapes resulting from tectonic, hillslope, fluvial, biologic and anthropogenic activity. Earth-science applications of LiDAR include coastal change studies (Sallenger *et al*. 1999), landslides monitoring (Dietrich *et al*. 2001; Glenn *et al*. 2006), volcanic deformation (Hasegawa *et al*. 2007), identification of faults (Haugerud *et al*. 2003; Sherrod *et al*. 2004; Cunningham *et al*. 2006; Kondo *et al*. 2008; Arrowsmith and Zielke, 2009), slip-rate estimate (Frankel *et al*. 2007). In the last decade, there are several studies on the geometry of fault scarps using high-resolution

LiDAR data (e.g., Chan *et al.* 2007; Begg and Mouslopoulou, 2010; De Long *et al*. 2010; Hilley *et al*. 2010; Amos *et al*. 2011). However, investigations on the spatial distribution of slope and aspect on active fault scarps, as well as the statistical analysis of these scarp parameters, are still lacking. To partly fill this gap, we extract slope and aspect values from an airborne LiDAR-derived DEM on selected fault scarps of a major, seismogenic fault located in central Apennines (Italy). Our aim is to study the fault scarp morphology and identify the effects of endogenous and exogenous processes on the scarp face through the statistical and spatial analysis of aspect and slope morphometric parameters. The method allowed the quantitative, high resolution mapping of the fault morphology, then representing a tool for the estimate of the tectonic and erosional processes. This tool may also support accurate and precise geological and geomorphological field mapping.

2. Methodology

Here, we provide a basic review of the time evolution of fault scarps and terminology in order to define the structural elements of fault morphology, then we describe the geological setting of the study area and the Pettino fault. Finally, we illustrate the LiDAR data elaboration procedure, the extraction of some geomorphometric parameters, and the statistical analysis aimed to capture fault morphology and processes recognition.

2.1 Morphology of fault scarps

Morphological scarps characterize most of dip to oblique-slip faults. Fault-scarp terminology is commonly derived from observations made on piedmont scarps (Wallace, 1977; Bull, 2007). The general evolution of a fault scarp in time and the principal morphologic features of a scarp are summarized in the sketch of Fig. 1, where the ideal built-up of a scarp by repeated

slips is shown, along with the effects of possible degradation and aggradation processes. The base of scarp and the crest are the lower and upper extremes of a fault scarp, respectively and the scarp height is measured as the vertical separation between them. The free-face is the fresh exposed surface resulting from slip on a fault. A fault scarp, once is formed, began immediately to degrade. The free-face retreats upslope and colluvial materials begin to accumulate at the base of the scarp, forming a debris slope. Renewed slip episodes on a pre-existing fault scarp may abruptly steepen the slope producing a characteristic segmented appearance of the topographic profile with a rounded crest and a steep free-face.

2.2 Study area

The Pettino fault is located in the L'Aquila town region within the central Apennines, a well-known seismically prone area. Here, the NE-verging thrust and fold mountain belt from Neogene compressive tectonics is dissected by an intense NE-SW striking extension that, since Late Pliocene time, have led to the formation of intermountain basins controlled by NW-SE striking faults (e.g., Doglioni, 1995; Cipollari and Cosentino, 1995; Ghisetti and Vezzani, 1999) (Fig. 2). The early Quaternary surface faulting associated to earthquakes larger than M>5.5 mostly occurred on these faults, which are characterized by normal to oblique-slips, and are up to 15-20 km long. These faults extend in depth to 10–15 km with dip 50°-70°, mostly SW-side down (Lavecchia *et al*. 1994; Vezzani and Ghisetti, 1998; Barchi *et al*. 2000; Galadini and Galli, 2000; Foglio CARG 2009). Pre-existing, NNE-SSW and ESE-WNW to NW-SE, low-angle (dip <45°) compressive structures also outcrop (Pizzi and Galadini, 2009) and, in many cases, their geometry influences the extensional tectonics, with reactivation of pre-existing structures (Ghisetti and Vezzani, 2002; Patacca *et al*. 2008; Di Luzio *et al*. 2009; Di Luccio *et al*. 2010). One of the normal faults bordering the northern side of the Aterno river, i.e., the Paganica fault,

reactivated up to the surface during the April 2009 L'Aquila sequence (e.g. Emergeo Working Group, 2010).

The main geological units of the area can be summarized as follows. Jurassic-Miocene limestones and marls, and Miocene sandstones represent the bedrock outcropping on the ridges and valley flanks. Quaternary deposits include Pleistocene breccias, lacustrine and alluvial deposits (Blumetti *et al*. 2002). Local debris alluvial fans occur at the foot of the valley.

We focus our analysis on the Pettino fault, a part of the Late Quaternary segmented system called the Upper Aterno fault system (e.g. Blumetti, 1995, 1997), which is responsible for the evolution of the L'Aquila basin, and likely, for the 1703 A.D., M>6 earthquake (Fig. 2).

The ca. 10 km long, 100°-120°-striking, 60° SW dipping Pettino fault emerges NW of the L'Aquila city center along the slope of the carbonatic Pettino ridge and marks the boundary between the hills dipping towards the southwest and Late Pleistocene sediments. As most of the faults in the Apennines, the limestone fault scarp is exposed, and a zone of cataclasite is in tectonic contact against the stratified slope deposits, giving rise to a fault scarp with an average height of 10 m. A vertical slip rate of 0.47-0.86 mm/yr since upper Pleistocene is assigned to the whole Upper Aterno fault system (Galadini *et al*. 2001).

We selected the Pettino fault because the associated scarps appear, at a field survey scale, quite continuous and with homogeneous characteristics along the trace; the scarps do not cut large urban areas for most of length, even if local modifications induced by anthropic activities occur along some portions.

2.3 LiDAR DEM representation

The LiDAR measures and collect multiple returns of a laser beam aimed at the ground and is able to discriminate between the first return, usually from the top of the forest canopy, and

the last return, from the bare earth surface. By isolating the last returns, LiDAR is capable of revealing the ground surface even in highly vegetated areas. The airborne LiDAR survey of the study area was performed and processed few days after the 6 April 2009 L'Aquila earthquake by the Civil Protection of Friuli Venezia Giulia (Italy) using an Optech ALTM 3100 EA Airborne Laser Terrain Mapper System. The main technical parameters related to the LiDAR acquisition and errors are listed in Table 1. Vertical errors (1σ) are less than 0.2 m and horizontal errors less than 0.54 m.

A regular 1 by 1 m DEM was created from the LiDAR bare-earth points cloud by means of the inverse distance weighted interpolation method with a 3 m search radius using the routine IDW of ArcInfo by ESRI. Within the constructed DEM, we select a 2.8 km x 2.1 km area including the central portion of the Pettino fault (Figs. 2 and 3). The shaded relief, slope and aspect digital maps derived from the DEM of the Pettino area are elaborated in order to recognize and select the fault scarps. Slope and aspect have been calculated using a 3 x 3 m moving window, which is the minimum window size to determine these parameters. Therefore, each 1 m x 1 m pixel of DEM has associated slope and aspect values.

DEM must be inspected using aerial photo or optical high resolution satellite images to discriminate fault scarps from scarps of different origin, like for example, manmade elements as roads, walls, quarries, etc.. Analytical steps of the fault scarp extraction include: 1) identification of the base and top of morphological scarps from the combined analysis of shaded relief images, slope, and aspect maps; 2) exclusion of scarps with evidence, based on high resolution satellite images (IKONOS and QUICKBIRD), of artificial modifications; 3) definition of a buffer area for each fault scarp bounded by the base and the top of the scarp as reference lines defined in 1); 4) elaboration of slope and aspect for each 1x1 m pixel of the DEM of the buffered area.

Based on the combined analysis of the shaded relief from DEM, IKONOS and QUICKBIRD images, and excluding all the scarps possibly affected by anthropic modification (roads, plantations, etc.), four fault scarp segments (hereafter S1, S2, S3 and S4 from SE to NW) have been selected among the Pettino traces (Fig. 3). Final dataset contains, for each point of the selected scarps, the following parameters: absolute position (lat, long), absolute altitude (meters a.s.l), distance in meters from origin of buffered area (distance of nearest reference point from the origin of reference line), relative elevation (quote relative to the nearest reference point), slope (degrees) and aspect (slope dip in degrees from North).

The values of relative elevation from the nearest reference point permit the measurement of fault scarps dimensions (vertical and horizontal) and allow the quantitative comparison between geometries of the different selected scarps. The number of points selected in each fault scarp is: 3139 (S1), 6512 (S2), 5511 (S3) and 2152 (S4).

2.4 Fault scarp morphology

The results of the selected dataset relative to S1, S2, S3 and S4 are summarized in Figs. 4 to 9. Figures 4 and 5 show the 3D view of the fault scarps and the elevation (in m) of the scarps along the fault strike. Fig. 6 summarizes the statistics (median, lower and upper quartile, variation range) of the altitude, slope and aspect in the selected fault scarps. Figure 5 shows that the scarps have the maximum elevations between 15 and 19.5 m. These scarps are deeply incised by gullies up to 15 m deep (e.g., in S3). The northern tip of S1 has the same elevation of the southern tip of S2., as well as S3 and S4, whereas a break in elevation of about 3 m occurs between S2 and S3. Therefore, a lateral continuity in the elevation characterizes S1 and S2, and S3 and S4. It is worth noting that the break in elevation occurs between the scarps S2 and S3 that are arranged in a left step. This step is also evidenced by the different altitude (m a.s.l.) of S2 and S3 (Fig. 6). The

median value, the interquartile distance and the variation range of slope decrease from S1 to S4, whereas the median value of aspect increase (Fig. 6). The preferred values in an aspect-slope, density contour projection (Fig. 7) of the S1-S4 DEM, also indicate a general decrease of slope (from 40° to 34°) from S1 to S4, and an increase of aspect (from 223° to 236°). The spatial variation of slope and aspect values along the scarps (Fig. 8) shows that the these values are not homogenously distributed within the scarps. In detail, the higher values of slope mainly occur in the middle and lower part of the scarps, in particular in S1 and S2. The distribution of the aspect values indicate along strike variations, with bands of nearly constant values roughly disposed parallel to the elevation and not equally spaced along the strike. Elevation vs. slope and aspect diagrams (Fig. 9) evidence that, in S1, S3 and S4, the higher slope values (35°-45°) concentrate in the lower part of the scarps at elevation < 4-5 m; at elevations > 4-5 m, the slope values generally decrease (25°-35°). The aspect shows more complex distributions with an increase in the dispersion of values as the elevation increases.

3. Discussion and conclusions

The collected data and results indicate that the height (crest to base) of S1 to S4 ranges between 12 and 19 m. The scarps are transversally eroded by drainage (see gullies represented by minima in elevation in Fig. 5). On average, the maximum elevation values are located in S2.

The values of the scarp height are larger than those reported in the literature on the basis of field data, which indicate an average 10 m high scarp for the Pettino fault (Blumetti, 1995, 1997; Galli *et al*. 2011). This difference probably reflects the larger uncertainty of the field topographic methods, which do not consent an along strike, spatially continuous sampling of the topography, with respect to a LiDAR-based analytical approach, which, on the contrary, permits to obtain spatially contiguous data.

The measured 3 m difference in scarp height between the southeastern tip of S3 and the northwestern tip of S2 is associated to a 110 m wide, 75 m high left-hand scarp step. The southeastern tip of S3, which is 12 m high, reaches the 15 m of overall cumulative deformation adding the about 3 m high scarps parallel to S3 located along the northwestern prolongation of the S2 segment (Fig. 3). Therefore, the left step between S2 and S3 has the significance of a fault overlap, lacking evidence of step-over traces. This has implications in the evaluation of the near field faulting hazard since the deformation during a slip event may be distributed on different, sub-parallel segments and not on a single one. Moreover, the detailed knowledge of the amount of scarp heights, representing the cumulated deformation from multi-slip events, is the base for long term estimates of the slip rate along faults. The 12 to 19 m high Pettino fault scarp (Fig. 5), is considered a post-glacial (ca. 18 ka) feature (e.g., Dramis, 1983; Giraudi and Frezzotti, 1997). Therefore, we calculate a long-term slip rate of the Pettino fault between 0.6 and 1.1 mm/yr.

The distribution of slope in S1, S3 and S4 (Figs. 8 and 9) record an increase in dip (from less than 35° to 45°, on average) in the lowest 4-5 m of the scarps. Such higher slope zone may represent a fresh fault scarp (see Fig. 1) possibly associated to the most recent faulting events. The about 10 m high, lower slope zone has the significance of an older, degraded scarp. This type of analysis of slope on active faults may give a quantitative constrain to the interpretation of scarps. As concern the distribution of aspect on the Pettino scarps (Figs. 6 and 9), we underline that the S4 aspect values concentrate in a more restricted range with respect to those of S1 to S3. This datum indicates that the S4 surface have a lower ‘rugosity’. This could be the result of less concentrated erosion processes, associated to a poorly mature surface drainage on S4 (Fig. 3).

Fig. 7 evidences a decrease of slope and an increase of aspect from S1 to S4. This reflects a progressive change in the fault scarp geometry on a length of 1.8 km (Fig. 3). This implies that surface faulting features may show a structural variability on short distances. In the Pettino case,

assuming that the maximum value of aspect in Fig. 7 is orthogonal to the fault strike, the strike change from N133°E to N146°E, i.e. 13° on 1.8 km. The maximum values of slope, which change from 40° (S1) to 34°(S4), could be associated to the changes in strike, thus reflecting a gentle flatting of the fault dip.

In summary, the results of the morphometric analysis on the Pettino fault scarps using airborne LiDAR-derived data highlight the efficacy of our approach in (a) the spatial characterization of scarps, (b) the definition of fault scarp complexity, and (c) understanding the relation among surface ruptures, fault geometry and behavior, and exogenous processes.

Acknowledgments

The LiDAR data was provided by Civil Protection of Friuli Venezia Giulia (Italy). We also thank two anonymous IJGIS reviewers for useful comments and Carlos H. Grohmann for the editorial handling.

References

CINTI, F.R., PANTOSTI, D., DE MARTINI, P.M. PUCCI, S., CIVICO, R., PIERDOMINICI, S., CUCCI, L., BRUNORI, C.A., PINZI, S. AND PATERA, A., 2011, Evidence for surface faulting events along the Paganica fault prior to the 6 April 2009 L'Aquila earthquake central Italy. *Journal of Geophysical Research*, **116**, B07308, doi:10.1029/2010JB007988.

AMOS, C.B., KELSON, K.I., ROOD, D.H., SIMPSON, D.T., ROSE, .S. 2010, Late Quaternary slip rate on the Kern Canyon Fault at Soda Spring, Tulare County, California. *Lithosphere*, **26**, pp. 411-417.

ARROWSMITH, J.R. and ZIELKE, O., 2009, Tectonic geomorphology of the San Andreas Fault zone from high resolution topography: An example from the Cholame segment. *Geomorphology*, doi:10.1016/j.geomorph.2009.01.002.

BARCHI, M., GALADINI, F., LAVECCHIA, G., MESSINA, P., MICHETTI, A.M., PERUZZA, L., PIZZI, A. and TONDI, E. 2000, Sintesi delle conoscenze sulle faglie attive in Italia Centrale: parametrizzazione ai fini della caratterizzazione della pericolosita` sismica. *Gruppo Nazionale per la Difesa di terremoti*, pp. 1-62.

BEGG, J.G. and MOUSLOPOULOU, V., 2010, Analysis of late Holocene faulting within an active rift using lidar, Taupo Rift, New Zealand. *Journal of Volcanology and Geothermal Research*, **190**, pp. 152–167.

BLUMETTI, A.M., BAGNAIA, R., FERRELI, L., GIULIANI, R., MATTONE, M., MICHETTI, A.M., SARVUCCI, R. and VITTORI, E., 1997, Fagliazione superfi ciale e tettonica quaternaria nell'alta Valle dell'Aterno. Abstract at Congress "Tettonica quaternaria del territorio italiano: conoscenze, problemi ed applicazioni", Parma, 25-27 February 1997.

BLUMETTI, A. M., 1995, Neotectonic investigation and evidence of paleosesmicity in the epicentral area of the January-February 1703, central Italy, earthquake. *In*: L. Serva and D. B. Slemmons eds. *Perspectives in paleoseismology*, Association of Engineering Geologists Special Publication, **6**, 83-100.

BLUMETTI, A. M., DI FILIPPO, M., ZAFFIRO, P., MARSAN, P. and TORO B., 2002, Seismic hazard of the city of L'Aquila Abruzzo-central Italy: New data from geological, morphotectonic and gravity prospecting analysis, *Studi Geologici Camerti*, **1**, pp. 7–18.

BULL, W.B., 2007, *Tectonic Geomorphology of Mountains: A New Approach to Paleoseismology*. Wiley-Blackwell, London.

CHAN, Y.C., CHEN, Y.G., SHIH, T.Y. and HUANG, C., 2007, Characterizing the Hsincheng active fault in northern Taiwan using airborne lidar data; detailed geomorphic features and their structural implications, *Journal of Asian Earth Sciences,* **31.3**, pp. 303-316.

CIPOLLARI, P., and COSENTINO, D., 1995., Miocene unconformities in the Central Apennines: geodynamic significance and sedimentary basin evolution. *Tectonophysics*, **252**, pp. 375–389.

CUNNINGHAM, D., GREBBY, S., TANSEY, K., GOSAR, A., and KASTELIC, V., 2006, Application of airborne LiDAR to mapping seismogenic faults in forested mountainous terrain, southeastern Alps, Slovenia. *Geophysical research Letters,* **33**, L20308, doi:10.1029/2006GL027014.

DELONG, S.B., HILLEY, G.E., RYMER, M.J.. and PRENTICE, C., 2010, Fault zone structure from topography: Signatures of en echelon fault slip at Mustang Ridge on the San Andreas Fault, Monterey County, California. *Tectonics*, **29**, TC5003, doi: 10.1029/2010TC002673.

DI LUCCIO, F., VENTURA, G., DI GIOVAMBATTISTA, R., PISCINI, A., and CINTI. F. R. 2010, Normal faults and thrusts re-activated by deep fluids: the 6 April 2009 Mw 6.3 L'Aquila earthquake, central Italy. *Journal of Geophysical Research*, **115**, B06315,doi:10.1029/2009JB007190

DI LUZIO, E., MELE, G., TIBERTI, M.M., CAVINATO, G.P. and PAROTTO, M., 2009, Moho deepening and shallow upper crustal delamination beneath the central Apennines. *Earth Planetary Science Letters*, **280**, pp. 1–12.

DIETRICH, W.E., BELLUGI, D. and ASUA, R.R., 2001, Validation of the Shallow Landslide Model, SHALSTAB, for Forest Management. *In: Land Use and Watershed: Human Influence on Hydrology and Geomorphology in Urban Forest Areas*. *Water Science Application AGU*, **2**, pp. 195-227.

DOGLIONI, C. 1995, Geological remarks on the relationships between extension and convergent geodynamic settings. *Tectonophysics,* **252**, pp. 253–267.

DRAMIS, F., 1983, Morfogenesi di versante nel Pleistocene superiore in Italia: I depositi detritici stratificati. *Geografia Fisica Dinamica Quaternaria*, **6**, pp. 180–182.

EMERGEO WORKING GROUP, 2010, Evidence for surface rupture associated with the Mw 6.3 L'Aquila earthquake sequence of April 2009 central Italy. *Terra Nova*, **22**, pp. 43–51,

FOGLIO CARG 1:50,000, 2009, *Cartografia Geologica Ufficiale*. Foglio CARG 359 L'Aquila.

FRANKEL, K.L., DOLAN, J. F., FINKEL, R. C., OWEN, L. A. and HOEFT, J. S., 2007, Spatial variations in slip rate along the Death Valley-Fish Lake Valley fault system determined from LiDAR topographic data and cosmogenic ^{10}Be geochronology. *Geophysical research Letters,* **34**, L18303, doi:10.1029/2007GL030549.

GALADINI, F. AND GALLI, P., 2000, Active tectonics in the Central Apennines Italy-input data for Seismic Hazard Assessment. *Natural Hazards*, **22**, pp. 225–270.

GALADINI, F., MELETTI, C. and VITTORI, E., 2001, Major active faults in Italy: available surficial data, Netherlands. *Journal of Geosciences,* **80,** pp. 273-296.

GALLI, P., GIACCIO, B., MESSINA, P., PERONACE, E. and ZUPPI, G.M., 2011, Palaeoseismology of the L'Aquila faults central Italy, 2009, Mw 6.3 earthquake: implications for active fault linkage. *Geophysical Journal International*, doi 10.1111/j.1365-246X.2011.05233.x

GHISETTI, F. AND VEZZANI, L., 1999, Depth and modes of Pliocene–Pleistocene crustal extension of the Apennines Italy. *Terra Nova*, **11**, pp. 67–72.

GHISETTI, F. and VEZZANI L., 2002, Normal faulting, transcrustal permeability and seismogenesis in the Apennines Italy. *Tectonophysics*, **348**, pp. 155–168.

GIRAUDI, C. and FREZZOTTI, M., 1997, Late Pleistocene glacial events in the central Apennines, Italy. *Quaternary Research,* **48**, pp. 280–290.

GLENN, N.F., STREUTKER, D.R., CHADWICK, D.J., THACKRAY, G.D. and DORSCH, S.J. 2006, Analysis of LiDAR-derived topographic information for characterizing and differentiating landslide morphology and activity. *Geomorphology*, **73**, pp. 131-148.

HASEGAWA, H., SATO, H.P. and IWAHASHI J., 2007, Continuous Caldera Changes in Miyakejima Volcano after 2001. *Bulletin of Geospatial Information Authority of Japan*, **54**, pp. 60-64.

HAUGERUD, R.A., HARDING, D.J., JOHNSON, S.Y., HARLESS, J., WEAVER, C.S., and SHERROD, B.L. 2003, High-resolution lidar topography of the Puget Lowland, Washington - A bonanza for earth science. *GSA Today*, **13**, pp. 4–10.

HILLEY, G.E., DELONG, S., PRENTICE, C., BLISNIUK, K. and ARROWSMITH, J.R., 2010, Morphologic dating of fault scarps using airborne laser swath mapping ALSM data. *Geophysical research Letters,* **37**, L04301, doi:10.1029/2009GL042044.

KONDO, H., TODA, S., OKUMURA, K., TAKADA, K. and CHIBA, T., 2008, A fault scarp in an urban area identified by LiDAR survey: A Case study on the Itoigawa–Shizuoka Tectonic Line, central Japan. *Geomorphology,* **101**, pp. 731-739.

LAVECCHIA, G., BROZZETTI, F., BARCHI, M., MENICHETTI, M. AND KELLER, J.V.A., 1994, Seismotectonic zoning in east-central Italy deduced from an analysis of the Neogene to present deformations and related stress fields. *Geological Society of America Bulletin*; **106**, pp. 1107-1120

PATACCA, E., SCANDONE, P., DI LUZIO, E., CAVINATO, G., and PAROTTO, M., 2008, Structural architecture of the central Apennines: Interpretation of the CROP 11 seismic profile from the Adriatic coast to the orographic divide. *Tectonics*, **27**, TC3006, doi:10.1029/2005TC001917.

PIZZI, A., and GALADINI, F., 2009, Pre-existing cross-structures and active fault segmentation in the northern-central Apennines Italy. *Tectonophysics*, **476**, pp. 304–319

ROBERTS, G. P. and MICHETTI, A.M., 2004, Spatial and temporal variations in growth rates along active normal fault systems: an example from The Lazio–Abruzzo Apennines, central Italy. *Journal of Structural Geology*, **26**, pp. 339–376.

SALLENGER, A.H., KRABILL, W., BROCK, J., SWIFT, R., JANSEN, M., MANIZADE, S., RICHMOND, B., HAMPTON, M., and ESLINGER, D., 1999, Airborne laser study quantifies El Niño-induced coastal change. *Eos Transactions American Geophysical Union*, **80**, pp. 92–93.

SHERROD, B.L., BROCHER, T.M., WEAVER, C.S., BUCKNAM, R.C., BLAKELY, R.J., KELSEY, H.M., NELSON, A.R. and HAUGERUD, R., 2004, Holocene fault scarps near Tacoma, Washington, USA. *Geology,* **32**, pp. 9-12.

STEWART, I.S. and HANCOCK, P.L., 1990, What is a fault scarp? *Episodes*, **13**, pp. 256–263.

VEZZANI, L. AND GHISETTI, F., 1998, Carta Geologica dell_Abruzzo, Scala 1:100,000. *SELCA*, Firenze.

WALLACE, R.E., 1977, Profiles and ages of young fault scarps, north-central Nevada. *Geological Society of America Bulletin,* **88**, pp. 1267-1281.

Figure captions

Figure 1. a) Sketch illustrating an idealized composite fault scarp profile and its time evolution. b) Different view of a composite fault scarp (simplified from Stewart and Hancock, 1990).

Figure 2. Structural schematic map of the L'Aquila town region (Central Apennines, Italy) with major faults and historical earthquakes epicenters. The faults located between L'Aquila and Montereale towns belong to the Upper Aterno fault system. Quaternary basins include Pleistocene breccias and lacustrine deposits. The remnant areas are Jurassic to Miocene limestones and marls, and Miocene sandstones. The dashed rectangle includes the study area shown in Fig. 3. Modified from Cinti e *et al*. (2011) and reference therein.

Figure 3. Shaded relief from LiDAR data of the area including the central sector of the Pettino fault (see Fig. 2). Red lines (numbered from S1 to S4) are the base of the fault scarps selected for this study. Black lines are the base of the fault scarps mapped but not included in our analysis.

Figure 4. 3D view of the selected S1 to S4 Pettino fault scarps (location in Fig. 3). The S1 to S4 bottom and crest are delineated with shaded lines; the elevation and distance along strike parameters are also shown.

Figure 5. Distance along strike vs. elevation of the S1 to S4 Pettino fault scarps.

Figure 6. Box-plot diagrams summarizing the statistics of altitude (m a.s.l.), slope (°) and aspect (°) parameters from LiDAR-derived DEM in the S1 to S4 scarps.

Figure 7. Circular plots of the density contours (in %) of the distribution of slope and aspect values (calculated from DEM) of pixels belonging to the S1 to S4 scarps.

Figure 8. Distribution of the slope (to the left) and aspect (to the right) values on the S1 to S4 scarp surface calculated from DEM.

Figure 9. Elevation vs. slope (up) and aspect (down) pseudo-circular plots for S1 to S4 scarps from DEM-extracted data. Each point represents a pixel.

Table 1. Summary of the LiDAR acquisition parameters.

System	Optech ALTM 3100 EA
Operating altitude	80 – 3500 m
Vertical accuracy	10 cm < 1000 m (1 σ) 15 cm < 2000 m (1 σ) 20 cm <3000 m (1 σ)
Horizontal accuracy	1/5500 x flying altitude (1 σ)
Range resolution	1 cm
Scan angle	Variable from 0 to ± 25°
Swath width	Variable from 0 m to 0.93 x altitude
Angular resolution	0.01°
Scan frequency	Variable, maximum 70 Hz
Laser wavelength	1064 nm
Laser repetition rate	Variable from 33 to 100 kHz
Beam divergence	Variable: 0.2 mrad (1/e) or 0.8 mrad (1/e)
"Eye safe" altitude limit	80 m - 0.8 mrad 400 m - 0.2 mrad
Intensity	Measurement of intensity of each pulse received
Collected data	Simultaneous measurement in range of first and last pulse for each pulse emitted
Laser classification	Class IV laser products (FDA CFR 21)
GPS receiver	Internal Novatel Millennium DL
Power requirements	28 VDC @35 A peak
Operating temperature	15-35 °C
Humidity	0-95 % non-condensing

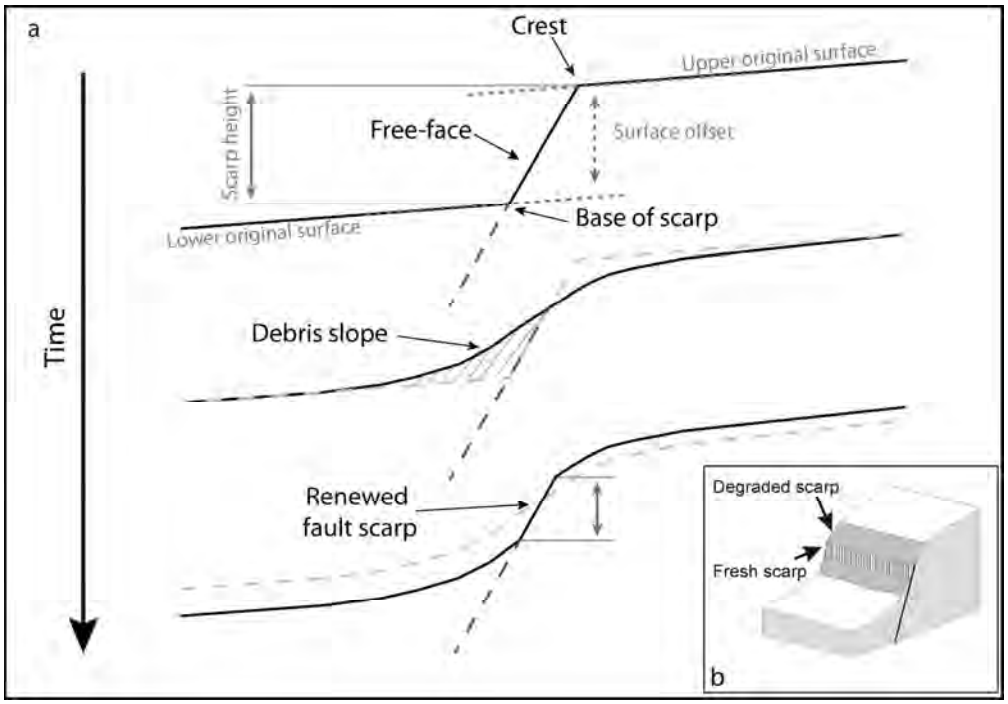

Figure 1. a) Sketch illustrating an idealized composite fault scarp profile and its time evolution. b) Different view of a composite fault scarp (simplified from Stewart and Hancock, 1990).
133x92mm (300 x 300 DPI)

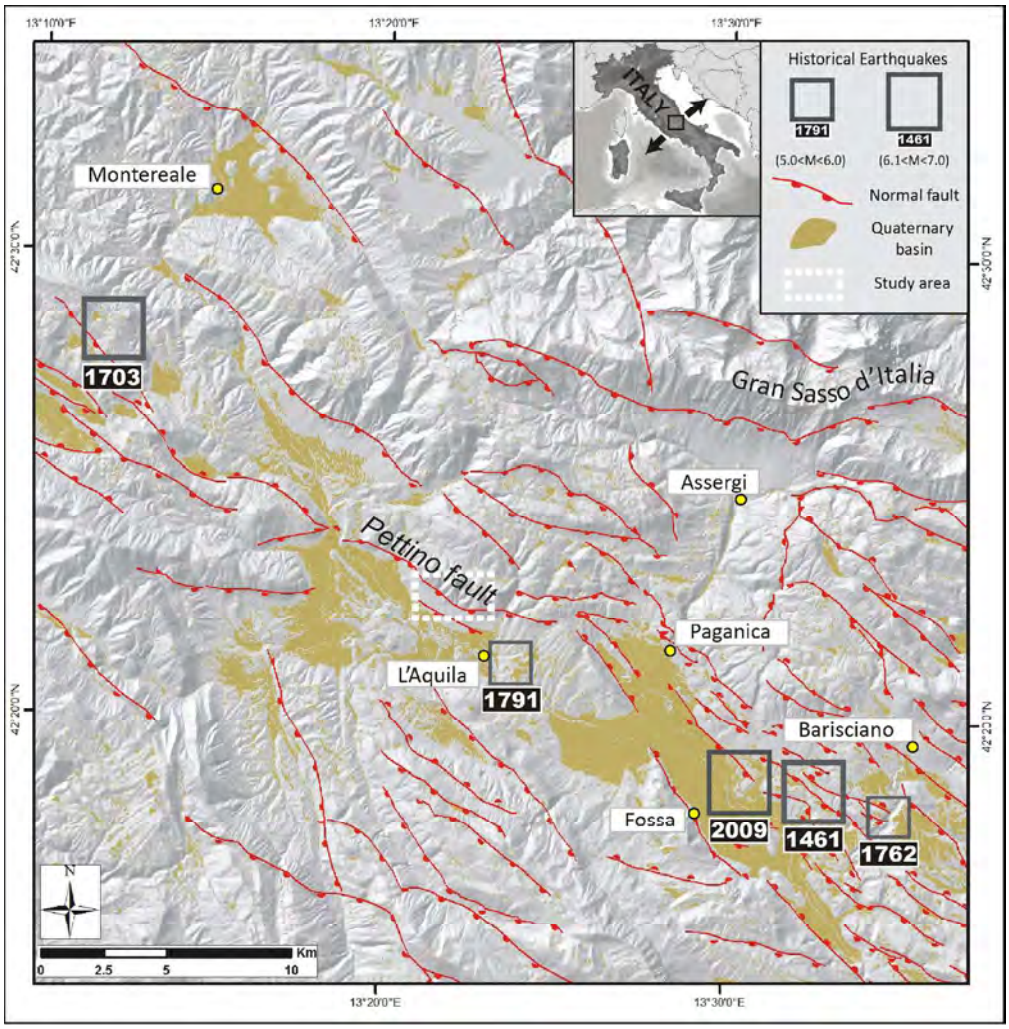

145x147mm (300 x 300 DPI)

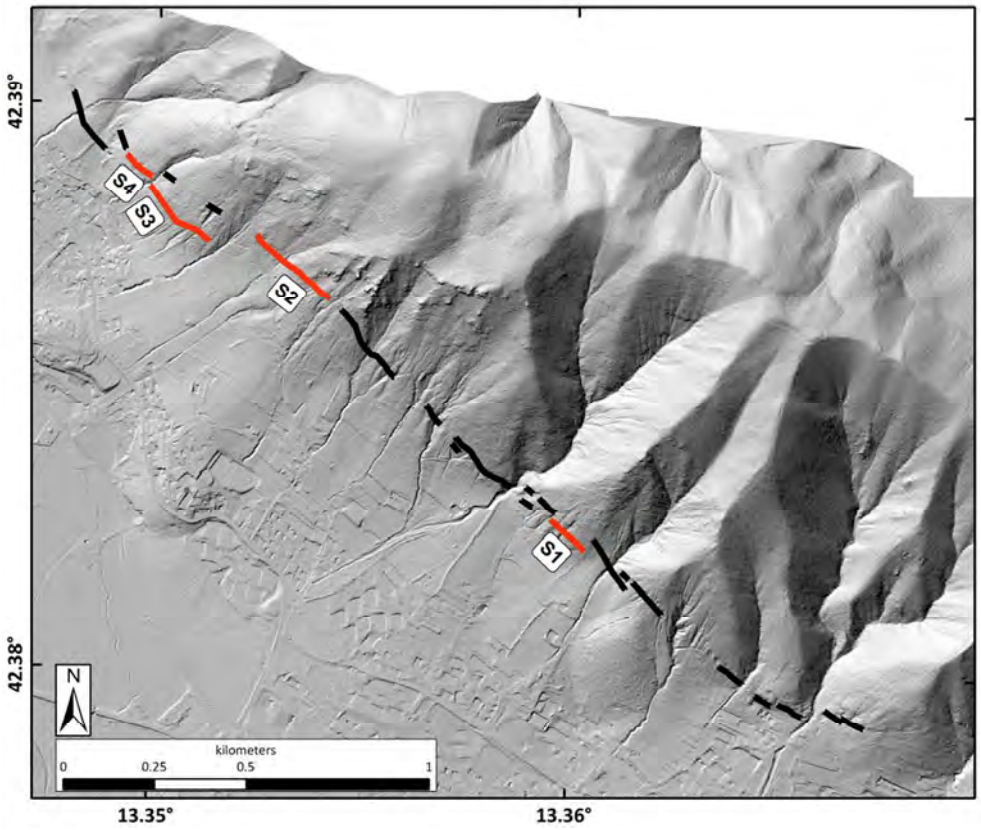

99x84mm (300 x 300 DPI)

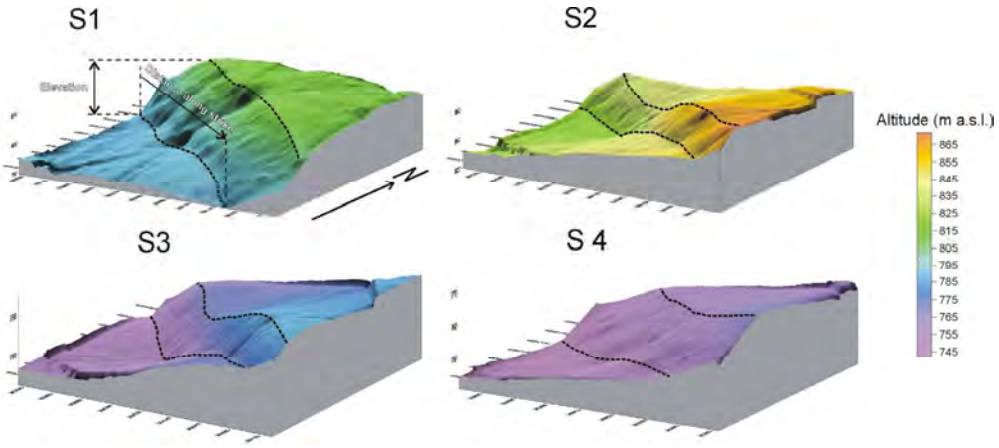

157x68mm (300 x 300 DPI)

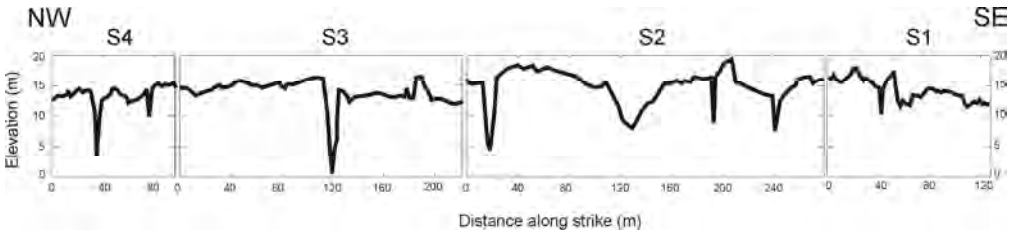

200x44mm (300 x 300 DPI)

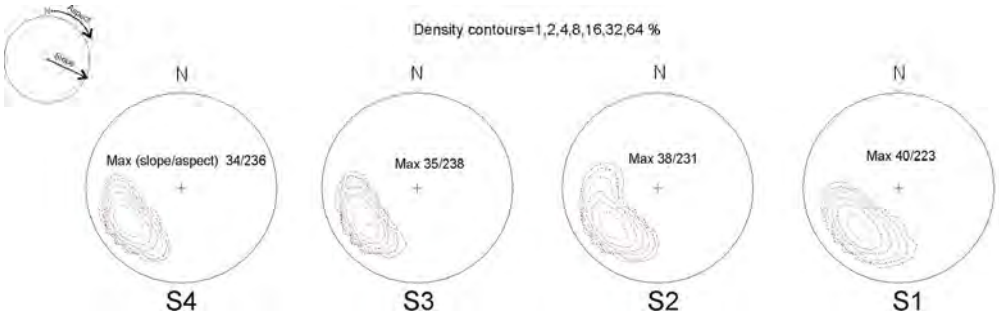

187x57mm (300 x 300 DPI)

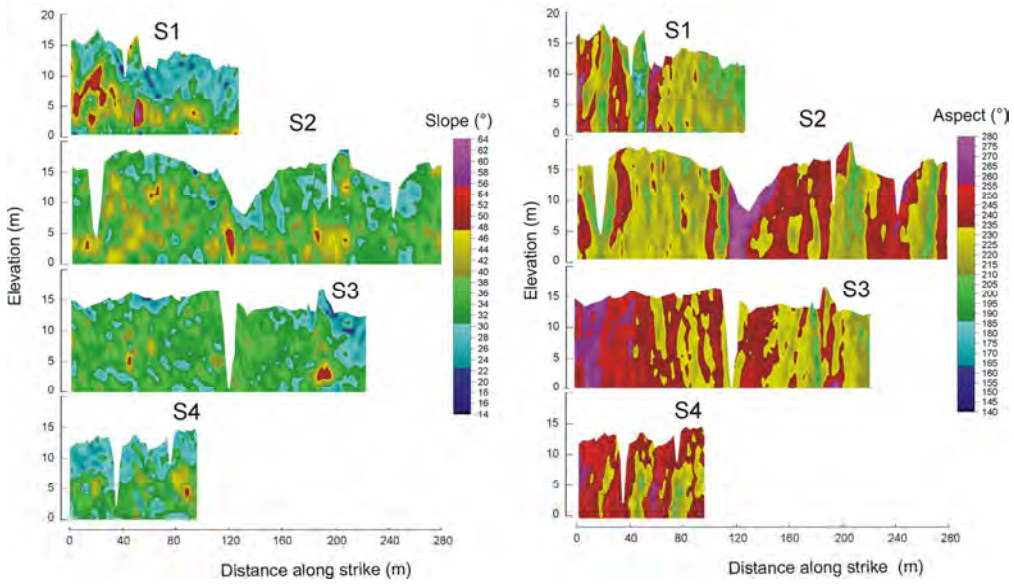

137x79mm (300 x 300 DPI)